

**Toward a precision medicine in Alzheimer's Disease:
blood phenomic fingerprint for diagnostic and
therapeutic developments**

Dissertation

Zur Erlangung des Doktorgrades (Dr. rer. nat.)

Der Mathematisch-Naturwissenschaftlichen Fakultät

Der Rheinischen Friedrich-Wilhelms-Universität zu Bonn

im Fach:

Molekulare Biomedizin

Vorgelegt von:

Ahmed Hameed Al-Saeedi

aus

Bagdad - Irak

Bonn 2020

Diese Arbeit wurde am ... mit Zustimmung der Mathematisch-Naturwissenschaftlichen Fakultät der Rheinischen Friedrich-Wilhelms-Universität Bonn angefertigt.

1. Gutachter: Prof. Dr. Joachim L. Schultze
2. Gutachterin: Prof. Dr. Anja Schneider

Promotionsdatum: 23.03.2020

Erscheinungsjahr: 2020

Diese Arbeit wurde mit Unterstützung des Deutschen Akademischen Austauschdienstes (DAAD) gedruckt.

Acknowledgment

First and foremost, I would like to express my sincere gratefulness to my eternal cheerleader, my supervisor **Dr. Eugenio Fava** for the continuous support of my Ph.D. study and related research, motivation, and immense knowledge. Deep grateful goes to my mentor **Dr. Wera Roth** for her patience and very detailed guidance. Her guidance helped me in all the times of research and writing of this thesis. I will miss our interesting and long-lasting discussions about the project.

I would like to thank my co-supervisor **Prof. Dr. med. Joachim Schultze**, his input matured the project a lot. **Prof. Dr. med. Anja Schneider** was more than a project collaborator, she brought always inimitable suggestions that helped to shape the project.

My sincere thanks also go to **Dr. Philip Denner** and **Birgit Kurkowsky**, who provided me the opportunity to join their automation facilities at DZNE Bonn. Without their precious support, it would not be possible to conduct this research.

My truthful appreciations to **Dr. Christoph Möhl** and **Manuel Schölling**, from the data and image analysis facility, who gave me a lot of support during the post-experimental work.

A very special gratitude goes out to all down at the Research Funders of the project, particularly **German Academic Exchange Service (DAAD)** for funding me and my family stay in Germany while I'm doing my PhD.

The **group members** and the rest of automation **co-workers** have been a source of friendships as well as good advice and collaboration. I owe them for the stimulating discussions, for the hours we were working together, and for all the fun we have had in the last four years.

Last but not the least, I would like to thank my family: My father **Hameed AlSaeedi**, who keeps supporting me to bring my dreams into truths. My Mom **Rabab Hussein**, the unlimited source of emotional support. My wife **Zainab Alhashemi** and my kids **Haider** and **Fatima**, who decided generously to join my adventure "Discover Deutschland" and been a source of inspiration during the hard days. To my family I would like to say:

عائلتي الكبيرة وعائلتي الصغيرة: لولا دعمكم المتواصل ما كنت قادر على تحقيق احلامي. شكرا لكم من القلب ❤️

Table of content

TABLE OF CONTENT	II
SUMMARY	V
1. INTRODUCTION	1
1.1. ALZHEIMER'S DISEASE (AD): THEORETICAL BACKGROUND	1
1.1.1. AD PATHOLOGY	1
1.1.2. THE ROLE OF INFLAMMATION IN AD PATHOLOGY	3
1.2. BIOMARKERS OF AD	5
1.2.1. DEFINITION OF BIOMARKERS	5
1.2.2. REVIEW OF CURRENT BIOMARKERS FOR AD	5
1.2.3. BLOOD-BASED BIOMARKERS OF AD ARE NEEDED FOR DIAGNOSTIC AND THERAPEUTIC DEVELOPMENTS	8
1.3. PRECISION MEDICINE FOR AD	10
1.3.1. DEFINITION OF PRECISION MEDICINE	10
1.3.2. BIOMARKER-GUIDED PRECISION MEDICINE FOR AD	13
1.4. STUDYING THE IMMUNE SYSTEM FOR BIOMARKER DEVELOPMENT AND PRECISION MEDICINE IN AD	14
1.4.1. THE IMMUNE SYSTEM	14
1.4.2. TOLL-LIKE RECEPTOR AND INFLAMMASOME ARE KEY PLAYERS IN THE INNATE IMMUNITY	16
1.4.3. THE ROLE OF INFLAMMASOME IN AD PATHOLOGY	18
1.4.4. TRANSCRIPTOME ANALYSIS TO STUDY IMMUNE-ASSOCIATED PATHWAYS	20
1.4.5. DYNAMIC INTERACTION OF CNS AND PERIPHERAL IMMUNE SYSTEM	21
1.5. HUMAN PERIPHERAL BLOOD MONONUCLEAR CELLS (PBMCs) AS A PROXY FOR THE IMMUNE SYSTEM	22
1.5.1. HUMAN PBMCs AS A HUMAN-DERIVED CELL MODEL	22
1.5.2. IMAGE ANALYSIS AS A TOOL FOR CELL-BASED ASSAY	23
1.5.3. SUPERVISED CLASSIFIER FOR THE CHARACTERIZATION OF PBMC CELLULAR COMPOSITION	27
1.6. MULTIVARIATE ANALYSIS OF THE MULTI-PARAMETRIC CELL-BASED ASSAY	30
1.6.1. ADVANTAGE OF MULTIVARIATE OVER THE UNIVARIATE ANALYSIS	30
1.6.2. CLUSTER ANALYSIS OF THE MULTI-PARAMETRIC CELL-BASED ASSAY	31
2. THE STUDY OBJECTIVE	33
3. MATERIALS AND METHODS	34
3.1. SUPERVISION AND TEAM CONTRIBUTIONS	34
3.2. MATERIALS	34
3.2.1. PATIENT COHORT	34
3.2.2. HEALTHY VOLUNTEER GROUP	35
3.2.3. REAGENTS	35
3.2.4. ANTIBODIES	36
3.2.5. ASSAY KITS	36
3.2.6. RECIPES	36
3.3. METHODS	37

3.3.1.	ISOLATION OF PBMCs FROM BUFFY COATS	37
3.3.2.	CELL COUNTING	38
3.3.3.	THE RECOVERY RATE OF VIABLE PBMCs AFTER THAWING	38
3.3.4.	PBMC CELL-BASED ASSAY	39
3.3.4.1.	Testing the automation platform	39
3.3.4.2.	Cell suspension and assay reagent preparations	40
3.3.4.3.	Automated high content screen assay	40
3.3.4.4.	Immunofluorescence staining	41
3.3.4.5.	PYCARD-TNF α staining	41
3.3.4.6.	Cell surface marker staining	42
3.3.4.7.	Confocal microscopy	42
3.3.4.8.	Cytokine measurements	42
3.3.4.9.	Supernatant collection for cytokine measurement	42
3.3.4.10.	Homogeneous Time Resolved Fluorescence (HTRF)-based assay for cytokine measurement	43
3.3.4.11.	AYOXXA LUNARIS™ Human 6-Plex Cytokine assay	43
3.4.	IMAGE ANALYSIS	43
3.4.1.	CONVENTIONAL SOFTWARE-BASED IMAGE ANALYSIS	43
3.4.2.	DEEP LEARNING APPROACH FOR PBMC SUBSETS CHARACTERIZATION	44
3.5.	SCREENING ASSAY OF PATIENT SAMPLES	45
3.6.	RNA-SEQ ASSAY	46
3.6.1.	SAMPLE PREPARATION	46
3.6.2.	LIBRARY GENERATION AND SEQUENCING	46
3.7.	STATISTICAL ANALYSIS AND MATHEMATICAL CALCULATIONS	47
3.7.1.	STATISTICAL ANALYSIS	47
3.7.2.	DATA NORMALIZATION TO MONOCYTE NUMBER	47
3.7.3.	CALCULATION OF THE COEFFICIENT OF VARIATION FOR INTER-ASSAY PRECISION	47
3.8.	CLUSTER ANALYSIS	48
3.9.	SOFTWARE	49
4.	RESULTS	50
<hr/>		
4.1.	PBMCs AS A PROXY FOR SYSTEMIC IMMUNE CHANGES DURING AD PATHOLOGY	50
4.1.1.	THE ROLE OF TOLL-LIKE RECEPTOR AND INFLAMMASOME IN AD PATHOLOGY	56
4.1.2.	QUANTITATIVE ANALYSIS OF THE INFLAMMASOME ACTIVATION ASSAY	59
4.1.3.	HOMOGENOUS CYTOKINE ASSAY	64
4.1.4.	ASSAY AUTOMATION AND VALIDATION	67
4.1.4.1.	Manual conduction versus automated cell-based assay	67
4.1.4.2.	Validation of the automated cell-based assay: intra-day variation	69
4.1.4.3.	Validation of the automated cell-based assay: inter-day variation	70
4.1.4.4.	Optimization of the automated cell-based assay	72
4.1.5.	THE INTER-INDIVIDUAL VARIATION OF THE HEALTHY PBMC DONORS	76
4.2.	DEVELOPMENT OF AN IMAGE ANALYSIS WORKFLOW TO ASSESS THE CELLULAR COMPOSITION OF A GIVEN PBMC SAMPLE	81
4.2.1.	CELL SURFACE MARKERS FOR PBMC SUBSETS CHARACTERIZATION	81
4.2.2.	CELL-TYPE CLASSIFICATION USING A MACHINE LEARNING APPROACH	85
4.3.	THE PATIENT COHORT ANALYSIS	91
4.3.1.	UNIVARIATE ANALYSIS OF THE PATIENT COHORT	93
4.3.2.	AGGREGATED DATA ACCORDING TO THE DISEASE DIAGNOSIS	103
4.3.3.	TRANSCRIPTOME ANALYSIS CAN DISSECT THE HEALTHY VERSUS DISEASE SAMPLES	106

4.3.4.	THE MULTI-PARAMETRIC ANALYSIS	108
5.	<u>DISCUSSION</u>	112
5.1.	STATE OF THE ART OF AD BIOMARKERS	112
5.2.	THE HUMAN PBMC <i>EX VIVO</i> ASSAY AS A PROXY FOR THE IMMUNE RESPONSE DURING AD	114
5.3.	A NOVEL ASSAY DESIGN TO STUDY THE IMMUNE SYSTEM	114
5.4.	MAXIMIZING THE USE OF PATIENT MATERIALS VIA A SIMULTANEOUS ASSAY WORKFLOW	115
5.5.	CHARACTERIZATION OF THE PBMC SAMPLE CELLULAR COMPOSITION	116
5.5.1.	CHARACTERIZATION OF PBMC CELLULAR COMPOSITION	116
5.5.2.	NOVEL MICROSCOPICAL PROOF THAT MONOCYTES MOUNT AN INFLAMMASOME RESPONSE	118
5.6.	SCREENING OF A PATIENT COHORT WITH THE ESTABLISHED PBMC ASSAY	119
5.6.1.	UNIVARIATE ANALYSIS FAILED TO BRING A PREDICTIVE MODEL OF AD	121
5.6.2.	TRANSCRIPTOME ANALYSIS CAN DISSECT HEALTHY VERSUS DISEASE SAMPLES	121
5.6.3.	MULTI-PARAMETRIC ANALYSIS CAN PROVIDE A PREDICTIVE MODEL OF AD	122
5.6.3.1.	Prediction features are therapeutic targets as well	123
5.7.	PBMC <i>EX VIVO</i> ASSAY FOR PRECISION MEDICINE OF AD	123
5.8.	THE <i>EX VIVO</i> PBMC ASSAY FOR DRUG DISCOVERY	124
5.9.	LIMITATIONS OF THE STUDY	125
5.10.	OUTLOOK	125
6.	<u>BIBLIOGRAPHY</u>	127
7.	<u>APPENDIX</u>	142
	INDEX I: FULL TABLE OF CLINICAL INFORMATION OF THE DISEASE DONOR (DD) SAMPLES	142
	INDEX II: ALL FEATURES THAT WERE COLLECTED FROM THE MULTI-PARAMETRIC ANALYSIS	143
8.	<u>LIST OF ABBREVIATIONS</u>	147
9.	<u>LIST OF FIGURES</u>	151
10.	<u>LIST OF TABLES</u>	152

Summary

There is an unmet clinical need to identify reliable blood biomarkers for Alzheimer's Disease (AD) that can be used for diagnostics and therapeutic purposes.

The complex nature of AD, single-readout approaches along with the inter-individual variation are among the major challenges for developing biomarkers towards stratification of AD patients. A multi-parametric immune-based assay combined with the rapidly advancing machine learning multivariate analysis presents itself as a powerful approach for blood-based disease detection.

In this study, peripheral blood mononuclear cells (PBMCs) have been used as a proxy for the peripheral immune changes in disease and healthy groups. Our PBMC *ex vivo* assay monitors the activities of the Toll Like Receptor (TLR) and the inflammasome as well as it provides a platform to characterize the gene expression profile using (RNA-seq) as well as the cellular composition. TLR and inflammasome activities were monitored via a high-content phenotypic assay, cell profiling and imaging-based approaches, flanked by a homogeneous readout, i.e. cytokine assay. The utilized multi-readouts workflow enables a detailed phenotypic description for the PBMC samples, aiming to identify a phenotype fingerprint that could be used in early diagnosis of the disease.

The cell-based assay was designed to overcome challenges associated with the heterogeneous pathological phenotype resulting from variable immune system responses using an automated platform of DZNE Bonn to scale-up the assay capacity and improving its reproducibility. The assay was validated against day-to-day variations and further enhanced by introducing a time-lapse analysis showing that differential response of monocyte, but not T or B cells, to the inflammasome activation. Moreover, an image-based analysis was established to characterize the cellular composition of investigated samples using a supervised neural U-Net-based pixel classifier.

The established PBMC assay was used to analyze a small pilot cohort of 20 patients (AD + depression + psychiatric controls) + three samples of healthy donors. The assay readouts were integrated into a feature vector analyzed with Support Vector Machine classifier in order to help in predicting the disease status for each of the tested samples.

The predictive model provides an excellent platform with an estimated 91% accuracy. The classifier precisely predicted and dissected the Samples of AD patients (n=6) from

depressed samples (n=5). Furthermore, the classifier assigned the most important features (readouts) for disease prediction, e.g. intracellular TNF production, that could be investigated for further therapeutic development. Nevertheless, the workflow needs to be validated with a larger cohort of AD patients as well as other immune related diseases in order to validate the selectivity and specificity of the platform. our PBMC workflow has a huge potential to be a key tool towards precision medicine in AD by patient stratification via immune phenotyping.

1. Introduction

1.1. Alzheimer's Disease (AD): Theoretical background

1.1.1. AD pathology

Alzheimer's Disease (AD) is a neurodegenerative disorder and it was described for the first time by the German psychiatrist Alois Alzheimer in 1907. At that time, he introduced a case-report of his patient Auguste Deter, a 51-year-old lady from Frankfurt that showed symptoms of progressive cognitive impairment, hallucinations, focal symptoms, delusions, and psychosocial incompetence. In his case-report, Alois Alzheimer clarified two characteristic hallmarks of AD patients: amyloid senile plaques that aggregate at synaptic space and neurofibrillary tangles that aggregates within the nerve body (Preethi and Vinyaga Moorthi 2017).

After more than a century of the first report about AD, there is still neither clear cause nor effective cure for AD. On the other hand, the number of AD patients is increasing as the world's population is continuously aging, and more individuals approach the age margin for this age-related disorder (Cummings, Lee et al. 2017). About 44 million people worldwide are currently living with AD (Alzheimer's 2019), and the number of patients is expected to exceed 100 million in the next 30 year (Cummings, Lee et al. 2017).

The development of senile plaques and neurofibrillary tangles, mainly in the hippocampus, are still considered the cornerstone of AD pathology (Chen, Guo et al. 2019). The senile plaques are formed essentially from the aggregation of amyloid beta ($A\beta$), a peptide of 36-43 amino acids. $A\beta$ is produced from the cleavage of the Amyloid Precursor Protein (APP) by the effects of β - and γ -secretases (**Figure 1**) (Heppner, Ransohoff et al. 2015). The insufficient clearance of soluble $A\beta$ monomers leads to accumulation and formation of insoluble $A\beta$ isoforms like $A\beta_{42}$. The latter represents the main component of senile plaques in some memory-related regions in the brain, e.g. the hippocampus. $A\beta_{40}$ is another isoform that ends up into fibrils aggregation. But, $A\beta_{42}$ is more amyloidogenic than $A\beta_{40}$ (causing faster fibril formation) and has a higher cellular toxicity. Of note, a biochemical analysis showed that aggregation of $A\beta_{42}$ can be inhibited by $A\beta_{40}$ (Qiu, Liu et al. 2015). On the other hand, the neurofibrillary tangles compose mainly from the filamentous aggregation of the phosphorylated microtubule-associated protein tau (known as tau). These tau aggregations stress the cellular organelles,

disturbing some neuronal functions like axonal transportation and leading eventually to cellular death (Šerý, Povová et al. 2013, Agamanolis 2016). It is still not clear what are the underlying mechanisms that trigger the initial conversion of naturally soluble proteins into filamentous insoluble aggregates of A β and phosphorylated tau (P-tau) (Brettschneider, Del Tredici et al. 2015).

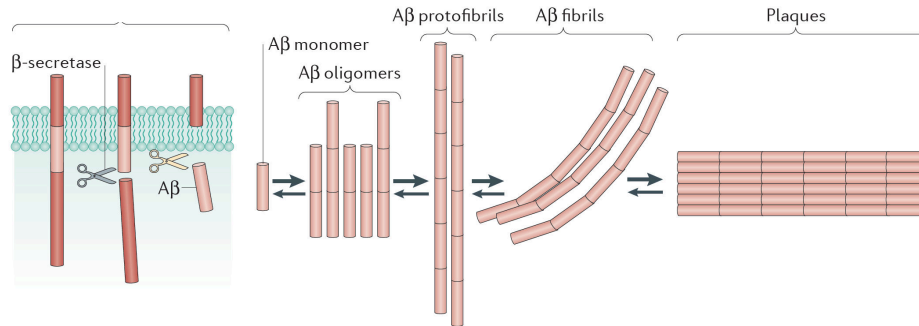


Figure 1: The formation of senile plaques.

β -secretases cleaves Amyloid Precursor Protein (APP) into amyloid beta (A β) monomers. A β aggregation leads to the formation of senile plaques. Adapted from (Heppner, Ransohoff et al. 2015).

The distribution of the A β plaques and neurofibrillary tangles within different brain areas over different disease stages was reported first in 1991 by H. Braak and E. Braak and it is known as Braak staging (Braak and Braak 1991). The Braak staging is comprised of six pathological stages indicating neuropathological Alzheimer's related changes. The first two stages are prodromal (transentorhinal stages I–II) in which transentorhinal layer is mildly altered, with almost no clinical sign of AD. The early moderate limbic stages (stages III–IV) are characterized by a striking affection of the transentorhinal region and proper entorhinal cortex and moderate changes in the hippocampus (mild cognitive impairment-MCI to early AD). Lastly, there is the moderate-late stage of isocortical changes (stages V–VI) where almost all isocortical association areas are destructed (the appearance of clinical AD) (Braak and Braak 1991). Furthermore, during the disease course, many brain regions undergo macroscopic atrophy including the hippocampus, amygdala, and associative regions of the neocortex (Calderon-Garciduenas and Duyckaerts 2017).

AD was investigated on a genetic level and it has been divided into two types: “sporadic” Alzheimer's disease (sAD) representing the vast majority of AD patients and familial Alzheimer's disease (fAD) which represents the minority (5%–10%) of AD cases (Bagyinszky, Youn et al. 2014). The genes Amyloid Precursor Protein (APP), presenilin1

(PSEN1), and presenilin2 (PSEN2) have been considered as major risk factors for fAD. Apolipoprotein E (ApoE) on the other hand has been considered as the most correlated risk factor for sAD (Lista, O'Bryant et al. 2015). Particularly, the APOE E4 allele has been linked to the pathology of AD (Bagyinszky, Youn et al. 2014). Salmon and colleagues have found that APOE E4+ participants revealed faster cognitive decline than the matched controls in a 4-year evaluation study (Salmon, Ferris et al. 2013). These four genes (APP, PSEN1, PSEN2, and APOE E4) were accepted as disease risk factors rather than direct indicators for disease occurrence (Bagyinszky, Youn et al. 2014). A substantial finding that emphasizes the role of both genetic mutations and immune dysfunction during AD pathology was the association between mutations in the encoding gene for the triggering receptor expressed in myeloid cells 2 protein (TREM2) and an increased risk of AD (Villegas-Llerena, Phillips et al. 2016). This finding emphasizes also the immune related role to AD pathology since the microglial cell surface receptor, TREM2 activates the signaling pathway ITAM (immunoreceptor tyrosine-based activation motif) via its trans-membrane binding partner TYROBP (also called DAP-12). The effect size of TREM2 mutation was similar to that of APOE mutation as a risk factor associated with AD (Villegas-Llerena, Phillips et al. 2016).

1.1.2. The role of Inflammation in AD pathology

Besides the formation of A β plaques and neurofibrillary tangles, a prominent response of the innate immune system and the activation of inflammatory processes were noticed in the brains of AD patients (Wyss-Coray 2006). Post-mortem studies revealed an increased expression of inflammatory mediators in brains of AD patients (Hoozemans, Veerhuis et al. 2011). Additionally, many epidemiological reports linked the use of anti-inflammatory drugs with reduced risk for AD (Hoozemans, Veerhuis et al. 2011).

The immune response, within the CNS, during AD is repeatedly labeled as “neuroinflammation”. It is currently well accepted that neuroinflammation is involved in the disease course (Labzin, Heneka et al. 2018, Sharman, Gyengesi et al. 2019). Nevertheless, it is still controversial whether the immune response is a cause or a consequence of the AD pathology. For example, A β aggregations have been reported to stimulate microglial cells to release IL-1 β which triggers an immune cascade. This means

that the neuroinflammation is the downstream event of A β aggregations (Heppner, Ransohoff et al. 2015). Vice versa, other studies showed that impaired function of microglial, which could occur due to aging process, causes inflammation and release of IL-1 β and this contributes to the development of neurodegeneration (Labzin, Heneka et al. 2018). In parallel, IL-1 β release from activated microglia has been reported to contribute to the phosphorylation of tau protein (Zilka, Kazmerova et al. 2012).

At the genetic level, there is currently an increased number of reports that identify changes in the differential expression profile of immune-associated genes. For instance, more than 20 genes have been characterized, via Genome Wide Association Studies (GWAS), to be associated with an increased risk of late-onset AD (LOAD). These include genes associated with immune responses (ABCA7, CD33, CR1, MS4A, CLU, EPHA1 and HLA-DRB5-HLA-DRB1), and encoding genes for proteins that are highly expressed in microglia (Sekar, McDonald et al. 2015).

In addition to neuroinflammation, the peripheral immune response was also reported to be involved in AD pathology. Krstic and colleagues showed that continuous activation of the peripheral immune system leads to the development of AD-like pathological changes in wild type (WT) mice (Krstic, Madhusudan et al. 2012). A recent analysis of 1,633 people showed that there is a positive association between frequent mid- and late-life peripheral inflammation and brain volume shrinkage (Walker, Hoogeveen et al. 2017). Of note, proinflammatory mediators, like IL-6 and TNF α , released via activation of the innate and adaptive immunity, have been reported to cross the blood-brain barrier (BBB) and activate microglial cells, contributing to an exacerbation of neurodegeneration (Boyko, Troyanova et al. 2017). Moreover, T and B cells have been noticed to infiltrate into choroid plexus (CP) and meninges during AD. Infiltrated CD4⁺ T cells play a role in maintaining cognitive and behavioral capacity (Cao and Zheng 2018). In particular, secreted IFN γ from CD4⁺ T helper cells I (Th I) is important for the social behavior by supporting neuronal circuits. Also, T helper cells II release IL-4 to stimulate astrocytes to express BDNF and regulating meningeal dendritic cells, facilitates eventually learning (Cao and Zheng 2018). Therefore, the peripheral immune response, via T cell infiltration, seems to play a pivotal role in regulating homeostatic functions of the brain. Despite those evidences, it is still not clear at which stage the immune response is started, but there is certainly a wide range of

immunological changes that can be studied for both diagnostic and therapeutic developments of AD.

1.2. Biomarkers of AD

1.2.1. Definition of biomarkers

The term “biomarker”, a combination of “biological marker”, is an accurately and reproducibly measured feature that indicates, objectively, the biological status observed from outside the patient. There is an enormous number of considerably overlapping biomarker’ definitions in the literature. Nonetheless, the National Institutes of Health Biomarkers Definitions Working Group has introduced, in 1998, a comprehensive definition for biomarker as “a characteristic that is objectively measured and evaluated as an indicator of normal biological processes, pathogenic processes, or pharmacologic responses to a therapeutic intervention”(Strimbu and Tavel 2010).

In addition to diagnostic purposes, biomarkers are of high importance for clinical trials as they are used to identify patients that are recruited for a trial. Besides, biomarkers are used to evaluate target engagement and assessing pharmacological hypothesis during therapeutics development (Cummings, Lee et al. 2017).

Biomarkers could be measured using biofluids like urine, cerebrospinal fluid (CSF), sputum, and blood. Blood biomarkers are of particular interest as the blood is easily accessible and it represents a proxy for a lot of physiological and pathological conditions as many biological aspects are reflected in the blood like inflammation states, metabolic activities, and organ functions (Strimbu and Tavel 2010, FDA 2014).

1.2.2. Review of current biomarkers for AD

AD is a type of dementia which is characterized by progressive decline of cognitive functions. The disease could be clearly detected via the clinical evaluation of the noticeable deterioration of cognitive functions. Additionally, the brain imaging techniques such as Positron-emission tomography (PET) and magnetic resonance imaging (MRI) are now widely used to diagnose AD (Snyder, Carrillo et al. 2014). PET is a nuclear-medicine-based imaging technique. It works via a radioactive substance, called a radiotracer, injected into the body to be tracked by the PET scanner. The radiotracer which was

absorbed by the tissue is analyzed to assess the metabolic status, the physiological (functional) conditions, the anatomical (structural) circumstances and the tissue biochemical properties (Hopkins 2019). PET scan is widely used to evaluate AD pathophysiology by characterizing the accumulation of the A β peptide within the brain along with neurofibrillary tangles of P-tau protein, although there is still no established Tau PET Tracer yet (Mosconi, Berti et al. 2010). Chien and colleagues introduced ¹⁸F-flortaucipir as a first published PET tracer with a capacity to quantify and visualize neurofibrillary tangles in AD patients (Chien, Bahri et al. 2013). ¹⁸F-flortaucipir (also known as ¹⁸F-AV-1451 or 18F-T807) is now an extensively used PET tracer for tau tangles in divers research studies. Nonetheless, the drawback of this tracer is that its absorption steady state is longer than the standard imaging time (Honer, Gobbi et al. 2018). Of note, Vogel and colleagues have recently studied spatial patterns of the tau-PET distribution using an unsupervised data-driven method (Vogel, Mattsson et al. 2019). They scanned a cohort of 123 AD, mild cognitive impairment and normal controls using ¹⁸F-flortaucipir PET to identify tau-PET patterns. The analysis produced five clusters of biologically meaningful spatial patterns, with the possibility of implementation for clinical settings (Vogel, Mattsson et al. 2019). Last but not least, the PET tracer 2-[¹⁸F]fluoro-2-Deoxy-D-glucose (PFDG- or FDG-PET) has become another powerful tool to study AD pathology. FDG-PET detects glucose hypometabolism which indicates the presence of pathological changes that have decreased the local synaptic activity or synaptic dysfunction in affected neurons (Noble and Scarmeas 2009).

The imaging cost is currently a limitation for using PET, thus it could be applied only for individuals of reported or suspected cognitive impairment (Noble and Scarmeas 2009). MRI is a noninvasive imaging technique using a transmitter and a receiver of radio frequency in order to visualize the body internal organs using an MR images. Image computation is done using the received frequency along with phase (timing) and space information which is then transferred into resonance signals. MRI enables imaging of the interior structure of a wide range of body organs (Moghbel, Alavi et al. 2016). For these reasons, MRI is commonly used in AD diagnosis. Unlike PET, MRI is used to capture the morphological changes in the brain structure as well as to detect brain connectivity issues. For example, MRI studies demonstrated a reduction in the functional connectivity of the

brain default mode network in AD and mild cognitive impairment (MCI) compared to matched controls (Kehoe, McNulty et al. 2014). Moreover, by using structural MRI, Morra et al. showed that there is a significant reduction in hippocampal volume in AD patients compared to the controls. The study was performed on 400 subjects who were clinically diagnosed with AD and mild cognitive impairment in addition to elderly healthy controls. Of note, the high-cost is one of the main drawbacks of MRI testing (Morra, Tu et al. 2009). CSF analysis is the most established diagnosis in the clinical settings of AD biomarkers. The story of using CSF for AD biomarker development started more than 20 years ago when Blennow et al and Motter et al published in 1995 independent studies to measure CSF levels of A β 42, P-tau, and total tau (T-tau) using enzyme-linked immunosorbent assays (ELISA) (Blennow, Wallin et al. 1995, Motter, Vigo-Pelfrey et al. 1995). These studies revealed an obvious elevation of T-tau and P-tau in CSF accompanied by a noticeable decrease in A β 42 in CSF samples from AD patients (Blennow, Wallin et al. 1995, Motter, Vigo-Pelfrey et al. 1995). Currently, A β 42 and P-tau represent the core CSF biomarkers of AD (Molinuevo, Ayton et al. 2018). The decreased A β 42 CSF level, accompanied by elevation of CSF T-tau and P-tau, have been estimated to have a sensitivity and specificity of around 85–90% to identify patients with AD (Blennow and Zetterberg 2015). Furthermore, decreased level of CSF A β 42/A β 40 ratio is currently a repeated finding in CSF of individuals with different AD stages (Hampel, Frank et al. 2010) and it has proved its utility as an established AD diagnostic routine (Lehmann, Delaby et al. 2018).

Other heavily investigated inflammatory CSF biomarkers of AD are α 1-antichymotrypsin (A1ACT) and interleukin-1 (IL-1) (Pirttila, Mehta et al. 1994). Unfortunately, these biomarkers brought always inconsistent results in AD patients (Anoop, Singh et al. 2010). Similarly, the CSF level of interleukin-6 (IL-6) has yielded always contradictory results in independent studies (Anoop, Singh et al. 2010).

1.2.3. **Blood-based biomarkers of AD are needed for diagnostic and therapeutic developments**

PET scan and CSF biomarker analyses are currently quite established for AD diagnostics. These methods, however, are restricted by the high-cost (brain imaging) and being invasive (CSF). These restrictions could be circumvented by the use of blood-based biomarkers as blood sampling is less invasive than CSF collection and usually less expensive than brain imaging. Moreover, clinical routines in the whole world are quite established for blood testing (Hampel, O'Bryant et al. 2018).

As the urge to develop blood-based detection of AD is growing, Alzheimer's Association and the Alzheimer's Drug Discovery Foundation (ADDF) called all the leading research groups for a meeting on April 12, 2013 to discuss the growing evidence that AD pathology is reflected in the periphery. The meeting discussed as well the challenges to address conclusive blood biomarker for AD (Snyder, Carrillo et al. 2014).

Tau was heavily investigated as AD blood biomarker and it was repeatedly detected in the periphery during the disease course (Tatebe, Kasai et al. 2017, Mielke, Hagen et al. 2018). It has been reported that the increase in plasma level of T-tau is associated with increased risk of cognitive decline. Additionally, increased plasma level of P-tau was linked to cognitive impairment (O'Bryant, Mielke et al. 2017). Unfortunately, P-tau is difficult to be measured in the plasma of AD patients because it needs a highly sensitive assay and plasma level of T-tau cannot be clearly correlated with the CSF T-tau concentration (Tatebe, Kasai et al. 2017, Mielke, Hagen et al. 2018).

In another line of research, A β 42 and A β 40/A β 42 ratio were extensively studied in the peripheral blood of AD patients (Tamaoka, Fukushima et al. 1996, De Jonghe, Cras et al. 1999, Shahpasand-Kroner, Klafki et al. 2018). Of note, Nakamura and colleagues have recently demonstrated a breaking through approach for the measurement of high-performance plasma amyloid- β biomarkers by immunoprecipitation coupled with mass spectrometry. A β 42 and A β 40/A β 42 ratio demonstrated high performance when predicting brain amyloid- β burden with about 90% accuracy when using PIB-PET as a "standard of truth" (Nakamura, Kaneko et al. 2018).

In addition to Tau and A β biomarkers, several additional candidates have been investigated as AD blood biomarkers like plasma phospholipids, microRNA expression

profiling, plasma proteins, and multi-analyte machineries targeting neuroinflammatory changes (Hudd, Shiel et al. 2019). For instance, plasma protein apolipoprotein J (Clusterin) has been reported as potential AD blood biomarker. A cohort of 1,532 healthy subjects has been analyzed by Weinstein and colleagues to evaluate the possibility of using plasma Clusterin as a predicting biomarker for incident dementia. Plasma level of Clusterin was found to be associated with increased risk of dementia only for subjects older than 80 years, while it was associated with reduced risk of dementia for subjects of age between 60-69 years old. Such results bring a big caution about interpreting the biomarker predictive utility without considering cohort subject age (Weinstein, Beiser et al. 2016). Another study, from Bacioglu et al, suggested that neurofilament light chain (NfL) could be regarded as a reliable CSF and blood biomarker to monitor disease progression and treatment response in mouse models and potentially in human α -synucleinopathies, tauopathies, and AD lesions (Bacioglu, Maia et al. 2016). They showed that NfL was elevated in both CSF and blood of patients with tauopathies, α -synucleinopathies, and AD as well. Additionally, Bacioglu et al have elevated the NfL plasma level via induced α -synuclein lesions and then they inhibited the NfL increase by the blocking of A β formation.

As an alternative for single target approaches, biomarker panels could be a more promising strategy. Recently, different types of protein panels have shown diagnostic or predictive capacity (Barroeta-Espar, Weinstock et al. 2019). Of note, O'Bryant and colleagues have identified a 21-protein panel demonstrated a positive predictive value (PPV) of 0.85 and a negative predictive value (NPV) of 0.94 in a preliminary validation (O'Bryant, Edwards et al. 2016). In the same line of research, Mapstone and colleagues introduced a set of ten peripheral blood phospholipids to predict phenoconversion to either MCI or AD with an accuracy of 90% in a timeframe of 2–3 year (Mapstone, Cheema et al. 2014). Furthermore, other panel-based studies for microRNAs, amino acids, and lipids demonstrated promising results, but large cross-sectional studies are still needed to validate these panels (Hampel, O'Bryant et al. 2018). More sophisticated approaches, that rely on more than a panel of proteins, are currently under ongoing development. For example, significant progress was achieved recently by Lin and colleagues (Lin, Huang et al. 2019). They introduced a predictive model, based on the decision tree, and used plasma

levels of valeryl carnitine and arginine in combination with age to dissect AD patients from healthy match controls with specificity of 86.7% and sensitivity of 60%.

Another direction of research was focused on the status of blood subsets. Blood cellular composition and the activation status of different blood subsets were reported to be altered during AD (Pluta, Ulamek-Kozioł et al. 2018). For example, T cells and B cells were reported to be decreased during AD pathology (Martorana, Bulati et al. 2012). Besides, T cells from AD patients exhibited a modified activity of antioxidant enzymes as well as an elevation of reactive oxygen species and the presence of DNA damage (Wojsiat, Prandelli et al. 2015). Moreover, platelets from AD patients demonstrated altered intracellular Ca^{2+} levels, serotonin uptake, and alterations in APP processing. These alterations were correlated with cognitive decline (Wojsiat, Laskowska-Kaszub et al. 2017).

Despite the massive effort over the last two decades to develop reliable AD blood biomarkers, the field was always suffering from lack of reliability and reproducibility. Up to now, there is no approved blood diagnosis of AD available for clinical use (Preische, Schultz et al. 2019).

1.3. Precision medicine for AD

1.3.1. Definition of precision medicine

Precision medicine (PM) is a medical diagnostic and curative model, which considers genetic, biomarker, phenotypic, and psychosocial characteristics of the individual during the medical intervention (**Figure 2**). PM aims primarily to characterize the interferences that are expected to effectively benefit the patients depending on the features of the individual and their pathological and physiological status. It should be mentioned that precision medicine does not mean necessarily developing unique treatment product for each individual. It rather means tailoring the therapeutic approaches toward a group of individuals having a similar biological profile (Hiller 2015).

PM is meant to address the limitations of “one-size-fits-all/magic bullet therapy”-based treatment approaches and classical symptom- and sign-based phenotypic diagnoses. This limitation is due to the fact that within a population of patients, there is a high heterogeneity to the extent that a single specific treatment cannot bring the same beneficial outcome to each individual in a population. PM tries to address this

heterogeneity in order to develop individual-tailored healthcare procedure that is able to overcome patient heterogeneity (Hampel, Vergallo et al. 2019). The PM term emerged quickly in the cancer field where it refers to the methodology of identifying an anticancer treatment protocol that mostly confers better treatment outcome within a subset of patients whose cancer displays specific molecular or cellular features (Yates, Seoane et al. 2018).

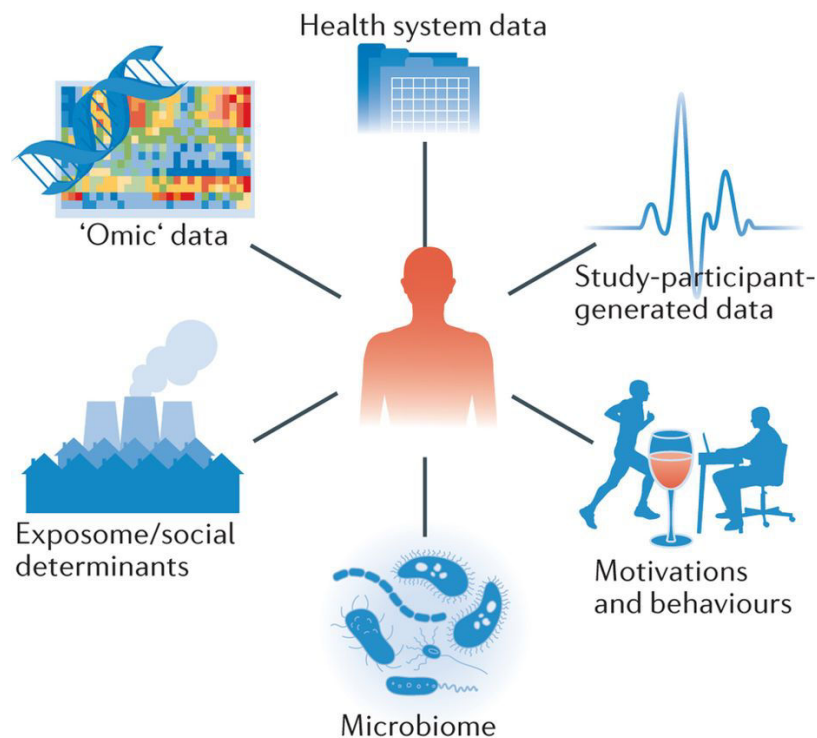


Figure 2: Precision medicine aims to stratify patients, according to the genetic, biomarker, phenotypic, and psychosocial characteristics of the individual. From (Antman and Loscalzo 2016)

Ultimately, PM medicine aims to save time and healthcare costs by selecting appropriate diagnosis and treatment as well as having a beneficial outcome for the patient. This avoids going through unnecessary interventions and saves the patients from using less or non-beneficial treatment. Thus, the importance of PM stems from the fact that it helps in developing a more effective decision-making procedure (Larry Jameson and Longo 2015, Gavan, Thompson et al. 2018). Due to the advantages of PM as a time-cost-outcome effective healthcare system, it has become of high importance for healthcare authorities in many countries. For instance, the German Federal Ministry of Education and Research

(BMBF) has initiated a wide plan to fund research in personalized medicine. The BMBF invested, between 2013 and 2016, 360 million euros for research in this context (German Federal Ministry of Education and Research 2013). In the USA, President Obama announced, in 2015, the launch of the Obama Precision Medicine Initiative as “a bold new research effort to revolutionize how we can improve health and treat disease”(House 2015).

In PM, the classical patient stratification was most commonly done based upon genomic changes and protein expression patterns (in simple words, using individual genetic information to predict body response). For example, Warfarin is an anticoagulant drug, which is known for its low therapeutic index and dose-response variability among patients, putting patients at high risk of bleeding. Borgiani et al. have reported three genes (CYP2C9, VKORC1, and CYP4F2), that in combination with patient weight and age can explain more than 60% of the patient response variability to Warfarin (Borgiani, Ciccacci et al. 2009). They suggested that testing these three genes could help to decide the optimum Warfarin dose and, therefore, reducing the risk of bleeding (Borgiani, Ciccacci et al. 2009). On the other hand, immunotyping is a growing strategy in the context of PM since the patient immune profile plays a crucial role in patient response to medical interventions (**Figure 3**)(Brodin and Davis 2017).

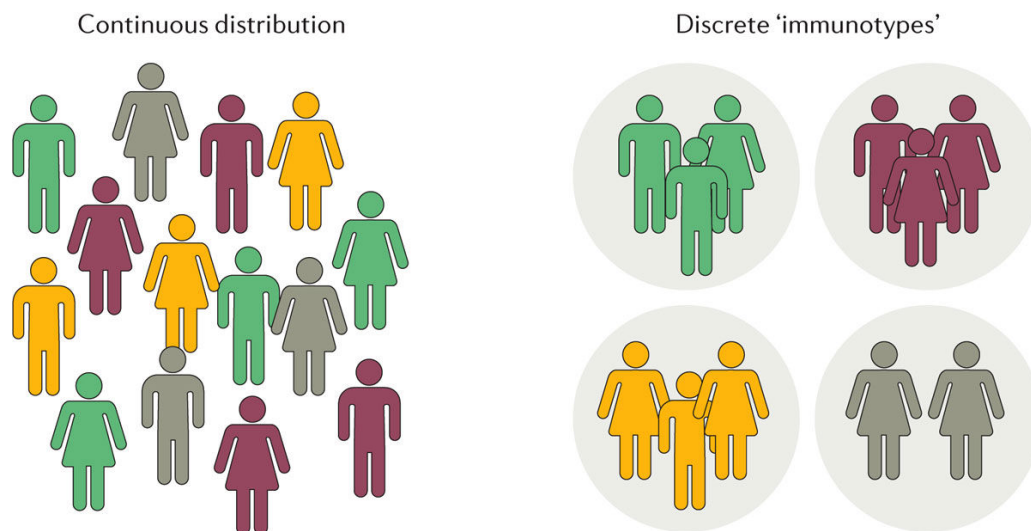


Figure 3: Understanding the immune variation within a population of patients or even healthy population could help a lot to predict the outcome of the healthcare procedures. Such individual stratification based upon immunotyping is a growing strategy in the context of precision medicine. Image from (Brodin and Davis 2017).

Immune profiling has been applied widely in the field of cancer. One implementation of immune profiling was in patients of peripheral T cell lymphoma (PTCL) who showed the possibility for subgrouping these patients according to their gene expression profile of some immune cells. A subgroup of PTCL patients that have specific expression profile of dendritic and B cells exhibited desirable clinical outcomes in response to a typical treatment routine. Another subgroup with no such expression profile exhibited extremely poor prognosis in response to same treatment protocol. Besides, macrophages from patients of that poor prognosis subgroup showed high expression level of some cell death checkpoint molecules, e.g. indoleamine 2, 3-dioxygenase protein. This means that these checkpoint molecules are potential therapeutic targets. Therefore, understanding the immune variation of PTCL patients plays a vital role to decide the direction of the intervention procedure (Sugio, Miyawaki et al. 2018).

1.3.2. Biomarker-guided precision medicine for AD

PM can represent a powerful approach to face the largely heterogeneous AD pathology. This can be done by developing a stratification methodology to dissect different AD patients' subsets based upon the immune profiles. This aims to shift the healthcare procedure from "population averages" into patient-tailored biomarker-guided targeted treatment (Hampel, Vergallo et al. 2019). Such healthcare models are believed to be of great benefit for AD patients as they are able to handle the disease heterogeneity (Hampel, O'Bryant et al. 2017). In order to approach the potential of PM for handling AD complexity and to develop an advanced paradigm of AD precision medicine, the international Alzheimer Precision Medicine Initiative (APMI) was launched in Paris in 2018 and it has been linked to the U.S. president Obama Precision Medicine Initiative (PMI). From APMI, four innovative translational neuroscience research programs have emerged; "MIDAS", "PHOENIX", "POSEIDON", and "VISION". The aim of these programs was to combine and integrate different aspects of neurosciences, facilitating the development of advanced AD precision medicine paradigm. Furthermore, APMI aims to standardize the academic routines and provide an assortment for the heterogeneous and multidimensional AD data" (Hampel, Toschi et al. 2018).

One of the early approaches in biomarker-guided PM was a series of studies to understand the underlying molecular mechanism of the AD pathology. For instance, neuroimaging provides the ability to assess the brain function via structural analysis and it has been found, using conventional and diffusion tensor MR scans, that the integrity of white matter decreases in the early stage of AD for some individuals (Fellgiebel, Wille et al. 2004). Besides, an MRI based study showed that some AD patients have a reduction in cerebral blood flow (Alsop, Detre et al. 2000). These pathological features are not applicable for all AD patients but they can be used person-wise, to start diagnostic and therapeutic intervention at early stages.

Recently, the development of the so-called Alzheimer's risk profile by developing a panel of genotypes, e.g. APOE and PSEN2, aided in risk stratification of AD. It also includes information about other factors that are linked to AD such as the individual educational level, the presence of other comorbidities, the current state of cognitive functions, diet, and lifestyle. This risk profile aims to give an indication of the person vulnerability for AD (Reitz 2016).

1.4. Studying the immune system for biomarker development and precision medicine in AD

1.4.1. The immune system

The immune system is a group of structures and processes that happen within the body to maintain homeostasis by protecting the body from damaging foreign bodies or even from pathological alterations within cells or tissues. The damaging foreign bodies include bacteria, viruses, and parasites while pathological alterations include abnormal cells that are derived from host tissues (Zimmermann 2018).

Vertebrates have evolved two complementary systems to identify and terminate pathogens: adaptive and the innate immune systems. The adaptive immune response is a pathogen-specific defense mechanism, where T and B cell express receptors that are generated through somatic gene rearrangement and hypermutation. This machinery ensures the availability of a virtually infinite repertoire of antigen receptors, allowing the adaptive immunity to specifically identify any type of microorganism (Chen and Nuñez 2010).

In contrast, the innate immune system is non-specifically able to identify a wide diversity of pathogens such as bacteria, virus and even fungi. This is done via a number of germline-encoded receptors called pattern-recognition receptors (PRRs). Many cell types express PRRs such as macrophages, monocytes, dendritic cells (DCs), neutrophils, and epithelial cells. PRRs enable the early detection of pathogens directly at the site of infection, making the innate immune system both fast and the first line of defense. Once the PRRs are activated, an inflammatory response is initiated through the secretion of cytokines and chemokines, e.g. IL-1 β , triggering the recruitment of immune cells, e.g. T and B cells, to the site of infection and to start the adaptive immune response (de Oliveira, Davis et al. 2019).

The classical "black and white" distinction between the adaptive and innate response cannot be valid anymore, because the recent molecular and genomic information showed clearly that there is a wide interaction between the function of the two systems (Sirisinha 2014). For instance, both dendritic cells (DCs) and macrophages work as antigen-presenting cells (APCs), linking the adaptive and innate response, because they activate immune response via cytokine release as well as presenting antigens to the T cells as major histocompatibility complex (MHC) molecules (Holleran, Lopetuso et al. 2017).

Inter-individual variability is considered as a big challenge for immune studies in healthy as well as patient-cohort studies (Brodin and Davis 2017). An example for this variation is the change in the frequencies of principal immune cell populations, e.g. monocytes, that vary in the blood of healthy adults (**Figure 4**). In the current study, we addressed this inter-individual variation via the quantification of monocyte, T and B cells in different healthy volunteer samples.

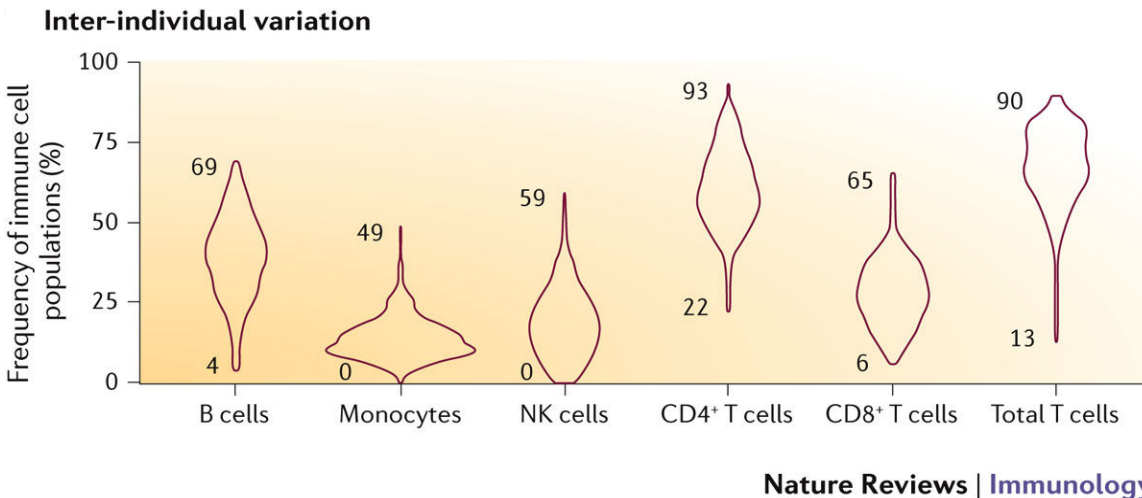


Figure 4: Variation in immune cells of healthy adults

Principal immune cell populations like monocytes, T and B cells are showing different cellular composition percentage from one healthy adult to another. Thus, inter-individual variation should be considered during the analysis of the immunity for both healthy and patient populations. Adjusted from (Brodin and Davis 2017).

1.4.2. Toll-like receptor and inflammasome are key players in the innate immunity

The innate immune system recruits a diversity of sensors to identify endogenous and exogenous potentially pathogenic ligands. An integral part of this set of sensors is the family of pattern recognition receptors (PRRs) (Schroder and Tschopp 2010). PRRs such as Toll-like receptors (TLRs) and Nucleotide oligomerization domain (NOD)-like receptors recognize pathogen-associated molecular patterns (PAMPs) released during viral, bacterial, fungal, and protozoan infections as well as danger-associated molecular patterns (DAMPs) released during cellular damage (de Oliveira, Davis et al. 2019). One of the best-characterized categories of PRRs are the TLR4 which recognize PAMPs, e.g bacterial lipopolysaccharide (LPS), triggering intracellular signaling cascades leading to downstream signaling that causes the activation of transcription nuclear factor κ B (NF- κ B), triggering the expression of many inflammatory mediators including tumor necrosis factor alpha (TNF α), pro-IL-1 β and pro-IL-18 (Scheiblich, Schlutter et al. 2017). On the other hand, NOD-like receptors (NLRs) are a group of PRR of intracellular scaffolding proteins that play a critical role in the regulation of innate immune responses, particularly NLR and pyrin domain- containing (NLRP) which serve as a sensor molecule for the multimeric signaling platform inflammasome (Franchi, Warner et al. 2009).

Inflammasomes regulate the innate immune response via controlling a sterile inflammatory response and triggering a unique type of cell death called pyroptosis (Latz and Duewell 2018). Inflammasomes are mainly composed of a sensor molecule (NLRP) or absent in melanoma 2 like receptors (ALRs) (**Figure 5 A**) as well as an adaptor protein PYCARD. PYCARD also known as ASC [apoptosis-associated speck-like protein containing a caspase activation and recruitment domain (CARD)]. The last component is the cysteine-aspartic acid protease (caspase 1 or CASP1) (**Figure 5 A**). Activated CASP1 cleaves pro-interleukin-1 β (pro-IL-1 β) and pro-IL-18 into their active forms. Inflammasome assembly eventually leads to pyroptotic cell death (Man and Kanneganti 2015, Broz and Dixit 2016). Two signaling processes are required for inflammasome activation. The first is called priming where TLR4 is activated via extracellular ligand on the cell surface, e.g. LPS, leading to the activation of NF- κ B pathway. This triggers upregulation of NLRP3, TNF α , pro-IL-1 β and pro-IL-18 (**Figure 5 B**). The second signaling process is the triggering of inflammasome assembly via diverse mechanisms. This includes the increase of K⁺ efflux, e.g. ATP stimulates the purinergic receptor (P2X7R), triggering K⁺ efflux (**Figure 5 B**) (Choi and Ryter 2014). Nigericin is a *Streptomyces hygroscopicus*-derived microbial toxin which perturbs the plasma membrane permeability and, as a microbial ionophore, it increases cellular potassium efflux leading to inflammasome activation (Locovei, Scemes et al. 2007). Another mechanism of activation is via lysosomal disruption after the engulfment of particulate structures such as crystalline, silica, asbestos, and A β (Schroder and Tschopp 2010). L-Leucyl-L-leucine methyl ester (LeuLeuOMe) is a lysosomal destabilization agent that is widely used to trigger inflammasome activation, as LeuLeuOMe accumulates within the lysosome and permeabilize its membrane leading to lysosomal disruption and eventually inflammasome activation (He, Hara et al. 2016, Nebel, Aslanidis et al. 2017).

There is a wide diversity of stimulants that can trigger inflammasome activation in different disease status; ATP (in necrosis), uric acid (in gout), Amyloid β (in AD), glucose (metabolic syndrome), cytochrome C (apoptosis), ROS (allergy), defensins (tuberculosis infection), HMGB1 (glaucoma), heat-shock protein (Japanese encephalitis virus infection), hyaluronic acid (airway hyperresponsiveness), fatty acids (obesity/type 2 diabetes), and

mitochondrial DNA in autophagy and apoptosis (Heneka, Kummer et al. 2013, Wang, Dong et al. 2019).

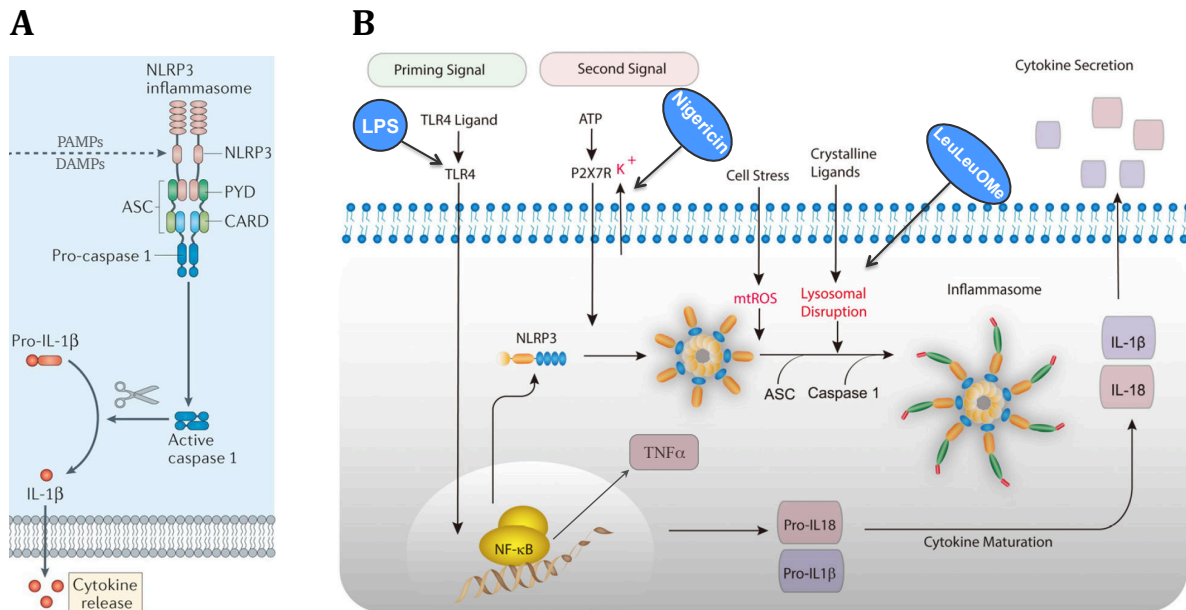


Figure 5: Inflammasome activation. (A) Inflammasome composes of NLRP sensor molecule, the adaptor protein ASC [apoptosis-associated speck-like protein containing a caspase activation and recruitment domain (CARD)] and caspase 1 (CASP1). Adapted from (Broz and Dixit 2016). (B) Inflammasome activation needs two signal processes; priming of TLR4 and activation signals via inflammasome activators like Nigericin and LeuLeuOMe. Modified from (Choi and Ryter 2014).

NLR- pyrin domain (PYD)-containing 1 (NLRP1) inflammasome was the first described inflammasome in 1999 (Bertin, Nir et al. 1999). Successively, other inflammasomes have been identified in the following years including NLRP2, NLRP3, NLRC4, and AIM2 inflammasome (Shao, Cao et al. 2018).

ASC speck formation or inflammasome speck formation assay is currently a standard measure of inflammasome activity, in different models of inflammation, and it is currently a standard readout for evaluating the NLRP3 inflammasome inhibition by wide range of drugs, e.g. non-steroidal anti-inflammatories (Heneka 2017).

1.4.3. The role of inflammasome in AD pathology

The inflammatory response of the innate immune system has been reported to play an important role in AD pathology (Labzin, Heneka et al. 2018). Microglial, as the brain-resident immune cells, reacts to the formation of amyloid plaques by engulfing A β and by releasing pro-inflammatory cytokines, e.g. IL-1 β , to the neighboring tissue (Tan, Yu et al.

2013). On the other hand, NLRP3 inflammasome, activated by fibrillar A β , has been described first by Halle et al. in 2008 to be linked to AD pathogenesis (Halle, Hornung et al. 2008). Heneka and colleagues showed that NLRP3 inflammasome deficiency caused a reduction in A β deposition in AD (APP/PS1) mouse model and both NLRP3- and caspase-1 knockouts brought strong protection against cognitive impairment in such animal model (Heneka, Kummer et al. 2013). Furthermore, Shi et al showed that treating Alzheimer's APP^{swe}/PS1^{dE9} mouse model with the antimalarial drug artemisinin inhibited NF- κ B activity, NLRP3 inflammasome activation and decreasing neuritic plaque burden, suggesting that the protective effect of artemisinin on AD pathology is due to inhibition of NF- κ B and NLRP3 inflammasome activation (Shi, Zhang et al. 2013).

The role of inflammasome in AD pathology could be also explained simply that both A β depositions as well as α -synuclein aggregations serve as danger signals DAMPs, initiating an inflammasome activation and consequently a wide innate immune response (Salminen, Ojala et al. 2008, Gordon, Albornoz et al. 2018). Albornoz et al have recently showed that α -synuclein aggregations trigger NLRP3 inflammasome activation (Gordon, Albornoz et al. 2018), whereas A β fibrils have been, since long time, reported to cause lysosomal damage initiating inflammasomes activation in mouse microglia (Salminen, Ojala et al. 2008). Besides, A β depositions and α -synuclein aggregations have been reported to activate PRRs, e.g. TLR2 and TLR4, triggering NF- κ B dependent gene expression of inflammasome components (Labzin, Heneka et al. 2018). Another hypothesis to explain the inflammasome role in neurodegenerative disease is the role of NLRP3 in the impairment of mitochondrial function through oxidative stress-mediated responses (Guo, Sun et al. 2013). In vivo studies of an AD amyloidosis rat model revealed that activation of NLRP3 inflammasome causes a deficit in synaptic plasticity (Qi, Klyubin et al. 2018). Besides, Chan et al have recently demonstrated that inhibiting NLRP3 activation, possibly through the regulation of p38 α MAPK signaling pathways and GSK-3 β , reduced microglia-mediated neurotoxicity, tau hyperphosphorylation and amyloidogenesis in SH-SY5Y cells (Chan, Krishnansamy et al. 2019). Therefore, the NLRP3 inflammasome is currently considered as a promising potential target for AD treatment (Heneka, Kummer et al. 2013, Shao, Cao et al. 2018).

1.4.4. Transcriptome analysis to study immune-associated pathways

Another aspect of studying the immune system is the transcriptome analysis of immune-linked pathways. Technologies of transcriptome analysis are nowadays used to characterize physiological status, pathological changes, and cellular activities. Next-generation sequencing of transcripts (RNA-seq) is currently the state-of-the-art technology to conduct the transcriptome analysis. It gives the opportunity to study the transcriptome at unsurpassed resolution and provides the possibility to re-analyzed the output data with no need to repeat the laboratory experiment (Mutz, Heilkenbrinker et al. 2013).

RNA-seq is divided into single cell RNA-sequencing and bulk transcriptome analysis. Single cell sequencing helps in studying rare cell populations, association between genes, uncovering regulatory pathways (Hwang, Lee et al. 2018), and tracking the development of distinct cell lineages (Schultze, Mass et al. 2019). Bulk transcriptome, on the other hand, enables a close optimal gene detection rate and provides very informative data that can help predicting cellular function of a defined cell subset within the cell population (Schultze and Aschenbrenner 2019). During the current project, the bulk transcriptome analysis was conducted to collect comprehensive information about the PBMC samples as a first step in transcriptome analysis.

RNA-seq has been intensively used in the field of immunology to study the immune-related genes. For instance, Sudhagar and colleagues have addressed the gene expression profile of immune cells during infection to understand the immune system behavior. This includes identifying the immune system strategies to overcome the infection and how the pathogen itself tries to escape these defense strategies, giving a better chance to develop effective therapeutic targets against infections (Sudhagar, Kumar et al. 2018). Another example of using RNA-seq in immunology is the characterization of the cellular composition of solid tumors in order to predict the immunotherapy outcome. This can be done using the so-called cell-type-specific reference gene expression profiles (RGEPs). Schelker and colleagues identified nine major cell-types, as well as three T cell subtypes present in solid tumor-derived RGEPs (Schelker, Feau et al. 2017).

As human peripheral blood mononuclear cells (PBMCs) were used as a cell model in the current project (discussed in details in next sections), it should be mentioned that the

inflammatory mechanisms that underly diverse autoimmune diseases have been characterized through transcriptomics analyses of PBMCs. For instance, type 1 diabetes mellitus (T1DM) demonstrated a transcriptional signature for the proinflammatory cytokine family of IL-1 β using transcriptomics analysis of PBMCs from T1DM patients (Foss-Freitas, Foss et al. 2008). In another study on PBMCs from rheumatoid arthritis (RA) patients, 330 transcripts were identified to be differentially expressed compared to healthy subjects (Sen, Kemppainen et al. 2017). Of note, a significant report has been recently published by Monaco et al who characterized, using RNA-seq and flow cytometry, 29 immune cell subsets within the peripheral blood mononuclear cell (PBMC) of healthy subjects. They obtained an RNA-seq dataset for these 29 subsets and identified “modules of cell type-specific, co-expressed, and housekeeping genes” (Monaco, Lee et al. 2019).

1.4.5. Dynamic interaction of CNS and peripheral immune system

The central nervous system (CNS) is the part of the nervous system that consists of the brain and spinal cord. For decades, CNS was considered as an immune-privileged compartment, which has its own defense machinery away from the peripheral immune system. However, in recent decades, the immune interaction between the brain and the periphery has been proven and evidences were reported about the dynamic interaction of the CNS and the peripheral immune system (Perry 2010). For instance, the brain responds to peripheral inflammations or infections by a set of metabolic and behavioral changes called sickness behavior (Harden, Kent et al. 2015). Sickness behavior is a synchronized set of behavioral changes that is derived by pro-inflammatory cytokines, e.g. IL-1 β and TNF α , and hormones, e.g. testosterone and oxytocin, leading to disturbances of appetite, decreased libido, cognition changes (reaction time), sleeping disturbances, and social withdrawal. Both the brain and the periphery play a mutual role in the development of such sickness behavior (Shattuck and Muehlenbein 2015).

In case of AD, there have been increased number of reports that the peripheral immune system is involved in disease pathology. It was mentioned before that monocytes from AD patients demonstrated an upregulated expression of NLRP3 and caspase-1 (Saresella, La Rosa et al. 2016). Besides, chronic systemic infections or inflammation have been reported as risk factors for AD and they were reported to accelerate the AD pathology progress (Perry 2010). Moreover, post-mortem analysis of AD patient' brains showed T

cell infiltration (Togo, Akiyama et al. 2002). Ferretti et al revealed that cerebral amyloidosis endorses T cell infiltration. These T cells were neither co-localized with A β aggregations nor locally proliferating. They also showed that infiltrated T cells had a low expression profile of macrophage activated interferon type 2 (IFN γ) (Ferretti, Merlini et al. 2016). On a different line of research, the immunoglobulin repertoire in the periphery of AD patients has been reported to be dysregulated. B cells demonstrated a spontaneous release of immunoglobulin without exogenous stimulation and the number of autoantibodies was significantly reduced in the sera of AD patients (Acharya, Nagele et al. 2013, Nagele, Han et al. 2013). Last but not least, peripheral leukocytes from AD patients have been demonstrated to show higher apoptotic cell death compared to the matched controls. This could be attributed to the increased sensitivity of leukocytes to apoptotic induction (Bergman, Salman et al. 2002). Ultimately, all these reports indicate that there is a high potential for capturing reliable immune changes in the peripheral blood of AD patients in order to be used as disease biomarkers.

1.5. Human peripheral blood mononuclear cells (PBMCs) as a proxy for the immune system

1.5.1. Human PBMCs as a human-derived cell model

Human peripheral blood mononuclear cells (PBMCs) include all the nucleated blood cells (monocytes, T cell, B cell, dendritic cells, and natural killer cells). PBMCs are usually isolated either from a whole blood sample or from buffy coats (blood fraction that includes only platelets and leukocytes). T cells represent the majority (50-80 %) of PBMCs, while monocytes form 10-20 %, and B cell 3.5-9 %. Dendritic and natural killer cells are very rare in PBMCs accounting for only 1–2% (Akdis, Palomares et al. 2012, Tan and Gery 2012, Kleiveland 2015). Monocytes are an important player in innate immune responses via releasing a wide range of inflammatory cytokines, e.g. IL-1b, and also through the expression of CD14 on the plasma membrane which belongs to the family of LPS receptors or antigens. On the other hand, T lymphocytes (T cells) present in PBMCs as CD4+ helper and CD8+ cytotoxic T cells with a ratio of roughly 2:1. CD4+ T cells are represented in further subsets like Th1, Th2, Th17, Th9, Th22, and regulatory T cells (Treg) (Sen, Kemppainen et al. 2017). Finally, B lymphocytes (B cells) constitute one of

the abundant components of PBMCs which originate, like many blood cells, from the bone marrow. These cells initiate antibody responses against pathogens via binding to pathogen's antigen by triggering an adaptive humoral immune response (Cooper 2015). PBMCs are widely used now in research studies as a human-derived cell model, because they are easy and inexpensive to acquire, as well as providing a more comprehensive overview of the immune system status than circulating serum or plasma markers (Kutscher, Dembek et al. 2013, Ma, Zhang et al. 2015, Huang, Dai et al. 2018). PBMCs have been used in research of asthma, allergies, as well as T1DM and cancer (Foss-Freitas, Foss et al. 2008, Payne, Zoon et al. 2013, Sen, Kemppainen et al. 2017). Moreover, as PBMCs include the essential components of the immune system like T cells and monocytes, they are widely used in research of immunology and vaccine developments. The PBMC *ex vivo* analysis provides different information about T cells activation or differentiation status. Also, in the context of the inflammasome, PBMCs provide information on priming and activation status of the innate immune system via monocyte monitoring. PBMCs were also used for AD studies as it has been reported that PBMCs of AD patients have an altered inflammasome activity (Saresella, La Rosa et al. 2016). As mentioned before, Saresella et al reported a change in the NLRP3 and Casp1 expression profile in PBMCs of AD patients and they suggested that functional monocytic inflammasome is only assembled in a late stage of AD but not during MCI (Saresella, La Rosa et al. 2016). Another study showed that PBMCs from AD patients have less B cells compared to the matched controls (Pellicano, Bulati et al. 2010). Other PBMC subsets showed no significant difference between patients and controls. The expression of some activation markers like CCR5 in T cells was already up-regulated in the untreated PBMCs of AD patients (Pellicano, Bulati et al. 2010). Using PBMCs as a cell model is challenging as the physiological status and presence of previous infections will affect the reactivity of immune cells as well as the cellular composition of the PBMC sample, meaning that PBMC sample is donor dependent. Therefore, donor-to-donor variation should be highly considered for experiments where samples from different donors are used (Kleiveland 2015).

1.5.2. Image analysis as a tool for cell-based assay

Digital imaging is a powerful technology for studying a wide range of cellular or tissue activities via providing in-depth spatial and temporal information in nanometer scale.

This helps to capture the cellular morphological features and localizing sub-cellular structures or proteins using labeling technologies, e.g. fluorescent tags. Imaging is, in general, inexpensive and easy to achieve, enabling the tracking of multiple phenotypic responses to genetic perturbations or drug treatments (Smith, Piccinini et al. 2018). Moreover, the confocal microscope can be used for both endpoint experiments as well as live imaging assays where living cells are continuously monitored before and cross the response to a specific treatment. For instance, during this project, PBMCs were stimulated to undergo inflammasome activation and they were monitored via the automated confocal microscope system CellVoyager 6000 (CV6000). Such automated imaging capacity provided the possibility to identify the PBMC subset responding to the inflammasome activation (**Figure 5**).

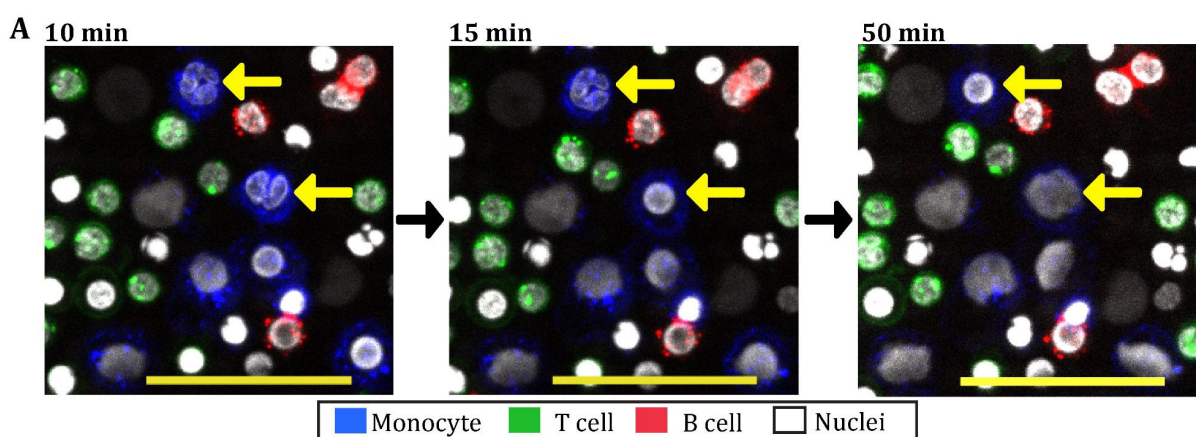


Figure 6: Example of automated image acquisition of stimulated PBMCs using the confocal microscope CellVoyager 6000 (CV6000).

PBMCs were continuously imaged over a period of one hour after they have been primed with LPS followed by 5 μ M Nigericin to trigger inflammasome activation. More details about the experiment are in the results chapter. Scale bar, 40 μ m.

The recent impressive advances in microscopical technologies, in both automation and computation, like the high-throughput microscopy systems, have enabled improvement of imaging techniques both quantitatively (ability to generate a large number of images per experiment) and qualitatively (ability to generate images that are rich in phenotypic information). This advancement enables to image systematically, and in an unbiased way a higher number of experimental objects compared to the manual imaging.

However, the number of images produced by an automated cell-based assay can range from thousands to millions, an obvious reason for its difficult analysis by human.

Subsequently, to obtain phenotypic signatures, researchers have come to rely on “phenotypic image analysis” techniques—computational methods that transform raw image data into useful phenotypic measurements (Caicedo, Cooper et al. 2017). Additionally, and most importantly, the processing of the images by automated image analysis is essential in producing quantitative data from the objects and therefore collecting quantitative information from phenotypic images. In essence, this allows then the use of statistical and analytical tools to understand how a specific treatment could affect cell morphology or some cellular activities. Thus, image analysis provides the possibility for unbiased and comprehensive analysis of the cell-based assay results as the analysis provides, systematically, a measurement for hundreds of features.

In principle, image analysis converts digital images into measurements of pixel intensity, object texture and morphology that, together, depict the state of a cell or object in an experiment. This conversion is done using computational algorithms that count for measurements (usually called features) by generating a table which illustrates feature measurements for every cell in an experiment (Smith, Piccinini et al. 2018).

The information from the digital images is provided in pixel-wise pattern. Pixels are grouped to distinguish the cell or object, from other cells/objects, and from the background in a process called segmentation. Segmentation of an object is a pixel classification process where a given pixel is assigned into being part of the object or not, i.e. being a foreground or a background (Sommer, Straehle et al. 2011). The cell area segmentation is usually done by identifying nuclei which then are used as seeds for the cell outline identification (**Figure 7**). This can be done with an appropriate algorithm which can be optimized according to the visual inspection of segmentation results. A predefined algorithm (called module) is used according to a previously known set of object parameters, e.g. expected size and shape. Such “module-based” analysis usually includes histogram-based methods, e.g. thresholding, watershed transformation, and edge detection for module optimization (Molnar, Jermyn et al. 2016). These predefined algorithms are usually packed together with its optimization parameters into an image analysis software.

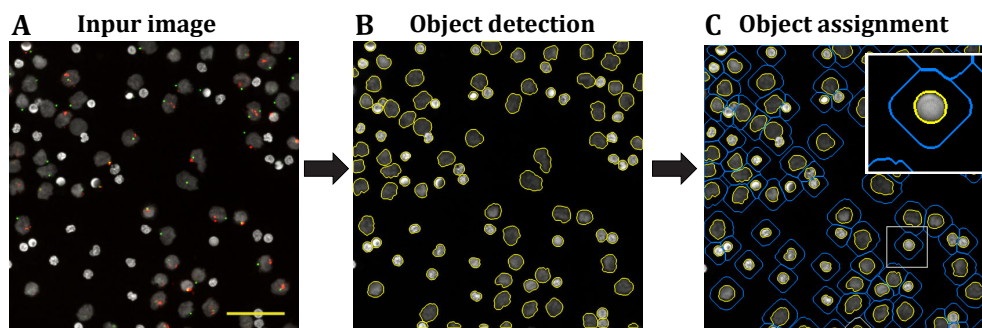


Figure 7: A simple example of image analysis workflow to detect nuclei of PBMCs using CellVoyager CV7000 Analysis Software. (A) Input image. (B) Nuclei segmentation. Nuclei were segmented using the signal from the Hoechst33342 staining. (C) Cell area defining. The cellular area was defined by extending nuclear area into an estimated distance.

There is a wide diversity of image analysis software that is currently used to analyze the images from cell-based assays. The processing of digital images was initiated at Jet Propulsion Laboratory of NASA's in the late 1960s (Sagar 2018), but the first public image analysis software was the Java-based software ImageJ which was developed by Wayne Rasband in the late 70s (Abràmoff, Magalhães et al. 2004). ImageJ was widely adopted by the biomedical researchers as it can be operated on all operating systems and it is available in the public domain. Most biomedical image formats are compatible with ImageJ and it is packed with a wide range of ready to use algorithms that can compute many image analysis tasks, e.g. object segmentation, intensity measurement, and object size (Abràmoff, Magalhães et al. 2004). A more sophisticated image analysis software was CellProfiler. It is a free, widely used tool to measure different cellular or tissue phenotypes for hundred or even thousands of images in a predefined set of modules called a pipeline. The pipeline is a combination of modules, each of them is allocated to measure a specific phenotype, e.g. cell size, or to perform a defined task like cellular segmentation or even to apply mathematical calculations, e.g. calculating the object mean intensity. CellProfiler was adopted widely worldwide since it was introduced in 2005 and it was cited more than 6,000 times (until 2018) (McQuin, Goodman et al. 2018). The main brands of automated microscopes are bundled with the proprietary image analysis software. In our case we used the CellVoyager CV7000 Analysis Software, an image analysis software that was developed by Yokogawa electronic incorporation to process images generated by

CellVoyager microscopes. The software provided a diversity of algorithms that can perform different types of analysis like object segmentation (**Figure 7**), brightness value, or even object granularity (Yokogawa 2015). The advantage of this software is the ability to reach all metadata from the CellVoyager microscope and its user-friendly graphical interface (GUI) when compared to CellProfiler.

1.5.3. Supervised classifier for the characterization of PBMC cellular composition

As described in the last section, the image analysis software uses predefined algorithms to process the digital images conducting diversity of measurement such as measuring pixels intensity and texture features, i.e. they are rules-based engines that conduct the analysis of previously written scripts (Smith, Piccinini et al. 2018). However, an alternative method to perform image analysis is to use supervised methods. In this kind of approach, the user “supervises” the process of pixel classification. Each class of pixels, is annotated with pixel values according to the user decision. The user decides on pixel values by selecting representative samples of a predefined type called training set. The algorithm then classifies all pixels in an image in a way that the classes should not overlap with each other or at least minimally overlap with other classes (Humboldt 2015).

Recently, machine learning (ML) and artificial intelligence (AI) algorithms have been used to analyze complex bioimages (e.g. histological section, MRI images, bright field etc.) that are not possible to be analyzed with the classical methods. In principle, ML refers to a set of automatic pattern-recognition computational tools that are currently used in a wide domain of applications including image analysis (Kan 2017). The powerful feature of ML algorithms is that the results are improving through a learning phase where the algorithm refines its analysis techniques during the processing of images set called training set, i.e. “the analysis results in a higher and higher probability of a precise interpretation over the time of training.” (Goldstein 2018). For instance, in the supervised ML, segmented objects are manually categorized (labelled) beforehand. Then, the algorithm uses the labels as a training set in order to predict labels for unknown objects. Thus, the main difference between classical and the ML image analysis is the methodology (although they both have a similar goal), with the privilege that ML algorithms are able to conduct much more complex analysis tasks that classical analysis software cannot handle. Furthermore,

classical image analysis requires several nontrivial and independent analysis steps while ML methods offer a good predictive performance and the possibility to replace traditional workflows with a single network architecture (Kensert, Harrison et al. 2019).

The most sophisticated ML methodology used widely in the bioimaging field is a type of artificial intelligence known as a convolutional neural network (Kensert, Harrison et al. 2019). In principle, neural networks are very powerful and scalable deep learning tools that are able to conduct complex Machine Learning tasks, e.g. classifying billions of images. The idea of neural networks was inspired from brain's architecture and how human neurons, using a binary connection system, process diversity of tasks like image processing, voice recognition, and even how to play video games (Kadhim and Abed 2020). One common example of neural network is the convolutional neuronal network (CNN), a multilayer neuronal network that uses convolutional layers to process very large and complex images. In the first convolutional layer, neurons are connected only to pixels in their receptive fields but not to every single pixel of the input image (**Figure 8**). The second neuron layer is connected to the first layer neurons, but only within a small rectangular sub-region. The reason for such architecture is to "concentrate on low-level features in the first hidden layer, then assemble them into higher-level features in the next hidden layer, and so on". CNNs are very powerful in processing images as their design is very common in real-world images (Géron 2018). The strength of CNNs comes from multiple intermediate layers that increase dramatically the feature representation, providing a "deeper" image understanding and this is the reason that CNNs are also called deep learning methods (Kan 2017).

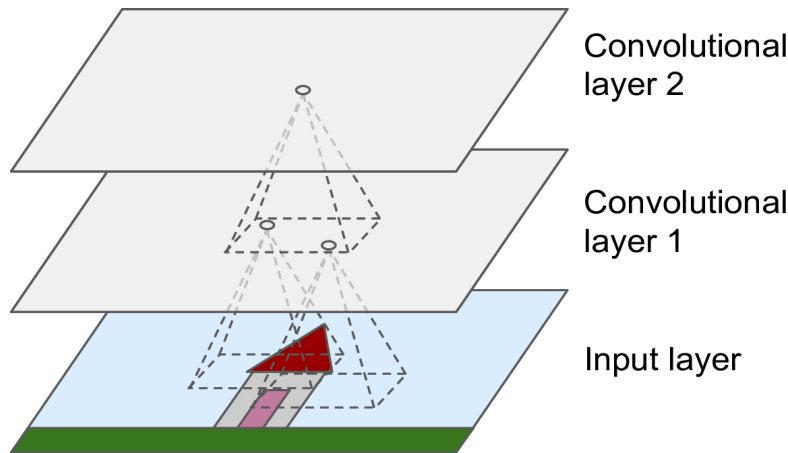


Figure 8: Principle concept of convoluted neural network.

Neurons in the first convolutional layer are connected only to pixels in their receptive fields but not to every single pixel of the input image. The second neuron layer is connected to the first layer neurons, but only within a small rectangle. Adapted from (Géron 2018).

Deep convolutional networks are very powerful CNNs image recognition models that are currently the state-of-the-art model for bioimages processing while they can serve as highly sophisticated classifiers that can process an enormous number of high-resolution images, achieving very complicated computational tasks (Alex Krizhevsky 2012, Ronneberger, Fischer et al. 2015). Nevertheless, the main drawback of these networks is the need for thousands of training images in order to achieve the learning phase (Olaf Ronneberger 2015). In contrast, the U-Net network is a training strategy where the network needs a lower number of images (often 20 images) to conduct the training (Olaf Ronneberger 2015).

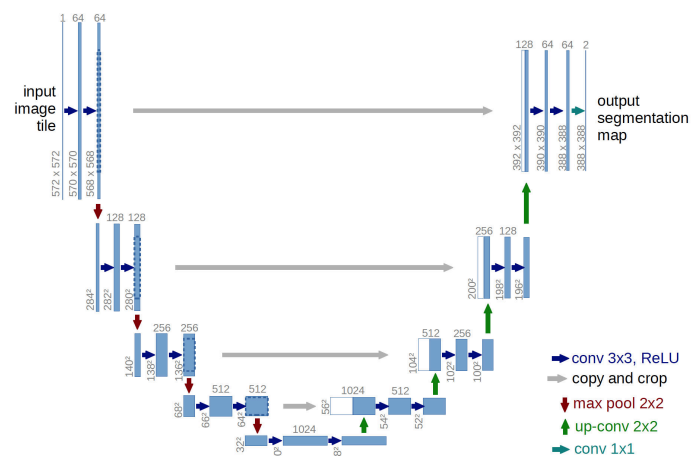


Figure 9: U-net network design of the lowest resolution (32x32 pixels) example.

Blue box: channel feature, the lower left edge of the box is image size, white boxes are duplicated feature maps different operation coded by colored arrows on the right. Adapted from (Olaf Ronneberger 2015).

For the characterization of PBMC cellular composition, supervised classification of pixels into image regions was done using a U-Net neural network. A classification was conducted with a U-Net based on a set of images used for training where labels were defined by the user utilizing The Interactive Learning and Segmentation Toolkit ilastik software. More details about this classification approach will be discussed in the Materials and Methods and in the Results chapters.

1.6. Multivariate analysis of the multi-parametric cell-based assay

1.6.1. Advantage of multivariate over the univariate analysis

The recent advancement in the technology of automated cell-based assay, together with the impressive advancement in image analysis algorithms have enabled to collect a wide range of phenotypic information from each single experiment. However, this leads to the generation of a very complex dataset of results from a given experiment, that needs to be analyzed with more sophisticated, multivariate analysis rather than the more commonly used univariate analysis. In principle, the aim of univariate analysis is to analyze different sets of samples with one variable (readout) using statistical methods like t-test or ANOVA test. It is usually a preferable first choice because of the ease of interpretation (Saccenti, Hoefsloot et al. 2014). On the other hand, multivariate analysis comprises a set of techniques used to extract efficiently useful information from the complex data of the multi-parametric cell-based assay by analyzing many variables at the same time (Collinet, Stöter et al. 2010). Thus, a main advantage of multivariate (also called multi-parametric) analysis over the univariate analysis is that it analyzes all variables simultaneously and deals with the simultaneous relationships among variables. Biologically speaking, multivariate analysis enables to study the response, or even interaction, between different cellular activities to a specific treatment or stimuli under exact same experimental conditions, hence analyzing different aspects of cellular behavior simultaneously (Cromwell, Hoxha et al. 2018). Moreover, and more importantly, univariate analysis, e.g. with t-test, could result in a non-significant difference between a set of samples, while multivariate analysis can analyze in depth the association between different assay variables demonstrating noteworthy differences between these samples (Saccenti, Hoefsloot et al. 2014). Last but not least, an empirically verifiable advantage of

the multivariate analysis over univariate methods is that multivariate analysis could serve as a predictive technique to predict, for example, the disease status of the experimental sample by using a training data set where the disease status was predefined (Habeck and Stern 2010) as it will be shown during this project. Nevertheless, caution should be brought to some disadvantages of the multivariate analysis like the need for expertise with extensive high knowledge of computational and mathematical methods, to fully control the analysis. Besides, whereas the difference between multivariate and univariate analysis is relatively easy to be identified, the same is not true for the large number of methods used in the field of multivariate analysis (Habeck and Stern 2010, Cromwell, Hoxha et al. 2018). Thus, the analysis methods need to be chosen based on the type of the data set and according to the scientific question to be addressed.

In our perspective of AD blood biomarkers, combined readouts assay might be able to provide an understanding of the disease pathological variability within patient's population. Our multi-parametric assay is a combination of phenotypic and immune status parameters that forms an umbrella to differentiate the disease versus healthy individuals using the multivariate analysis.

There are many types of multivariate analysis, including principal component analysis (PCA), factor analysis, discriminant analysis, and clustering methods. Cluster analysis is a very common type of multivariate analysis (Akopov, Moskovtsev et al. 2013) and it was used during this project and will be discussed in the next section.

1.6.2. Cluster analysis of the multi-parametric cell-based assay

Cluster analysis is a popular multivariate analysis which can group the data of multi-parametric assays by conducting a machine learning task. It exhibits the data internal structure by showing the degree of their similarity for each group of separate objects (clusters) (Akopov, Moskovtsev et al. 2013). Cluster analysis was used to address the issue of inter-individual variability among patients such as the variability in response to brain stimulation (Pellegrini, Zoghi et al. 2018). The strength of such analysis to handle the inter-individual variability was attributable to the fact that cluster analysis helped to categorize patients according to their response patterns, as responder or non-responders despite that the variability comes from diversity of factors, e.g. genetics, gender, age, etc. (Pellegrini, Zoghi et al. 2018). This is because that the algorithm splits large data sets into

smaller subgroups that are mutually exclusive based on patterns or trends in the dataset. This increases similarity, i.e. homogeneity, within subgroups and simultaneously increases the difference or the heterogeneity between subgroups (Hair, Anderson et al. 1998). In line with this, a multi-parametric functional assay analyzed with cluster multivariate analysis is potentially a powerful strategy to handle the inter-individual variability within AD patients that was described during this introduction. Besides, the cluster analysis helps to study the simultaneous interaction between different factors contributing to the AD pathology.

A big issue in the field of clustering is the lack of clear definition of a “good clustering”. For example, assigning all observations to one single cluster seems as an outstanding outcome according to the clustering definition, but in fact, it gives no insightful information about the dataset. In parallel with this issue, there are currently many clustering methods, e.g. hierarchical, K-means, and density-based clustering, making the decision for one clustering strategy a non-trivial task and highly situation dependent (Rottger 2016). Despite the fact that clustering methods such as hierarchical and K-means clustering are widely used for biomedical data (Xu and Wunsch 2010), support vector machine classifier (SVM) was used to analyze the multi-parametric data generated during this project. This is because SVM is a well-known supervised learning method to process data with a low number of samples and a high number of features like the data generated during this project (Fabian Pedregosa, Gaël Varoquaux et al. 2011). SVM is a classification discriminator defined officially by a separating hyperplane. The method is based on a training annotation used to categorize new examples (Patel 2017). The SVM classifier uses normalizations which encourages the SVM to generate sparse weights, which makes the biological interpretation of the SVM results easier. Finally, feature selection is a key point of this method to avoid any overfitting issues during the data analysis (Fabian Pedregosa, Gaël Varoquaux et al. 2011). Identification of the most robust features is not only important for the conduction of the classification, but also for the investigation of the biological pathways behind this feature.

2. The study objective

This research thesis was part of a research project aimed to identify blood biomarkers of AD. Blood biomarkers would be of great diagnostic and therapeutic values in AD management since blood is easily accessible and can be simply implemented in clinical routines. Unfortunately, blood-based biomarkers of AD suffered always from the lack of reliability and the reproducibility (Hampel, O'Bryant et al. 2018) despite the high number of studies which addressed this issue (2,871 reports were published until end of April 2019). One of the main reasons for this phenomenon is that many different factors contribute to the complex pathology of AD. We believe that the development of a reliable and robust blood-based detection of AD would first necessitate the use a multi-parametric functional assay and second the use a multivariate analysis of the given assay. Therefore, we developed a multi-parametric assay to monitor a diversity of readouts in the peripheral immune system, e.g. TLR4 activation, inflammasome activation, cytokine release, expression status, and cellular composition. There are increased number of reports that demonstrated alterations in peripheral immunity during AD pathology. PBMCs were used as a cell model to investigate the presence of immune changes in the periphery of AD patients since they include the main immune cells like monocytes, T and B cells. The multi-parametric assay readouts were analyzed with a supervised machine learning classifier in order to develop an immune predictive phenotypic model for AD. The classifier was trained using the sample clinical annotation provided by clinicians for the given samples.

The prediction model would be of great value in the field of precision medicine while it can help in improving the decision of health care model in AD management. Furthermore, the classifier annotates the most important readouts (features) that were used to predict the sample clinical status. These features could be further investigated as therapeutic targets.

The results of this research thesis could be used as a pilot data to further validate the classifier in a bigger cohort of patient.

3. Materials and Methods

3.1. Supervision and team contributions

Prof. Dr. Joachim Schultze was the official supervisor for this Ph.D. The project was done in the laboratory of Dr. Eugenio Fava at the German Center for Neurodegenerative Diseases (DZNE), Bonn. Dr. Fava, as a group leader, and Dr. Wera Roth, as a project manager, were responsible for the original ideas, general supervision of the experimental designs, data analyses and thesis manuscript preparation.

Daisy Axt (technical assistance) helped in performing some of the project experiments. Dr. Kristian Händler and Dr. Thomas Ulas, from the laboratory of Prof. Dr. Schultze, were responsible for the experimental and analytical analysis of the RNA-seq data.

The patient cohort was provided, collaboratively, by Prof. Dr. Anja Schneider. She also provided a lot of advice and ideas for the steering of the project.

Dr. Christoph Moehl and Manuel Schoelling, from Image and Data Analysis Facility (IDAF) in the core facilities of DZNE Bonn, gave a lot of support to the project. They supported the image analysis approaches as well as conducting the cluster analysis of the multi-parametric assay and the supervised machine learning classification during the cellular composition analysis.

3.2. Materials

3.2.1. Patient cohort

A cohort of 20 patients, including 9 females and 11 males, was used for this project. The cohort was provided by Prof. Dr. Anja Schneider. Blood samples were collected between 2014-2015 at the DZNE, Göttingen. The isolation of PBMCs was conducted in Prof. Schneider's laboratory. The cryopreserved PBMC samples were stored in liquid nitrogen at the DZNE Bonn until the day of the experiment. The volunteer patients were subjected to a set of laboratory tests, including CSF analysis and MRI, in addition to clinical evaluation (see details in **Index I**). The clinical evaluation was done via the Mini-Mental State Exam (MMSE) and the Consortium to Establish a Registry for Alzheimer's Disease (CERAD) PLUS scale for AD patients volunteers. The cohort included 6 AD patients and 5 depressed patients and 9 samples of other diseases (**Index I**). The cohort mean age was 71 years with a range of 55-83 years old.

Local ethics committee approval and written informed consent from the patients were obtained following the requirements of the Ethical Committee.

3.2.2. Healthy volunteer group

The German Red Cross (DKR) provided the buffy coats from blood donations of healthy volunteers. The buffy coats were collected according to the German “guideline to the preparation of blood and blood components and the use of blood products”. Each donation was tested, by DKR, for HBsAg, HCV-Ak, HIV-1/2-Ak, Lues-Ak, and Anti-HBc. The buffy coats were usually delivered two days after the blood donation.

Furthermore, some buffy coats were provided by the university clinic Bonn (UKB). These buffy coats were tested, by UKB, for HCV-AK, HBc-AK, HBs-AG, HIV-1/2-Ak, Syphilis TP, HCV- NAT, HIV-NAT, and HBV-NAT. These UKB buffy coats were processed for PBMC isolation after over-night storage at 4°C.

3.2.3. Reagents

Table 1. Reagents and compounds

Reagent or compound name	Catalogue number	Company
Bovine Serum Albumin	A1470	Sigma Aldrich, USA
CIPROFLOXACIN Kabi 200mg/100ml	PZN:3277618	Fresenius Kabi Deutschland GmbH, Germany
Dimethyl sulfoxide, cell culture grade (DMSO)	A3672	AppliChem GmbH, Germany
DPBS, no calcium, no magnesium	14190094	Thermo Fisher Scientific, USA
Fetal Bovine Serum, heat-inactivated	F9665	Sigma Aldrich, USA
HEPES	15630056	Thermo Fisher Scientific, USA
Hoechst 33342, bisBenzimide	B2261-100mg	Sigma Aldrich, USA
L-Alanyl-Glutamine, 200mM Biochrom	K 0302	Biochrom, Germany
Leu-Leu-OMe·HCl	4578	Chem-Impex International, USA
Lipopolysaccharide from E. coli O111:B4 (LPS)	tlrl-3pelps	Invivogen, USA
LUNARIS™ Human 6-Plex Cytokine Kit	LHCY-20050S	AYOXXA, Germany
Nigericin	N1495	Life Technologies, UK

Pancoll human, density: 1.077 g/ml	P04-60500	Pan BioTech, Germany
Pierce™ 16% Formaldehyde	28908	Thermo Fisher Scientific, USA
QIAzol Lysis Reagent	79306	QIAGEN, Germany
Recovery™ Cell Culture Freezing Medium	12648010	Thermo Fisher Scientific, USA
RPMI 1640 liquid medium	F 1215	Biochrom, Germany
Triton™ X-100	T8787	Sigma Aldrich, USA

3.2.4. Antibodies

Table 2. Antibodies

Antibody name	Catalogue number	Company
Anti-human PYCARD-Dy488	LS-C180936-100	LSBio, USA
Anti-human TNF α (D1G2) - Alexa Fluor® 647	12771	Cell Signaling Technology, USA
Anti-human CD3 - Alexa Fluor® 488	344810	BioLegend, USA
Anti-human CD19 - Alexa Fluor® 647	302222	BioLegend, USA
Anti-Human CD14 - PE	562691	BD, USA

3.2.5. Assay Kits

Table 3. Kits

Kit name	Catalogue number	Company
Human TNF alpha kit	62HTNFAPEG	Cisbio, France
Human IL1 β kit	62HIL1BPEG	Cisbio, France
AYOXXA LUNARIS™ Human 6-Plex Cytokine assay	LHC-1000061S	AYOXXA, Germany

3.2.6. Recipes

PBMC cell culture medium

- RPMI 1640 500 ml
- L-Alanyl-Glutamine, 200mM 10 ml (2% V/V)
- HEPES, 1M 12.5 ml (2.5% V/V)
- Ciprofloxacin Kabi 2.5 ml (0.5% V/V)
- Hi-FBS 50 ml (10% V/V)

Blocking buffer for cell surface markers (CDs) staining (1% BSA/PBS)

-
- Dulbecco's phosphate-buffered saline (PBS), calcium, no magnesium 1,000 ml
 - Bovine serum albumin (BSA), low endotoxin, lyophilized powder 10 g

BSA powder was mixed with PBS in a glass beaker using magnetic stirrer, 300 ml of the solution were filtered using filtering flask. Then the prepared solution was stored at 4 °C. The remaining solution was used to prepare PYCARD Blocking Buffer.

Blocking-permeabilization buffer PYCARD-TNF α staining (0.5% Triton 1%BSA/PBS)

- 1% BSA/PBS remaining in the beaker from 1% BSA/PBS preparation 700 ml
- Triton™ X-100 for molecular biology 3.5 ml

Mix in the beaker using magnetic stirrer then filter-sterilize. Store the prepared solution at 4 °C

Leu-Leu-OMe-HCl 1M stock

- Dissolve 295 mg in 1 ml DMSO (AppliChem)
- Aliquot à 50 μ l
- Store at -20 °C

Nigericin free acid 10 mM stock

- Dissolve 10 mg Nigericin in 1.38 ml DMSO (AppliChem)
- Aliquot à 40 μ l
- Store at -20 °C

Hoechst 33342 10mg/ml stock

- Dissolve 10 mg in 1 ml DMSO (AppliChem).
- Aliquot à 100 μ l
- Store at -20 °C

3.3. Methods

3.3.1. Isolation of PBMCs from buffy coats

PBMCs were isolated from buffy coats using Pancoll Density Gradient Medium (PDGM) from Pan BioTech. Buffy coats were provided by DKR or UKB as described before. A 20 ml aliquot of the buffy coat was mixed with 15 ml PBS and the mixture was loaded on top of 15 ml PDGM in a 50 ml Falcon tube. The (blood-PBS-PDGM) Falcon tube was centrifuged for 20 minutes at 700 g (without breaks or de-acceleration). After centrifugation, the mononuclear cells from the plasma/Pancoll interface (**Figure 10**) were collected into fresh tubes. The collected cells were washed three times with PBS before they were

counted (see cell counting next section) and resuspended in an equal volume of Gibco freezing media to get 1×10^7 cells/ml. Each cryovial was loaded with 1 ml freezing media (containing 1×10^7 PBMCs) and stored overnight at -80°C in an isopropanol freezing container. Finally, PBMCs were permanently stored in a liquid nitrogen tank (LN2).

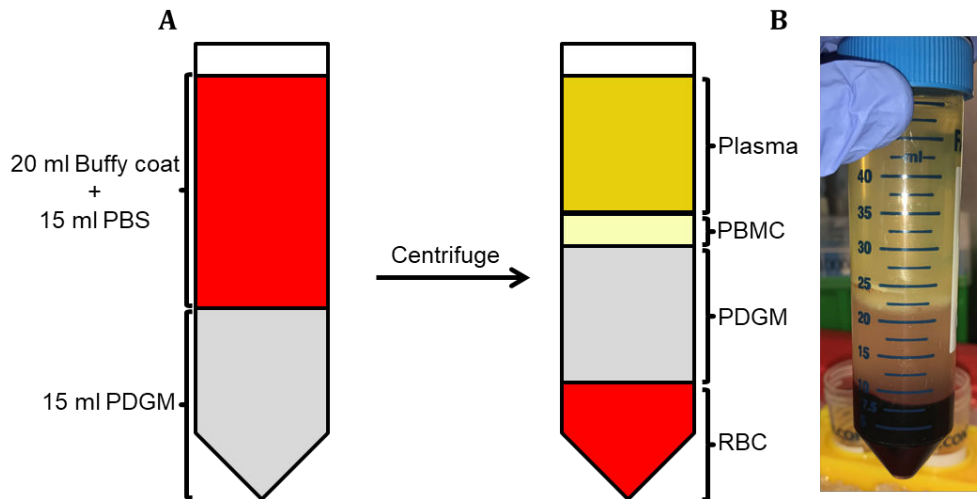


Figure 10: PBMC isolation from buffy coat.

(A) Layers of Pancoll Density Gradient Medium (PDGM) and buffy coats before and after centrifugation in a 50-ml Falcon tube. (B) A photo from one of the project buffy coats isolation (after centrifugation) depicting the density gradient layers (from top; plasma, PBMC, PDGM, and red blood cells (RBCs)).

3.3.2. Cell counting

PBMCs were counted using Vi-CELLXR Cell Viability Analyzer (Beckman Coulter). For each sample, 500 μl of cell suspension was used as a counting sample. The counting sample was loaded into the Vi-CELLXR sample loading chamber. The total number of cells, the total number of viable cells and the cell viability were directly provided by the Vi-CELLXR software.

3.3.3. The recovery rate of viable PBMCs after thawing

After PBMCs have been isolated, they were stored in liquid nitrogen until the day of the experiment. On the day of the experiment, frozen PBMCs were thawed in the water bath for approximately 2 minutes, until the vial contents were mostly thawed (small ice clump was still visible). Thawed PBMCs were transferred from cryotubes into a 50-ml Falcon tube containing 9 ml of medium. Cells were centrifuged for five minutes at 350 g to wash off the residual DMSO. PBMCs were resuspended in 1 ml of medium, using a pipette, then diluted up to 3 ml. The total number of viable cells and cell viability were obtained as

described before. The recovery rate was defined as the percentage of the viable cells recovered after thawing the cryopreserved samples. It was expressed by the percentage of viable cells divided by the original number of frozen cell (10 million cells per vial).

3.3.4. PBMC cell-based assay

3.3.4.1. Testing the automation platform

The assay was moved from manual performance into automated cell seeding and reagents pipetting to scale up the assay and improve its consistency. The first step was to check that the automation platform delivers an accurate amount of liquid according to the assay design. Thus, the 96-head Biomek NX^P was used to load a full 384-well plate with 40 μ l of PBS per well and real volume inside each well was measured via Echo[®] 550 Liquid Handler.

The mean volume per well was 40.79 μ l with a Coefficient of Variation (CV) less than 2% (Figure 11).

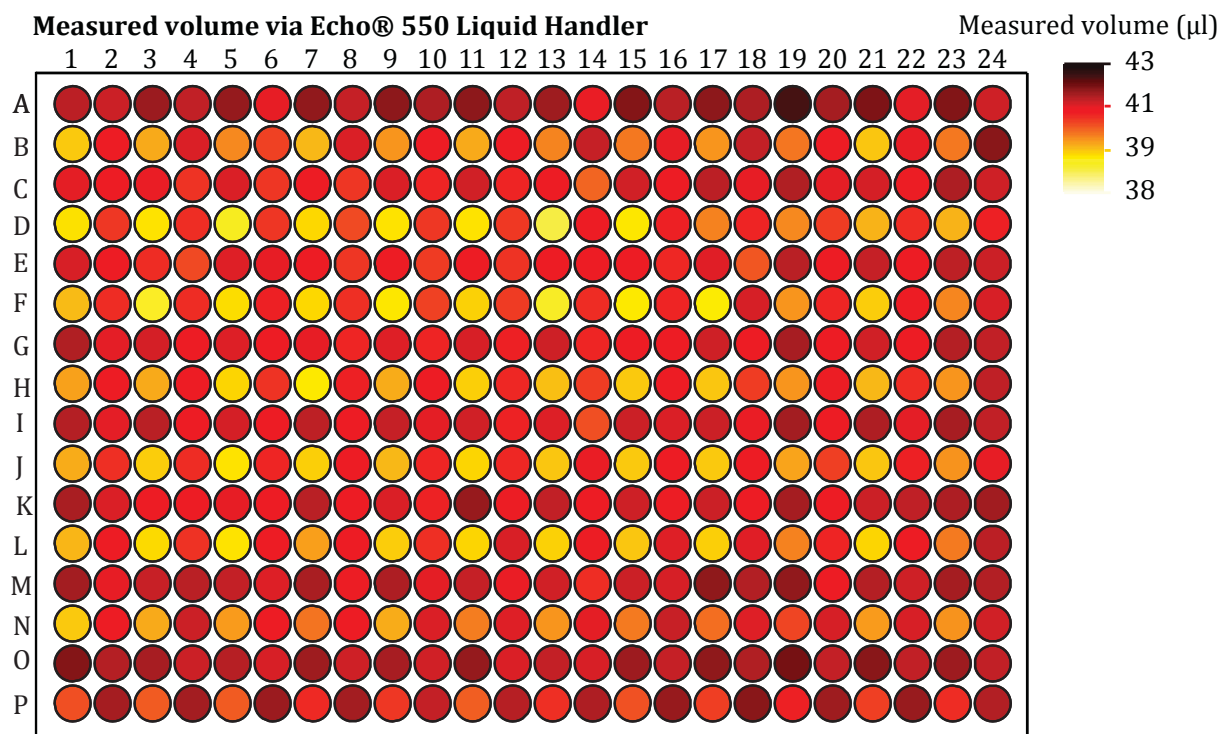


Figure 11: Liquid pipetting accuracy of the 96-head Biomek NX^P.

The accuracy of Biomek NX^P automated liquid transfer was checked using an Echo[®] 550 Liquid Handler. A full 384-well plate was loaded with 40 μ l per well and the real liquid volume inside each well was measured via the Echo[®] 550. The mean volume per well was 40.79 μ l with a CV of less than 2%.

3.3.4.2. Cell suspension and assay reagent preparations

Frozen PBMCs were thawed and counted as described before. The cell suspension was prepared with a concentration of 1×10^6 cell/ml and the suspension was transferred into a 96-deep well source plate.

LPS was prepared into a working solution of 60 ng/ml. Into a 40 μ l of cell culture, 20 μ l of the LPS working solution was added to obtain a concentration of 20 ng/ml on cell.

LeuLeuOMe was prepared into a working solution of 0.8 mM (0.2 mM on cell). First, it was resolved in DMSO at a stock concentration of 1 M and stored in aliquots at -20 °C. To conduct the screen, 1 M LeuLeuOMe was diluted in 40 mM HEPES in PBS pH 7.4 to an intermediate concentration of 0.8 mM (i.e. 4-fold concentrated). Then, 20 μ l of 0.8 mM LeuLeuOMe was added to 60 μ l of the cell culture to get a concentration of 0.2 mM on cells. Nigericin was prepared into a working solution of five μ M (20 μ M on cell). First, 10 mM Nigericin was diluted in complete media to an intermediate concentration of 20 μ M (i.e. 4-fold concentrated). Then, 20 μ l of 20 μ M Nigericin was added to 60 μ l of the cell culture to get a concentration of 20 μ M on cell.

3.3.4.3. Automated high content screen assay

Cells were seeded using 96-head Biomek NX^P (BECKMAN COULTER). The 384-head Biomek NX^P was used for the pipetting of both LPS and the inflammasome activator. The cells fixation with paraformaldehyde (PFA) as well as the staining were done using the 384-head Biomek NX^P. Finally, the assay plates were imaged in the automated confocal microscope CV6000 (Yokogawa Inc.).

Cells were seeded in 384-well assay plate (Perkin Elmer Inc.) using a concentration of 4×10^4 cells per 40 μ l media per well. The cells were immediately treated with 20 μ l LPS for 2 h followed by an inflammasome activation either using LeuLeuOMe for 0.5 h or Nigericin for 1 h. During priming and activation, cells were incubated at 37 °C, 5% CO₂, and 95% humidity. After activation has been done, cell-free supernatants were harvested and stored at -80 °C until they were used for cytokine assays. Cells on assay plate were fixed with 4% PFA in PBS without Ca²⁺/Mg²⁺, and stained with Hoechst 33342, anti-PYCARD, and anti-TNF α .

Samples were seeded in rows in the 384-well assay plate (**Figure 12**). Each sample was cultured on 48 replicate wells (2 rows). Four assay conditions were applied column-wise

(untreated, LPS, LPS + activator, and activator only). 6 columns were used for each assay condition. This resulted in 12 replicates of sample per condition. For each experiment, two sister plates were cultured. The first plate was used for LeuLeuOMe activation, while the second one was used for Nigericin activation. The cells in the plate were stained with anti-TNF α and anti-PYCARD (describe later). However, four replicate wells from each sample were stained with cell surface marker in case of untreated and LPS conditions.

Untreated						LPS						LPS + LeuLeuOMe						LeuLeuOMe						
1	2	3	4	5	6	7	8	9	10	11	12	13	14	15	16	17	18	19	20	21	22	23	24	
A	HD1	HD1	HD1	HD1	HD1	HD1	HD1	HD1	HD1	HD1	HD1	HD1	HD1	HD1	HD1	HD1	HD1	HD1	HD1	HD1	HD1	HD1	HD1	A
B	HD1	HD1	HD1	HD1	HD1	HD1	HD1	HD1	HD1	HD1	HD1	HD1	HD1	HD1	HD1	HD1	HD1	HD1	HD1	HD1	HD1	HD1	HD1	B
B	HD2	HD2	HD2	HD2	HD2	HD2	HD2	HD2	HD2	HD2	HD2	HD2	HD2	HD2	HD2	HD2	HD2	HD2	HD2	HD2	HD2	HD2	HD2	C
C	HD2	HD2	HD2	HD2	HD2	HD2	HD2	HD2	HD2	HD2	HD2	HD2	HD2	HD2	HD2	HD2	HD2	HD2	HD2	HD2	HD2	HD2	HD2	D
C	HD3	HD3	HD3	HD3	HD3	HD3	HD3	HD3	HD3	HD3	HD3	HD3	HD3	HD3	HD3	HD3	HD3	HD3	HD3	HD3	HD3	HD3	HD3	E
D	HD3	HD3	HD3	HD3	HD3	HD3	HD3	HD3	HD3	HD3	HD3	HD3	HD3	HD3	HD3	HD3	HD3	HD3	HD3	HD3	HD3	HD3	HD3	F
D	HD4	HD4	HD4	HD4	HD4	HD4	HD4	HD4	HD4	HD4	HD4	HD4	HD4	HD4	HD4	HD4	HD4	HD4	HD4	HD4	HD4	HD4	HD4	G
E	HD4	HD4	HD4	HD4	HD4	HD4	HD4	HD4	HD4	HD4	HD4	HD4	HD4	HD4	HD4	HD4	HD4	HD4	HD4	HD4	HD4	HD4	HD4	H
E	HD5	HD5	HD5	HD5	HD5	HD5	HD5	HD5	HD5	HD5	HD5	HD5	HD5	HD5	HD5	HD5	HD5	HD5	HD5	HD5	HD5	HD5	HD5	I
F	HD5	HD5	HD5	HD5	HD5	HD5	HD5	HD5	HD5	HD5	HD5	HD5	HD5	HD5	HD5	HD5	HD5	HD5	HD5	HD5	HD5	HD5	HD5	J
F	HD6	HD6	HD6	HD6	HD6	HD6	HD6	HD6	HD6	HD6	HD6	HD6	HD6	HD6	HD6	HD6	HD6	HD6	HD6	HD6	HD6	HD6	HD6	K
G	HD6	HD6	HD6	HD6	HD6	HD6	HD6	HD6	HD6	HD6	HD6	HD6	HD6	HD6	HD6	HD6	HD6	HD6	HD6	HD6	HD6	HD6	HD6	L
G	HD7	HD5	HD5	HD5	HD5	HD5	HD5	HD5	HD5	HD5	HD5	HD5	HD5	HD5	HD5	HD5	HD5	HD5	HD5	HD5	HD5	HD5	HD5	M
H	HD5	HD5	HD5	HD5	HD5	HD5	HD5	HD5	HD5	HD5	HD5	HD5	HD5	HD5	HD5	HD5	HD5	HD5	HD5	HD5	HD5	HD5	HD5	N
H	HD8	HD8	HD8	HD8	HD8	HD8	HD8	HD8	HD8	HD8	HD8	HD8	HD8	HD8	HD8	HD8	HD8	HD8	HD8	HD8	HD8	HD8	HD8	O
	HD8	HD8	HD8	HD8	HD8	HD8	HD8	HD8	HD8	HD8	HD8	HD8	HD8	HD8	HD8	HD8	HD8	HD8	HD8	HD8	HD8	HD8	HD8	P
	PYCARD + TNF α				CD3,14, &19		PYCARD + TNF α				CD3,14, &19		PYCARD + TNF α											

40 μ l cell suspension/well

Figure 12: Assay plate design

PBMCs of each healthy donor (HD) were cultured on 2 rows of the 384-well assay plate, meaning 48 replicate wells. The assay conditions (untreated, LPS, LPS + activator, and activator only) were applied column-wise. 6 columns were used for each assay condition. This assay design provided the opportunity to test 12 replicates per condition for each sample. Cell were stained with anti-TNF α and anti-PYCARD (describe later). However, four replicate well from each sample were stained with cell surface markers in case of untreated and LPS conditions.

3.3.4.4. Immunofluorescence staining

3.3.4.5. PYCARD-TNF α staining

Cells were fixed for 15 minutes using 4% PFA (prepared in PBS). Then, the fixation solution was taken out and cells were blocked/permeabilized for 20 minutes with 0.5% Triton X-100 in PBS containing 1% BSA. After the removal of blocking solution, cells were incubated for 1 h at room temperature (RT) with 20 μ l Dy488-conjugated rabbit anti-PYCARD antibody from LSBio (1:500 in PBS containing 1% BSA, 0.5% Triton X-100) and Dy647-conjugated rabbit anti-TNF α (D1G2) mAb from CST (1:50 in PBS containing 1% BSA, 0.5% Triton X-100), in addition to 1 μ g/ml Hoechst 33342. At the end of staining time cells were washed 1x with 20 μ l FBS/PBS. Finally, 30 μ l FBS/PBS were added per well and assay plates were stored at 4 $^{\circ}$ C until plate imaging.

3.3.4.6. Cell surface marker staining

After the cells have been fixed for 15 minutes with 4% PFA, they were blocked with 20 ml 1% BSA/PBS for 20 minutes at RT. The blocking solution was removed and cells were incubated for 1 h in the dark at RT with anti-human CD3- AF488 (1:500, BioLegend), anti-human CD14 - PE (1:50, BD), and anti-human CD19- AF 647 (1:100, BioLegend) in addition to 4 µg/ml Hoechst 33342. At the end of staining time, cells were washed 1x with 20 µl FBS/PBS. Finally, 30 µl FBS/PBS was added per well and assay plates were stored at 4°C until plate imaging.

3.3.4.7. Confocal microscopy

Image acquisition was carried out using the automated confocal imaging system CellVoyager CV6000 (Yokogawa Inc.). Images were captured using three channels, in case of PYCARD-TNF α staining, including: Hoechst 33342, DyLight 488, and DyLight 647.

Four channels were used in case of cell surface marker staining, including Hoechst 33342 (DNA), DyLight 488, DyLight 568, and DyLight 647.

For each well, 16 or 32 fields were imaged and maximum-intensity projections were generated from Z-stacks. Exposure times were chosen to prevent saturation and allow quantification in the linear range.

A minimum of 300 cells which corresponds to 16 microscopic field views were analyzed per well, using a 40x objective with water immersion and no binning. Images were analyzed using the CellVoyager analysis support software (Yokogawa Inc.) or CellProfiler.

3.3.4.8. Cytokine measurements

3.3.4.9. Supernatant collection for cytokine measurement

PBMCs were seeded, incubated with LPS, and activated by inflammasome activator as described. At the assay endpoint, 60 µl of supernatant were harvested per well into a 384-well collection plate using the 384-head Biomek NX^P. The collection plate was centrifuged for 3 minutes at 350 g to remove remaining cells in the supernatants. Aliquots of 16 or 8 µl were transferred to a 384-microtiter storage plate. The storage plates were centrifuged for 15 seconds to settle the supernatant in the bottom of the well. Finally, the storage plates were sealed with aluminum foil and stored at -80 °C until further processing.

3.3.4.10. Homogeneous Time Resolved Fluorescence (HTRF)-based assay for cytokine measurement

Supernatants were collected, processed and stored as described before. For cytokine quantification, cell-free supernatants were thawed and analyzed by Homogeneous Time Resolved Fluorescence (HTRF) human IL-1 β and HTRF human TNF α kits according to the manufacturer's instructions. The plates were measured with a SpectraMax Paradigm Multi-Mode Micro-Plate Reader (Molecular Devices).

3.3.4.11. AYOXXA LUNARIS™ Human 6-Plex Cytokine assay

Supernatants were collected, processed and stored as described before. To measure the cytokine release, cell-free supernatants were thawed and analyzed by AYOXXA LUNARIS™ Human 6-Plex Cytokine assay according to the manufacturer's instructions. The AYOXXA assay plates were analyzed with the LUNARIS™ BioChip reader. Data were analyzed with LUNARIS™ Analysis Suite.

3.4. Image analysis

3.4.1. Conventional software-based image analysis

The CellVoyager analysis support software was used for automated image analysis (Yokogawa Inc.). An image analysis routine was developed for single-cell segmentation and the identification of PYCARD speck formation, in addition to detection of the intracellular TNF α aggregations. The total number of cells was determined based on the Hoechst 33342 signal. TNF α production was monitored by the anti-TNF α -Dy568 signal, and PYCARD speck formations were visualized by anti-PYCARD-Dy488 staining. Primed or TNF α positive cells were identified via TNF α signal morphology and intensity characteristics linked to their corresponding primary cell objects. The percentage of priming activity was calculated as the number of TNF α positive cells per total number of cells set to 100%. Inflammasome activated or PYCARD speck positive cells were identified via PYCARD signal morphology and intensity characteristics that linked to their corresponding primary cell objects. The percentage of PYCARD specking activity was calculated as the number of PYCARD speck positive cells per total number of cells set to 100%.

3.4.2. Deep learning approach for PBMC subsets characterization

To characterize the PBMC subset composition, a cell-type classification was done according to nucleus morphology and cell-type-specific marker intensity in the nucleus neighborhood. Cell surface markers of T cells (CD3⁺), B cells (CD19⁺), and monocytes (CD14⁺) were used as cell-type-specific markers. A pixel-based supervised classification was done using a U-Net neural network (Ronneberger, Fischer et al. 2015). To perform the classification, Dr. Christoph Moehl and Manuel Schoelling, from the IDAF facility at DZNE Bonn, have developed a tool called YAPiC, Yet Another Pixel Classifier (based on deep learning) (<https://yapic.github.io/yapic/>). YAPiC implements a classification with U-Net based on training labels that can be collected by the user with the Interactive Learning and Segmentation Toolkit (ilastik). For the ilastik labeling (**Figure 13**), 20 representative images were used. On each image, an average of two example objects were labeled for each class (and 7 objects were labeled for each of monocyte and negative or unstained cells). Objects were labeled according to their cell surface marker staining and objects with bean kidney-like shape were labeled as monocytes (Sahu, Bethunaickan et al. 2014).

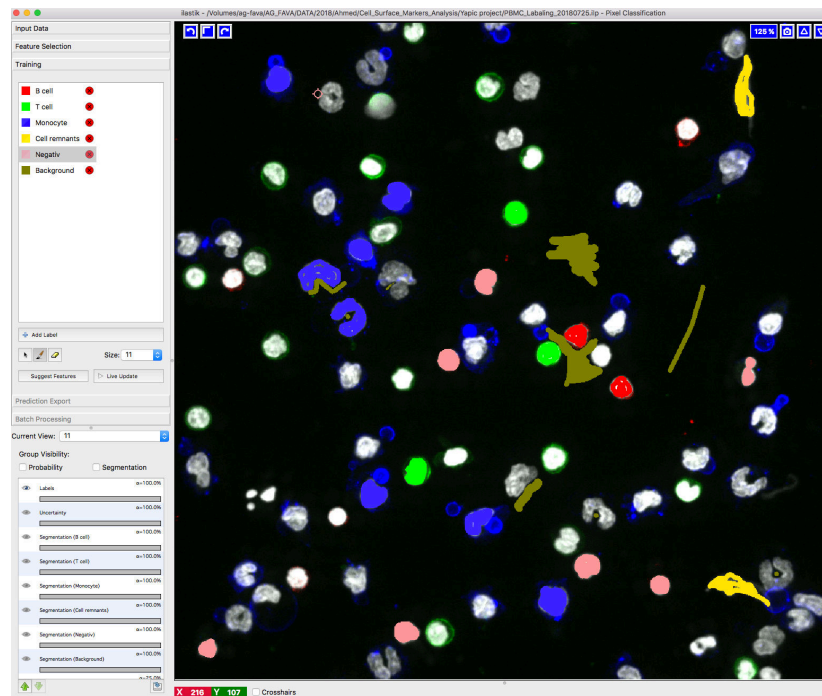


Figure 13: ilastik software to label PBMCs.

The Interactive Learning and Segmentation Toolkit ilastik was used to label PBMCs, that had been stained for T cells (green, CD3⁺), B cells (red, CD19⁺), and monocytes (blue, CD14⁺) markers. Unstained cells were labeled as marker negative or as cell remnants.

After labeling, YAPiC started a learning phase using the labeled example objects from ilastik, to develop a set of prediction rules. The rules were used to predict the unlabeled objects in the whole data set. The output is a class probability per pixel (**Figure 42** in Results).

Finally, a CellProfiler pipeline was used for cell object segmentation and classification into distinct cell-types depending on cell-type probability (from the pixel classification).

3.5. Screening assay of patient samples

The assay was performed in the department of Laboratory Automation Technologies (LAT) of the Core Research Facilities & Services (CRFS) at DZNE Bonn. 384-well assay plates were used to seed three PBMC samples of healthy donors, in addition to five samples from patients per day (**Figure 14**). This means that four days were needed to screen the 20 samples of patients. The three samples from healthy donor (HD04, HD05, and HD06) were repeated on each screening day and each assay plate.

On each experiment, two sister plates were prepared, one for LeuLeuOMe and one for Nigericin activation as described before. The assay design included: 48 replicates per sample, 12 replicates per condition, four treatment conditions. For LPS + activator, and the activator only conditions, there were 12 replicates per donor, which were stained for anti-PYCARD, anti-TNF α , and Hoechst 33342 staining. For the untreated and the LPS conditions, four replicates were stained for anti-CD3, anti-CD14, anti-CD19 and Hoechst 33342. The remaining 8 replicates were stained for PYCARD, anti-TNF α , and Hoechst 33342.

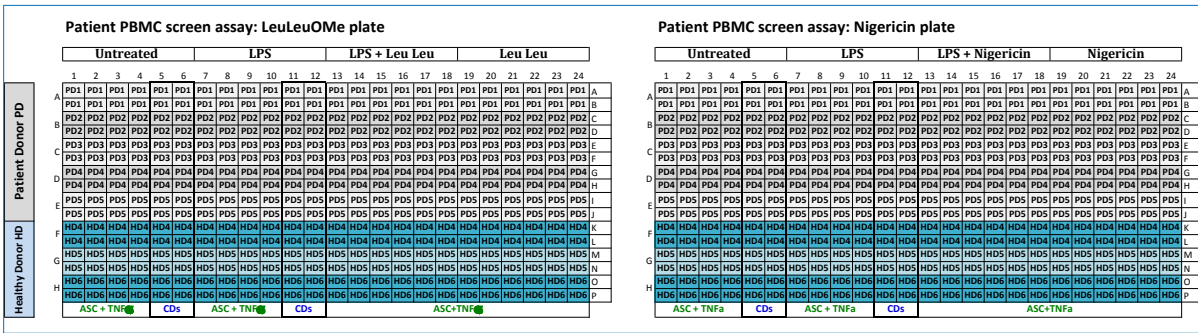


Figure 14: Assay plate design for the patient PBMC screening assay.

Two sister 384-well assay plates were cultured per experiment (LeuLeuOMe and Nigericin plates). Each plate was used to culture 5 PBMC samples from the patients (grey wells) and three samples from healthy donors (blue wells). On each plate, four treatment conditions (untreated, LPS, LPS + activator, and the activator only) were applied. For each sample, 48 replicates were tested, meaning 12 replicates per condition. All replicates from LPS + activator and the activator only conditions were stained for anti-PYCARD, anti-TNF α , and Hoechst 33342. For the untreated and the LPS conditions, 4 replicates were stained for anti-CD3, anti-CD14, anti-CD19, and Hoechst 33342. The remaining 8 replicates were stained for PYCARD, anti-TNF α , and Hoechst 33342.

3.6. RNA-seq assay

3.6.1. Sample preparation

During the patient screening and immediately after cell thawing, an aliquot of 2E5 cells was put aside for RNA-seq sample preparation. Aliquots were placed into Eppendorf tubes, centrifuged for five minutes in Heraeus™ Pico™ 17 microcentrifuge with 12,000 rpm at RT. Media was aspirated and the cell pellet was resuspended in 700 μ l QIAzol. Finally, tubes were stored at -80 °C until they were processed for RNA-seq.

3.6.2. Library generation and sequencing

RNA-seq and its relevant data analysis were conducted in the laboratory of Prof. Dr. Joachim Schultze. Dr. Kristian Händler conducted the laboratory experiment and Dr. Thomas Ulas conducted the data analysis. Smart-seq2 (Picelli, Faridani et al. 2014) was used for the generation of full transcript sequencing libraries using standard reagents and procedures as described by Picelli et al. In short, cells were thawed and immediately placed in lysis buffer containing 0.2% TritonX-100 and a ribonuclease inhibitor that blocks RNA degradation and stabilizes the RNA. The lysis solution also contained free dNTPs and oligo-dT oligonucleotides (30-nt poly-dT stretch and a 25-nt universal 5' anchor sequence) to prime the subsequent RT reaction on polyadenylated RNA

sequences. The SMART RT reaction was performed at 42 °C for 90 minutes using commercial SuperScript II (Invitrogen) and a TSO. A pre-amplification PCR of 14 cycles was performed to generate double-stranded DNA from the cDNA template. Tagmentation and subsequent PCR amplification using the Nextera XT kit (Illumina) was used to quickly and efficiently construct sequencing libraries from the amplified cDNA. Samples were pooled and clustered at 1.4pM on a NextSeq500 system (Illumina) to generate ~10M single-end reads per sample using High Output v2 chemistry. Sequencing data were demultiplexed using bcl2fastq2 v2.20 and pseudo aligned to Homo_sapiens.GRCh38.rel79.cdna.all.fa.gz transcriptome using kallisto v.0.44.0.

3.7. Statistical analysis and mathematical calculations

3.7.1. Statistical analysis

Statistical analyses were performed using Microsoft Excel 2011 and JMP 14 software. One-way Analysis of variance (ANOVA) and unpaired two-tailed Student's t-tests were used to test for significance. *P* values of <0.05 were considered significant. Error bars represent the standard deviations (SD) or the standard error of the mean (SEM).

3.7.2. Data normalization to monocyte number

The inflammasome activation rate was calculated first by dividing the number of activated (PYCARD positive) cells to the total number of cells. Then, the inflammasome activation rate was normalized to the number of monocytes. The normalization was done donor-wise per assay plate. This means that the monocyte percentage of the untreated PBMCs of one sample is used to normalize the inflammasome activation rate of that sample on this particular plate. The monocyte percentage of the untreated PBMC population was used to normalize the activation rate for all the assay conditions. The monocyte percentage of the untreated PBMCs was used also to normalize the percentage of intracellular TNF α positive cells, TNF α release, and IL-1 β release.

3.7.3. Calculation of the Coefficient of variation for inter-assay precision

The inter-assay precision or assay stability was evaluated via the coefficient of variation. The inflammasome activation assay was performed repeatedly over three days. PBMCs from 6 healthy donors were used for this experiment. For each donor, the stability of

sample performance was assessed by calculating the inter-day Coefficient of Variation (CV). The CV was calculated using the following formula:

$$CV_{\text{inter}} = \frac{\sqrt{(ns^2)}}{\bar{Y}_i}$$

where :

n is the number of aliquots run each day,

s² is the variance of the mean of each day's results,

\bar{Y}_i is the overall mean of specimen i.

The CV was calculated treatment-wise, meaning that e.g. the replicates from LPS + Nigericin were calculated separately from the replicates of the untreated condition. The number of replicates on each day were always 12 replicates.

3.8. Cluster analysis

The cluster analysis was conducted by Manuel Schoelling, from the IDAF facility at DZNE, Bonn. The combined dataset from the multi-parametric assay of patient screen were 71 readouts (see the full table in **Index I**). The feature table (**Index I**) was piled up from the cell-based assay readouts (64 features) and the clinical information of the patients (7 features). The table was designed in a way that each row represents a sample ID with a long vector of 71 features. Some features were excluded to avoid bias analysis ('CSF_t_tau', 'CSF_p_tau', 'CSF_Ab42', 'Ab42_40_Ratio'). Readout values were normalized with z-score transformation ($z = \mu/\sigma$). This is to standardize features by removing the mean and scaling to unit variance. A supervised learning workflow was conducted using the discriminative Support Vector Machine (SVM) classifier from (Fabian Pedregosa, Gaël Varoquaux et al. 2011) using normalized data. The latter encourages the SVM to generate sparse weights, which makes biological interpretation of the SVM results easier. This algorithm uses labeled training data (disease label) to categorize new examples (samples). Feature selection was limited to the most representative five features. A heatmap was created from the most representative five features. Finally, a confusion matrix was created to

check the prediction accuracy. The calculations were performed using scikit-learn 0.20.0 (Fabian Pedregosa, Gaël Varoquaux et al. 2011) and Python 3.5.

3.9. Software

Table 4. Software

Software name	Developer	Version	Other versions which were used
CellProfiler	Broad Institute	3.0.0	2.2.0
ilastik	ilastik developers	1.3.0	
ImageJ (Fiji)	Hank Oppenheimer	2.0.0	
JMP	SAS Institute Inc.	14.0	13.0 and 10.0
Microsoft Excel 2011	Microsoft Inc.	14.7.2	Excel 2016
CellVoyager CV7000 Analysis Software	Yokogawa Inc.	3.5.1.18	
LUNARIS™ Analysis Suite	AYOXXA	LAS-0001	

4. Results

4.1. PBMCs as a proxy for systemic immune changes during AD pathology

In the last two decades, there were continuous reports providing evidence that AD pathology is associated with changes in the peripheral circulation (Preische, Schultz et al. 2019). Recently, Nakamura and colleagues have developed a proteomic approach to detect different A β cleavage forms in the peripheral blood of AD patients (Nakamura, Kaneko et al. 2018). Furthermore, the peripheral immune system has been reported to be altered during AD pathology (Saresella, La Rosa et al. 2016, Hampel, O'Bryant et al. 2018, Labzin, Heneka et al. 2018, Hudd, Shiel et al. 2019). For instance, a recent study described a positive correlation between the expression of phosphorylated cAMP responsive element binding protein 1 (pCREB1) in PBMCs of AD patients and its expression in the postmortem brain, indicating concomitant changes in the central and peripheral immune components during the disease course (Bartolotti and Lazarov 2019). Although it is still not clear whether the peripheral immune changes are a cause or a consequence for the AD pathology, the systemic immune response can potentially be used as a proxy to detect pathological alterations in the CNS. (Kenny, Jimenez-Mateos et al. 2018). The goal of this project is to identify AD blood biomarkers via immune profiling of individual donors. For this goal, PBMCs were utilized as an *ex vivo* model to detect the immune changes within the blood of AD patients. As shown in **Figure 15 A**, first PBMCs were isolated either from buffy coats of healthy volunteers or blood samples of AD- and depressive patients (as shown in **Table 5**). PBMCs were used to develop a functional multiplexed cell-based assay. Particularly, the following cellular components were monitored by automated confocal microscopy: a) intracellular TNF α , b) PYCARD complex formation and c) chromatin/nucleus (**Figure 15 B**). The assay was also flanked by homogenous readouts for IL-1 β and TNF α release. Furthermore, transcriptome analysis was conducted to evaluate the expression profile of the PBMC samples in the naïve status. Finally, the supernatants of PBMCs at the assay endpoint were collected and used to conduct a multiplexed proteomic analysis using the Olink inflammation panel, a protein panel of 96 inflammatory biomarkers (data not shown).

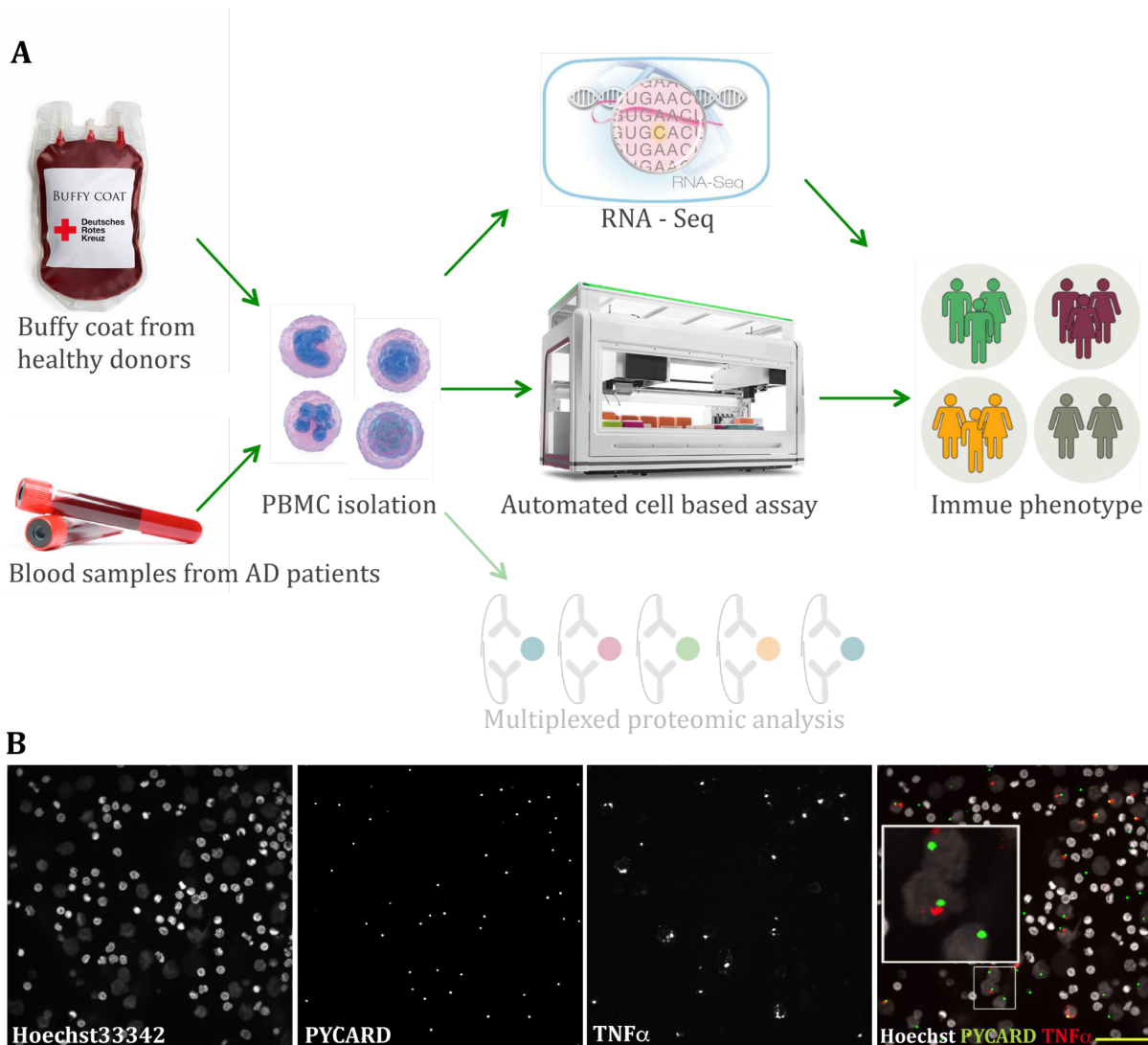


Figure 15: A. General overview of the PBMC project workflow.


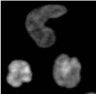
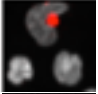
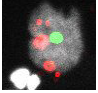
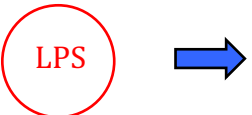
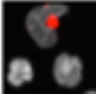
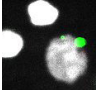
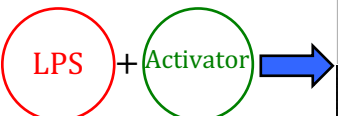
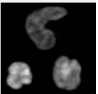
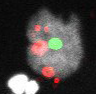
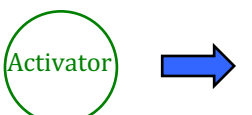
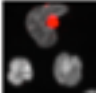
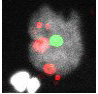
Buffy coats, provided by the German Red Cross, or blood samples from AD patients were used to isolate PBMCs. PBMCs were then used to conduct an automated cell-based assay and an RNA-Seq analysis. The harvested supernatants from the cell culture were used in our laboratory to conduct a multiplexed proteomic analysis using the Olink inflammation panel (results are not shown). The output is a set of parameters that can be used to derive a signature of immune features to evaluate and predict the disease status of the PBMCs sample donor. **B. cellular components that were monitored using the automated cell-based assay.** Intracellular TNF α , PYCARD complex formation, and chromatin/nucleus were investigated using a functional multiplexed cell-based assay. Scale bar, 40 μ m.

In contrast to previously published blood marker studies of AD, the assay setup takes in consideration the analyses of different cellular compartments and cytokine release as well as transcriptome analysis and disease status of the sample donor. The lack of reproducibility was a major challenge in the development of AD blood-based biomarkers

(Hampel, O'Bryant et al. 2018). This might be because the majority of the blood-based biomarker development attempts have been based on a single marker/target. Thus, to develop a reliable and robust blood-based detection of AD, this work focused on the development of a multiplexed functional assay with a multivariate data collection from different sources. Hence, the assay enables generating a complexed feature signature obtained by transcriptome analysis, functional assay data, cytokine release, proteomic analysis, and clinical data for each sample. This feature signatures (immune phenotypes) were analyzed by a machine-learning algorithm to detect the significant differences among the whole set of features for both AD patients and control donors.

The functional assay was designed to enables confronting the immune system with a set of experimental conditions, i.e. LPS, LPS + inflammasome activator, activator alone, and untreated, thereafter, the response of the PBMC sample was analyzed (**Figure 16**). Untreated PBMCs, that showed neither intracellular TNF α production nor inflammasome activation, represented the normal control phenotype. On the other hand, untreated PBMCs, that produced intracellular TNF α indicated that these PBMCs were already primed, i.e. TLR signaling was activated. PBMCs, that showed inflammasome activation after activator treatment alone, were considered as either already primed or the activator mediated a priming effect in addition to its activation capability (**Figure 16**).

In summary, this assay design enhances the possibility of capturing the expected physiological and pathological phenotypes. In other words, this assay setup can evaluate the immune system in the steady state and it enables the exploration of potential diverse immune responses observed under different experimental conditions.

Condition	Phenotype	Biological explanation
		Normal phenotype
		PBMCs were already primed
		PBMCs were already primed and activated
		Normal phenotype; LPS caused TNF α expression.
		PBMCs were already activated or LPS caused activation
		PBMCs were neither primed nor responded to LPS priming
		Inflammasome activation due to LPS and activator effect
		PBMCs were already primed
		Activator alone triggers inflammasome activation because it has priming and activation effect or immune system was already primed

----- Many other phenotypes are possible

Figure 16: Potential phenotypes that can be obtained from the cell-based assay.

Untreated PBMCs from healthy donors were expected to show a normal control phenotype, i.e. neither intracellular TNF α production nor inflammasome activation (no Inflammasome speck-positive cells). TNF α production was expected from LPS-treated PBMCs. However, the production of TNF α in the untreated cells indicated that PBMCs were already primed.

To translate this assay concept into a multi-parametric assay approach, an assay workflow was developed to monitor the phenotypic changes under different experimental conditions (**Figure 17**). We developed an automated assay rather than manual conduction to reduce the experimental error and to improve assay repeatability. The PBMC assay workflow was started by seeding the cells in 384-well assay plate. The cells were primed with 20 ng/ml LPS for 2 h followed by inflammasome activation either by 0.2 mM LeuLeuOMe for 0.5 h or 5 μ M Nigericin for 1 h. After inflammasome activation had been triggered, cell-free supernatants were collected to measure IL-1 β and TNF α

release. Fifteen minutes were required to fix PBMCs with PFA. Two staining sets were used on the same assay plate; Hoechst 33342, anti-PYCARD and anti- TNF α , whereas the other set of staining was Hoechst 33342, anti-CD3, anti-CD14 and anti-CD19 to characterize the cellular composition of the PBMC sample. Automated imaging was conducted by automatic confocal microscope. The obtained images were analyzed first by utilizing the Yokogawa analysis software in order to score the PYCARD complex formation, intracellular TNF α and nuclei objects (**Figure 21**). For the analysis of cell surface marker expression, a more sophisticated analysis was needed to obtain reliable and reproducible results. Hence, a machine learning approach was developed to process the staining images (see section 4.2 for more details).

The assay was performed under 6 different treatment conditions, namely untreated, LPS, LPS + Nigericin, LPS + LeuLeuOMe, Nigericin alone, and LeuLeuOMe alone.

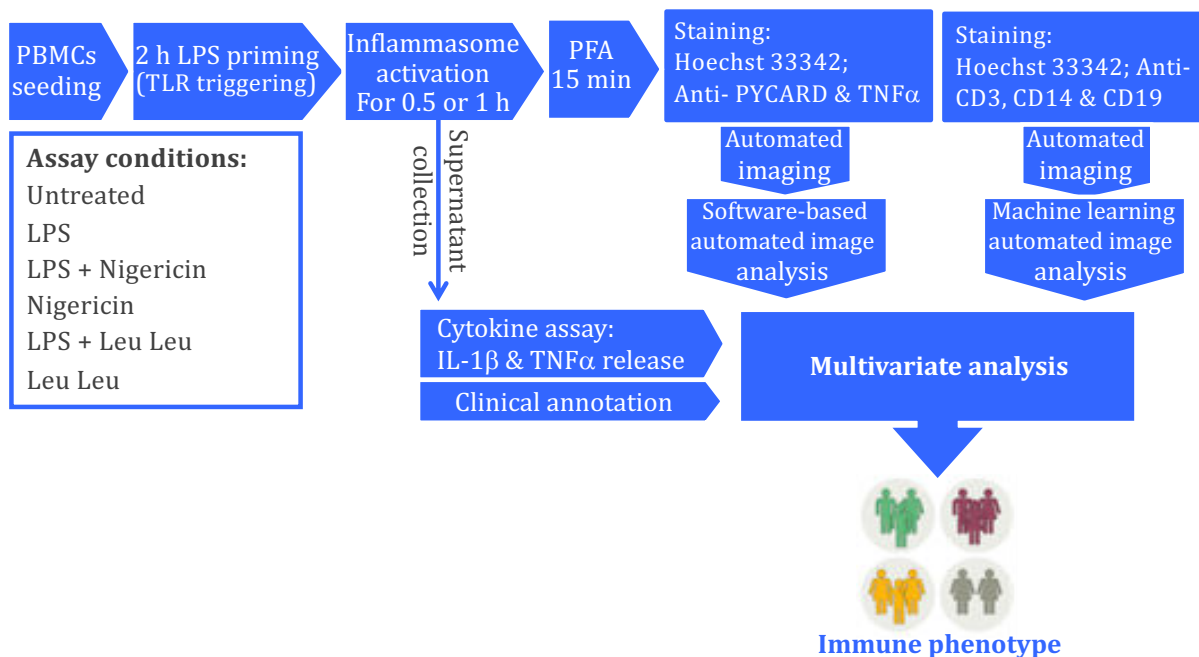


Figure 17: Schematic of PBMC multi-parametric assay workflow

A 384-well assay plate was used to seed PBMCs. cells were primed for 2 h with 20 ng/ml LPS followed by inflammasome triggering either by 0.5 h of 0.2 mM LeuLeuOMe or 1 h of 5 μ M Nigericin. In order to perform cytokine assay, supernatants were collected after the activation has been done. Cells were fixed with 4% PFA. Finally, fixed PBMCs were stained either with Hoechst 33342, anti-PYCARD and anti- TNF α or with Hoechst 33342, anti-CD3, anti-CD14, and anti-CD19. Imaging was conducted using automated CellVoyager 6,000 microscope. Images were analyzed using CellVoyager analysis software to assess inflammasome activation. A supervised machine-learning was developed to process the images of CD3, 14, and 19 staining. The combined data from the image analysis, cytokine assay, and the clinical data were used to perform a multivariate analysis addressing an immune phenotype for the PBMC sample donor.

The data from the image analysis, cytokine assays and the clinical annotation of the PBMC samples were combined to a multi-parametric dataset and a multivariate analysis was conducted to create an immune fingerprint for the disease status (**Figure 18**). This means that the feature vectors, from the multi-parametric assay, were analyzed with multivariate analysis to predict the sample disease status (see section 4.3.4 for more details).

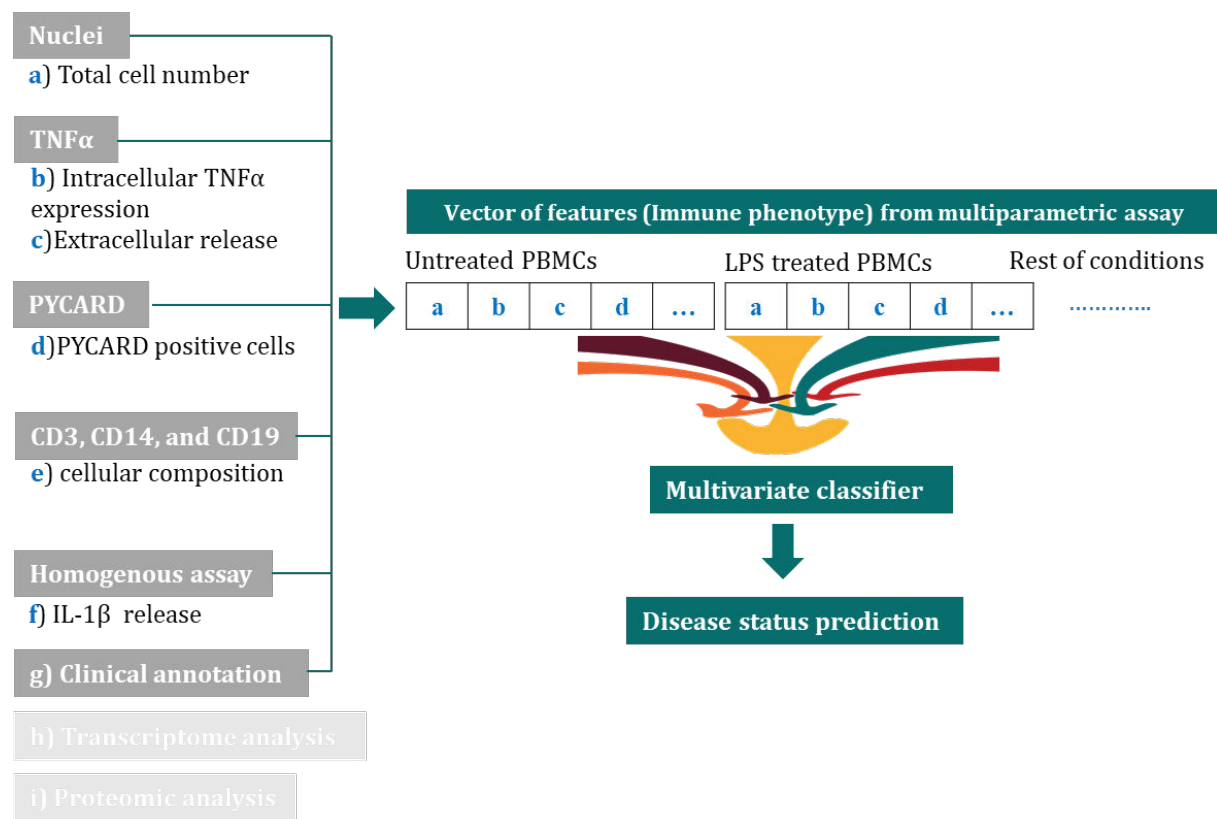


Figure 18: PBMC multi-parametric assay workflow

A multi-parametric assay was developed to monitor intracellular TNF α production, PYCARD complex formation and chromatin/nucleus. The assay was also flanked by homogenous readouts for IL-1 β and TNF α release. The cellular compositions of the PBMCs were assessed by cell surface marker expression, i.e. CD3, CD14, and CD19. The data generated from the assay was assembled into a vector of features for each sample (immune phenotype). Feature vectors were analyzed with a multivariate classifier to predict the sample disease status. Furthermore, a transcriptome analysis was conducted to evaluate the expression profile of the PBMC sample in naïve status. In parallel, PBMCs were used in our laboratory to conduct a multiplexed proteomic analysis (data not shown). The data from transcriptome analysis and proteomic analysis have not been integrated into the multivariate analysis.

4.1.1. The role of Toll-like receptor and inflammasome in AD pathology

It was revealed, in the introduction of this thesis, that the PRRs such as TLRs and NLRP play a key role during AD pathology (de Oliveira, Davis et al. 2019). The first report about the association between NLRP3 inflammasome and AD pathology was published in 2008 by Halle et al. In their work, the authors identified A β ₁₋₄₂ as a trigger for the inflammasome sensor molecule NLRP3. It was suggested that A β causes lysosomal damage resulting in the release of cathepsin B (Halle, Hornung et al. 2008). The assembly of NLRP3 inflammasome requires a prerequisite step (priming) where inflammasome components are expressed. During priming, a ligand, e.g. LPS, binds TLR4 activation and this triggers a conformational change that leads to the activation of NF- κ B pathway, expressing the inflammatory components NLRP3, TNF α , pro-IL-1 β , and pro-IL-18 (Labzin, Heneka et al. 2018). Hence, the intracellular TNF α production was used as a readout of a successful triggering of TLR4 pathway. LPS was used to prime the PBMCs, triggering the TLR4, in order to evaluate the immune response of the PBMC sample and the activation status of this pathway. PBMCs were seeded in a 384-well assay plate and primed for 2 h with 20 ng/ml LPS. The primed PBMCs were stained with anti-TNF α in addition to the chromatin staining Hoechst 33342. As expected, LPS-priming of the PBMCs resulted in the intracellular production of TNF α (**Figure 19 B**) whereas, PBMCs with no LPS treatment showed no TNF α production (**Figure 19 A and D**). This experiment showed the successful LPS induced TNF α production in the PBMCs *ex vivo* assay. Thus, TNF α production was used during this study as a readout to evaluate the priming status of the PMBC sample as well as a readout to be combined with other readouts during the multivariate analysis.

The second essential signal process for inflammasome activation is the triggering of the inflammasome assembling. Thus, Nigericin was used to trigger the inflammasome activation after PBMCs had been primed with LPS. In brief, PBMCs were primed with 20 ng/ml LPS for 2 h followed by 5 μ M Nigericin for 1 h. Then, PBMCs were stained for Hoechst 33342 and the inflammasome adapter protein PYCARD as PYCARD complex formation has been widely used as an indicator for inflammasome activation.

As expected, full activated PBMCs showed a high rate of inflammasome activation (inflammasome speck-positive cells) (**Figure 20 C**). The untreated and the only primed PBMCs (**Figure 20 A and B**) showed no PYCARD complex formations.

This experiment was a proof of concept of the capability of triggering inflammasome activation in PBMCs.

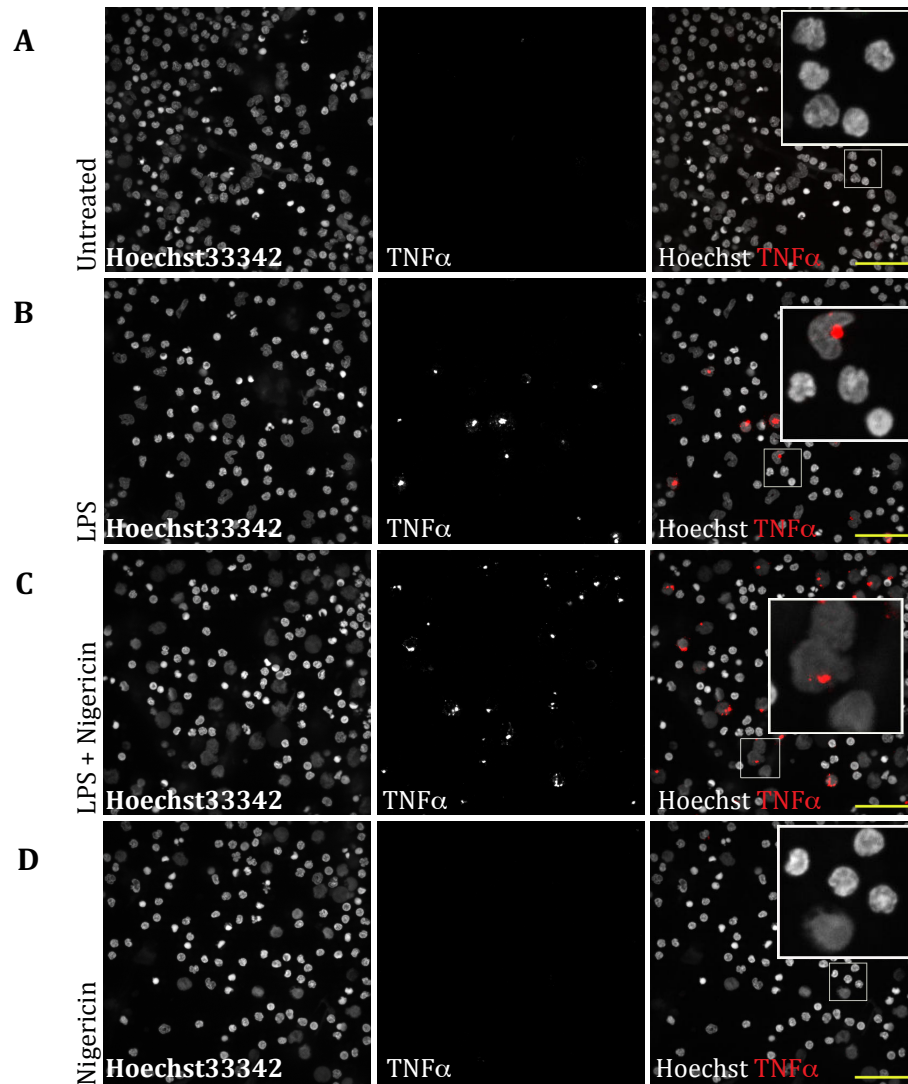


Figure 19: Intracellular TNF α production.

LPS-primed PBMCs were stained with anti-TNF α and the chromatin stain Hoechst 33342. TNF α production was used as an indicator for successful cell priming. PBMCs priming with 20 ng/ml LPS for 2 h resulted in intracellular production of TNF α (B) while PBMCs with no LPS treatment, untreated, or Nigericin only treated showed no production of TNF α (A and D). Scale bar, 40 μ m.

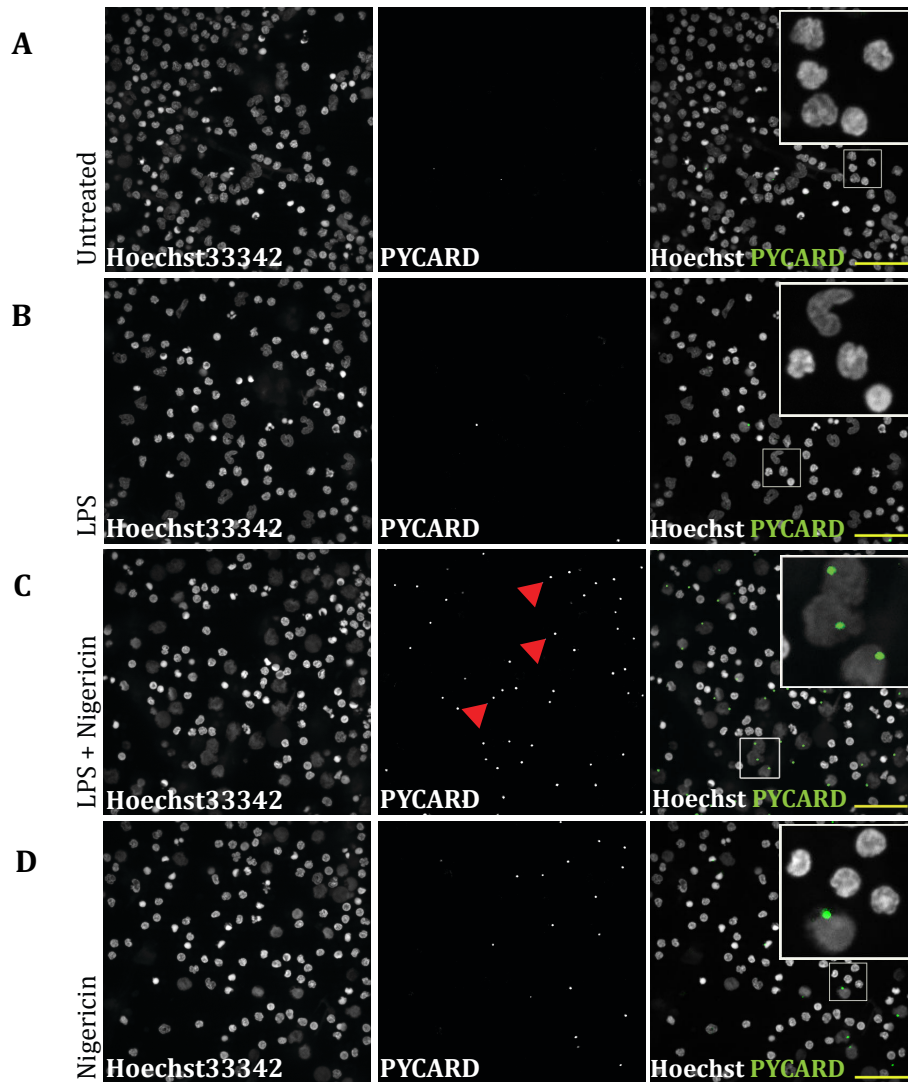


Figure 20: Inflammasome PYCARD speck formation assay.

PBMCs were stained with Hoechst 33342, and co-stained with, inflammasome adapter protein PYCARD antibody. PYCARD complex formation was used as an indicator for inflammasome activation. Merged images of the two staining showed that treatment with 20 ng/ml LPS for 2 h followed by 5 μM Nigericin for 1 h (C) results in a high number of activated cells (Inflammasome speck-positive cells). Treatment with only Nigericin (D) resulted in few activated cells. Treatment with only LPS (B) or untreated cells (A) caused not activation. Scale bar, 40 μm.

4.1.2. Quantitative analysis of the inflammasome activation assay

In order to quantitatively describe the phenotypic changes of the cell-based assay, an image analysis workflow was developed to process the images of Hoechst 33342, anti-PYCARD and anti- TNF α staining. The Yokogawa analysis software is an analysis software provided by Yokogawa incorporation to analyze the images generated by the Yokogawa CellVoyager 6,000 microscope. The software was used to identify and quantify cells that had mounted an inflammasome response as well as cells that expressed intracellular TNF α (**Figure 21**). Nuclei were segmented using the channel of the Hoechst 33342 staining (**Figure 21 B**). Then, the cellular cytoplasmic area was defined by expanding the nuclear area into an estimated value (**Figure 21 C**). The software detected the PYCARD complex formation “specks” (**Figure 21 E**) and assigned the “specks” that were located within the cellular area to the cell objects. Cells with PYCARD complex formation were annotated as activated cells (inflammasome speck-positive cells in **Figure 21 F**). in parallel, intracellular TNF α was detected (**Figure 21 H**) and assigned to the cell objects. The cells with intracellular TNF α production were then annotated and quantified as TNF α positive or primed cells (**Figure 21 I**).

A similar workflow was developed using the CellProfiler software to quantify the percentage of both primed and activated cells. CellProfiler is a widely used software for analyzing images of cell-based assays. No significant difference was found in the results obtained from the two software applications in terms of the number of cells per well (**Figure 22 A**) and inflammasome activation rate (**Figure 22 B**). This indicated the robustness of the analysis workflow that was used for each software. The workflow of the Yokogawa analysis software was used as a routine analysis for this study due to its high compatibility with the Yokogawa microscope.

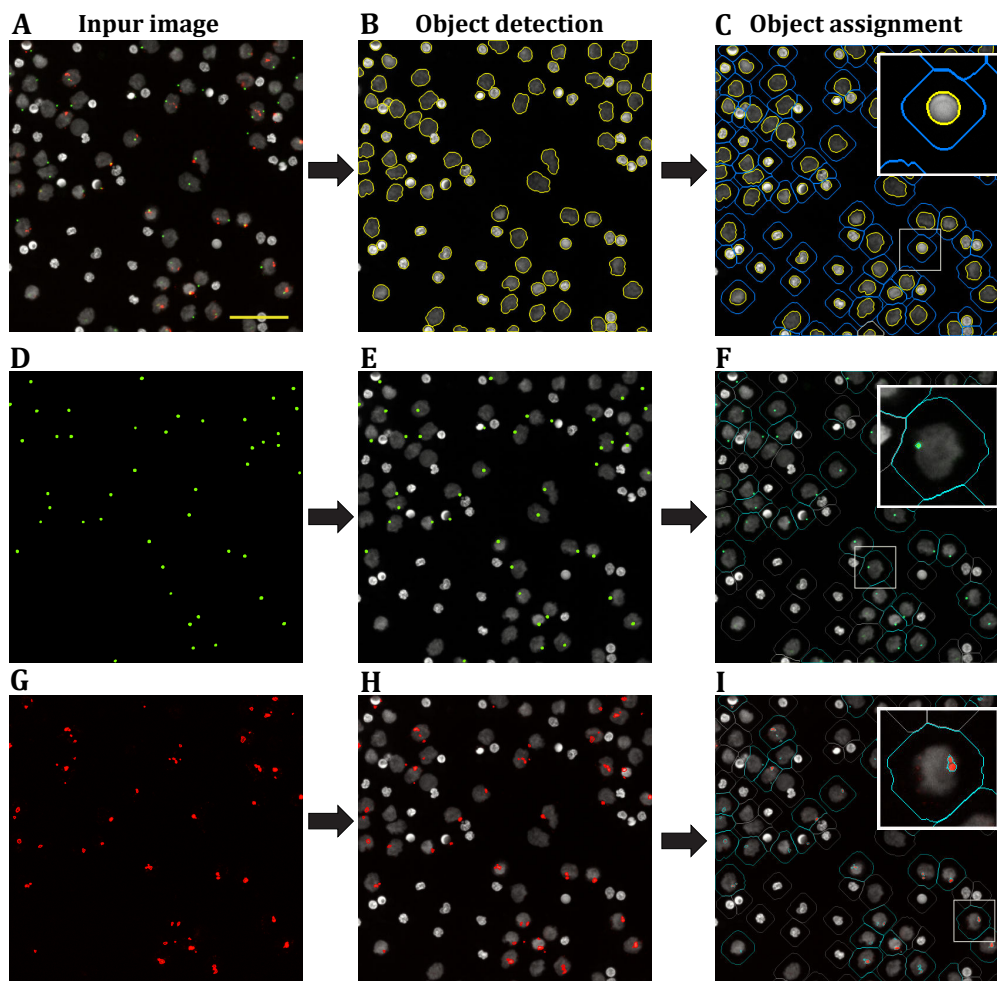


Figure 21: The image analysis workflow.

An image analysis pipeline was developed, via Yokogawa software, to identify and quantify inflammasome speck- positive cells and to assess the priming status as well. **(A) Input image.** Input images of three channels of the same field were used as an input to the software. **(B) Nuclei segmentation.** Nuclei were segmented using the image from the Hoechst33342 staining. **(C) Cell area defining.** The cellular cytoplasmic area was defined by expanding the nuclear area. **(D) "Specks" signal recognition.** Aggregated PYCARD protein or "specks" were detected via the channel of anti-PYCARD staining. **(E) Association/linkage of "specks" to the cellular area.** The software annotated the speck(s) located within the cellular area as real specks. **(F) "Cells with speck" annotation.** The cells with speck(s) were annotated and quantified as speck positive or activated cells. **(G) TNF α signal recognition.** Expressed TNF α protein was detected via the image of the channel of anti-TNF α staining. **(H) Association/linkage of TNF α signal to the cellular area.** The software annotated the TNF α production within the cellular area as a real signal. **(I) "Cells with TNF α signal" annotation.** The cells with TNF α were then annotated and quantified as TNF α positive, primed cells. The pipeline detection accuracy was checked using at least five representative images from each assay plate meant to be analyzed. Scale bar, 40 μ m.

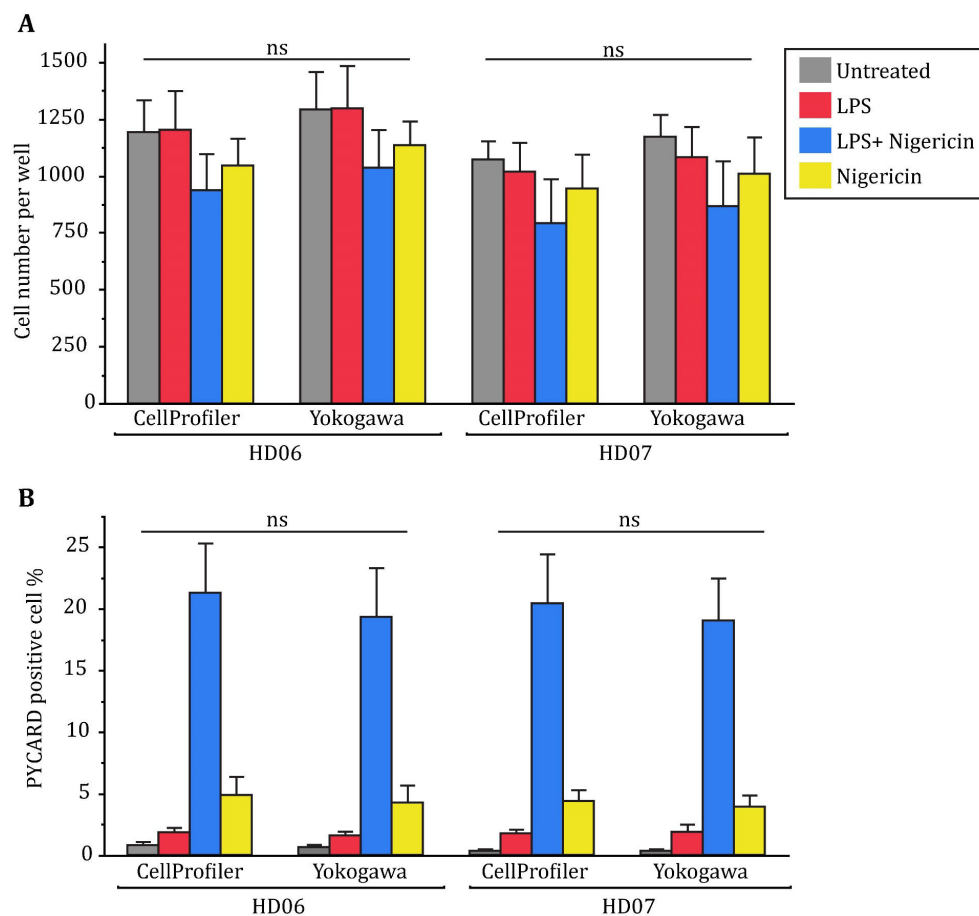


Figure 22: Comparison of the two image analysis workflows (Yokogawa versus CellProfiler)

Both the total cell number (A) and the inflammasome activation rate (B) were quantified using the Yokogawa analysis software (as described in **Figure 8**). A CellProfiler pipeline was developed for cell segmentation and PYCARD signal detection as well. Both of the two software brought the same results as presented in this figure. Error bars represent the standard deviation. For untreated or LPS treated cells, $n=8$ wells, while $n=12$ for the other conditions. Test of significance t-Test; ns (non-significant) $P > 0.05$.

As described before, the cell-based assay was conducted under 6 experimental conditions (**Figure 17**). We wanted to quantitatively identify the effect of these conditions on both the $\text{TNF}\alpha$ production and the inflammasome activation. As proof of principle, the inflammasome activation assay was conducted by using PBMCs isolated from healthy donor 04 (HD04). The percentage of $\text{TNF}\alpha$ positive cells and the inflammasome activation rate were used as readouts of this experiment. As a baseline phenotype, untreated PBMCs showed neither $\text{TNF}\alpha$ production nor inflammasome activation (**Figure 23**). LPS induced more than 10% of the cells to express $\text{TNF}\alpha$ although it caused a very low inflammasome activation rate ($\sim 1\%$). This was in consistence with the concept that while priming needed only TLR4 activation, inflammasome activation needed both priming and

triggering signal processes. For the “LPS + Nigericin” (full activation) condition, 10% of the cells expressed TNF α . This was similar to the “LPS only” condition, meaning that Nigericin treatment did not affect TNF α production. However, there was a remarkable increase in the inflammasome activation rate (around 27%) compared to LPS treated cells (~1%), confirming again the two-signal safety catch mechanism for inflammasome activation. Interestingly, the inflammasome activation was around 5% for Nigericin treated cells (Figure 23 B) Although Nigericin treatment alone caused no TNF α production (Figure 23 A).

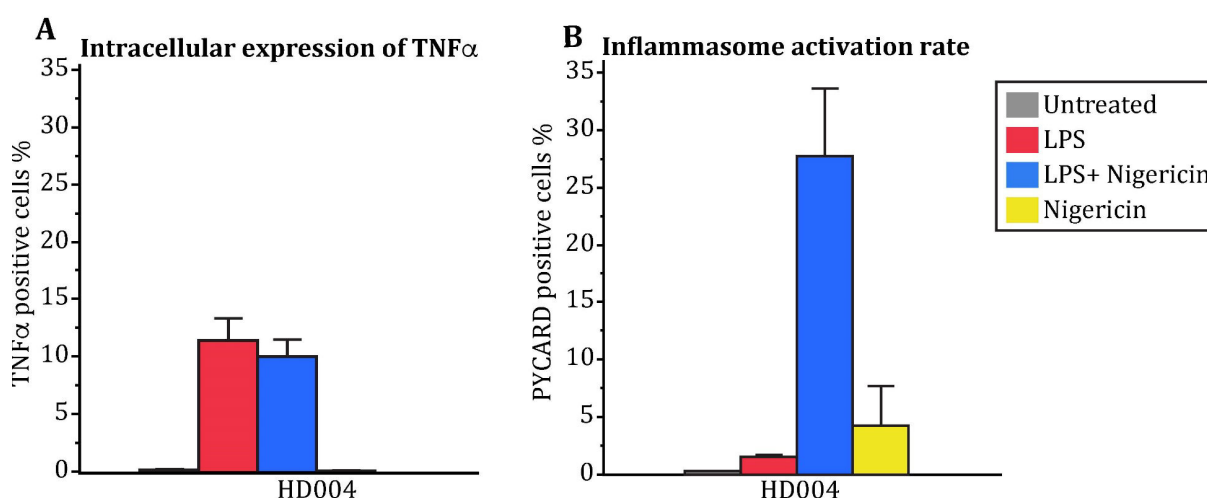


Figure 23: Priming status and inflammasome activation upon Nigericin activation

(A) Intracellular TNF α production. Treatment with 20 ng/ml LPS for 2 h caused a notable increase in the percentage of TNF α positive cells (~12%) compared to the control conditions (untreated, or Nigericin treated cells). (B) Inflammasome speck formation assay. Around 27% of PBMCs mounted an inflammasome activation after LPS + Nigericin treatment. The inflammasome activation rate was around 5% for Nigericin treated cells. Untreated or LPS only treated cells showed a very low activation rate. The depicted results were for PBMCs that were isolated from buffy coats of healthy donor 4 (HD04). Error bars represent the standard deviation. For untreated or LPS treated cell, n= 8 wells, while n=12 for the other conditions.

The same experiment and quantitative analysis as done using Nigericin activation (Figure 23) were conducted for LeuLeuOMe as an inflammasome activator using the same donor (HD04) (Figure 24). As mentioned in the introduction of this thesis, the reason to choose LeuLeuOMe was that it mimics the protein aggregation pathology in many neurodegenerative diseases like α -synuclein aggregation in Parkinson’s disease or phosphorylated Tau and A β in AD (Koh, Aye et al. 2015).

Similar to the Nigericin experiment, LPS treatment induced TNF α production but did not result in inflammasome activation, while full activation, i.e. LPS followed by LeuLeuOMe treatment, caused an inflammasome activation rate of ~13%. In this case, the activation rate was lower when compared to the full activation condition in the Nigericin experiment, which was around 27%. In contrast to Nigericin, LeuLeuOMe alone caused a lower inflammasome activation rate (~1%) compared to 5% activation by the Nigericin alone treatment.

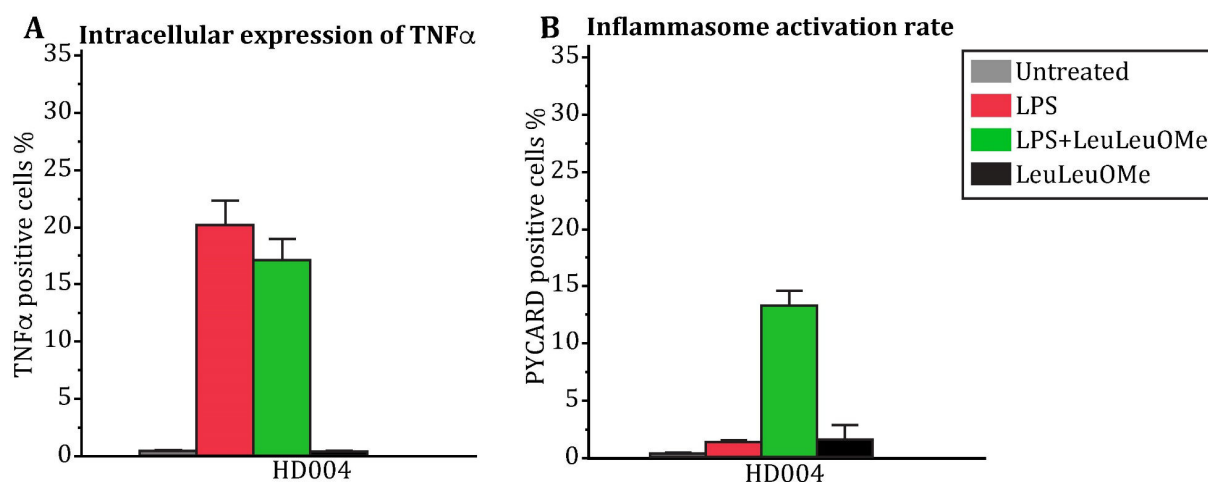


Figure 24: Priming status and inflammasome activation upon LeuLeuOMe treatment.

(A) Intracellular TNF α production. Treatment with 20 ng/ml LPS for 2 h caused a notable increase in the number of TNF α positive cells (20%) compared to the control conditions (untreated, or LeuLeuOMe treated cells). (B) Inflammasome speck formation assay. Around 13% of PBMCs mounted an inflammasome activation after LPS + LeuLeuOMe treatment. Untreated or LPS only treated cells showed a very low activation rate. The depicted results were for PBMCs that was isolated from buffy coats of healthy donor 4 (HD04). Error bars represent the standard deviation. For untreated or LPS treated cell, n= 8 wells, while n=12 for other conditions.

The quantification analysis of these two experiments in a healthy donor showed how PBMCs respond, differently, to different assay conditions, meaning, different phenotypic changes could be obtained by challenging the cells with a diversity of experimental conditions. This is a central point of our assay design that allows to fully assess the immune phenotype of each sample under different conditions related to the innate immunity status.

4.1.3. Homogenous cytokine assay

Treating PBMCs with LPS causes not only an intracellular production of TNF α but also the release of TNF α into the culture media (van der Bruggen, Nijenhuis et al. 1999). On the other hand, inflammasome assembly converts pro-caspase-1 into active caspase-1. The latter cleaves pro-IL-1 β and pro-IL-18 into their active forms. IL-1 β release is widely used as indicator of inflammasome activation (Man and Kanneganti 2015, Broz and Dixit 2016). Therefore, we flanked our image-based readout with the quantification of the release of TNF α and IL-1 β in a homogeneous assay as a functional readout of TLR activation and inflammasome complex assembly and activation, respectively.

For this scope, the HTRF[®] cytokine assay was used to measure the release of IL-1 β and TNF α . The HTRF[®] technology is widely used in HCS assays. It is advantageous over classical ELISA assays because it is fast (needs no washing), the sample volume could be reduced to 8 μ l, and thus more than one cytokine could be measured from one sample (Degorce, Card et al. 2009).

After PBMCs have been primed and inflammasome activation was triggered, cell-free supernatants were harvested for cytokine release measurements. The harvested supernatants were used to perform HTRF assay for both IL-1 β and TNF α .

As expected, LPS caused a higher release of TNF α into the supernatant (400 pg/ml) compared to the conditions with no LPS treatment (**Figure 25 A**), while it caused no increase in IL-1 β release compared to untreated PBMCs (**Figure 25 B**).

The full activation condition (LPS followed by Nigericin treatment) depicted a remarkable increase in IL-1 β release (2,000 pg/ml) compared to the other conditions (**Figure 25 B**). This is consistent with the widely accepted concept that inflammasome activation is a prerequisite for IL-1 β release.

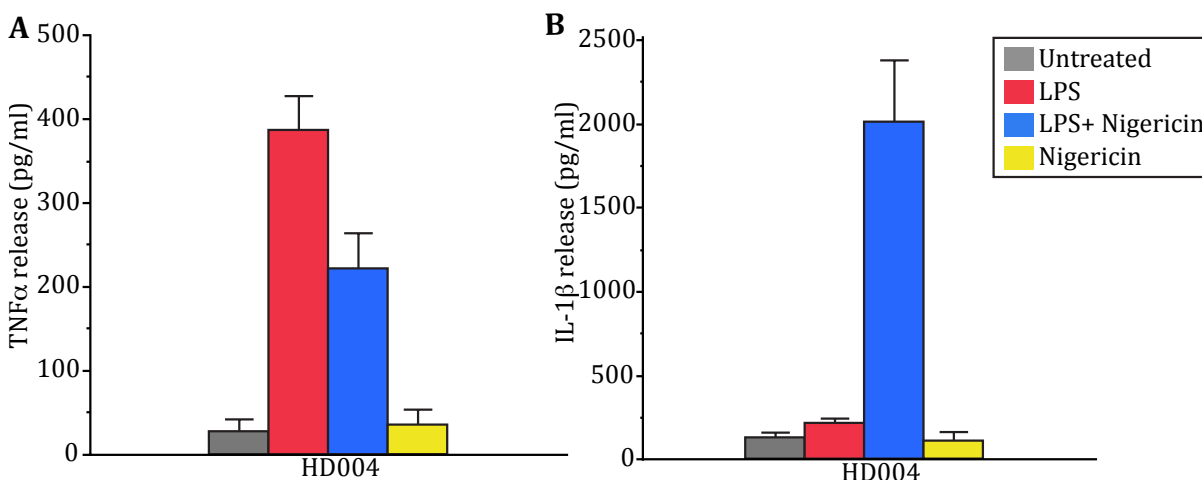


Figure 25: HTRF[®] cytokine assay using Nigericin as an inflammasome activator

TNF α and IL-1 β release were measured using HTRF[®] cytokine assays. Cell-free supernatants were harvested after PBMCs have been primed and activated. **(A)** TNF α release into the supernatant. LPS caused PBMCs to release TNF α into the supernatant in a higher amount compared to the conditions with no LPS treatment. **(B)** IL-1 β release into the supernatant. The release of IL-1 β was higher from PBMCs that were both primed and activated with Nigericin compared to control treatment conditions (untreated, LPS and Nigericin treated cells). Error bars represent the standard deviation, n=6.

The same experiment and analysis were conducted using LeuLeuOMe as inflammasome activator (**Figure 26**) and a similar result was obtained in the case of LeuLeuOMe, i.e. LPS alone caused a release of TNF α but not of IL-1 β while inflammasome activation was a prerequisite for IL-1 β release.

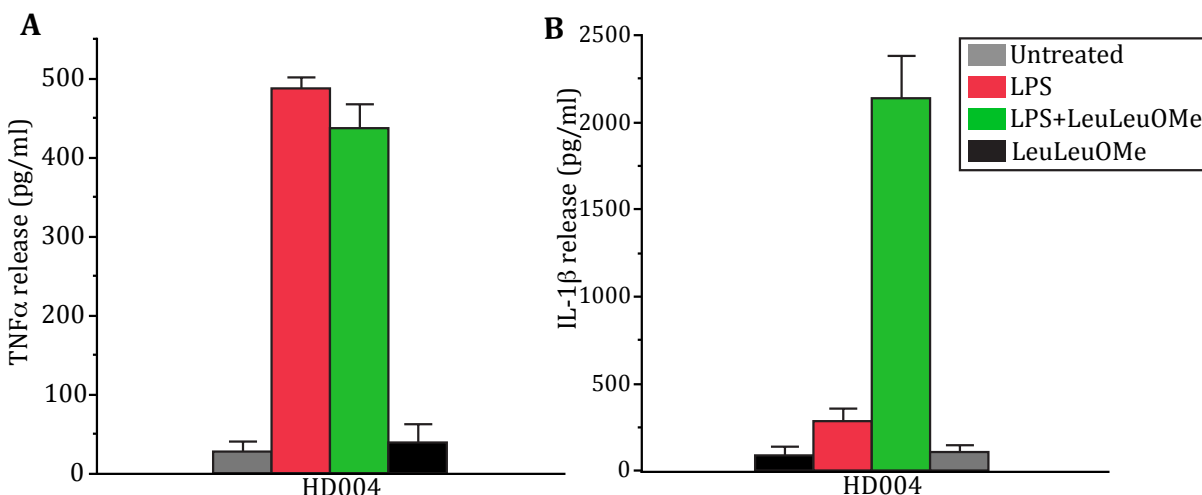


Figure 26: HTRF[®] cytokine assay using LeuLeuOMe as inflammasome activator

TNF α and IL-1 β release were measured using HTRF[®] cytokine assays. Cell-free supernatants were harvested after PBMCs have been primed and activated. **(A)** TNF α release into the supernatant. LPS caused PBMCs to release TNF α into the supernatant in a higher amount compared to the conditions with no LPS treatment. **(B)** IL-1 β release into the supernatant. The release of IL-1 β was higher from PBMCs that were primed and activated, with LeuLeuOMe, compared to control treatment conditions (untreated, LPS, and Nigericin treated cells). Error bars represent the standard deviation, n=6.

These two experiments (**Figure 25** and **Figure 26**) confirmed that TNF α and IL-1 β release can be successfully used as functional readouts to evaluate TLR activation and the functional inflammasome complex assembly in the PBMC *ex vivo* assay.

IL-1 β release was also measured using the AYOXXA LUNARIS™ assay technology (**Figure 27**). This assay was recently developed by the German company AYOXXA using a bead-based technology. The detected IL-1 β release was higher in the case of the AYOXXA assay in comparison to the HTRF assay. However, the pattern of release was the same in both technologies in terms of the effect of the different treatment conditions. For example, in both technologies, LPS followed by Nigericin treatment caused the highest release, around 40% higher compared to LPS + LeuLeuOMe.

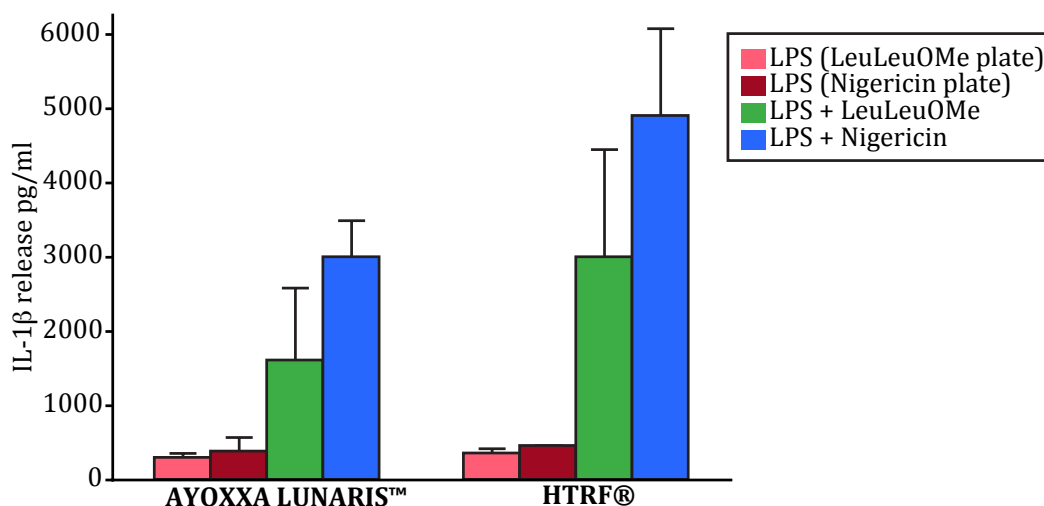


Figure 27: Comparison of the HTRF® and AYOXXA LUNARIS™ assays for the quantification of IL-1 β release.

The IL-1 β release was measured using the HTRF® versus the AYOXXA LUNARIS™ assay. Cell-free supernatants were harvested after PBMCs have been primed and inflammasome assembly has been triggered, either by LeuLeuOMe or Nigericin. The HTRF® cytokine assay was used to quantify the IL-1 β release into the supernatant. The same supernatants from the same experiment and same donor were also used to perform a cytokine assay using LUNARIS™ Human 5-Plex Cytokine kit from AYOXXA. The detected IL-1 β release was higher in the case of the AYOXXA assay than in the conducted HTRF assay. However, the pattern of release was the same in both technologies in terms of condition effect. For example, LPS + Nigericin caused an increase in the release by around 40% compared to LPS + LeuLeuOMe in both assays. Error bars represent the standard deviation. HTRF, n=6. AYOXXA assay, n=2 (LPS condition) and n=4 (primed and activated).

This experiment showed that the pattern of response of the PBMCs to the experimental conditions is biology-dependent rather than technology- or technique-dependent.

In conclusion, the HTRF assay technology was used routinely, during the course of this study because it is an established and widely accepted technology in the field of high content screening assays.

4.1.4. Assay automation and validation

The PBMC cell-based assay was developed first on a 96-well assay plate format involving manual pipetting which interfered with the assay reproducibility. One of the limiting factors to implement the assay using clinical material was the limited number of cells available which affects the number of replicates and conditions that can be processed per single experiment. The second limiting factor was related to the assay stability and its reproducibility due to the variation in processing time between the first and last donor to be seeded on the same assay plate (see assay design in 3.3.4.3 and 3.5). Finally, the use of a manual assay allowed the processing of only a few samples per day. For these reasons, we developed an automated assay using a fully robotized laboratory automation pipeline. The advantages of using an automated assay enables: a) upscaling the number of samples/day and reducing the number of cells utilized for each data point (Thomas 2010) hence enabling to test more samples under many experimental conditions on one single experiment, b) increasing repeatability and reproducibility of the assay by performing a consistent procedure, which cannot be attained by manual pipetting (Zanella, Lorens et al. 2010, Fraietta and Gasparri 2016). This reduced the inter- and intra-assay variability (more details in 4.1.5.2 and 4.1.5.3). Therefore, we transferred the PBMC *ex vivo* assay from a manual pipetting regime to an automated cell-based assay using the automation platform at the DZNE Bonn (see Materials and Methods for more details).

4.1.4.1. Manual conduction versus automated cell-based assay

It has been reported that automation might affect the assay outcome (Ibold, Frauenschuh et al. 2007). Therefore, we wanted to test the effect of the automation on the response of PBMCs in the context of inflammasome activation. The inflammasome assay was conducted back-to-back to manual and automated pipetting using the same samples, in order to compare the assay performance in terms of cell number and inflammasome activation rate. Two healthy donors (HD06 and HD07) were used for this experiment. 60,000 PBMCs per well were seeded and the inflammasome assay was conducted as

described before. The first observation was that automated cell seeding and liquid dispensing increased the number of settled cells per well remarkably (**Figure 28 A**). The explanation is that by using an automated liquid handler it was possible to reduce the speed of liquid dispensing during the assay and this, in turn, increased the cell attachment during the seeding process.

On the other hand, the inflammasome activation rate was significantly increased in case of the automated cell-based assay (**Figure 28 B**) for both healthy donors (HD06 and HD07).

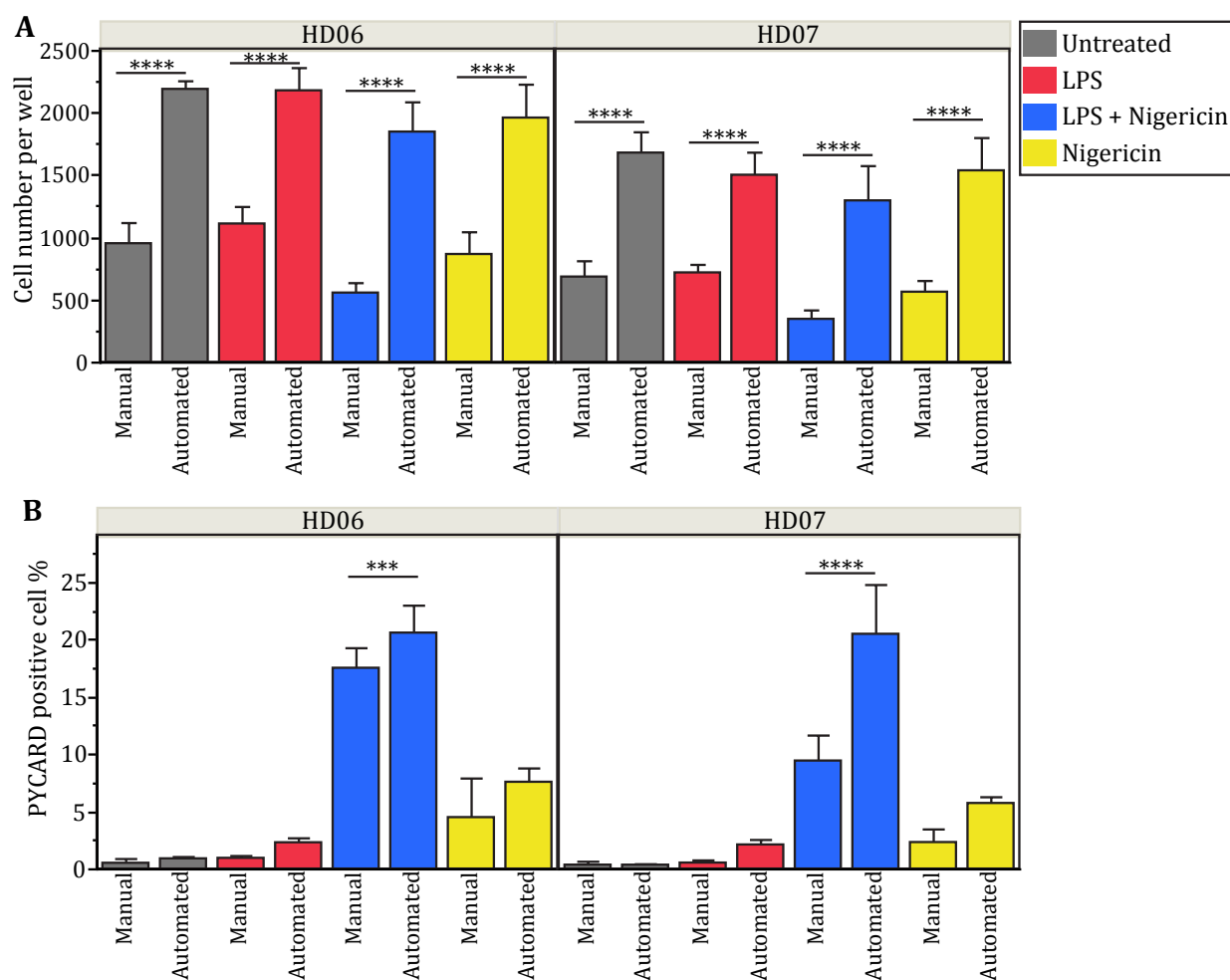


Figure 28: Manual versus automated PBMC seeding, priming, and activation.

The cell number per well (A) was higher in case of automated cell seeding, priming, and activation in case of all assay conditions and for both PBMC samples that were used for this experiment compared to the manual performing. Inflammasome activation rate (B) was also higher when the assay was performed in the automation platform. Error bars represent the standard deviation. Student t-test was used to test for statistical significances. Test of significance t-Test; ns (non-significant) $P > 0.05$, *** $P < 0.001$, **** $P < 0.0001$.

In summary, the automated cell-based assay enabled us to increase the number of samples processed per day as well as to increase the assay quality by increasing the number of events analyzed to capture and describe the phenotype of each sample. Therefore, we successfully managed to implement the automation platform to conduct the experiments of all upcoming results in this thesis.

4.1.4.2. Validation of the automated cell-based assay: intra-day variation

Developing the assay from manual conduction to an automated cell-based assay required to check the performance through an assay validation procedure. Therefore, validation experiments were conducted to assess many assay aspects such as assay repeatability (intra-day variability) and assay reproducibility (inter-day variability) (FDA 2018).

The first validation experiment assessed the well-to-well seeding variation (intra-day variability) by calculating the coefficient of variation (CV). The CV is a widely accepted parameter to evaluate the assay variation (Lilly 2004). Usually, a CV of 20% reflects a good assay performance (Lilly 2004). To analyze the CV of well-to-well cell number, untreated PBMCs from four healthy donors were seeded in a 384-well assay plate (**Figure 29**). For each donor, 96 wells were seeded with cells that were then stained with Hoechst 33342 in order to quantify the cell number per well. Based on the recommendation by Lilly (Lilly 2004), a CV of less than 20% was desirable to accept the assay variation.

The results of the CV analysis showed that our cell seeding technique was reliable (**Figure 29 A and B**), since all of the tested donors showed a CV of less than 20% (**Figure 29 B**). To test whether liquid dispensing during different assay steps affects the variation from well to well, the same experiment was repeated in the context of LPS priming before the Hoechst 33342 staining was performed (**Figure 29 C and D**). Again, all of the four tested healthy donors showed a CV of less than 20% (**Figure 29 D**). Therefore, this validation experiment showed that our seeding technique resulted in an acceptable inter-well variation in terms of the absolute cell number per well.

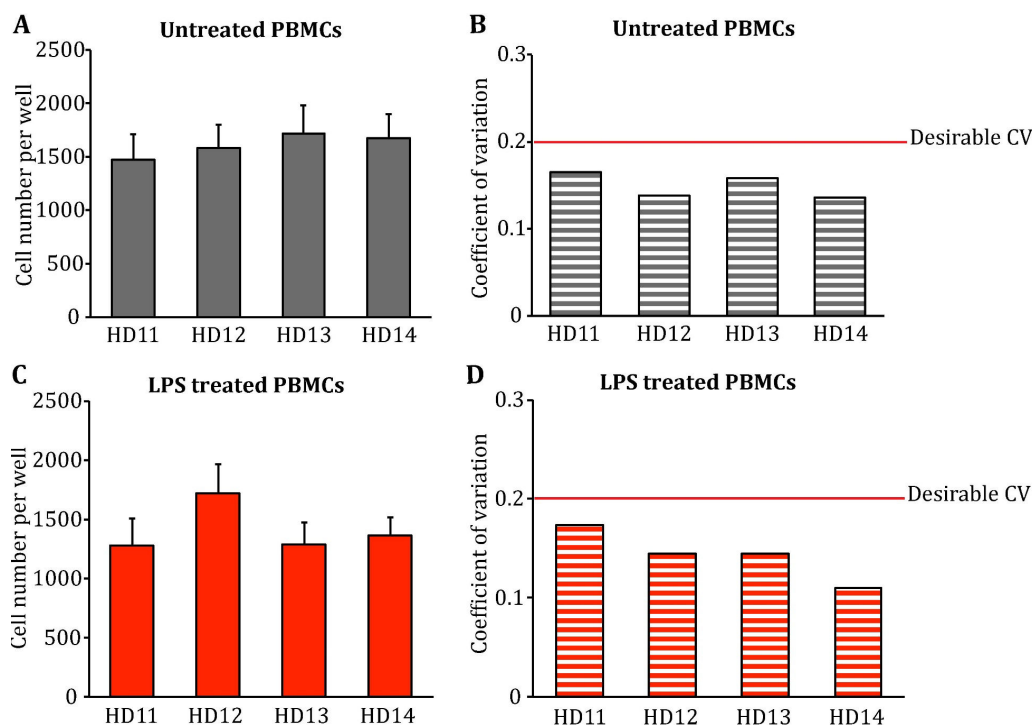


Figure 29: Inter-well variation of the automated cell seeding.

A 384-well assay plate was seeded with PBMCs from four healthy donors (96 wells per donor). After seeding, cells were stained with Hoechst 33342 to quantify the cell number (A). For untreated PBMCs, the inter-well coefficient of variation (CV) was less than 20% for all donors (B), indicating an acceptable level of variation from well to well. The same experiment was repeated with LPS treated PBMCs (C and D) and the CV was also less than 20% for all donors. Error bars represent the standard deviation, n=96.

4.1.4.3. Validation of the automated cell-based assay: inter-day variation

Another aspect of assay validation is the evaluation of assay reproducibility (day-to-day variability). The assay reproducibility can be performed by the assessment of the assay precision, “the closeness of agreement between independent test results obtained from homogenous test material under stipulated conditions of use” (EMA 2009). Therefore, we studied the assay reproducibility by conducting the inflammasome activation assay, as described before, over multiple repetitions. The PBMC inflammasome assay was repeated over three different days, using 6 healthy donors in order to evaluate the assay variation (Figure 30).

The coefficient of variation (CV) was used to assess the assay variation. According to the Assay Guidance Manual of Eli Lilly (Lilly 2004), an assay CV between 15-30% is considered as an acceptable variation for an established cell-based assays and a CV equal to 20% or less is usually reflecting good assay repeatability (Lilly 2004). Nevertheless,

according to EMA guideline of method validation, a CV of 35% could be also taken as an acceptable variation of some assays, e.g. assays with a high concentration of analytes (EMA 2009). However, the FDA guideline of Bioanalytical Method validation prefers a CV of less 25% variation (FDA 2018).

The CV analysis of the 3-day repetitions showed that the CV was lower than 30% for all samples. HD04, HD19, HD23, and HD24 showed a CV of less than 20%, whereas HD20 and HD26 had a CV of $\sim 25\%$ (**Figure 30 B**).

Although the variation of less than 20% is widely taken as a criterion of stable assay but a CV of 25% is still widely accepted as well. Particularly when considering that PBMCs represent a heterotypic cell model which is sensitive to a wide range of parameters. Therefore, this experiment can be used as a proof of assay stability of the PBMC *ex vivo* assay.

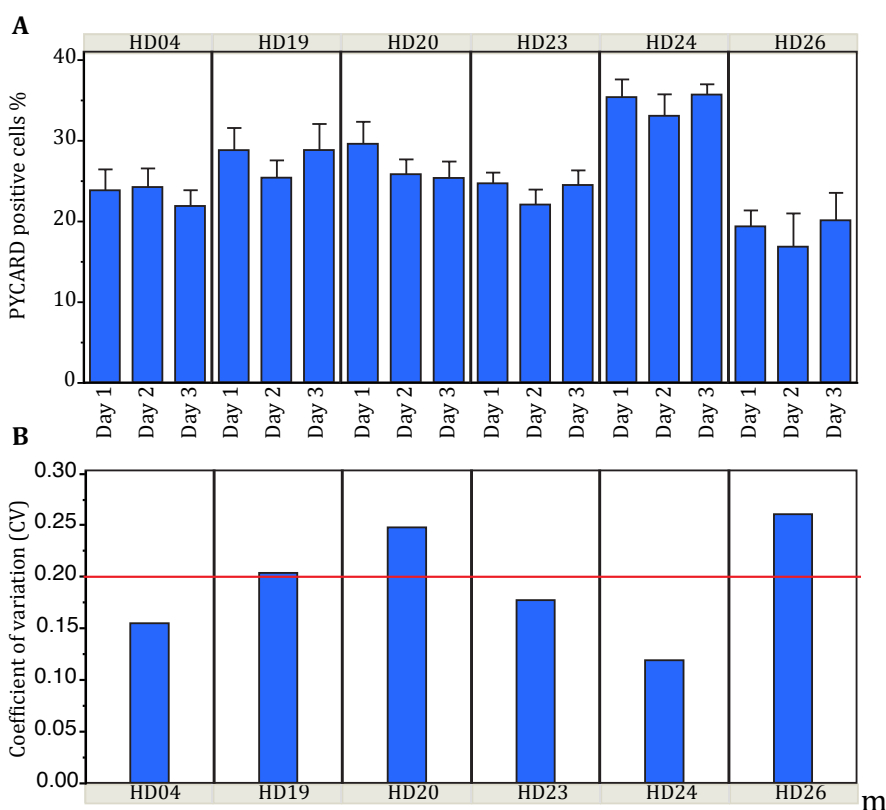


Figure 30: Assay stability experiment

PBMCs from 6 healthy donors were primed with LPS and activated with Nigericin as described before. The experiment was repeated over three different days to check the assay reproducibility. (A) Inflammasome activation rate. The activation rates of each sample were comparable over the three repetitions. HD06 showed the lowest activation rate, while HD24 was the highest. (B) Coefficient of variation (CV) of 3-day repetitions. HD20 and HD26 showed a CV of 25%. The rest of the donors showed a CV of less than 20%. The CV was calculated as described in the Materials and Methods chapter. Error bars represent the standard deviation.

4.1.4.4. Optimization of the automated cell-based assay

Increasing the number of the seeded cells per well allows capturing more events to describe the phenotype. However, the amount of PBMCs to be used in each experiment should be carefully considered. This is mainly because PBMCs from patients are usually a limited resource of material. Therefore, in order to define the number of PBMCs seeded per well, the cell density per well and its effect on inflammasome activation were studied in a cell titration experiment (**Figure 31**). The aim was to identify the optimized cell number to be seeded per PBMCs sample in each well of the assay plate (**Figure 31**). PBMCs from two healthy donors (HD06 and HD07) were seeded in a titration series of 20,000, 30,000, 40,000, and 60,000 cells in each well. The automated inflammasome activation assay was conducted as described before. For each well, the total number of cells captured in 16 microscopic fields were quantified at the end of assay (**Figure 31 A**). The obtained cell number was then compared to the cell number originally seeded at the beginning of the assay, demonstrating that seeding more PBMCs results in a higher number of cells at the end of the assay.

The inflammasome activation rate was not affected by the number of seeded cells, except in case of plating 20,000 cells per well of HD06 PBMCs (**Figure 31 B**) which corresponds to a low number of seeded cells. Therefore, reducing the cell number from 60,000 to 20,000 cells per well did not affect the rate of inflammasome activation regardless of the PBMC sample used. Thus, we defined 40,000 as a standard number of cells to be seeded per well in every experiment. The reason to choose 40,000 rather than 20,000 cells was to ensure to capture a sufficient number of cells per image field and well (**Figure 31 A**).

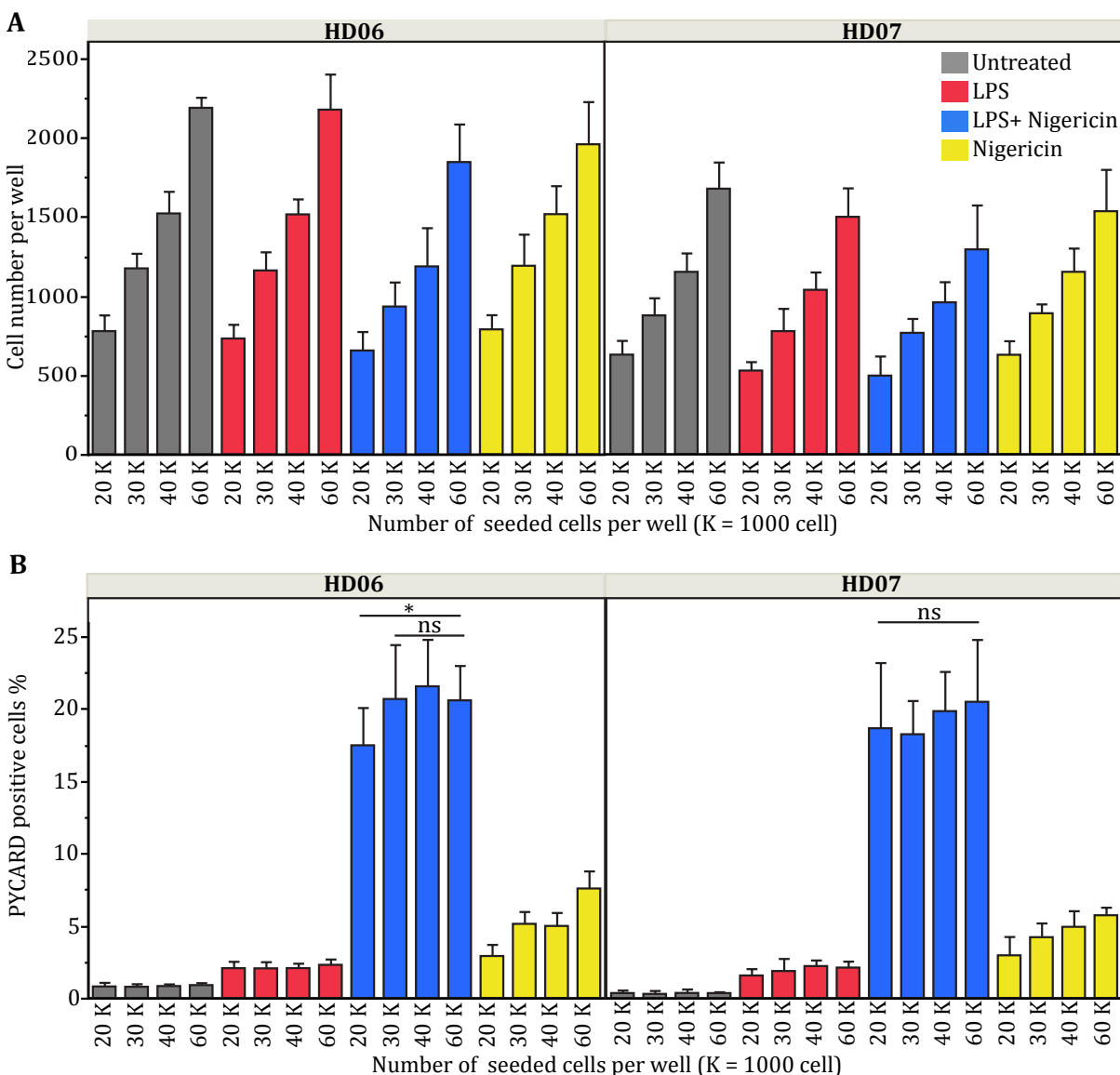


Figure 31: Cell titration experiment

PBMCs from two healthy donors (HD06 and HD07) were seeded in a cell titration experiment. 20,000, 30,000, 40,000, and 60,000 cells were seeded per well. The average cell number per well (A) quantified at the assay endpoint was associated with the number of cells that were originally seeded at the beginning of the assay. Increasing the number of seeded cells resulted in a higher number of cells at the end of the assay. The inflammasome activation rate (B) was not affected by number of seeded cells in the case of both HD07 and HD06. However, the activation was significantly reduced when 20,000 cells per well were seeded (HD06). Finally, 40,000 cells per well were used as standard cell density in the course of this project. Error bars represent the standard deviation. The experiment was repeated two times. For the untreated and the LPS condition $n=8$ wells, for the other conditions $n=12$. One-way ANOVA test: ns $P \geq 0.05$, * $P < 0.05$.

Next, a titration experiment was performed to study the effect of the Nigericin concentration on the inflammasome activation rate (Figure 32). An automated inflammasome activation assay was conducted as described before. A range of Nigericin

concentrations between 2.5-12.5 μM was used to trigger inflammasome activation. The concentrations between 2.5-12.5 μM caused very comparable activation rates ($\sim 30\%$). 1.25 μM Nigericin caused less activation ($\sim 17\%$) compared to the higher concentrations between 2.5-12.5 μM . Finally, the concentrations of 0.31 and 0.63 μM caused the lowest activation rate (less than 10%). 5 μM was chosen as standard Nigericin concentration during the course of this project.

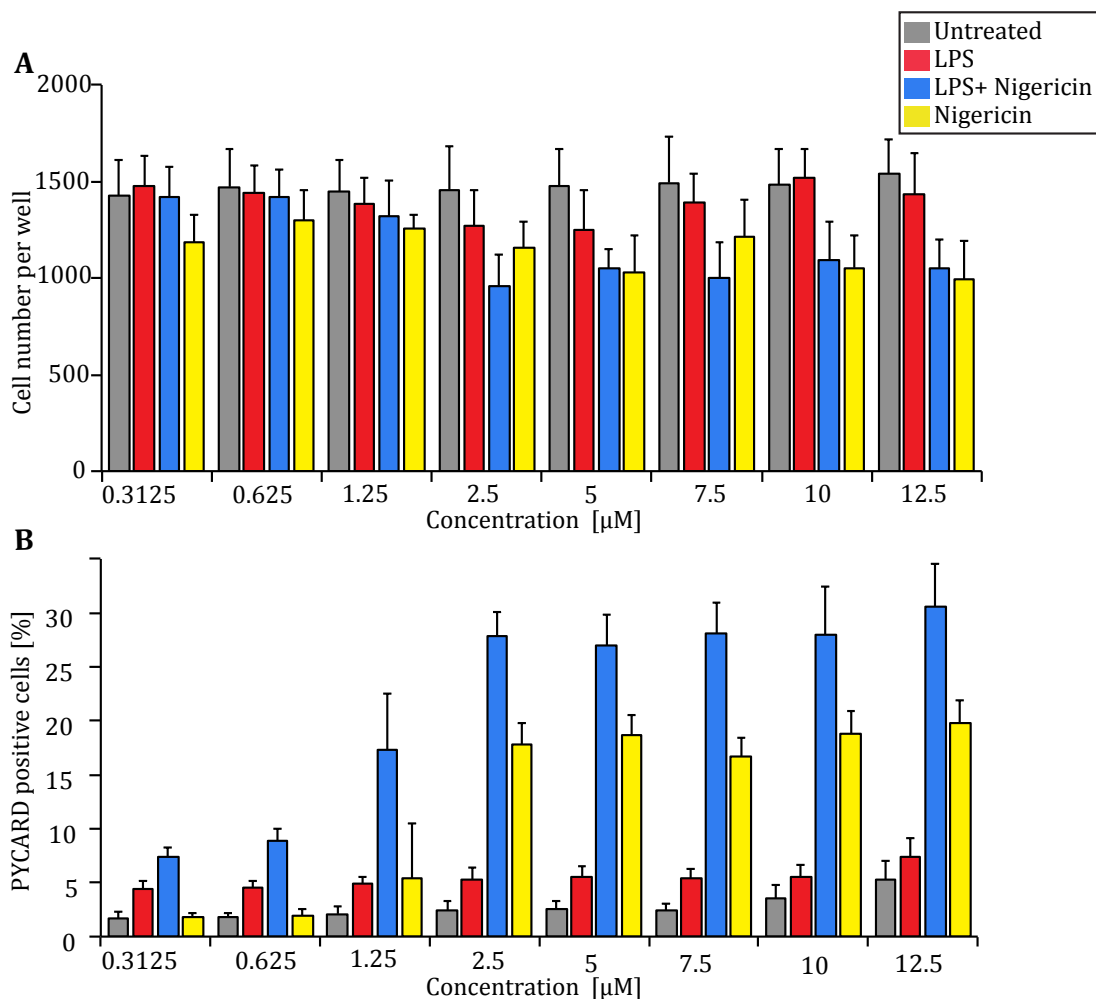


Figure 32: Nigericin titration experiment.

titration experiment was performed to study the effect of different Nigericin concentrations on the inflammasome activation rate. PBMCs were primed with LPS followed by treatment with increasing Nigericin concentrations. The Nigericin concentrations tested did not show any effect on the resulting cell number (A). To induce inflammasome activation (B) a range of Nigericin concentrations between 2.5-12.5 μM was used and resulted in a comparable activation rate. 1.25 μM Nigericin caused less activation, while the concentrations of 0.3125 and 0.625 μM caused the lowest activation rate. The experiment was repeated two times. The concentration of 5 μM was used as standard Nigericin concentration in the course of this project. The depicted results were derived from healthy donor 15 (HD15). Error bars represent the standard deviation, $n=12$.

Next, the effect of increasing LeuLeuOMe concentrations on the inflammasome activation rate was studied in a titration experiment (**Figure 33**) and a LeuLeuOMe concentration range of 0.013 - 1 mM was used. Although 0.2 mM LeuLeuOMe caused the highest response, there was no remarkable change in the response when the LeuLeuOMe concentration was in a range of 0.1-1 mM. LeuLeuOMe concentrations between 0.0125 - 0.05 mM caused very low activation (~2%). Therefore, 0.2 mM LeuLeuOMe was used as the standard LeuLeuOMe concentration during the current study.

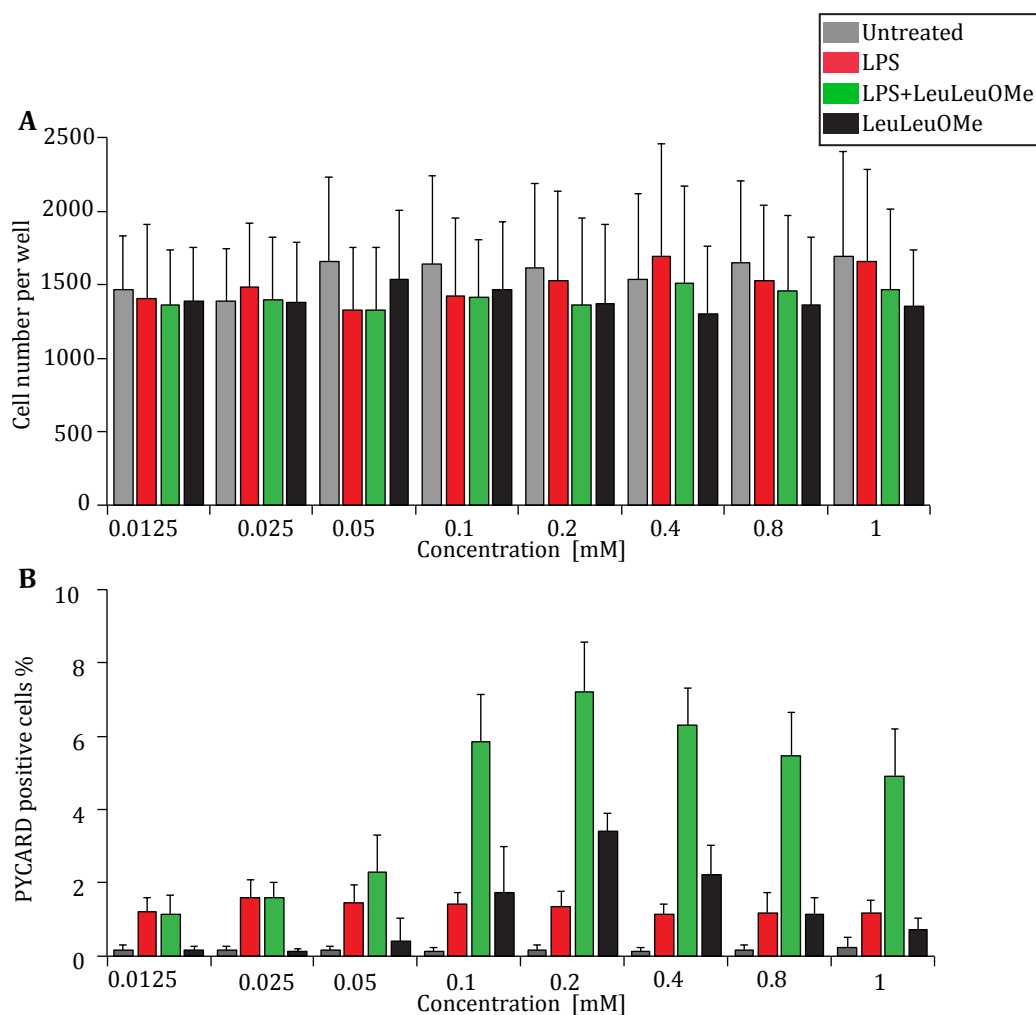


Figure 33: LeuLeuOMe titration experiment.

A titration experiment was performed to study the effect of LeuLeuOMe concentration on the inflammasome activation rate. PBMCs were primed with LPS and stimulated for 30 minutes with LeuLeuOMe. The average cell number per well (**A**) was not affected by increasing LeuLeuOMe concentrations. To induce inflammasome activation (**B**) a range of LeuLeuOMe concentrations between 0.1125 mM and 1 mM was used. A LeuLeuOMe concentration of 0.2 mM caused the highest response. However, there was no remarkable change in the response when the LeuLeuOMe concentration was in a range of 0.1 - 1 mM. LeuLeuOMe concentrations between 0.0125 - 0.05 mM caused very low activation. The experiment was repeated two times. The concentration of 0.2 mM was used as the standard LeuLeuOMe concentration during the course of this project. The depicted results were derived from healthy donor 15 (HD15). Error bars represent the standard deviation, n=12.

Finally, a titration experiment was performed to study the effect of the LPS concentration on the inflammasome activation rate (**Figure 34**). This experiment showed that changing the LPS concentration between 1- 200 ng/ml did not affect the activation rate. The concentration of 5 ng/ml was used as standard concentration of LPS during this thesis.

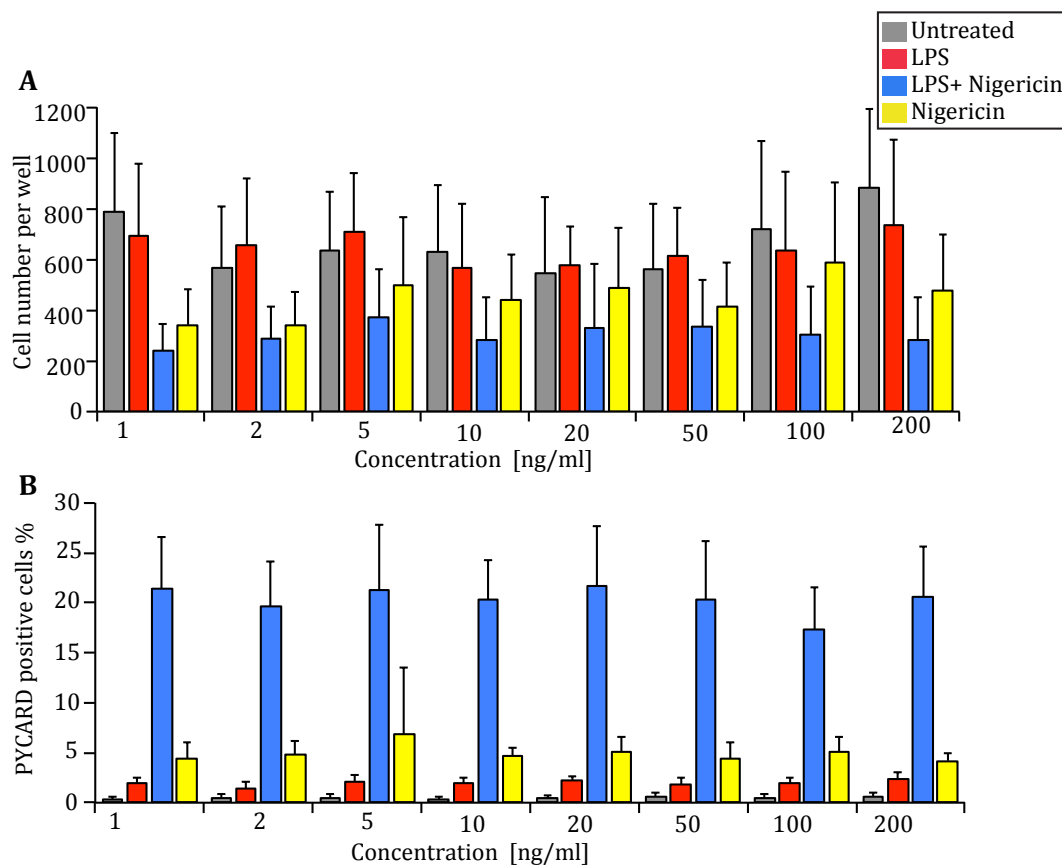


Figure 34: LPS titration experiment.

A titration experiment was performed to study the effect of the LPS concentration on the inflammasome activation rate. PBMCs were primed with LPS and activated with 5 μ M Nigericin for 1 h. This experiment showed that LPS concentrations between 1-200 ng/ml did not affect the activation rate (**B**) and that the cell number was not affected (**A**). The experiment was repeated two times. The concentration of 5ng/ml was used as standard LPS concentration in the course of this project. The depicted results were derived from healthy donor 14 (HD14). Error bars represent the standard deviation, n=12.

4.1.5. The inter-individual variation of the healthy PBMC donors

The results depicted in **Figure 30** showed clearly that the analyzed six PBMC samples respond differently from each other in terms of the inflammasome activation rate although they were all isolated from healthy donors. This result was expected as the immunological profile of each individual is unique and is subject to physiological and environmental influences. Hence, isolated PBMCs from healthy volunteers represent a dynamic status that can vary among individuals. However, inter-individual variation of

healthy blood samples needs to be carefully analyzed in biomarker studies with the final aim to establish the physiological window of fluctuation (Maes, Landuyt et al. 2013). Addressing this variability provides necessary information for understanding the response of PBMCs in the case of both healthy and diseased individuals. Therefore, the question was whether different samples of healthy donors may show different responses in terms of the main readouts of our PBMC *ex vivo* assay, namely intracellular TNF α production, TNF α release, inflammasome activation rate and IL-1 β release. PBMCs from three healthy donors (HD04, HD05, and HD06) were used to conduct this experiment in **Figure 35**.

HD04 and HD05 showed very comparable intracellular TNF α production (10% positive cells) while HD06 exhibited lower production (5%) (**Figure 35 B**). However, the response pattern was changed in case of the TNF α release into the cell culture supernatant. LPS treated PBMCs from HD04 showed a higher release of TNF α (400 pg/ml) compared to HD05 (200 pg/ml TNF α), whereas HD06 showed a low release of 60 pg/ml (**Figure 35 B**).

In the case of the inflammasome activation rate (**Figure 35 C**), 25% of both primed and activated HD04 PBMCs mounted an inflammasome response while the activation rate was only 4% in case of HD06 for the same treatment condition. HD05 showed an intermediate rate of inflammasome activation (10%) compared to the other donors.

The measurement of IL-1 β release depicted the same pattern that was observed in the inflammasome activation rate, meaning that HD04 was the highest responder and HD06 had been the lowest (**Figure 35 D**).

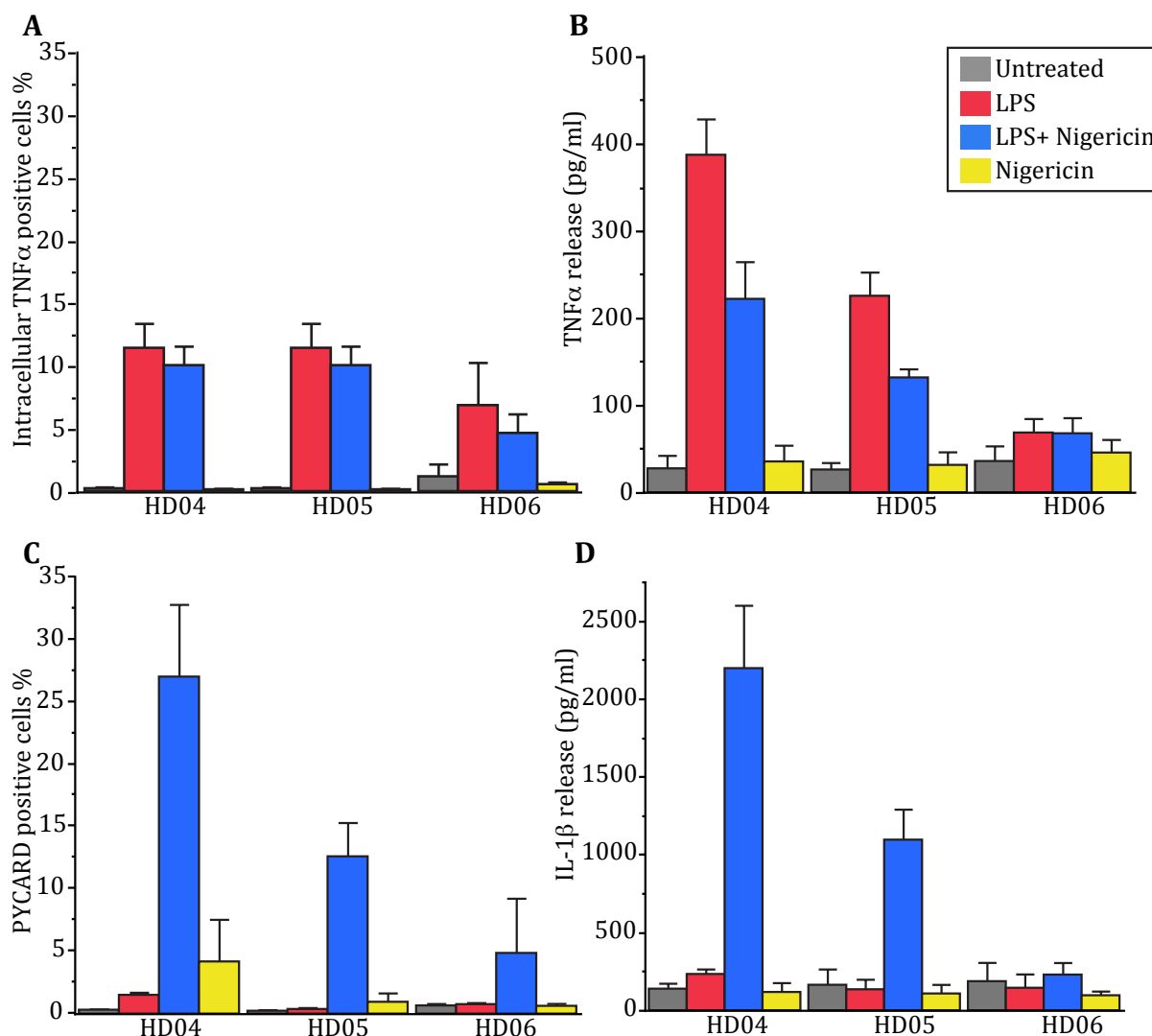


Figure 35: Performance of three healthy donors (using Nigericin as inflammasome activator).

Three PBMC samples (HD04, HD05, and HD05) were isolated from buffy coats of healthy volunteers and used to conduct this experiment. (A) Intracellular TNF α production. HD04 and HD05 showed a comparable percentage of TNF α positive cells whereas HD06 had been the lowest. (B) TNF α release assay. For LPS treated cells, HD04 was the highest and HD06 was the lowest in case of TNF α release. (C) Inflammasome activation assay. The inflammasome activation correlated with TNF α release, meaning the donor with high TNF α release, HD LPS + 04, showed high inflammasome activation and vice versa. (D) IL-1 β release. The release of IL-1 β was higher from PBMCs that were both primed and activated with Nigericin, compared to the no activation conditions (untreated, LPS, and Nigericin treated cells). Error bars represent the standard deviation. For untreated or LPS treated cell, n= 8 wells, while n=12 for the other conditions.

The same experiment and analysis in **Figure 35** were repeated using LeuLeuOMe as an inflammasome inducer (**Figure 36**). The results of this experiment were even more consistent between priming status and the inflammasome activation rate, meaning that

HD04 was the highest responder for all of the four assay parameters, HD06 was always the lowest and HD05 was an intermediate responder compared to the others.

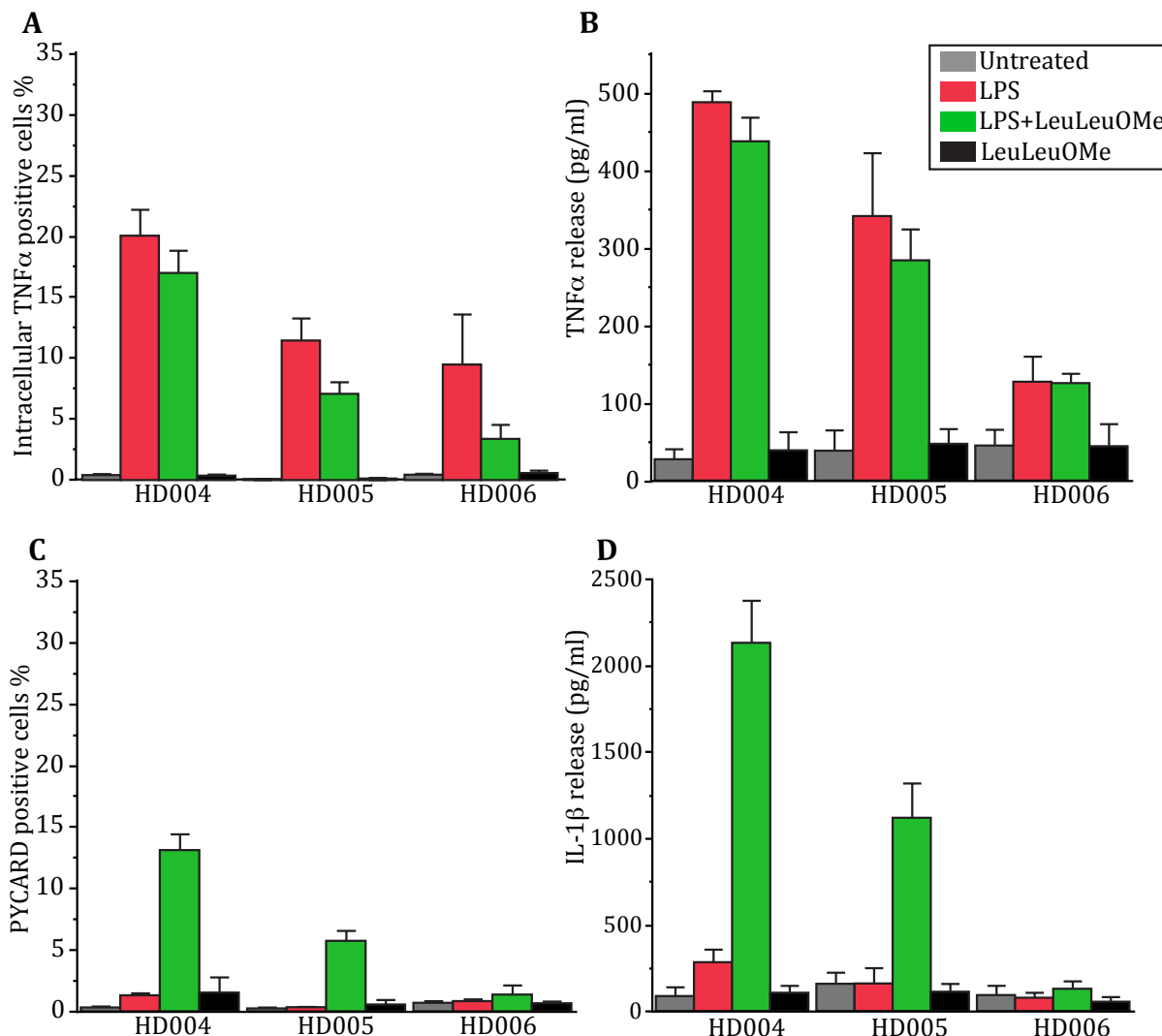


Figure 36: Immune response of three healthy donors using LeuLeuOMe as inflammasome activator. The same experiment in **Figure 35** was also performed using LeuLeuOMe as inflammasome activator. The same trend obtained from using Nigericin was also repeatedly shown with LeuLeuOMe, meaning HD04 was the highest performer, this time with all of the four readouts (A, B, C, and D). HD05 showed always an intermediate response, while HD06 was the lowest among the three healthy donors that were used for this experiment. Error bar is the standard deviation. For untreated or LPS treated cell, n= 8 wells, while n=12 for other conditions.

These two experiments (**Figure 35** and **Figure 36**) revealed that PBMC samples which exhibited a high priming profile showed at the same time a high inflammasome activation rate. Similarly, high inflammasome activation resulted in a high release of IL-1 β . These results illustrated how the cell-based assay readouts were associated with each other, i.e.

high activation of TLR caused a high activation of inflammasome which in turn caused high release of IL-1 β . The experiment showed also different healthy PBMC samples could vary according to the immune status of the donor.

To address whether the inter-individual variation of the healthy PBMCs in **Figure 35** and **Figure 36** was due to the sample quality, we conducted a quality check of our cryopreserved PBMC samples. The recovery rate was used in previous studies to evaluate the sample isolation and cryopreservation quality (Kleeberger, Lyles et al. 1999). The recovery rate is defined as the percentage of viable cells recovered after thawing the cryopreserved samples on the day of the experiment. We expressed the recovery rate by percentage of viable cells divided by the original frozen cell number (10 million cells per vial). To analyze the recovery rate of the PBMC samples, six healthy PBMCs samples were analyzed over a three-day experiment (**Figure 37**). For each healthy PBMC sample, the recovery rate was very stable over the three-day repetitions. However, the six samples exhibited different average recovery rates. For example, HD14 showed an average recovery rate of approximately 30%, while HD12 and HD16 showed a recovery rate of 80% (**Figure 37**).

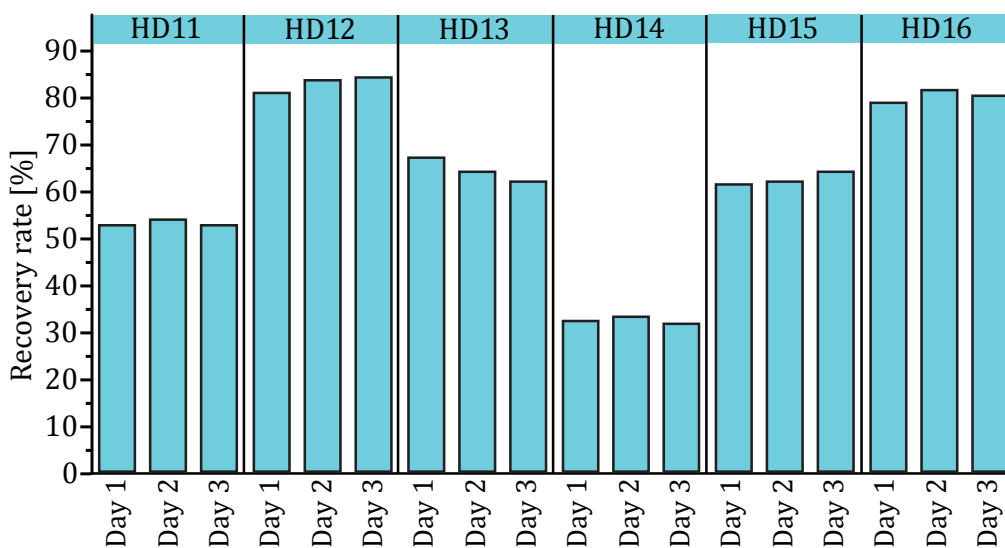


Figure 37: Percentage of viable cells recovered from thawing PBMC vial per day (Recovery rate)

Ten million cells were frozen after PBMC isolation. Viable cells were calculated after thawing the cryopreserved PBMCs. The recovery rate is expressed as the percentage of the viable cells recovered after thawing divided by the original frozen cell number. The recovery was very stable over the 3-day repetitions. The average recovery of each sample was different among the six samples analyzed.

We investigated the association between the recovery rate and the percentage of Inflammasome speck-positive cells. Thus, the recovery rate analysis was flanked by the

assessment of the inflammasome activation rate of the same samples (**Figure 38**). From the depicted results in **Figure 38**, it not possible to conclude that the two parameters were associated with each other. For example, both HD12 and HD16 showed a recovery of around 80%. But, HD12 showed an activation rate of about 22% while the activation rate of HD16 was around 27%. Thus, the obtained data suggested that the recovery rate did not affect the extent of an inflammasome response in PBMCs and that the inter-individual variation of inflammasome activation is not due to quality issue.

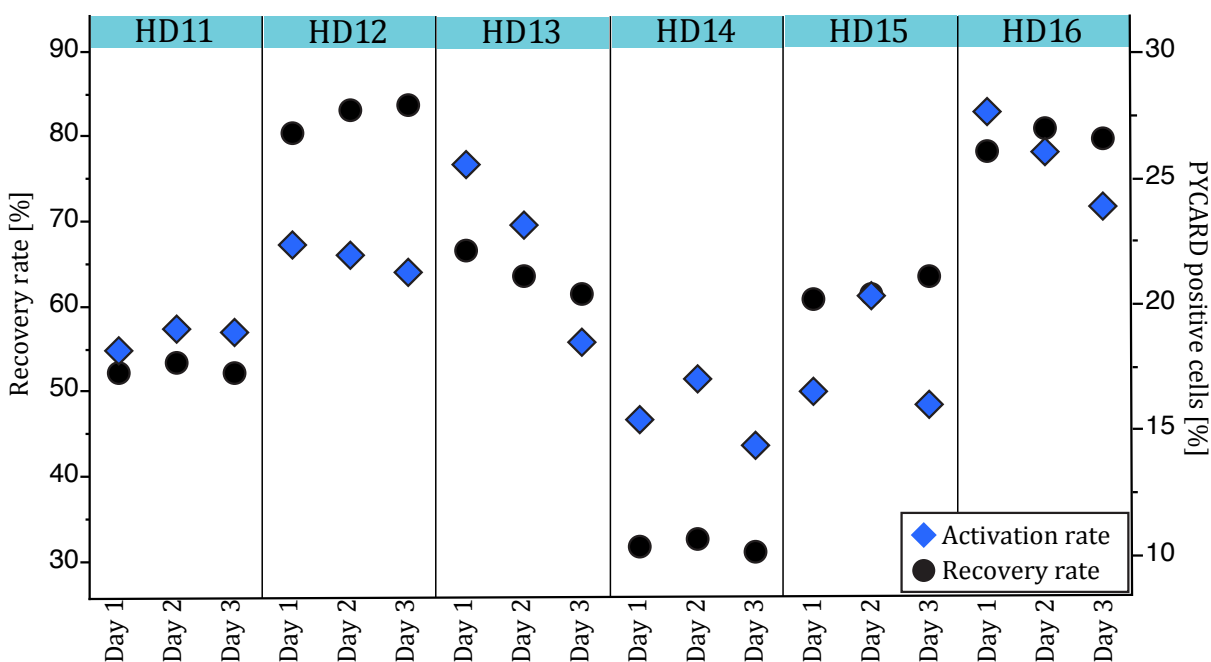


Figure 38: The inflammasome activation rate and the percentage of viable cells

10 million cells were frozen after PBMC isolation. The number of viable cells was determined after the PBMC vial had been thawed on the day of the experiment. The recovery rate was defined as the percentage of viable cells recovered after thawing divided by original number of frozen cells. For each healthy donor PBMC sample, the recovery was stable over the three-day experiment. However, different recovery rates were obtained from different healthy donor samples. We studied the association between the inter-individual variation of inflammasome activation and sample recovery rate. Here, we depicted the inflammasome activation rate, LPS + Nigericin condition, for a set of healthy donors and their recovery rate. It was shown that the difference in the activation rate cannot be explained by the recovery rate of the sample. Error bars represent the standard deviation, n=12 for the activation rate.

4.2. Development of an image analysis workflow to assess the cellular composition of a given PBMC sample

4.2.1. Cell surface markers for PBMC subsets characterization

PBMCs, as a heterotypic cell system, comprise of different types of immune cells such as monocytes, T cells, B cells, dendritic cells, and natural killer cells among others. T cells represent the most abundant cell type within the PBMC cell system with a range of 50-

80%, followed by monocytes with 10-20%, and B cells with 3.5-9%. Dendritic and natural killer cells are very rare in PBMCs accounting for only 1–2% (Akdis, Palomares et al. 2012, Tan and Gery 2012, Kleiveland 2015). The heterogeneity of the PBMC cell components is widely varied within the healthy population (Maes, Landuyt et al. 2013). For example, changing the percentage of monocyte to the double (from 10% -20%) is still considered within the normal range of the healthy population (Maes, Landuyt et al. 2013).

Knowledge about the cellular composition and the abundance of cell types within the PBMC cell system supports data analysis and interpretation when PBMCs are used as cell model in a cell-based assay. For example, it could provide information on how the percentage of a subset could affect the inflammasome activation rate (as it will be shown later). Therefore, an image-based immunocytochemistry (ICC) approach was developed in order to characterize the PBMC cellular composition in the cell-based assay. Our setup was focused on the most abundant cell types of the PBMC cell system. These are T cells, B cells and monocytes. The cell surface markers CD3, CD19, and CD14 were used to identify T cells, B cells and monocytes in the PBMC sample, respectively (**Figure 39**). The chromatin stain Hoechst 33342 was used to visualize the nuclei.

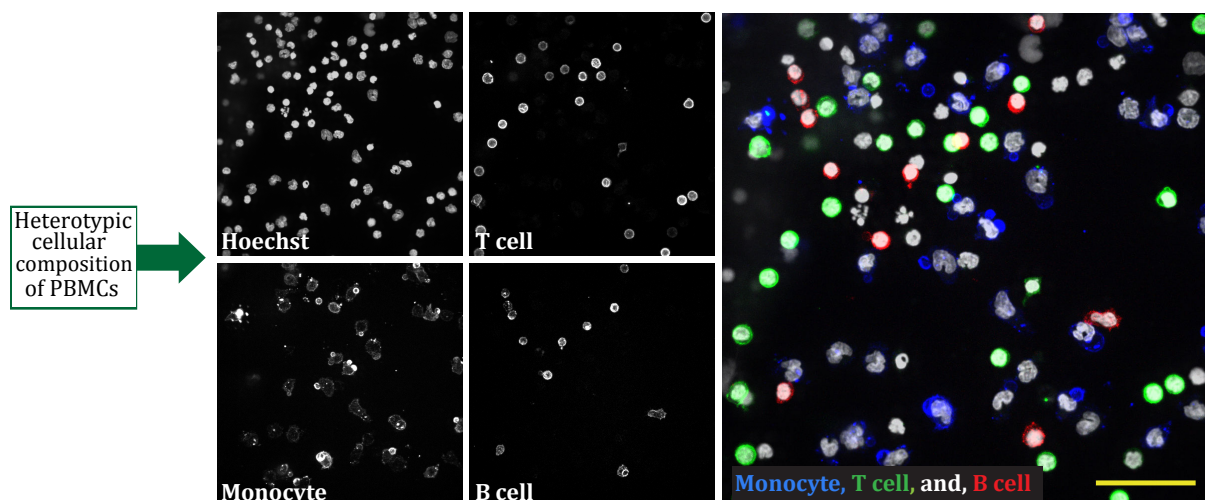


Figure 39: Cell surface marker staining.

An immunocytochemistry (ICC) approach was developed in order to characterize the PBMCs cellular composition in the cell-based assay. The cell surface markers CD3, CD19, and CD14 were used to identify T cells, B cells and monocytes, respectively. The marker staining was highly specific and the number of double or triple positive cells was low. Scale bar, 40 μ m.

As depicted in **Figure 39**, the majority of cells were positive for one of the three (monocyte, B and T cell) markers, reflecting that T cells, B cells and monocyte are the most abundant cell types in the PBMC cell system within the cell-based assay. This is consistent

with flow-cytometry-based studies showing that these cellular subsets represent more than 90% of the PBMC sample (Akdis, Palomares et al. 2012, Tan and Gery 2012, Kleiveland 2015).

The emerging question at this point was which cell type within the PBMC population was capable to mount an inflammasome response. There is increasing evidence that TLRs and NLRP3 inflammasome activation are triggered in monocytes rather than other PBMC cell types (Mizote, Wakamatsu et al. 2014, Ahmad, Mishra et al. 2017). For instance, Ahmed and colleagues have shown in a flow cytometry-based study that PYCARD complex formation occurred within stimulated monocytes (Ahmad, Mishra et al 2017). In the current project, we wanted to show by live imaging that monocytes, but not T or B cells, mount an inflammasome response. Thus, a time-lapse experiment of stimulated PBMCs was conducted as follows. Living cells were stained with monocyte, T cell and B cell surface markers and Hoechst 3342. Stained PBMCs were seeded in a 384-well assay plate and primed with LPS for two hours, followed by 5 μ M Nigericin treatment for one hour. The live imaging was started immediately after Nigericin addition. At this point, monocytes (CD14⁺) were still showing the typical kidney-bean shaped nucleus (**Figure 40 A**). Nevertheless, after 15 minutes of Nigericin stimulation, monocytes started to undergo morphological changes by shrinkage of the nuclear area and rounding of the nucleus shape. Following this phase, after \sim 50 minutes Nigericin stimulation, the contracted round-nuclei expanded to a characteristic morphology showing a large nuclear area. Additionally, at this time point monocytes have completely lost their CD14 signal. In contrast, T and B cells showed no morphological changes in response to LPS + Nigericin treatment (**Figure 40 A**). Similarly, untreated or LPS treated PBMCs, including the monocyte, showed also no morphological changes (data are not shown).

Therefore, it was concluded that monocytes undergo morphological changes in response to LPS + Nigericin treatment. However, to understand the relationship between the observed morphological changes and the inflammasome activation, live imaging of PYCARD-CD14 stained PBMCs was conducted immediately after Nigericin activation had started (**Figure 40 B**). PBMCs were stained in vivo with Hoechst 33342 and anti-CD14 before they were seeded in a 384-well plate, followed by LPS-priming and Nigericin

stimulation as described before. During the priming step, the PYCARD antibody was added to the cell culture medium.

Monocytes that responded to the inflammasome activator (Nigericin) exhibited morphological changes and showed at the same time inflammasome complex formation (**Figure 40 B**) as visualized by anti-PYCARD staining, providing evidence that monocytes represented the cell type in the PBMC cell system mounting an inflammasome response. With these two experiments, we provided evidence that monocytes, but neither T nor B cells, mount the inflammasome activation in response to LPS + Nigericin treatment.

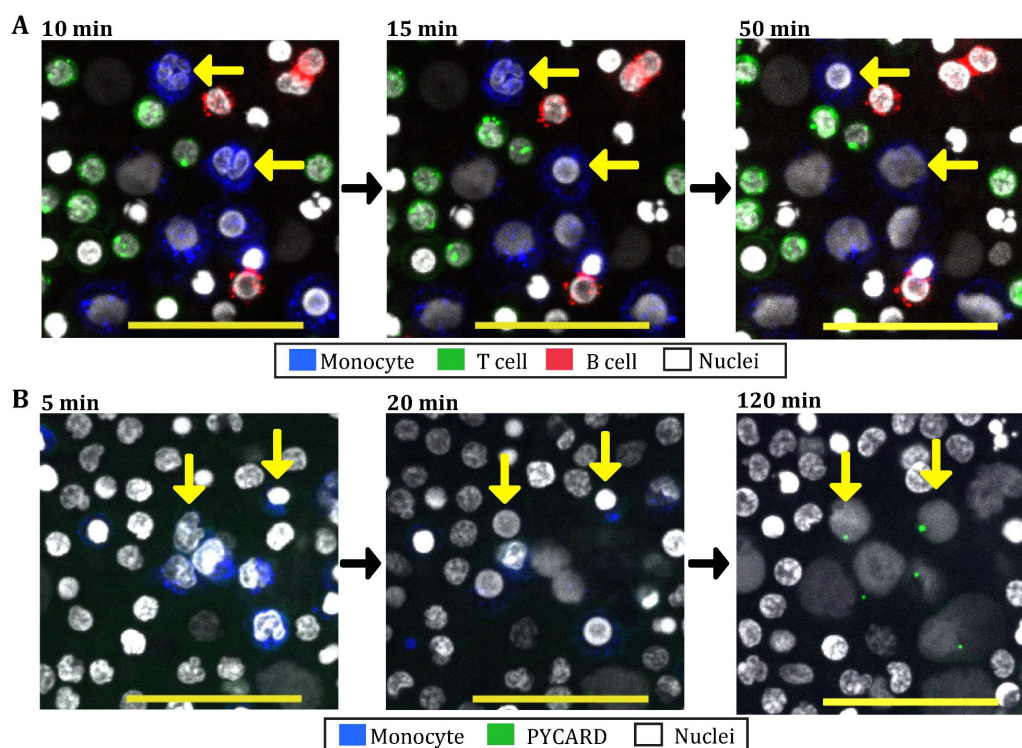


Figure 40: Time-lapse of stimulated PBMCs.

(A) Monocytes respond to LPS priming followed by Nigericin stimulation. PBMCs were stained in vivo for Hoechst 33342 (white color), monocytes (blue CD14⁺ cells), T cells (green CD3⁺ cells) and B cells (red CD19⁺ cells). Stained PBMCs were seeded in a 384-well plate and primed with LPS followed by 5 μ M Nigericin treatment. The time-lapse was started 10 minutes after the addition of Nigericin. Images were taken every 4 minutes for 12 times. **10 minutes after the addition of Nigericin**, some monocytes (next to yellow arrows) still had the typical kidney-bean shaped nucleus. **While ~15 minutes after Nigericin addition**, some monocytes (next to yellow arrows) started to undergo morphological changes by shrinkage of the nuclear area forming a round-nucleus. **~ 50 minutes after Nigericin addition**, monocytes had completely lost their CD14 signal forming a characteristic morphology of monocyte (responded monocyte). Neither T nor B cells revealed any morphological changes. **(B) Activated monocytes showed inflammasome complex formation.** In a parallel experiment, PBMCs were stained in vivo for Hoechst 33342 and anti-CD14 before they were seeded, primed with LPS and stimulated with Nigericin. During LPDS-priming, the PYCARD antibody was added to the culture medium. The time-lapse was started 5 minutes after Nigericin adding. Images were taken every 5 minutes for 120 minutes. Activated monocytes revealed clear inflammasome complex formation, indicating that monocytes represent the cell type which is capable to mount an inflammasome response. Scale bar, 40 μ m.

4.2.2. Cell-type classification using a machine learning approach

In light of the results from the time-lapse experiment (**Figure 40**), we decided to quantify the priming status and inflammasome activation rate relative to the monocyte number and not to the total number of cells. Furthermore, we quantified T and B cells to collect more information about the PBMC sample. Therefore, an image analysis routine was developed to process the images obtained from the cell surface marker staining. As conventional intensity-threshold-based image analyses was limited to correctly analyze the images obtained, we needed to develop a more sophisticated image analysis tool for this task. Therefore, a supervised machine learning algorithm was developed and used for this purpose. This method was successful in handling the complexity of the images. The complicity of our image dataset could be explained by the following reasons: first, CD markers are not 100% cell-type specific. CD3 is widely accepted as a T cell marker. However, it is expressed to a small extent also on the B cell plasma membrane (Nagel, Mobs et al. 2014). Furthermore, cell surface marker expression, and hence its signal intensity, on the cell membrane are affected by the functional status of a given cell, meaning that the signal intensity of a marker is not always the same for a given PBMC subset, e.g. T cells, rather than it varies according to the immune status of sample donor. Furthermore, LPS has been reported to alter the expression of CD14 (monocyte marker). Landmann and colleagues have reported that LPS reduces membrane CD14 expression in the first six hours of incubation before the expression started to increase as incubation time was increased (Landmann, Knopf et al. 1996). In our setup, PBMCs were incubated with LPS for two hours. Thus, CD14 expression was expected to be reduced in LPS treated conditions compared to untreated PBMCs.

Due to these challenges described above, conventional intensity-based image analysis tools failed to perform reliable segmentation. Thus, the cell-type classification was conducted utilizing a machine learning approach that was using all markers available in the images e.g. cell surface marker signal intensity as well as chromatin features from Hoechst 33342 staining in order to derive information to correctly classify pixel probability belonging to one given object class (i.e. T cell, monocyte, B cell, background, cell remnants). To achieve this goal a pixel-based supervised classification was done using U-Net neural network using the YAPiC tool developed by IDAF facility at DZNE Bonn

(<https://yapic.github.io/yapic/>). YAPiC performed the classification based on training labels that were collected by the user with the Interactive Learning and Segmentation Toolkit *ilastik*. For the *ilastik* labeling, 20 representative images were selected. In each image, two example objects, in average, were labeled for each class (and 7 objects were labeled for each of the monocyte and negative unstained cells) (see **Materials and Methods** for more details). Objects were labeled according to their cell surface marker staining. Objects exhibiting typical kidney-like nuclear morphology were labeled as monocytes (Sahu, Bethunaickan et al. 2014).

Labeled PBMCs were subjected to the YAPiC software application to conduct the training phase using a High-Performance Computer (HPC). As depicted in **Figure 41**, YAPiC was improving its performance over the repeated iterations (over 3-days training). The prediction error (training loss) was reduced over training time. Training loss was calculated by a cost function formula (Bonn 2019) which compared the original object annotation provided by the user to the object classification assigned by YAPiC. Eventually, YAPiC performance reached a high accuracy level (training loss close to zero) where its classification rules had been optimized to be used to assign unlabeled objects.

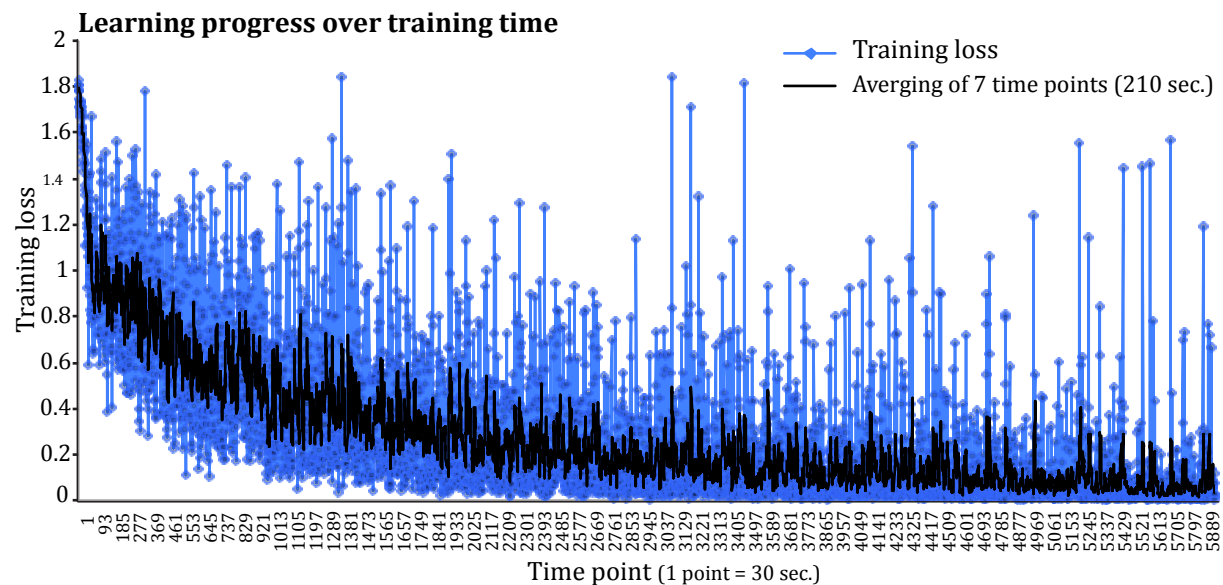


Figure 41: YAPiC learning phase.

Labeled example objects, from *ilastik*, were subjected to YAPiC to derive the prediction rules. YAPiC was optimizing its performance to improve the training loss (the prediction accuracy). The training loss is calculated by applying a mathematical formula (<https://yapic.github.io/yapic/>) that compared the original object annotation provided by the user to the classification of that object by YAPiC. During the 3-day training, the average training loss (black line) was improved, reaching an error close to zero.

As YAPiC applied the classification rules to assign all objects in the data set to a cell-type, the output represented a map of pixel probability intensity (**Figure 42**). This map was visually compared to the original raw data images in order to check the prediction accuracy (see a representative example in **Figure 42**). The comparison showed that the algorithm accuracy to assign each object into a cell class was high (close to 100%). Moreover, the algorithm predicted the CD14 negative kidney-like shape nuclei as monocyte nuclei based on the object chromatin features, reflecting the high accuracy of the developed tool.

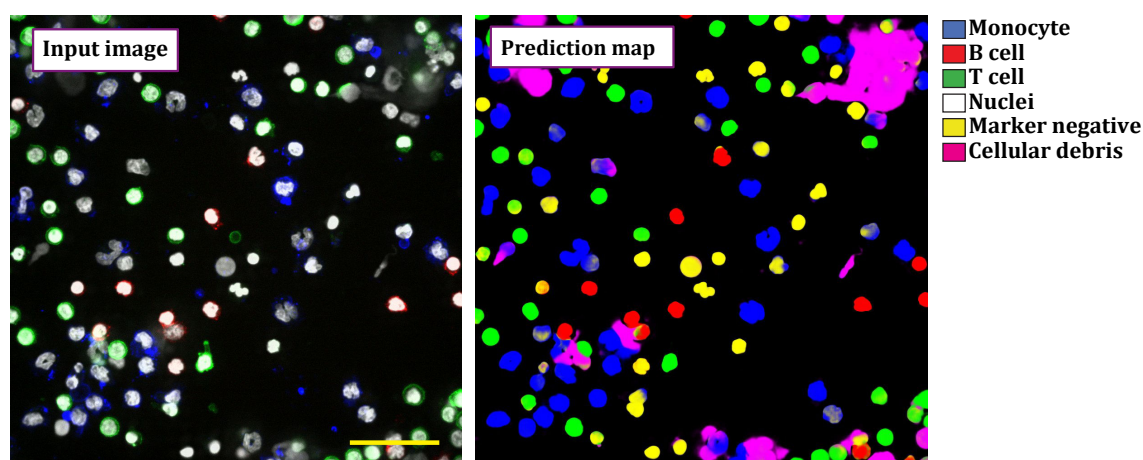


Figure 42: The accuracy of YAPiC prediction output.

After the YAPiC learning phase was completed and the prediction rules were identified, YAPiC predicted the cell-type of all objects in the training set. The output was a class probability per pixel. The prediction was very accurate when the merged prediction images were compared to the marker staining on the input images, as it is depicted in these representative images. Interestingly, YAPiC was able to correctly label the kidney-like shape nuclei as monocyte nuclei, although some of these cells were not stained with the monocyte marker. Scale bar, 40 μ m.

The reliability and reproducibility of YAPiC performance were assessed using a complex dataset. The cellular composition of three healthy donors (HD04, HD05, and HD06) was analyzed using a dataset of four independent experiments. In each experiment, duplicate plates were prepared using the same PBMC vial.

The cellular compositions of every untreated PBMCs sample over the 4-days independent experiments were comparable (**Figure 43**). For HD04 18% of the cells were identified as T cells compared to 50% of T cells that were obtained in PBMCs of donor HD05. For the

monocyte percentage, HD04 showed $\pm 30\%$ of monocytes, while both HD05 and HD06 samples contained 17% monocytes.

Beyond, our analysis showed a low percentage of unclassified cells (**Figure 43** grey subset) which represent cells with a prediction of less than 50% probability. The classifier was trained not to assign these cells into a cell class, to avoid any random or false classification.

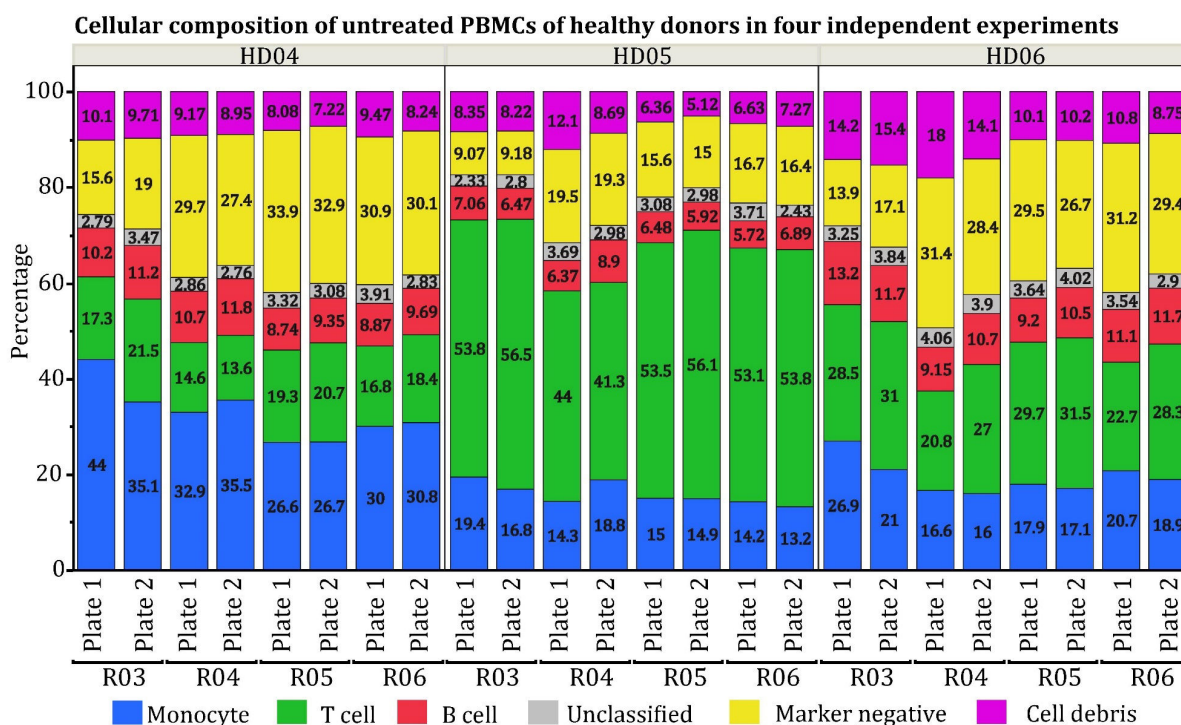


Figure 43: YAPiC prediction consistency was evaluated using untreated PBMCs

3 healthy donors (HD04, HD05 and HD06) from four independent experiments (Run 03 (R03), R04, R05, and R06) were used to analyze the prediction robustness. Each of the repeated experiments included two plates that were seeded from the same vial of PBMCs. The cellular composition of each PBMCs sample over the different repetitions was comparable. For example, in HD04, the T cell percentage over the four repeated experiments accounted for 18%, while it was around 50% in case of HD05. n=4.

The same experiments and analyses in **Figure 43** were repeated using LPS treated PBMCs (**Figure 44**). As mentioned before, LPS had been reported to reduce CD14 (monocyte marker) expression within two hours of LPS incubation. Thus, it was necessary to confirm that the algorithm was able to handle the LPS effect on the signal of monocyte marker.

The quantification analysis depicted in **Figure 44** showed that the results of plate one and plate two of each experiment were comparable, particularly for the monocyte percentages

(Figure 44, blue bars). Most importantly, the percentage of monocyte was slightly lower compared to untreated PBMCs due to the reduction of the CD14 signal by the effect of LPS. This could also explain the slight increase in the percentages of unclassified cells compared to the results obtained by the analysis of untreated PBMCs, i.e. the reduction in the CD14 expression reduces the prediction probability of cell-class monocytes, causing these objects to be assigned as unclassified objects.

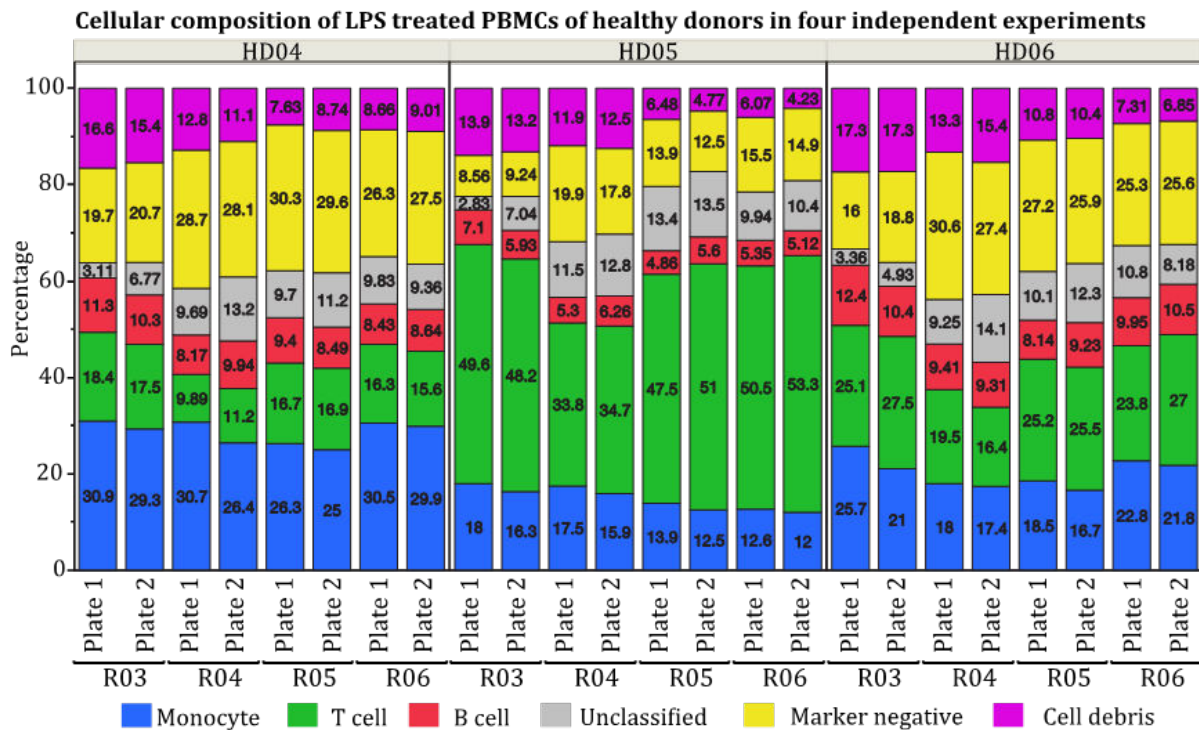


Figure 44: YAPiC prediction consistency was evaluated using LPS-treated PBMCs

The same analysis in Figure 43 was repeated using LPS treated cells. The monocyte percentage was more consistent compared to the untreated PBMCs. However, the monocyte quantification was slightly lower in the case of LPS-treated cells compared to the results obtained by the analysis of untreated cells from a given sample. The cellular composition was unique for each of the three samples of healthy donors tested in this analysis. For instance, HD04 showed the highest monocyte percentage (30%) and HD05 showed the lowest (~15%). n=4.

The results of this experiment (Figure 43 and Figure 44) showed that our analysis workflow was a reliable method to be used on a routine basis during this project. All the upcoming results of the analysis of the cellular composition of PBMCs were generated using the YAPiC analysis workflow.

To assess the effect of normalization of the inflammasome activation rate relative to the monocyte number, we compared the normalized inflammasome activation rate to

activation rate calculated to the total number of cells (**Figure 45**). For this analysis, PBMCs from two healthy donors (HD04 and HD05) were used to address whether the normalization procedure could affect the results of the assay.

The data suggested that the assay output could be changed significantly by ignoring the monocyte number and calculating the activation to the total number of cells. For LPS + Nigericin condition, the normalized activation rate of HD04 was 80% compared to 30% activation rate calculated by applying the total number of cells (**Figure 45**), while in the case of HD05, the normalized activation rate was ~110% in case of the LPS + Nigericin condition and the activation rate calculated according to the total number of cells was 25% for the same condition. Theoretically, the monocyte activation should not exceed 100%. But this is a normalized value rather than real one. Technically, it was not possible to combine anti-CD14 with TNF α -PYCARD staining in the endpoint assay since monocyte lost its CD14 signal after inflammasome activation (see **Figure 40**). Hence, the monocyte percentage in the untreated PBMCs was used to estimate the monocyte number in the LPS + activator and the activator only conditions (see **Materials and Methods** for details).

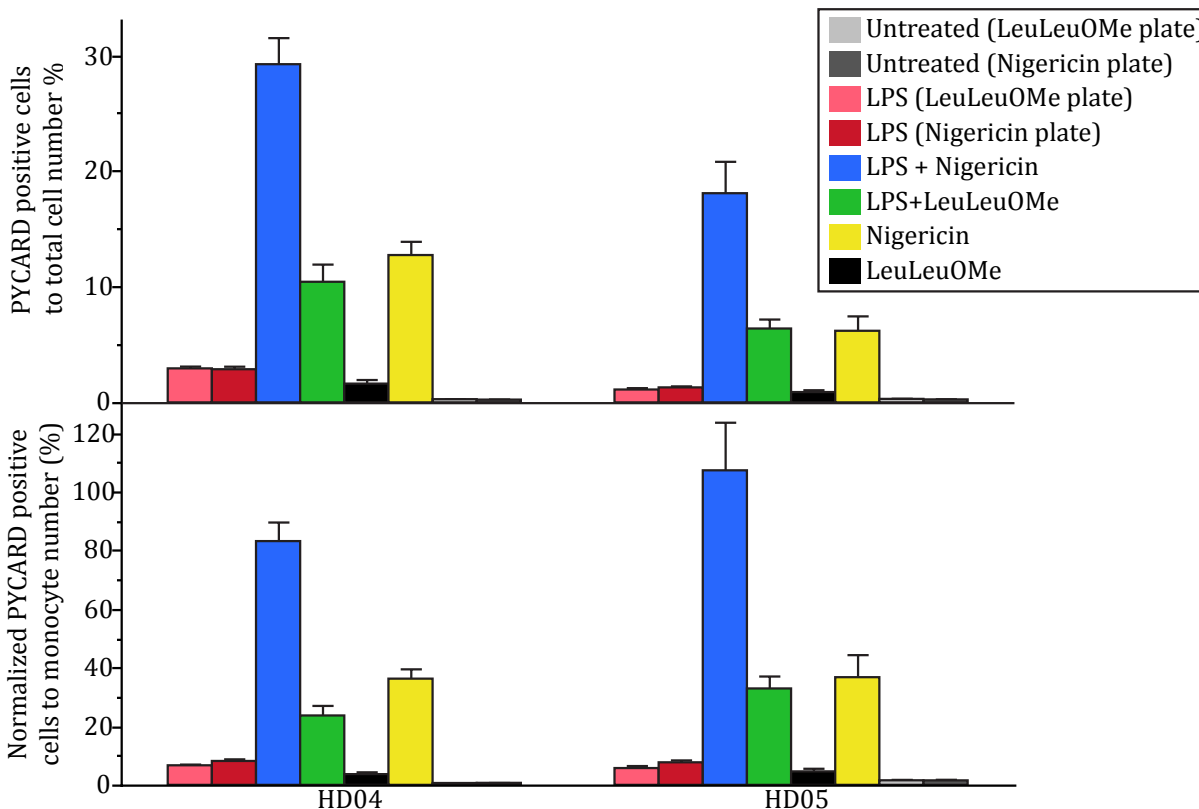


Figure 45: Normalization of inflammasome activation rate to the monocyte number

As it was shown during the live cell imaging experiment of stimulated PBMCs, monocytes represented the responder cell type mounting an inflammasome response. Thus, it was more accurate to normalize the inflammasome activation rate to the monocyte cell number. Interestingly, LPS + Nigericin treated PBMCs showed a high inflammasome activation rate (30%) in case of HD04 while it was around 15% in the case of HD05. However, after normalization HD05 showed higher (LPS + Nigericin) activation (110%) compare to HD04 (80%). Error bars represent standard deviation. For untreated or LPS treated cell, n= 8 wells, while n=12 for other conditions.

Although the caveat of this normalization approach, activation exceeded 100% for two samples during this project, it was still more appropriate to calculate the readout measurements to the estimated the monocyte number rather than to the total number of cells because using the total number of cells was ignoring the inter-donor variation in the number of monocytes. Therefore, for the upcoming sections of this thesis, all the results were normalized to the monocyte number.

4.3. The patient cohort analysis

The established PBMC multi-parametric assay was used to analyze a cohort of 20 patients including nine females and eleven males. Samples were provided by Prof. Anja Schneider.

Blood samples were collected between 2014-2015 at the DZNE Göttingen and the isolation of PBMCs was conducted in Prof. Schneider's laboratory at the collection site. The cryopreserved PBMCs were stored in liquid nitrogen at the DZNE Bonn until the day of the experiment. During the collection of the blood samples, patients were subjected to a set of laboratory tests including CSF analysis, MRI scans and clinical evaluation (see details in **Index I**). The clinical evaluation was done via the Mini-Mental State Exam (MMSE). The patient average age was 71 (55-83) year old and the cohort was composed of six AD patients, five depressive donors and nine samples of other diseases (**Table 5** and **Index I** for details).

Table 5: Clinical information of the Disease Donor (DD) samples.

ID	Sex	Diagnosis	Age (year)	MMSE	CSF t-tau (pg/ml)	CSF p-tau (pg/ml)	Ab42 (pg/	Ab42/40 ratio	AD CSF Biomarkers
DD01	Female	Depression	55	24	133	30	995	1.1	
DD02	Female	AD	73	23	175	36	333	0.32	
DD03	Male	Other	76	21	140	34	1169	1.2	Negative
DD04	Male	Other	82	25	335	65	911	1.3	
DD05	Male	Other	76	-	-	-	-	-	
DD06	Male	Other	83	25	-	-	-	-	
DD07	Female	Other	78	26	263	51	1302	0.74	Negative
DD08	Male	AD	64	30	362	68	501	0.46	
DD09	Male	AD	54	21	500	84	441	0.46	Positive
DD10	Male	Other	73	29	-	-	-	-	
DD11	Female	Other	76	24	238	35	1041	1.2	Negative
DD12	Female	AD	77	18	683	125	843	0.49	Positive
DD13	Male	Depression	58	-	189	36	936	0.96	
DD14	Female	Depression	81	-	-	-	-	-	Negative
DD15	Female	AD	82	20	282	56	641	0.39	Positive
DD16	Male	AD	77	26	360	83	596	0.45	Positive
DD17	Male	Depression	68	-	-	-	-	-	
DD18	Male	Other	71	25	485	105	792	0.55	Positive
DD19	Female	Depression	53	-	-	-	-	-	
DD20	Female	Other	77	25	162	46	813	2.3	

Depressed samples served as age-matched controls as the donors of these samples were within the same age range of the AD sample donors and as they were isolated by the same laboratory. Furthermore, the NLRP3 inflammasome was reported to play a role in metabolic danger signals and the stress exposure in the major depressive disorder (Kaufmann, Costa et al. 2017). Li et al pointed out that inhibition of the NLRP3

inflammasome might be a therapeutic target for the treatment of depression (Li, Liu et al. 2019).

Three healthy PBMCs samples (HD04, 5, and 6) were used to compare the disease versus healthy immune response on all the screening days. The screen was conducted over four days. On every day (Run), five patients and three healthy donor samples were processed. Therefore, HD04, HD05, and HD06 served two aims, i.e. as control samples to compare patient versus healthy donor and to evaluate the assay quality during the screening days as they were included in all experiments.

Finally, it should be mentioned that the samples were processed in a blinded manner until the complete screen was conducted and the first preliminary analysis was finished.

4.3.1. Univariate analysis of the patient cohort

The first data processing step regard the results of the multi-parametric assay was the univariate analysis. The results of each feature of the patients versus the healthy volunteer screen was analyzed individually to assess the responses of the PBMC donors. The samples quality was analyzed by calculating the percentage of the recovered viable cells (**Figure 46**). Although it was previously shown in **Figure 38** that there was no association between recovery rate and inflammasome activation, the cell recovery still reflected the quality of the cell isolation procedure and the cryopreservation quality (Kleeberger, Lyles et al. 1999).

It should be mentioned that the patient samples were isolated and stored between 2014-2015 (**Index 1**) while the three samples from healthy volunteer were isolated in 2016 and finally, the screen was conducted in 2017. Thus, the recovery rate analysis was necessary to evaluate the impact of a longer storage period in the case of the patient cohort samples. The average number of recovered viable cells from the healthy donor samples was 77% (**Figure 46**), while the patient samples depicted three subgroups. Firstly, samples including DD19, 08, 17, and 13 showed recovery rates close to the samples of healthy donors (75%). Other samples including DD04, 5, 6, 9 and DD15 showed a lower recovery rate than the average recovery rate of the samples from healthy donors (60%). Finally, Disease Donor DD1 and DD20 showed a low recovery rate of 32%, which could be due to either the isolation quality or to the fact that the samples were more sensitive for longer

storage periods. In general, the recovery rate for the majority of the samples did not reflect an isolation or a storage issue compared to the healthy volunteer samples.

The cellular compositions of samples of the patients and healthy donors were characterized to describe in more details the sample phenotype (**Figure 47**). PBMCs from each donor were seeded on duplicate plates (see **Materials and Methods**). The cellular composition of each sample, on the two plates, was very comparable (**Figure 47**). The PBMC donors DD01, 06, 07, 11 showed a low monocyte percentage. T cell percentage was highly variable (16- 55%) among all PBMC donors. No increase or decrease in one subset, e.g. monocyte was found to be associated with the change of another subset like T cells. In general, the variation of the immune cell frequencies within the PBMC samples is reflecting the variation in the immune status of the sample donors.

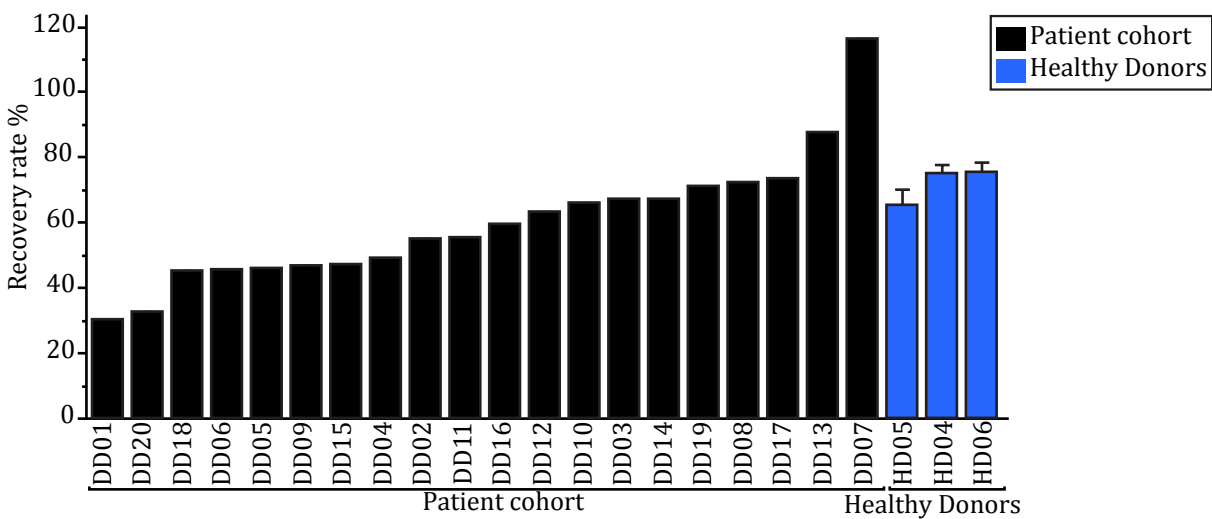


Figure 46: Percentage of viable cells recovered from cryopreserved PBMCs of the patient and the healthy volunteer samples

The recovery rate for the healthy donor samples was 77%, while the recovery rate of the patient samples depicted a diversity of recovery rates. For instance, Disease Donor DD1 and DD20 showed a low recovery rate of 31%. Patient samples DD19, 08, 17, and 13 showed a recovery rate of 80%, which was close to the average of the recovery rate of the healthy volunteer samples. DD07 showed a recovery rate of 120%. This could be explained by the fact that the number of cells that were frozen in this vial was more than the written number of cells on the vial. Error bars represent the standard deviation. For patient samples, n=1 and n=4 for samples of healthy donors.

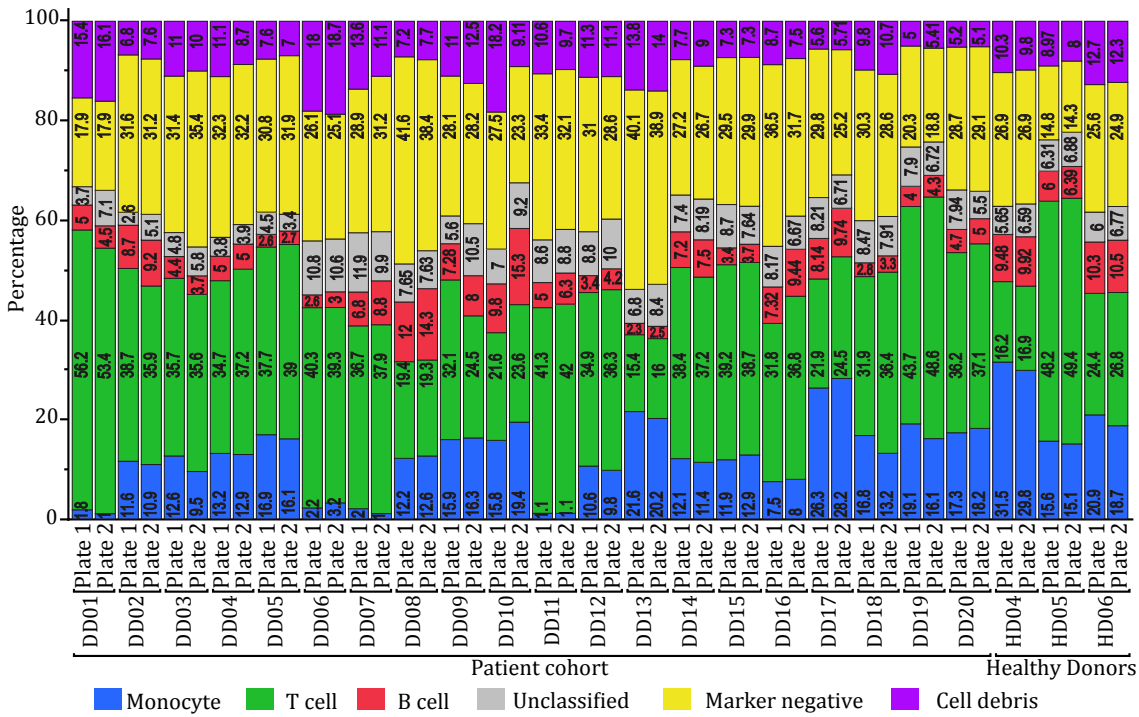


Figure 47: Cellular composition of the untreated PBMC samples of the patient and healthy donors
 The cellular composition of untreated PBMC samples derived from patients and healthy volunteers was investigated to describe better the sample phenotype. The untreated PBMCs of each sample were analyzed on two assay plates. For each donor, the cellular composition was comparable to the replicate plate, indicating the robustness of the quantification approach. Interestingly, four patient samples (DD01, 06, 07, and DD11) showed a low percentage of monocyte. For patient samples n=4 and n=16 for healthy volunteer samples.

Intracellular TNF α production was analyzed for each donor of all samples to assess the sample priming status (**Figure 48**). The percentage of primed monocytes (TNF α positive) different among the samples, reflecting the variety of the TLR activation status of the PBMCs samples. For example, LPS treated monocytes from DD01, 3, 5, 6, 11 and 14 showed low percentage of intracellular TNF α positive cells (less than 40%), while samples from healthy volunteer showed a higher percentage of intracellular TNF α positive cells of 87%. The remaining disease samples exhibited a range of TNF α positive monocytes between 40-80%. Interestingly, 30% of untreated monocytes from DD11 and DD06 exhibited TNF α production, indicating that these samples might had been already primed. The untreated cells from the rest of samples showed no TNF α production.

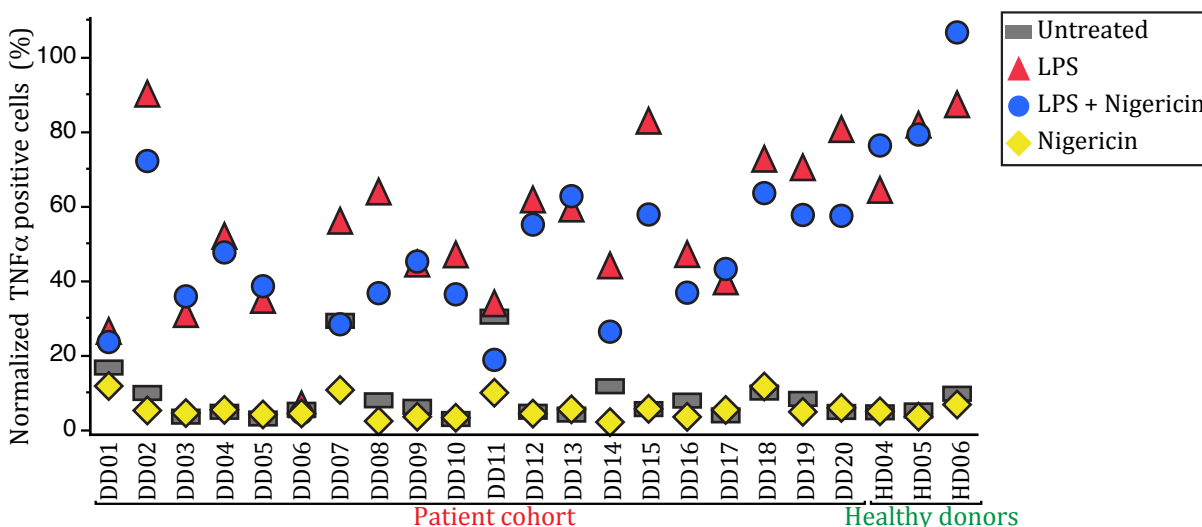


Figure 48: Assessment of intracellular TNF α production for each donor in the plates of Nigericin as an inflammasome activator

The percentage of primed monocytes that expressed TNF α was diverse among the investigated samples. Conditions of no LPS treatment showed low production of TNF α , indicating that there had been no pre-primed PBMCs in this collection of samples, except the untreated PBMCs from DD11 and DD06 that showed 30% of intracellular TNF α positive cells. The healthy donors showed in general higher TNF α production than the disease samples. For the disease samples: n= 8 for untreated and LPS condition, n=12 for other the conditions; for healthy sample: n= 32 for untreated and LPS condition, n=48 for the other conditions. Data were normalized according to the monocyte percentage (see Materials and Methods).

Intracellular TNF α production was also studied in the plate where LeuLeuOMe was used as an inflammasome activator (LeuLeuOMe plate). Consistently with Nigericin plate, samples of healthy donors showed a higher percentage of TNF α positive cells compared to the patient samples. The patient disease samples (DD01, 3, 5, 6, and 14) showed a low percentage of TNF α positive cells. Unlike the Nigericin plate, untreated monocytes from DD11, however not DD06, exhibited percentage of TNF α positive cells of 30%. LPS treated PBMCs from 16 out of 23 samples showed percentage of TNF α positive cells than the inflammasome fully activated (LPS + LeuLeuOMe treated) PBMCs of the same donor.

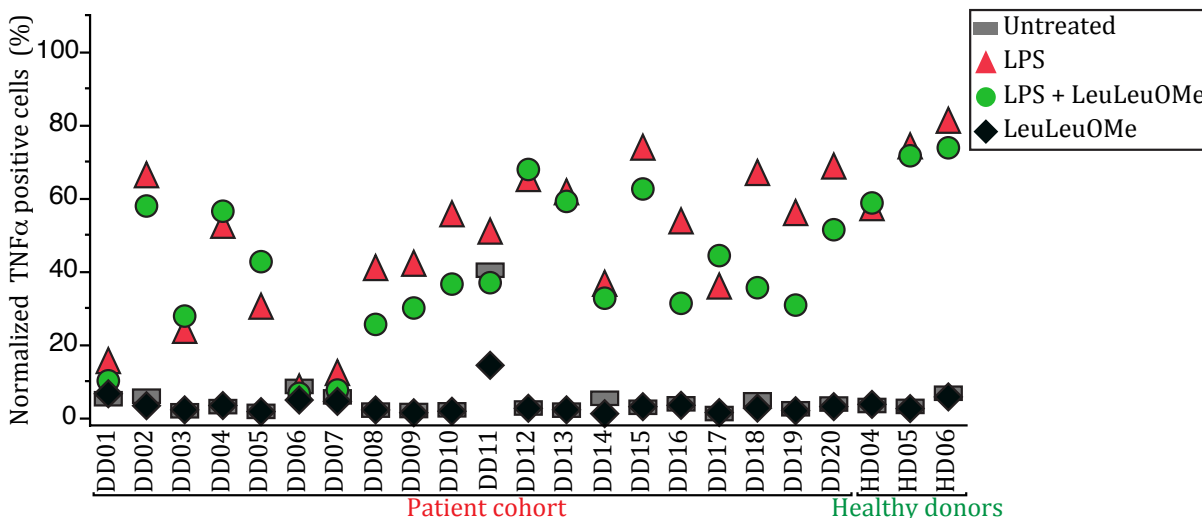


Figure 49: Assessment of intracellular TNF α production for all samples in the plates of LeuLeuOMe as an inflammasome activator

The same analysis in **Figure 48** was conducted for LeuLeuOMe plate. For most of the samples, the LPS only treated PBMCs showed higher intracellular TNF α production than the inflammasome fully activated (LPS + LeuLeuOMe treated) PBMCs. In contrast to the Nigericin plate, untreated PBMCs from DD11 exhibited low intracellular TNF α production. For patient samples: n= 8 for both untreated and LPS conditions, whereas n=12 for the other conditions; for healthy donor samples, n= 32 both untreated and LPS conditions, whereas n=48 for the other conditions. Data were normalized according to the monocyte percentage (see Materials and Methods).

The functional analysis of TNF α release (**Figure 50**) confirmed the results of the phenotypic analysis of intracellular TNF α production (**Figure 48** and **Figure 49**), meaning that LPS caused the activation of TLR4 and consequently the release of TNF α . Furthermore, the untreated PBMCs showed neither intracellular production nor release of TNF α and the same was for the activator only treated cells.

Again, patient donor samples showed the same three sub-groups that have been seen in the results of intracellular TNF α production; high, intermediate and low TNF α release. LPS treated monocytes from DD01, 3, 6, and 14 showed a low release of TNF α (0.5 pg/ml per monocyte), while samples from healthy volunteer group showed an average TNF α release of 1.5 pg/ml per monocyte. The remaining disease donor samples exhibited a range of TNF α release around 1.5 pg/ml per monocyte.

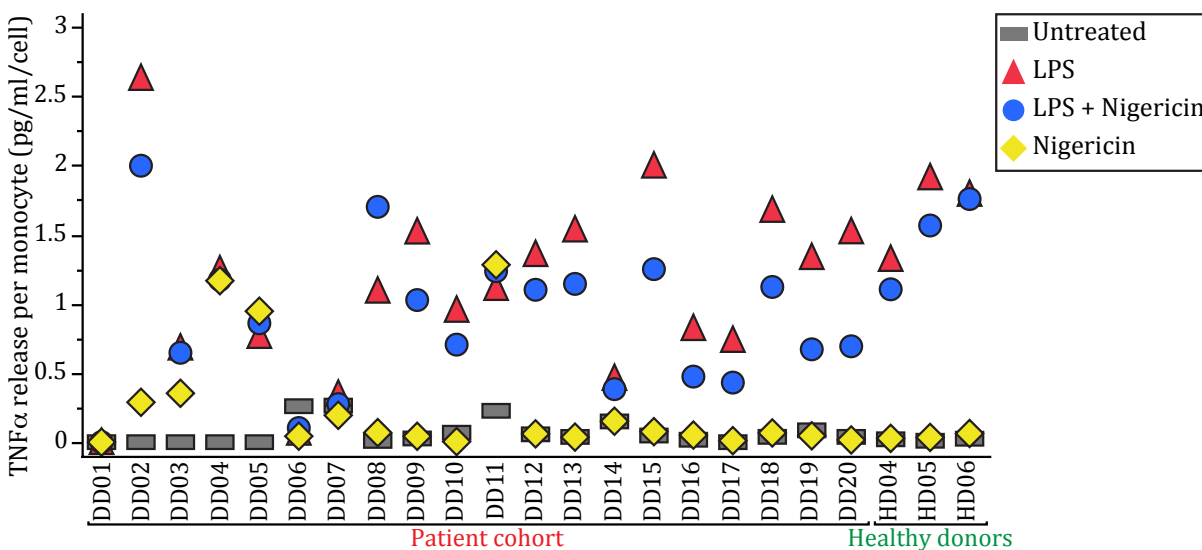


Figure 50: Assessment of TNF α release in response to Nigericin-mediated inflammasome activation normalized to the percentage of monocytes.

As it was shown in case of intracellular TNF α production (**Figure 48** and **Figure 49**), there was high diversity in the TRL activation status of the sample donors and the samples of healthy donors showed in general high release of TNF α . For patient samples: n= 8 for both untreated and LPS conditions, whereas n=12 for the other conditions; for healthy donor samples, n= 32 both untreated and LPS conditions, whereas n=48 for the other conditions. Data were normalized according to the monocyte percentage (see Materials and Methods).

The analysis of LeuLeuOMe plate (**Figure 51**) resulted in the same pattern of results that have seen in the results of Nigericin plate in **Figure 50**. LPS treated monocytes from DD01, 3,4, 5, 6, 7, and 11 showed a low average release of TNF α (0.5 pg/ml per monocyte), while the remaining of disease donor samples exhibited average TNF α release around 1.5 pg/ml per monocyte. As it has seen in the Nigericin plate, samples from healthy volunteer group showed an average TNF α release of 1.5 pg/ml per monocyte.

In conclusion, the results of TNF α release confirmed the phenotypic observation that was captured under image-based analysis, meaning that LPS can activate the TLR pathway in PBMCs.

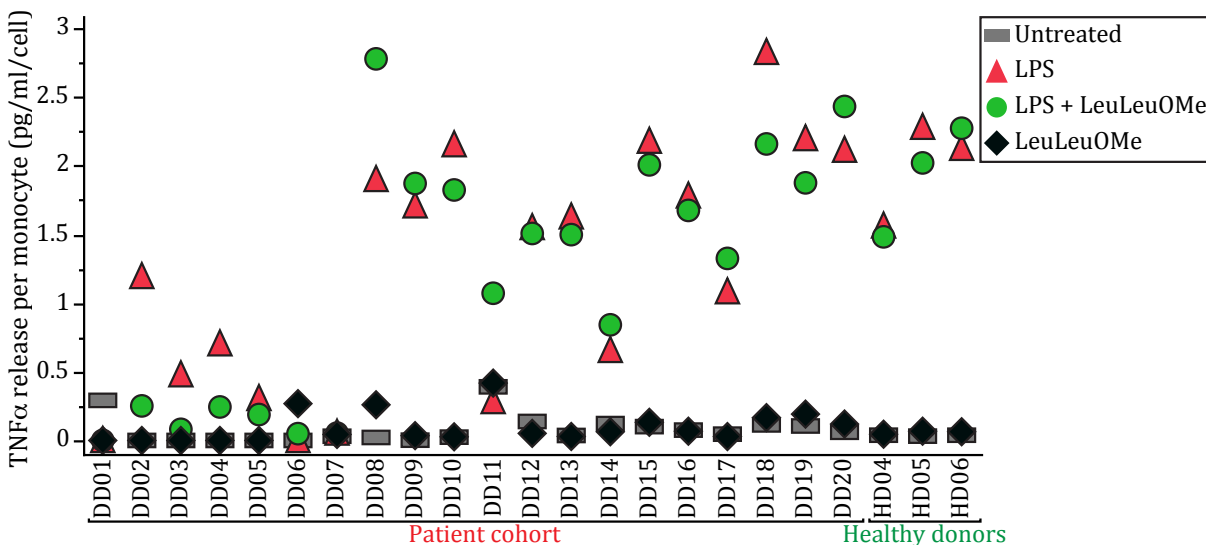


Figure 51: Assessment of TNF α release in response to LeuLeuOMe-mediated inflammasome activation normalized to the percentage of monocytes.

The same analysis in **Figure 51** was conducted using the assay plate of LeuLeuOMe mediated inflammasome activation. The first 6 patient samples showed a low release of TNF α while the rest of samples showed a heterogeneous trend. For patient samples: n= 8 for both untreated and LPS conditions, whereas n=12 for the other conditions; for healthy donor samples, n= 32 both untreated and LPS conditions, whereas n=48 for the other conditions. Data were normalized according to the monocyte percentage (see Materials and Methods).

The percentage of monocytes that mounted an inflammasome response was analyzed using Nigericin as an inflammasome activator (**Figure 52**). The LPS + Nigericin condition showed an inflammasome activation rate between 50-70% for all samples, except DD06, DD02 and HD06 that showed an activation rate of 17%, 110%, and 130%, respectively. Interestingly, inflammasome activation occurred in 30% of the untreated monocytes of the patient DD11 mounted (**Figure 52** grey rectangle) where no inflammasome activation was expected. However, a more detailed analysis is needed to confirm that TLR pathway and inflammasome machinery were already activated in the PBMCs of this patient donor. This univariate analysis showed that it is hard to correlate the inflammasome activation and disease status by using only a single variable.

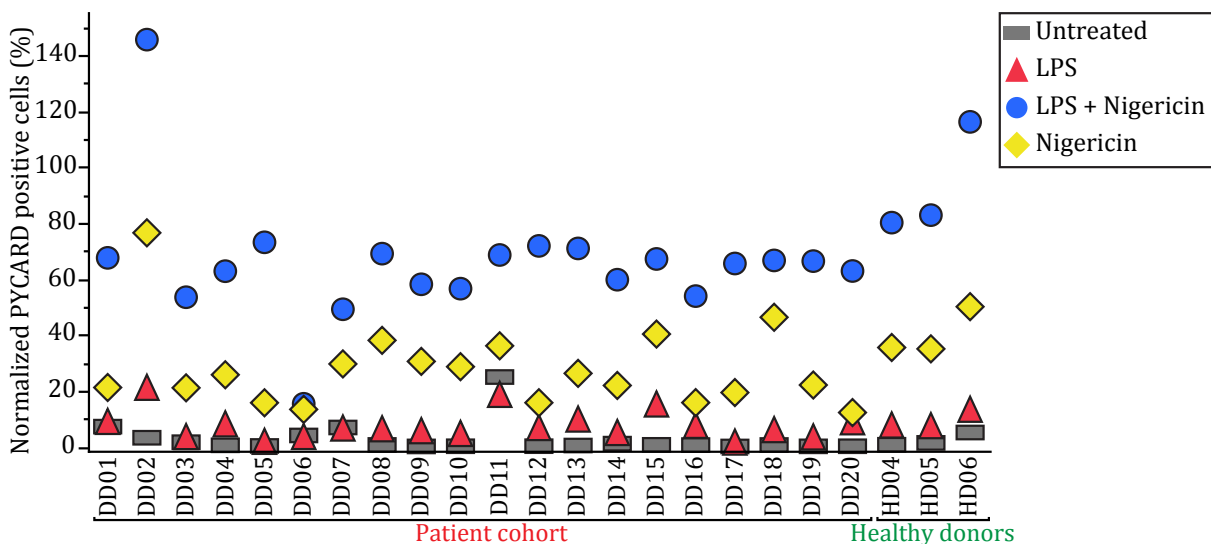


Figure 52: Assessment of the inflammasome activation rate in response to Nigericin-mediated inflammasome activation normalized to the percentage of monocytes

LPS + Nigericin condition (blue circle) showed the highest inflammasome activation rate for all samples compared to the other conditions. For the LPS + Nigericin condition, the majority of samples showed an inflammasome activation rate between 50-70%. Interestingly, inflammasome activation occurred in 30% of the untreated monocytes of the patient DD11 mounted (grey rectangle) where no inflammasome activation was expected. For patient samples: n= 8 for both untreated and LPS conditions, whereas n=12 for the other conditions; for healthy donor samples, n= 32 both untreated and LPS conditions, whereas n=48 for the other conditions. Data were normalized according to the monocyte percentage (see Materials and Methods).

During the analyzing of the samples from the healthy volunteer group (**Figure 35** and **Figure 36**), the LeuLeuOMe caused less inflammasome activation compared with Nigericin. For the patient donor samples, LeuLeuOMe caused less inflammasome activation (**Figure 53**) in comparison to Nigericin (**Figure 52**). Of note, inflammasome activation occurred in 60% of the untreated monocytes of DD11 in case of LeuLeuOMe, while it was about 50% in case of Nigericin plate (no activation was expected).

In summary, this analysis showed that sample subgrouping, using the inflammasome activation rate, does not help to discriminate the patient samples from the control samples. This was crystal clear in the case of LPS + Nigericin condition, in which most of the samples showed an activation rate close to 60%.

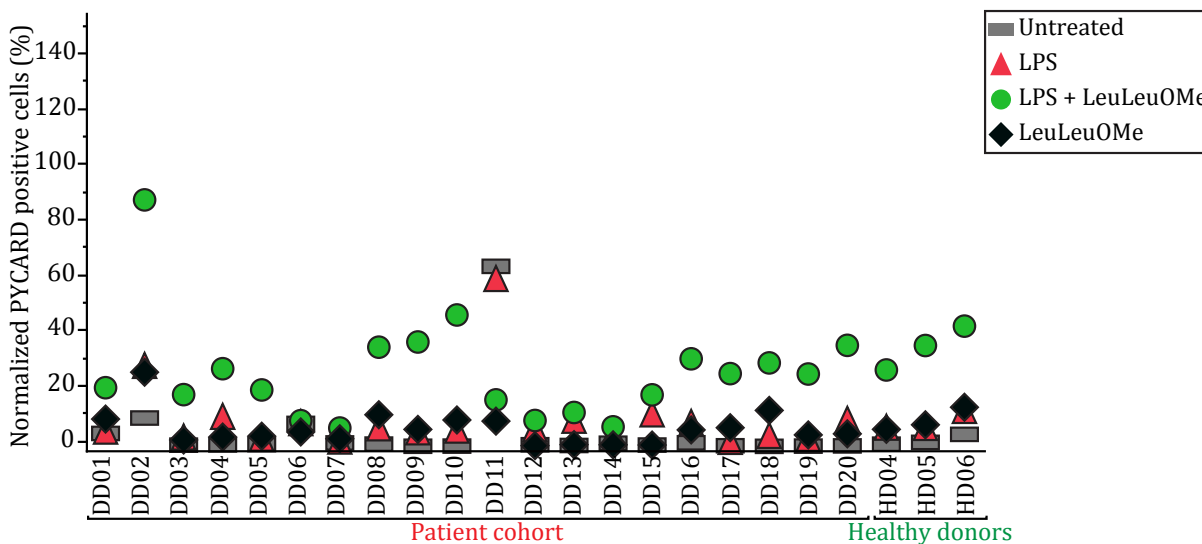


Figure 53: Assessment of the inflammasome activation rate for each donor in response to LeuLeuOME activation.

The same analysis in **Figure 52** was conducted for the plates where LeuLeuOME was used as an inflammasome activator. The LPS + LeuLeuOME treated cells for all samples resulted in less inflammasome activation compared to the LPS + Nigericin treated cells of a given sample (**Figure 52**). The untreated monocytes from DD11 depicted an inflammasome activation rate of 60% which was even more than the activation rate of the untreated cells of the same sample on the Nigericin plate. For patient samples: n= 8 for both untreated and LPS conditions, whereas n=12 for the other conditions; for healthy donor samples, n= 32 both untreated and LPS conditions, whereas n=48 for the other conditions. Data were normalized according to the monocyte percentage (see Materials and Methods).

The results, of inflammasome activation rate that have seen in **Figure 52**, were confirmed by the functional assay of IL-1 β release (**Figure 54**). Priming the cells with LPS and followed by Nigericin-mediated inflammasome activation were required to induce IL-1 β release. This is, in turn, confirmed the two-signal safety catch mechanism for inflammasome activation. Interestingly, treatment with Nigericin alone caused some inflammasome activation (**Figure 52**) however not IL-1 β release (**Figure 54**).

LPS + LeuLeuOME treated PBMCs showed a different pattern of inflammasome activation if compared to Nigericin plate. Some patient samples (DD01, 6, 7, and 11) exhibited extremely low release of the IL-1 β (**Figure 55**). Whereas other samples showed low IL-1 β release like DD03, 12, 13, 14, and 15.

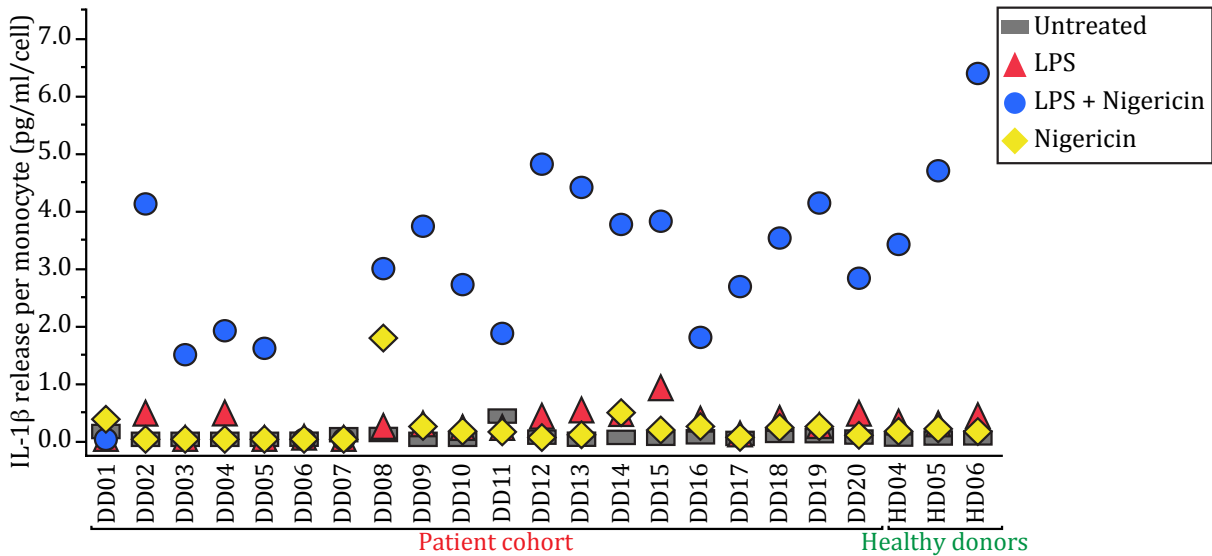


Figure 54: Assessment of IL-1 β release into the cell culture supernatant for each donor upon Nigericin activation

Only the conditions of fully activated PBMCs (LPS + Nigericin) showed high release of IL-1 β in all samples, except DD01, regardless of disease status. These results confirmed that inflammasome assembly is a prerequisite for active IL-1 β release as only LPS + Nigericin condition results in higher cytokine release for the majority of samples. For patient samples, n= 12 and n=48 for healthy donor samples. Data were normalized according to the monocyte percentages (see Materials and Methods).

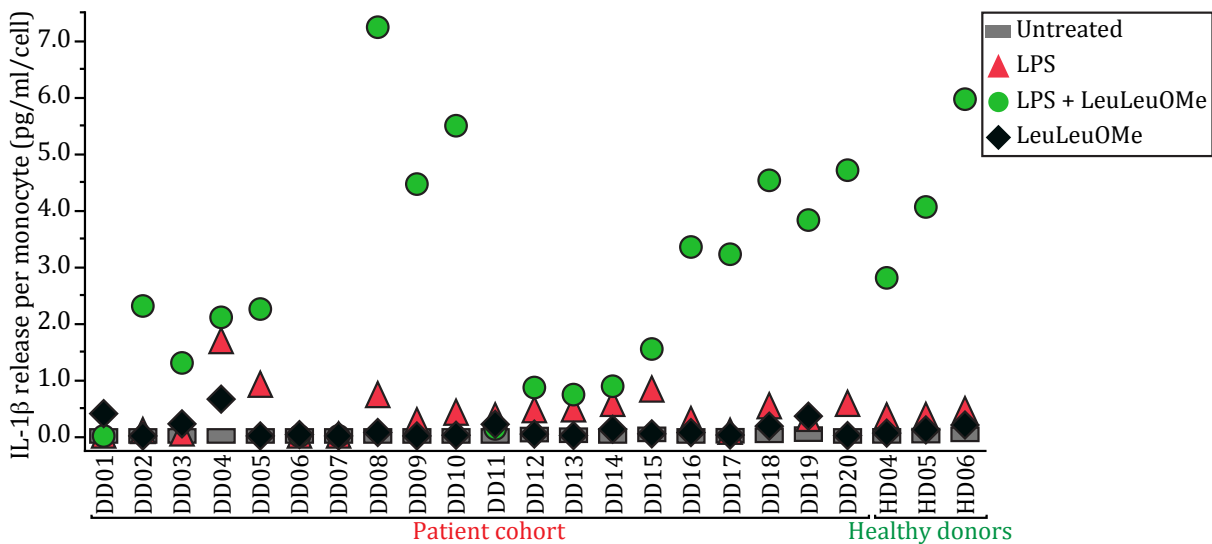


Figure 55: Assessment of IL-1 β release into the supernatant for each donor upon LeuLeuOMe activation

The same analysis in **Figure 54** was conducted using the data of the plate where LeuLeuOMe was used as an inflammasome activator. The conditions of fully activated PBMCs (LPS + LeuLeuOMe) showed a low release of IL-1 β for the samples DD01, 6, 7, and 11. DD08 exhibited higher IL-1 β release than the samples of healthy donors in case of the fully activated condition. For patient samples, n= 12 and n=48 for healthy donor samples. Data were normalized according to the monocyte percentages (see Materials and Methods).

4.3.2. Aggregated data according to the disease diagnosis

An analysis of aggregated data was conducted, trying to dissect the samples of AD patients from samples of depressive patients and the samples of healthy donor group. Samples were grouped according to the clinical diagnosis (**Table 5**). Consequently, the data of each group were aggregated to be compared with the other groups as follow; samples of AD patients (6 samples), depressive patients (5 samples), and healthy donors (3 samples).

For Nigericin plates, the group of healthy donors showed a significantly higher response from both groups of patient samples and for all of the four cell-based assay readouts, i.e. intracellular TNF α production, TNF α release, inflammasome activation rate, and IL-1 β release (**Figure 56 A, B, C, and D**). However, results showed no significant difference in the response of AD group from the group depression, for all of the four assay readouts.

For LeuLeuOMe plates, intracellular production of TNF α showed a significant difference between healthy groups and the patient groups, i.e. both the group of AD and the group of depressive patients (**Figure 56 A, B, C, and D**). However, the other assay readout showed no difference between the two groups of patients.

In conclusion, the analysis of the aggregated data, in case of Nigericin plates, showed that it is possible to discriminate the healthy from patient samples with this level of analysis. However, the dissection of the samples of AD from ones from depressed patients is not possible with such analysis and more sophisticated analysis is needed. This sophisticated analysis will be introduced in the section of multivariate analysis.

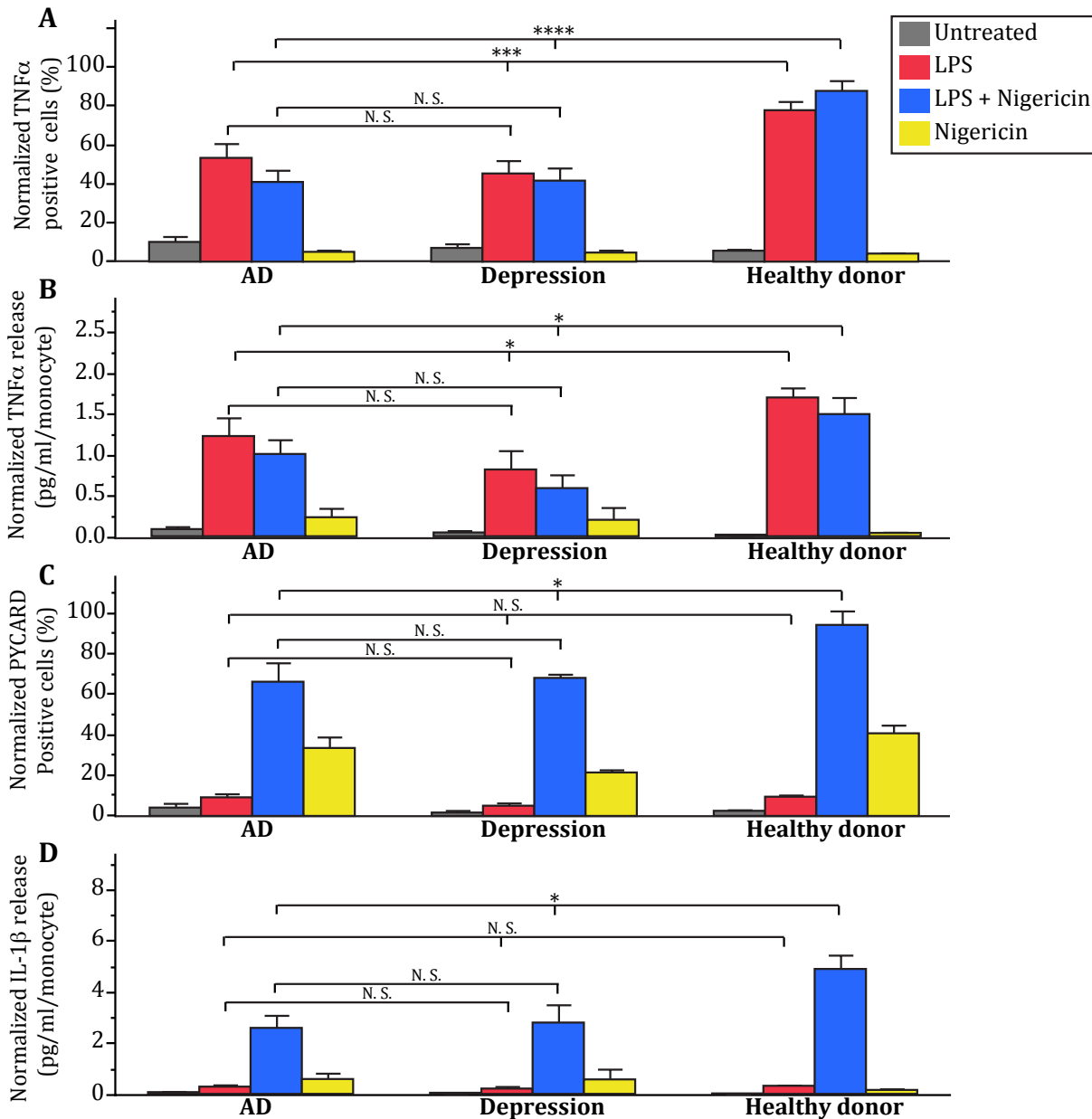


Figure 56: Data aggregation according to disease status (Nigericin plates)

(A) The percentage of TNF α positive cells showed no difference between the group of AD and the group of depressed patients, while the group of healthy donors responded differently from both AD and depression groups. (B) TNF α release (pg/ml/monocyte) into the supernatant was not significantly different between depression and AD groups, however those two groups responded differently from the samples of healthy donor group (C) Inflammasome activation rate was statistically similar between the group of AD and the group of depressed patients, however those two groups responded differently from the group of healthy donors. (D) IL-1 β release (pg/ml/monocyte) into supernatant. The results showed no difference between the group of AD and the group of depressed patients. However, the two groups of patient samples responded differently from the group of healthy donors. Error bars represent the standard error of the mean (SEM). Test of significance t-Test; N.S. (non-significant) $P > 0.05$, * $P \leq 0.05$, *** $P < 0.001$, **** $P < 0.0001$. For samples of AD patients, $n = 11$; $n = 6$ for samples of depressed patients, and $n = 3$ for samples of healthy donors. Data were normalized according to monocyte percentage (see Methods). Samples were grouped according to the clinical diagnosis in **Table 5**.

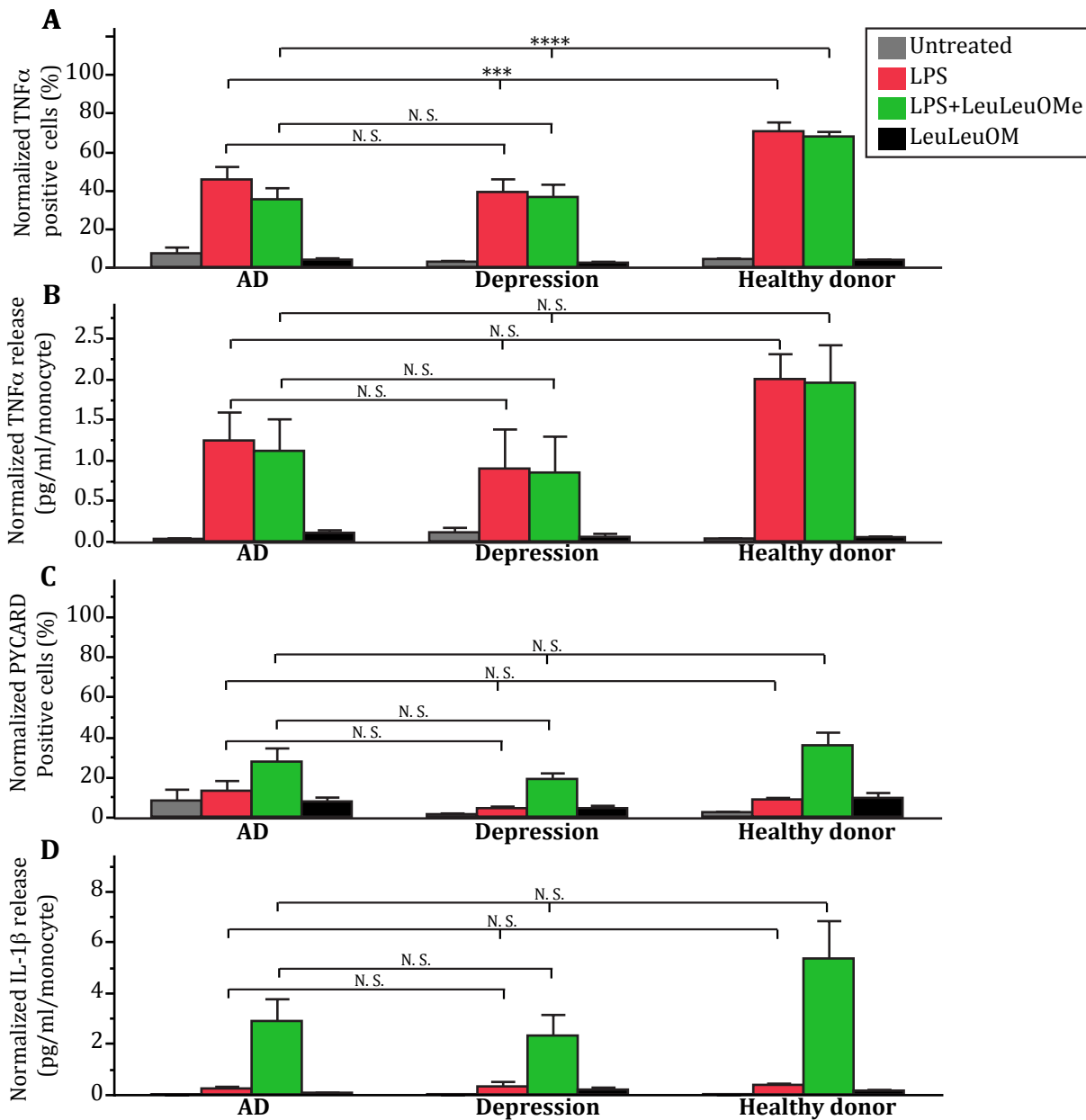


Figure 57: Data aggregation according to disease status (LeuLeuOMe plates)

The same analysis in

Figure 56 was conducted using the data of LeuLeuOMe plates. **(A)** The percentage TNF α positive cells. There was no difference between the group of AD and the group of depressed patients, while samples of the healthy donors responded differently from both AD and depressed patients. **(B)** TNF α release (pg/ml/monocyte) into supernatant. There was no difference in the release of TNF α among the groups of healthy, depression, and AD donors. **(C)** Inflammasome activated rate. The results were statistically the same among the three groups of samples. **(D)** IL-1 β release (pg/ml/monocyte) into supernatant. Also, there was no difference in the release of IL-1 β among the three groups of healthy, depression, and AD donors. Error bars represent the standard error of the mean (SEM). Test of significance t-Test; N.S. (non-significant) $P > 0.05$, * $P \leq 0.05$, *** $P < 0.001$, **** $P < 0.0001$. For samples of AD patients, $n = 11$; $n = 6$ for samples of depressed patients, and $n = 3$ for samples of healthy donors. Data were normalized according to monocyte percentage (see Materials and Methods). Samples were grouped according to the clinical diagnosis in **Table 5**.

4.3.3. Transcriptome analysis can dissect the healthy versus disease samples

To study the transcriptional status in the patient samples, a transcriptome analysis was conducted to assess the gene expression profile of both patient and samples of healthy donors. RNA-seq was used because it enables the study of transcriptome at high resolution. RNA-seq is advantageous over the classical microarrays for many reasons, particularly the possibility to reanalyze the output data with no need to repeat the laboratory experiment (Hoeijmakers, Bártfai et al. 2013). Smart-seq2 was utilized for the generation of full transcript sequencing libraries using standard reagents and procedures as described by (Picelli, Faridani et al. 2014). Samples were pooled and clustered at 1.4pM on a NextSeq500 system (Illumina) to generate ~10M single-end reads per sample using High Output v2 chemistry. Sequencing data was demultiplexed using bcl2fastq2 v2.20 and pseudo aligned to Homo_sapiens.GRCh38.rel79.cdna.all.fa.gz transcriptome using kallisto v.0.44.0.

The status of gene expression was analyzed for healthy versus disease up- and down-regulated genes (**Figure 58**). The samples of healthy donors were clustered together and for both up- and down-regulated genes. However, the Samples of AD patients scattered within the samples of depressed patients, i.e. it was not possible to differentiate the AD from depressed patients. A more sophisticated and in-depth analysis of the RNA-seq data might dissect the samples of AD patients from the ones of depressed patients. For example, the rare variants could be investigated in the current dataset as many previous studies investigated them as potential AD biomarker (Humphries and Kohli 2014, Cacace, Van den Bossche et al. 2015).

To study the biological processes that are associated with gene expression changes, Gene Ontology (GO) enrichment analyses of gene expression was conducted (**Figure 59**). Some immune linked pathways emerged as up- and down-regulated within the patient samples. This included pathways like cellular-defense response, leukocyte homeostasis, response to LPS, ...etc. This is consistent with the literature reporting that immune changes occur in the peripheral blood during the AD disease (Wyss-Coray 2006), (Labzin, Heneka et al. 2018, Sharman, Gyengesi et al. 2019).

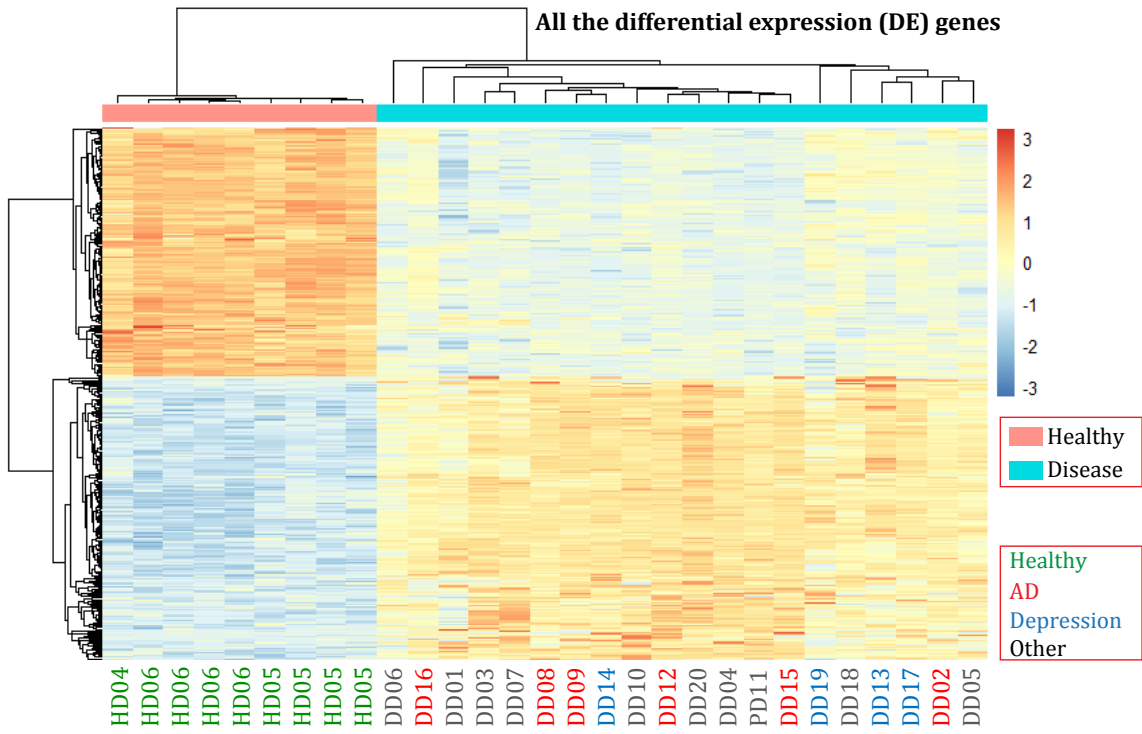


Figure 58: The status of gene expression in samples healthy versus diseased donors
 Transcriptome analysis was conducted for the differential expression levels of all samples of healthy and patient donors. The hierarchical clustering showed that the samples of healthy donors were successfully dissected from the patient samples. However, the sub-clustering of the patient samples was not able to differentiate between the samples of depressed AD patients. The clinical healthy expression profile was used as a baseline for the up- versus down-regulation of gene expression.

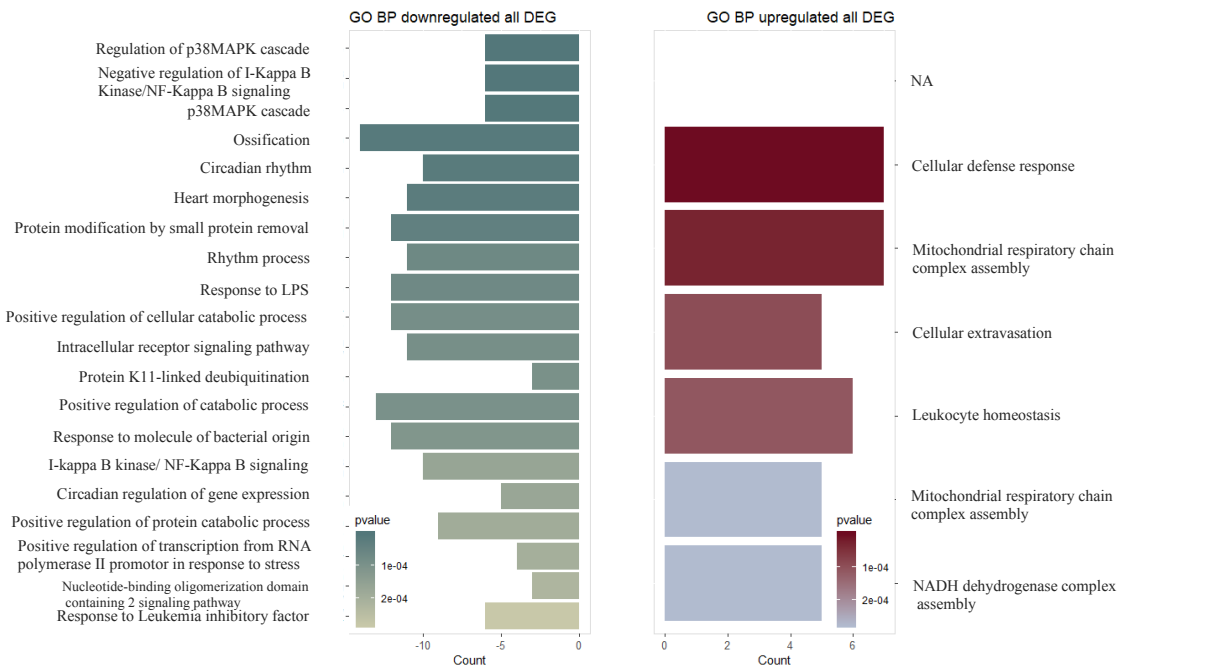


Figure 59: Immune linked up- and down-regulated pathways in the patient samples.
 Some immune linked pathways have emerged to be associated with the up- and down -regulated genes in the patient samples. This includes pathways like cellular defense response, leukocyte homeostasis, and response to LPS.

4.3.4. The Multi-parametric analysis

The aim of the univariate analysis was to analyze different sets of samples with one variable (readout) using statistical methods like t-test or ANOVA test. In general, the first choice is preferred because of the ease of interpretation (Saccenti, Hoefsloot et al. 2014). On the other hand, the multivariate analysis represents a set of techniques used to efficiently extract useful information from high-dimensional dataset of the multi-parametric assays (Collinet, Stöter et al. 2010). The main advantage of a multivariate (multi-parametric) analysis over the univariate analysis is that it analyzes all variables simultaneously and considers the simultaneous relationship among variables. Multivariate analysis facilitates the studying of the responses or interactions between different cellular activities to a specific treatment or stimuli under similar experimental conditions (Cromwell, Hoxha et al. 2018). More importantly, the univariate analysis, e.g. t-test, could bring a non-significant difference between a set of samples, while multivariate analysis can analyze in-depth the association between different assay variables demonstrating noteworthy differences between these samples (Saccenti, Hoefsloot et al. 2014). Therefore, a cluster analysis, a type of multivariate analysis, was conducted to assign samples into smaller subgroups that are mutually exclusive based on patterns or trends in the dataset.

The first was to collect 71 features (variables) from both the clinical annotation of the patients and the multi-parametric PBMCs *ex vivo* assay (see the table of features in **Index II**). The table of features was established from the cell-based assay readouts (64 features) and the clinical information of the patients (seven features). Each row within the table represented a sample ID together with a vector of 71 features.

The feature vectors were analyzed with the support vector machine (SVM) algorithm. SVM is a supervised machine learning to achieve classification or regression tasks, mostly used as a classifier. The algorithm works by plotting every feature data as a point in n-dimensional space (n= number of features) with the value of each feature being the value of a particular coordinate. The classification is then done by finding the best possible hyper-plane that differentiates the given class (Ray 2017).

The reason behind the utilization of the SVM was because it is an effective algorithm in cases where the number of dimensions (variables) is greater than the number of samples.

This is the case in this data set which encompasses a sample size of 23 and a total number of 71 features (scikit-learn 2018). Dealing with many features of small numbers of subjects could cause the so-called “curse of dimensionality” that results from high dimensional data. For instance, a high number of dimensions (features) with low sample size could result in an overfitting issue (i.e. the classifier fits the low number of observations very closely). Furthermore, the SVM algorithm conducts a feature selection analysis to reduce the number of variables, avoiding overfitting (scikit-learn 2018). This analysis could be beneficial in characterizing the features that are important to identify a disease status as shown later.

The classifier output presented a disease prediction of the sample donor. The prediction accuracy of the SVM algorithm was 91% of the total cases. The correctly predicted samples were 21, out of 23 samples, according to the clinical annotation provided with the samples. The confusion matrix analysis revealed a high accuracy and the precision of the classifier. The accuracy is the ratio of the correctly predicted samples to the whole pool of patient and samples of healthy donors. It addresses the following question: How many samples did the classifier correctly label out of all the samples, whereas the precision is the ratio of the actual class of the samples by the predicted samples of the given class. It answers the following question: How many, of the predicted samples, is considered as a true prediction (Ghoneim 2019).

The overall prediction accuracy was 91% and the precision was 100% for Samples of AD patients as well as for the samples of healthy donors. Whereas the precision for the samples derived from depressive patients was 80%. Interestingly, DD05 was misclassified as a sample of a depressive patient and the actual class was “other” (**Figure 60 A**). However, checking the record of that sample showed that the patient had signs of clinical depression, however, did not meet the full criteria of depression that was used for the other four depressive patients and therefore it was assigned by the medical doctor as “other”. Therefore, it might be that DD05 had some depression associated immune changes that were captured by the classifier, i.e. the classifier had a biological-based decision.

As described before, the SVM algorithm conducted a feature selection analysis to identify features that provided a high weight in distinguishing a group of samples from another

group. A heatmap was created to show the most representative features for the dissection of each group of samples (**Figure 61**). This heatmap showed that some features were important for the classifier. For instance, the feature (F#07) was important to dissect the samples of healthy donors from the rest of the samples and the feature (F#02) was strongly relevant for Samples of AD patients. The biological pathways behind these features could be further investigated for more insight information.

A Sample prediction

Dono ID	Disease	prediction
DD02	AD	AD
DD08	AD	AD
DD09	AD	AD
DD12	AD	AD
DD15	AD	AD
DD16	AD	AD
DD01	Depression	Depression
DD13	Depression	Depression
DD14	Depression	Depression
DD17	Depression	Depression
DD19	Depression	Other
HD04.2	Healthy donor	Healthy donor
HD05.2	Healthy donor	Healthy donor
HD06.2	Healthy donor	Healthy donor
DD03	Other	Other
DD04	Other	Other
DD05	Other	Depression
DD06	Other	Other
DD07	Other	Other
DD10	Other	Other
DD11	Other	Other
DD18	Other	Other
DD20	Other	Other

B Confusion matrix analysis

		prediction			
		AD	Depression	Healthy	Other
Actual class	AD	6	0	0	0
	Depression	0	4	0	1
	Healthy	0	0	3	0
	Other	0	1	0	8
Precision		100%	80%	100%	89%
Overall accuracy		91%			

Figure 60: Sample prediction accuracy: Confusion matrix analysis

A. prediction for all samples. **B.** confusing matrix analysis. The results revealed a high prediction accuracy as 21 Out of 23 (20 patients + 3 samples of healthy donors) observations were predicted accurately (accuracy = 90%). The precision of the prediction was 100% in case of the six Samples of AD patients as all of them were predicted precisely as AD. However, the precision for samples of depressed patients was 80%.

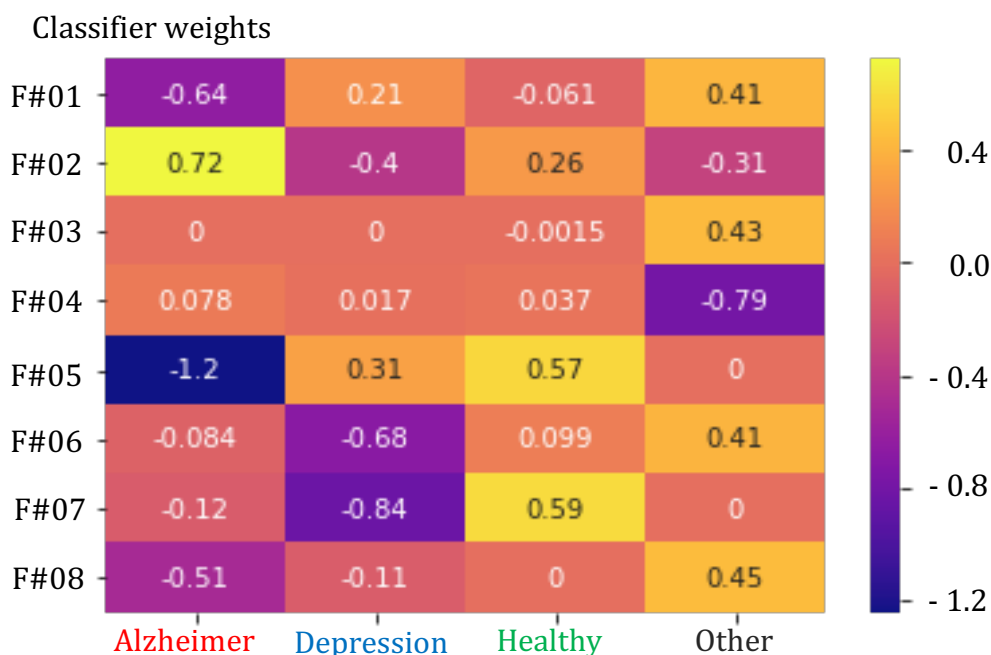


Figure 61: Heatmap of the most representative features for disease prediction

This heatmap showed that some features were important for the classifier. For instance, feature 7 (F#07) was important to dissect the samples of healthy donors from the rest of the samples. While feature 2 (F#02) was strongly important for Samples of AD patients. Features were coded for confidentiality purposes.

In conclusion, the results of the cluster analysis (**Figure 60** and **Figure 61**) revealed a high prediction accuracy and gave an indication about the features that were most associated with AD prediction (features are not shown for confidentiality purposes). These features might be studied for more in-depth investigation and therapeutic development.

As previously mentioned, the number of samples utilized for this study was low (20 sample plus three samples of healthy donors). For more conclusive analyses, bigger sample size is needed. Nevertheless, the results were considered as a proof of concept for the developed approach, where the multi-parametric assay was flanked by the multivariate machine learning analysis to predict the disease status of the sample donors.

5. Discussion

5.1. State of the art of AD biomarkers

Neuroimaging techniques, e.g. PET and MRI, are currently quite established to identify the pathological changes occurring during AD (Snyder, Carrillo et al. 2014). Nevertheless, the expensiveness is the main drawback of these techniques. CSF biomarker analyses, on the other hand, are also quite established for AD diagnostics, but they are invasive (Anoop, Singh et al. 2010). Blood diagnosis would be of great advantage because it is easily accessible and blood tests are often less expensive and therefore convenient for daily routine. Furthermore, there is a big hope that the peripheral blood changes can be captured at the early stages of AD pathology (Kenny, Jimenez-Mateos et al. 2018). This is because of the increasing reports that AD pathology starts at the CNS level, many years before the appearance of cognitive signs and these changes were reflected in the periphery (Kenny, Jimenez-Mateos et al. 2018). For instance, the deposition of A β has been reported to start years if not decades prior to cognitive decline, as shown by published data from human longitudinal PET analyses of A β deposition (Jack, Knopman et al. 2013). Considering that A β can act as a strong DAMP, it appears likely that the pathological progress from the early accumulation of A β to later hallmarks of disease progression, e.g. tau phosphorylation and hippocampus atrophy, is influenced and might be driven by, innate immune responses (Heneka 2017). If the pathological progress is influenced or driven by immune response, then one has to consider that the immune changes could be captured a while before the appearance of AD cognitive signs.

An early detection of AD is also important for therapeutic development because the current therapeutic interventions are unable to cure the irreversible structural changes happening in the brain at late stages of the disease (Ghezzi, Scarpini et al. 2013, Bagnoli, Piaceri et al. 2014, Marcus, Mena et al. 2014, Kenny, Jimenez-Mateos et al. 2018).

Despite the huge efforts in the field of AD blood biomarker development, there is currently no reliable approved blood detection of AD (Preisiche, Schultz et al. 2019). The lack of AD blood biomarkers hindered also therapeutic development as there was only a low number of AD patients accepting CSF sample donation. Additionally, the high cost of brain imaging restricts the possibility to conduct brain image-based studies (Hampel, O'Bryant et al. 2018). A major obstacle approaching a reliable AD blood-based detection was that the

developed approaches lack reproducibility and selectivity (O'Bryant, Mielke et al. 2017). The imprecise identification of the disease stage of the studied subjects was one of the reasons causing the lack of reproducibility and selectivity (Lin, Huang et al. 2019). Another challenge in the field of AD biomarker development is the phenotypic variability within AD patient populations. This variability stems from patient's genetic and immune variation as well as elderly comorbidities (Hampel, Toschi et al. 2018). The heterogeneity of the immune system causes a high variability even among healthy individuals. Brodin and colleagues have conducted a systems-level analysis of 210 healthy twins between 8 and 82 years of age. The study pointed out an extensive heterogeneity in immune-based parameters among healthy individuals (Brodin, Jojic et al. 2015). For AD patients, the inter-individual variation is also the result of multiple factors contributing to the complex disease pathology. Hence, one of the main reasons for failing to introduce a reliable AD marker might be because the majority of the blood-based biomarker development attempts have been based on a single marker/target. Thus, to develop a reliable and robust blood-based detection of AD, this work focused on the development of a multiplexed functional assay with a multivariate data collection from different sources. The assay enables generating a complexed signature of features obtained by transcriptome analysis, functional assay data, cytokine release, proteomic analysis, and clinical data. The feature signature of each donor (immune phenotype) was analyzed by a machine-learning algorithm to detect the significant differences among the whole set of features for both AD patients and control donors.

The current study focused mainly on the human immune system which is considerably variable between individuals, but relatively stable, over time, for every single individual (Brodin and Davis 2017). We developed a high-throughput assay enabling the simultaneous measurement of cell-types, TLR4 activation, inflammasome activation, cytokine release and RNA expression level from the same blood sample. Such diverse readouts offer an opportunity to analyze the variation of the human immune system at a system's scale.

The PYCARD speck formation assay is developing towards a standard measure of inflammasome activity in different models of inflammation and it is currently a standard readout for evaluating the NLRP3 inflammasome inhibition by a wide range of drugs, e.g.

non-steroidal anti-inflammatories (Heneka 2017). We used the readouts of the inflammasome speck formation assay, e.g. number of activated cells and the total number of cells, as variables in the multivariate analysis.

5.2. The human PBMC *ex vivo* assay as a proxy for the immune response during AD

The human PBMC *ex vivo* assay can serve as a proxy for the *in vivo* response of the immune system since PBMCs include essential components of the immune system like B cells, T cells and monocytes. The PBMC *ex vivo* analysis provided different information about the immune system. For instance, as it was seen during this study, that the TLR pathway and the inflammasome machinery can be studied via the monitoring of monocytes.

PBMCs are widely used nowadays in research studies as a human-derived cell model (Kutscher, Dembek et al. 2013, Ma, Zhang et al. 2015, Huang, Dai et al. 2018). Additionally, PBMCs were increasingly used for AD researches (Hugon, Mouton-Liger et al. 2018, Vérité, Page et al. 2018). Saresella and colleagues used PBMC-derived monocytes to show that NLRP3 and caspase-1 are upregulated in patients with severe AD (Saresella, La Rosa et al. 2016). Another study showed that PBMCs from AD patients had a lower B cell percentage and a reduced absolute number in comparison to age-matched controls (Pellicano, Bulati et al. 2010).

5.3. A novel assay design to study the immune system

In the current study, we developed an automated assay workflow to reduce the experimental error, decrease the required reagents and to improve the assay repeatability. In this assay, an essential pathway of the innate immune system was studied via different aspects like TLR activation, inflammasome speck formation/activation, cytokine release, RNA expression level as well as the cellular composition. The novelty of the assay derived from the usage of peripheral blood cells as a cell model under several experimental conditions, including the triggering of the TLR pathway and the inflammasome machinery or both of them in comparison to the naïve, untreated cells as a control condition. This assay design provided the opportunity to capture the normal control phenotypes as well as any deviation from them, indicating a pathological

condition. For instance, treating PBMCs with LPS is expected to induce intracellular TNF α expression. However, presence of intracellular TNF α expression in untreated PBMCs could indicate a pathological alteration of the innate immune system, such as TLR4 pathway activation.

The previous published system-level analyses of the immune systems were usually conducted under the steady-state conditions (Brodin and Davis 2017, Kaczorowski, Shekhar et al. 2017, Tanamati, Stafuzza et al. 2019). The current assay setup can evaluate the immune system in the steady-state and it enables the exploration of potential diverse immune responses observed under different experimental conditions

As a routine readout, IL-1 β release was used as an endpoint indicator of inflammasome activation (Kesavardhana and Kanneganti 2017, Latz and Duewell 2018, Shao, Cao et al. 2018). Furthermore, inflammasome activation was monitored in this project, at different entry points. First, the successful priming was monitored via intracellular TNF α expression, induced by LPS via TLR pathway activation. Second, the assembly of the inflammasome multi-protein complex was monitored via the formation of the inflammasome speck by immunocytochemistry analyses of the adapter protein PYCARD. Finally, IL-1 β release was measured as a consequence of inflammasome activation. Finally, we monitored the morphological changes following the inflammasome, starting with chromatin condensation to rapture of the nuclei (Man and Kanneganti 2015, Broz and Dixit 2016). This comprehensive assay design enables the collection of detailed information about the immune system in to develop an exhaustive immune profile of the PBMC sample.

5.4. Maximizing the use of patient materials via a simultaneous assay workflow

The available number of PBMCs from each patient was very limited (mostly a single vial of 1×10^7 cells). Therefore, there was a need for a simultaneous assay workflow that maximizes the use of the available biomaterials. Thus, every single sample was processed towards the inflammasome activation assay, cytokine release assay, cellular composition analyses, proteomic analyses and RNA expression profiling in a parallel setup (**Figure 15** And **Figure 17**). A 384-well plate format was used to reduce material consumption and to process multiple samples per single experiment (Jones, Michael et al. 2004). The HTRF cytokine assay was used to reduce the amount of supernatant needed to conduct the

cytokine assay (Cisbio 2017). Furthermore, automated cell culturing and reagent pipetting was applied to follow a consistent handling routine, which cannot be accomplished manually. Additionally, automation enabled scale-up the assay substantially, giving the possibility to test more samples under several experimental conditions on one single experiment (Ibold, Frauenschuh et al. 2007). The assay automation enabled to considerably reduce inter and intra-assay variability. This was seen during the validation of the assay (**Figure 30**).

5.5. Characterization of the PBMC sample cellular composition

5.5.1. Characterization of PBMC cellular composition

PBMCs represent a heterotypic cell model. B cells account for 3.5-9 %, monocytes for 10-20%, while T cells represent the most abundant cell type in the PBMC population with around 50-80% (Akdis, Palomares et al. 2012, Tan and Gery 2012, Kleiveland 2015). Nevertheless, the percentage of these cell types frequently varies extensively in the blood of different healthy individuals (Brodin, Jojic et al. 2015). This immune inter-individual variation should be appreciated in the patient cohort studies (Brodin and Davis 2017). Understanding this variability provides insight information about PBMC behavior (Maes, Landuyt et al. 2013). Thus, the immune variation of healthy adults was of high consideration in the current study. As expected, our cellular composition analysis of a panel of healthy donor samples revealed a considerable inter-individual variation (**Figure 43**).

To characterize the cellular composition of the PBMC samples, a supervised machine learning approach was established using the U-Net network. The conventional software-based image analysis was not persuasive to process the images of the cell surface marker staining. This was due to many reasons such as the fact that CD markers are not 100% cell-type specific. For example, CD3 is widely accepted as a T cell marker. However, it is expressed to a small extent on the B cell membrane (Nagel, Mobs et al. 2014). Furthermore, the CD marker expression on the cell membrane was donor-dependent and was affected by the functional status of a given cell. An increase of the cell surface marker expression on the cell membrane caused a high signal intensity under the microscope and vice versa, making the settings for a signal threshold very challenging. Last but not least,

LPS has been reported to alter the expression of CD14 (a monocyte marker). (Landmann, Knopf et al. 1996) has reported that LPS reduces the expression of CD14 in the first 6 h of incubation before the expression is continually increased by prolonging the incubation time. Thus, CD14 expression was expected to be reduced within our PBMC assay window of 2 h LPS incubation. This means that the experimental treatment conditions affected the signal intensity of CD14.

Due to these facts, a more sophisticated image analysis approach was needed to ensure a robust cellular composition analysis which was able to handle these mentioned challenges. Recently, machine learning (ML) and artificial intelligence (AI) algorithms have been used to analyze complex bioimages (e.g. histological section, MRI images, bright field etc.) that are not possible to be analyzed with the classical methods. In principle, ML refers to a set of automatic pattern-recognition computational tools that are currently used in a wide domain of applications including image analysis (Kan 2017). The most sophisticated ML methodology used widely in the bioimaging field is a type of artificial intelligence known as a convolutional neural network (Kensert, Harrison et al. 2019). In principle, neural networks are compelling and scalable deep learning tools that are able to conduct complex Machine Learning tasks, e.g. classifying billions of images. One common example of neural network is the convolutional neuronal network (CNN), a multilayer neuronal network that uses convolutional layers to process very large and complex images. Deep convolutional networks are persuasive CNNs image recognition models that are currently the state-of-the-art model for bioimages processing while they can serve as highly sophisticated classifiers that can process an enormous number of high-resolution images, achieving very complicated computational tasks (Alex Krizhevsky 2012, Ronneberger, Fischer et al. 2015). Nevertheless, the main drawback of these networks is the need for thousands of training images in order to achieve the learning phase (Olaf Ronneberger 2015). In contrast, the U-Net network is a training strategy where the network needs a lower number of images (often 20 images) to conduct the training (Olaf Ronneberger 2015). U-Net is currently the state-of-the-art deep learning-based method for segmenting images using convolutional layers integrated with skip connections. It consists of down sampling, bridge and up sampling blocks and it has the advantage of the ability to be appropriately trained using an extremely low amount of data

compared to other training networks, e.g. Neural Network (Kolařík, Burget et al. 2019). We performed a supervised classification of pixels into image regions using U-Net neural network. The network was trained using example images of the cell type markers of monocyte, T and B cells. These images were labeled with examples of each of the mentioned cell types. The network was trained to classify the object into a cell type depending not on the cell type marker staining as well as the nuclei morphology. The images generated from the CD staining were used to detect cell-type-specific marker intensities and to analyze the nucleus neighborhood. This method was validated with a complex data set of three healthy donors tested in a 4-day repetition experiment with 2 plates per day and two assay conditions (**Figure 43** and **Figure 44**). This data set ensured a valid evaluation of the analysis workflow. The analysis nicely revealed a very consistent quantification of the number of cells for each class per PBMC donor over different repetitions and plates. The analysis also revealed a considerable inter-individual variation as it was expected. Furthermore, the quantification of monocytes revealed a slight decrease in the number of cells in the case of the LPS condition compared to untreated PBMCs. As pointed out earlier, this could be explained by the fact that LPS causes a decrease in CD14 expression within the assay timeframe (Landmann, Knopf et al. 1996).

5.5.2. **Novel microscopical proof that monocytes mount an inflammasome response**

In light of the inter-individual variation of the cellular composition of human PBMCs, there was the need to identify and quantify the cell type within the PBMC population that is mounting the inflammasome response. Many previous studies have provided first evidence that supported the suggestion that monocytes mount the inflammasome activation (Netea, Nold-Petry et al. 2009, Shin, Kang et al. 2012, Ahmad, Mishra et al. 2017, Varghese, Patel et al. 2019). For instance, Ahmad and colleagues have shown via a flow cytometry approach that the PYCARD speck formation was seen within stimulated monocytes. They showed also that speck positive monocytes release IL-1 β and PYCARD scaffolds into the extracellular space coincidentally with pyroptotic cell death (Ahmad, Mishra et al 2017). In the presented study, we introduced a novel microscopical proof that monocytes mount the inflammasome activation within our assay. T and B cells did not show inflammasome activation under live Nigericin stimulation. Interestingly, the live

tracking of the inflammasome assembly (**Figure 40**) showed that the cells undergo first a chromatin condensation by forming round nuclei followed by a rapid expansion of the nucleic area resulting in a leftover of an “activated monocyte” morphology. Chromatin condensation, cytoplasmic swelling and finally, osmotic lysis of the cell represent the typical morphological changes of the pyroptotic cell death (Miao, Rajan et al. 2011).

After cell lysis and as a consequence of an inflammasome response, CD14 signal shedding was noticed due to the disruption of cell membrane integrity by the effect of pyroptosis (**Figure 40 A**). Shedding of the CD14 signal represents a technical limitation during the endpoint assay, i.e. after the cells have been stimulated and eventually fixed with PFA, it was not possible, at this point, to quantify the monocyte numbers due to the loss of the CD14 signal during inflammasome activation. Thus, during the course of this project, the monocyte number was quantified only for untreated and LPS only treated cells where no inflammasome activation was expected. The number of monocytes in the untreated PBMCs of a given sample was used to estimate the monocyte number in the PBMCs of the other conditions for that sample. All the assay readouts were normalized to the monocyte number during this study. We believe that normalizing to the monocyte number was more informative rather than using the total cell number since the calculation of the inflammasome activation by dividing the Inflammasome speck-positive cells by the total number of cells was not considering the fact that the monocyte number varies sample-wise.

5.6. Screening of a patient cohort with the established PBMC assay

After it was established and implemented into the automation platform at the DZNE, the multi-parametric PBMC assay was used to analyze a cohort of 20 patients including 9 females and 11 males. The cohort was composed of 6 AD patients and five patients with depression and 9 samples of other diseases (see **Index I**). There were many reasons to select samples from depressive patients. First, the NLRP3 Inflammasome was reported to play a role in metabolic danger signals or stress exposure in the major depressive disorder (Kaufmann, Costa et al. 2017). Second, Li et al pointed out that inhibition of the NLRP3 inflammasome might be a therapeutic target for the treatment of depression (Li, Liu et al. 2019). This means that selecting samples from depressed patients for this analysis gave the opportunity to evaluate the assay selectivity for the AD patients as well as to

investigate the inflammasome activation status of depressed patients. Third and most important, the samples from depressed patients served as age-matched controls since the donors of these samples were within the same age range as the AD sample donors. Finally, all the PBMC samples of this cohort were isolated at the same site laboratory (DZNE Göttingen).

In addition to age-matched controls, three healthy in-house isolated PBMC samples were used (HD04, 5, and 6). These samples were isolated from buffy coats provided by the German Red Cross with no clinical information. However, the reason to choose these three samples from healthy volunteers was that these samples were used intensively during the development of the PBMC assay. Furthermore, the screen was performed over four screening days. In addition to the three samples from healthy volunteers, five patients were screened per day (Run). Due to this assay design, the three samples from healthy volunteers were used repeatedly on all screening days. Therefore, the PBMC control samples HD04, HD05 and HD06 served two aims, first, comparing the patient versus the samples from healthy volunteers and second, to evaluate the assay quality during the screening days. However, using PBMC samples of healthy volunteers from the Red Cross had its own caveat since no age information was provided. It was expected that the healthy donors are usually less than 50 years old as elderly people in many cases were not allowed to donate blood due to the presence of comorbidities. Knowing that the immune status is different between young and older people makes the Red Cross samples not the perfect controls when they were obtained from young people. In essence, it is important that the controls for AD studies are healthy elderly donors (age-matched controls) because aging has been reported to be associated with increased systemic inflammation (Latz and Duweil 2018). Latz and Duweil described “inflammaging” as an emerging term to define the process that links aging to the elevated system inflammation (Latz and Duweil 2018). Thus, the inflammation status of healthy young subjects might not reflect the immune status of elderly individuals.

Last but not least, healthy controls should have usually a Mini-Mental State Examination (MMSE) score above 25 and a Clinical Dementia Rating (CDR) score of 0 (Llano, Bundela et al. 2017), such information was not available for our healthy controls.

5.6.1. Univariate analysis was limited to bring a predictive model of AD

With the advance in age, healthy individuals become more heterogeneous in terms of their immune profile and immune cell population frequencies. This is usually due to a diversity of environmental exposures during lifetime (Kaczorowski, Shekhar et al. 2017). Within the group of AD patients, the immune diversity was expected to be even higher. Most of the AD patients were +65 years old and had have a wide range of comorbidity. Thus, it was arduous to find an immunological feature that consistently shows the same range of values over a cohort of AD patients. This might be the main reason that our univariate analysis was limited to bring the diagnostic model for AD. Though, the analysis revealed a distinct immune profile of the healthy donors compared to the patient samples, which was not observed for AD patients versus patients with depression (**Figure 56**). However, the data showed clearly that for AD patients, there was a change of the systemic immune response when compared to the healthy donors, i.e. the inflammasome activation rate was altered.

In summary, the main take-home message from the univariate analysis was that to discriminate AD patients from healthy volunteers and from patients with depression, a more sophisticated multivariate analysis was needed.

5.6.2. Transcriptome analysis can dissect healthy versus disease samples

For the patient cohort analysis, the samples from healthy volunteers were clustered together for both up- and down-regulated genes (**Figure 58**). However, although healthy control samples dissected significantly from the ones of patient donors, the samples from AD patients were scattered within the samples derived from patients with depression. It was not possible with such a standard primary analysis to differentiate AD from depression patients. More sophisticated analysis was needed to differentiate AD from depression and from other disease samples. For example, noncoding RNAs were reported to be elevated during AD pathology (Faghihi, Modarresi et al. 2008, Lee, Moon et al. 2015, Magistri, Velmeshev et al. 2015). Thus, data extracted from the RNA-seq of the patient cohort could be analyzed for noncoding RNAs. Another possible analysis is the rare variants as many previous studies investigated rare variants as potential AD biomarkers via transcriptomic profiling. The majority of these rare familial variants are single amino acid substitutions and show dominant, fully penetrant co-segregation with early-onset AD

(Humphries and Kohli 2014, Cacace, Van den Bossche et al. 2015). Such kind of deeper analysis has not been done during the course of this study. Furthermore, Monaco et al have recently published a transcriptomic dataset of 29 immune cell subsets within PBMCs of healthy individuals and identified “modules of cell type-specific, co-expressed, and housekeeping genes” (Monaco, Lee et al. 2019). Such data could be used to conduct a differential expression analysis of the dataset generated during this study.

Single-cell sequencing has many advantages over bulk RNA-seq, e.g. it helps to study rare cell populations, the association between genes, to uncover regulatory pathways (Hwang, Lee et al. 2018) and to track the development of distinct cell lineages (Schultze, Mass et al. 2019). However, during this study bulk transcriptome analysis was conducted, because our focus was to collect comprehensive information about the PBMC samples which can be done via the bulk transcriptome (Schultze and Aschenbrenner 2019).

The gene ontology (GO) enrichment analysis revealed that some immune linked pathways have emerged as up- and down-regulated within the patient samples. This included pathways like cellular defense response, leukocyte homeostasis and response to LPS. This again confirmed that there were immune changes that could be identified in the peripheral blood during AD pathology.

5.6.3. Multi-parametric analysis can provide a predictive model of AD

As discussed before, the majority of the previous attempts to develop AD biomarkers were done by studies focusing on single targets and thus were unable to address the complexity of the AD pathology. Alternatively, a multi-parametric assay flanked by machine learning multivariate analysis could introduce an understanding of the variability of disease pathology within a patient population. Implementation of machine learning for multivariate data analysis is a powerful tool for analyzing many variables (features) simultaneously and exploring characteristic patterns that cannot be captured by the human. The PBMC multi-parametric assay is a combination of immune readouts that enable describing the phenotype of the PBMC sample. This phenotype was used then to differentiate the disease versus healthy individuals via the multivariate analysis.

The prediction accuracy of our multivariate analysis was excellent. A prediction accuracy of 91% was obtained via the confusing matrix analysis. The prediction selectivity analysis was promising as well. The precision of prediction or prediction selectivity was 100% for

samples from AD patients and the healthy donors as well. The precision of prediction for the samples of depressed patients was the lowest with a precision of 80%, though it is still a good performance. Interestingly, DD05 was misclassified as a sample of a depressive patient and the actual class was "other" (**Figure 60 A**). However, checking the record of that sample showed that the patient had signs of clinical depression, however, did not meet the full criteria of depression that was used for the other four depressive patients and therefore it was assigned by the medical doctor as "other". Therefore, it might be that DD05 had some depression associated immune changes that were captured by the classifier, i.e. the classifier had a biological-based decision.

A big caution should be considered here that the sample size was limited to 23 samples (20 patients + three healthy donors) including all the clinical subgroups, which increased the risk of false discovery. Repeating the analysis using a bigger cohort of patients as well as a larger cohort of healthy donors is therefore necessary. The performance of this immune signature needs also to be evaluated in terms of its ability to differentiate selectively and precisely the samples from AD patients from other immune-associated diseases such as diabetes mellitus and Parkinson disease.

5.6.3.1. Prediction features are therapeutic targets as well

As described before, the SVM algorithm conducted a feature selection analysis to reduce the number of variables, avoiding overfitting (scikit-learn 2018). The most representative features are the features that were used the most for the prediction process (**Figure 61**). Features with a high classifier weight could be interesting therapeutic targets as well. The biological pathways behind these features can be further investigated for more insight information. This could be a future perspective that can be further investigated. For confidentiality purposes, the details of the features cannot be discussed in this thesis.

5.7. PBMC ex vivo assay for precision medicine of AD

There are currently continuously increasing efforts to understand the reason behind the individual variation in the drug response. These research efforts try to identify the genetic variation of drug targets, metabolism, transport and safety in order to provide effective and safe treatments or interventions for subjects with specific profiles. As PBMCs represent a compelling cell model to explore potential toxic reactions, they recently

developed to a very popular model for pharmacogenomics studies (Pourahmad and Salimi 2015). Additionally, the PBMC assay which was developed in this project represents HCS-compatible assay and constitutes a ready-to-go assay for studies of person-tailored therapeutic development studies.

In the perspective of the AD healthcare procedure, the PBMC assay could provide a supportive implementation for primary care physicians to approach an empirically based judgment on individuals who need a referral for more expensive (PET scan) and invasive (CSF sampling) procedures. This reduces the number of inappropriate referrals, meaning better access to CSF samples and PET scan facilities. The *ex vivo* human PBMC response can be used instead of the investigation of *in vivo* human immune response to evaluate and decide for individual-tailored healthcare measures.

Sophisticated patient stratification is an urgent need for both therapeutic and diagnostic developments of AD, since clinicians have appreciated in recent years that disease variation is more complex than to be identified by classical hallmarks of the disease only, i.e. amyloid plaques and neurofibrillary tangles (Kovacs 2012). The immune phenotyping of AD patients, via the PBMC assay, provides the opportunity for better patient stratification.

5.8. The *ex vivo* PBMC assay for drug discovery

Evaluation of potential immune-related adverse effects has become an important prerequisite for the development of drugs, chemical compounds and even the personal care products. In parallel, there are increasing efforts to minimize the use of animals for toxicity studies due to ethical considerations as well as to the public opinion. Thus, there is an urge to develop more *in vitro* or *in silico* models to be used for therapeutic development studies (Pourahmad and Salimi 2015). PBMCs are not only serving this goal, but they also represent a human-derived cell model, therefore being more relevant to study human immune response rather than animal models.

Nevertheless, innate immunity for NLR and in particular NLRP3 activation has not been tested routinely despite provided evidence that certain drugs can trigger this pathway and induce serious side effects, like in the case of statins (Henriksbo, Lau et al. 2014).

The PBMC assay, as discussed in the last section, provides the opportunity for patient stratification which is also necessary for drug development. For instance, it can help to

identify different AD patient subsets leading for better therapeutic development, while ignoring the AD patient stratification might jeopardize the clinical trials, delaying the development of effective AD interventions. Furthermore, stratifying the AD patients at early disease stages, if it is possible, could considerably help to develop potent and effective drugs (Kovacs 2012).

5.9. Limitations of the study

The main limitation of the current study was the low sample size of both healthy volunteers and patient donors. This imposed many statistical and mathematical limitations. For example, SVM is a well-known algorithm to process a dataset of low sample size with high dimensionality of features. overfitting (Fabian Pedregosa, Gaël Varoquaux et al. 2011, Patel 2017). Furthermore, using a low sample size to train the classifier increases the risk of false discovery (Patel 2017).

The age of the healthy control needs urgently to be considered during inflammation focused studies of AD. This because the inflammation status is age-dependent according to the concept of inflammaging (Latz and Duewell 2018). However, no information was available about the age of healthy donors from the German Red Cross.

Finally, another important limitation of the study was not to consider the effect of comorbidities and/or pharmacological treatment of the patients. These can influence the status of the immune system and give a false positive/negative outcome. This influence needs to be considered in the future prospect of the project.

5.10. Outlook

Analyzing a patient cohort of larger sample size is necessary to validate the prediction model that have been developed in the current project. Currently, our lab considers the analysis of a high number of samples from both AD patients as well as healthy controls. This is, however, beyond the scope of this thesis.

There has been an increasing interest in recent years to address the immune variation across healthy individuals, while it is quite known nowadays that healthy individuals respond differently to the same immunological challenges. For example, receiving

seasonal influenza vaccines caused in some healthy individuals to exhibit vigorous antibody responses against any future attack of influenza virus, whereas other vaccinated individuals show no protective response (Kaczorowski, Shekhar et al. 2017). To understand such resemblances and variances in the immune responsiveness, an intangible framework for assessing and studying inter-individual immune differences will be helpful. In the context of AD biomarkers, it is necessary to understand the inter-individual variation of healthy individuals before conducting the differential analysis between healthy individuals and AD patients. This could be addressed by analyzing a big cohort of samples from healthy volunteers in order to study inter-individual variation, not only at the level of individual measurements, but at the systems-level across a high number of healthy donors. Furthermore, analyzing the inter-dependencies between the immune system components would enable us to identify how the different immune readouts co-vary in health and disease (Shao, Cao et al. 2018).

6. Bibliography

- Abràmoff, M. D., P. J. Magalhães and S. J. Ram (2004). "Image processing with imageJ." Biophotonics International **11**(7): 36-41.
- Acharya, N. K., E. P. Nagele, M. Han and R. G. Nagele (2013). "Autoantibodies: double agents in human disease." Sci Transl Med **5**(186): 186fs119.
- Agamanolis, D. (2016). "ALZHEIMER'S DISEASE." from <http://neuropathology-web.org/chapter9/chapter9bAD.html>.
- Ahmad, F., N. Mishra, G. Ahrenstorf, B. S. Franklin, E. Latz, R. E. Schmidt and L. Bossaller (2017). "Evidence of inflammasome activation and formation of monocyte derived ASC-specks in HIV-1 positive patients." AIDS.
- Akdis, M., O. Palomares, W. van de Veen, M. van Splunter and C. A. Akdis (2012). "TH17 and TH22 cells: a confusion of antimicrobial response with tissue inflammation versus protection." J Allergy Clin Immunol **129**(6): 1438-1449; quiz1450-1431.
- Akopov, A. S., A. A. Moskovtsev, S. A. Dolenko and G. D. Savina (2013). "[Cluster analysis in biomedical researches]." Patologicheskaja fiziologija i eksperimental'naja terapija(4): 84-96.
- Alex Krizhevsky, I. S., Geoffrey E. Hinton (2012). ImageNet classification with deep convolutional neural networks. Proceedings of the 25th International Conference on Neural Information Processing Systems - Lake Tahoe, Nevada. Volume 1.
- Alsop, D. C., J. A. Detre and M. Grossman (2000). "Assessment of cerebral blood flow in Alzheimer's disease by spin-labeled magnetic resonance imaging." Ann Neurol **47**(1): 93-100.
- Alzheimer's, T. A. a. o. (2019). "Alzheimer's: Facts and Figures." from <https://www.alz.org/alzheimers-dementia/facts-figures>.
- Anoop, A., P. K. Singh, R. S. Jacob and S. K. Maji (2010). "CSF Biomarkers for Alzheimer's Disease Diagnosis." International journal of Alzheimer's disease **2010**: 606802.
- Antman, E. M. and J. Loscalzo (2016). "Precision medicine in cardiology." Nat Rev Cardiol **13**(10): 591-602.
- Bacioglu, M., L. F. Maia, O. Preische, J. Schelle, A. Apel, S. A. Kaeser, M. Schweighauser, T. Eninger, M. Lambert, A. Pilotto, D. R. Shimshek, U. Neumann, P. J. Kahle, M. Staufenbiel, M. Neumann, W. Maetzler, J. Kuhle and M. Jucker (2016). "Neurofilament Light Chain in Blood and CSF as Marker of Disease Progression in Mouse Models and in Neurodegenerative Diseases." Neuron **91**(1): 56-66.
- Bagnoli, S., I. Piaceri, S. Sorbi and B. Nacmias (2014). "Advances in imaging-genetic relationships for Alzheimer's disease: clinical implications." Neurodegener Dis Manag **4**(1): 73-81.
- Bagyinszky, E., Y. C. Youn, S. S. An and S. Kim (2014). "The genetics of Alzheimer's disease." Clin Interv Aging **9**: 535-551.
- Barroeta-Espar, I., L. D. Weinstock, B. G. Perez-Nievas, A. C. Meltzer, M. Siao Tick Chong, A. C. Amaral, M. E. Murray, K. L. Moulder, J. C. Morris, N. J. Cairns, J. E. Parisi, V. J. Lowe, R. C. Petersen, J. Kofler, M. D. Ikonovic, O. López, W. E. Klunk, R. P. Mayeux, M. P. Frosch, L. B. Wood and T. Gomez-Isla (2019). "Distinct cytokine profiles in human brains resilient to Alzheimer's pathology." Neurobiology of Disease **121**: 327-337.
- Bartolotti, N. and O. Lazarov (2019). "CREB signals as PBMC-based biomarkers of cognitive dysfunction: A novel perspective of the brain-immune axis." Brain, Behavior, and Immunity.

- Bergman, M., H. Salman, Y. Beloosesky, M. Djaldetti and H. Bessler (2002). "Are peripheral blood cells from patients with Alzheimer disease more sensitive to apoptotic stimuli?" *Alzheimer Dis Assoc Disord* **16**(3): 156-160.
- Bertin, J., W. J. Nir, C. M. Fischer, O. V. Tayber, P. R. Errada, J. R. Grant, J. J. Keilty, M. L. Gosselin, K. E. Robison, G. H. Wong, M. A. Glucksmann and P. S. DiStefano (1999). "Human CARD4 protein is a novel CED-4/Apaf-1 cell death family member that activates NF-kappaB." *J Biol Chem* **274**(19): 12955-12958.
- Blennow, K., A. Wallin, H. Agren, C. Spenger, J. Siegfried and E. Vanmechelen (1995). "Tau protein in cerebrospinal fluid: a biochemical marker for axonal degeneration in Alzheimer disease?" *Mol Chem Neuropathol* **26**(3): 231-245.
- Blennow, K. and H. Zetterberg (2015). "The past and the future of Alzheimer's disease CSF biomarkers-a journey toward validated biochemical tests covering the whole spectrum of molecular events." *Front Neurosci* **9**: 345.
- Bonn, I. f. i. D. (2019). "Yet Another Pixel Classifier (based on deep learning)." from <https://yapic.github.io/yapic/>.
- Borgiani, P., C. Ciccacci, V. Forte, E. Sirianni, L. Novelli, P. Bramanti and G. Novelli (2009). "CYP4F2 genetic variant (rs2108622) significantly contributes to warfarin dosing variability in the Italian population." *Pharmacogenomics* **10**(2): 261-266.
- Boyko, A. A., N. I. Troyanova, E. I. Kovalenko and A. M. Sapozhnikov (2017). "Similarity and Differences in Inflammation-Related Characteristics of the Peripheral Immune System of Patients with Parkinson's and Alzheimer's Diseases." *Int J Mol Sci* **18**(12).
- Braak, H. and E. Braak (1991). "Neuropathological staging of Alzheimer-related changes." *Acta Neuropathologica* **82**(4): 239-259.
- Brettschneider, J., K. Del Tredici, V. M. Lee and J. Q. Trojanowski (2015). "Spreading of pathology in neurodegenerative diseases: a focus on human studies." *Nat Rev Neurosci* **16**(2): 109-120.
- Brodin, P. and M. M. Davis (2017). "Human immune system variation." *Nat Rev Immunol* **17**(1): 21-29.
- Brodin, P., V. Jovic, T. Gao, S. Bhattacharya, C. J. Angel, D. Furman, S. Shen-Orr, C. L. Dekker, G. E. Swan, A. J. Butte, H. T. Maecker and M. M. Davis (2015). "Variation in the human immune system is largely driven by non-heritable influences." *Cell* **160**(1-2): 37-47.
- Broz, P. and V. M. Dixit (2016). "Inflammasomes: mechanism of assembly, regulation and signalling." *Nature Reviews Immunology* **16**: 407.
- Cacace, R., T. Van den Bossche, S. Engelborghs, N. Geerts, A. Laureys, L. Dillen, C. Graff, H. Thonberg, H. H. Chiang, P. Pastor, S. Ortega-Cubero, M. A. Pastor, J. Diehl-Schmid, P. Alexopoulos, L. Benussi, R. Ghidoni, G. Binetti, B. Nacmias, S. Sorbi, R. Sanchez-Valle, A. Llado, E. Gelpi, M. R. Almeida, I. Santana, M. Tsolaki, M. Koutroumani, J. Clarimon, A. Lleo, J. Fortea, A. de Mendonca, M. Martins, B. Borroni, A. Padovani, R. Matej, Z. Rohan, M. Vandenbulcke, R. Vandenberghe, P. P. De Deyn, P. Cras, J. van der Zee, K. Sleegers and C. Van Broeckhoven (2015). "Rare Variants in PLD3 Do Not Affect Risk for Early-Onset Alzheimer Disease in a European Consortium Cohort." *Hum Mutat* **36**(12): 1226-1235.
- Caicedo, J. C., S. Cooper, F. Heigwer, S. Warchal, P. Qiu, C. Molnar, A. S. Vasilevich, J. D. Barry, H. S. Bansal, O. Kraus, M. Wawer, L. Paavolainen, M. D. Herrmann, M. Rohban, J. Hung, H. Hennig, J. Concannon, I. Smith, P. A. Clemons, S. Singh, P. Rees, P. Horvath, R. G. Lington and A. E. Carpenter (2017). "Data-analysis strategies for image-based cell profiling." *Nature Methods* **14**: 849.

- Calderon-Garciduenas, A. L. and C. Duyckaerts (2017). "Alzheimer disease." Handb Clin Neurol **145**: 325-337.
- Cao, W. and H. Zheng (2018). "Peripheral immune system in aging and Alzheimer's disease." Mol Neurodegener **13**(1): 51.
- Chan, E. W. L., S. Krishnansamy, C. Wong and S. Y. Gan (2019). "The NLRP3 inflammasome is involved in the neuroprotective mechanism of neural stem cells against microglia-mediated toxicity in SH-SY5Y cells via the attenuation of tau hyperphosphorylation and amyloidogenesis." NeuroToxicology **70**: 91-98.
- Chen, G. Y. and G. Nuñez (2010). "Sterile inflammation: Sensing and reacting to damage." Nature Reviews Immunology **10**(12): 826-837.
- Chen, L., X. Guo, Z. Li and Y. He (2019). "Relationship between long non-coding RNAs and Alzheimer's disease: a systematic review." Pathology Research and Practice **215**(1): 12-20.
- Chien, D. T., S. Bahri, A. K. Szardenings, J. C. Walsh, F. Mu, M. Y. Su, W. R. Shankle, A. Elizarov and H. C. Kolb (2013). "Early clinical PET imaging results with the novel PHF-tau radioligand [F-18]-T807." Alzheimers Dis **34**(2): 457-468.
- Choi, A. J. and S. W. Ryter (2014). "Inflammasomes: molecular regulation and implications for metabolic and cognitive diseases." Mol Cells **37**(6): 441-448.
- Cisbio. (2017). "HTRF Cytokine cell-based assays." 2019, from <https://www.cisbio.com/drug-discovery/htrf-cytokine-cell-based-assays>.
- Collinet, C., M. Stöter, C. R. Bradshaw, N. Samusik, J. C. Rink, D. Kenski, B. Habermann, F. Buchholz, R. Henschel, M. S. Mueller, W. E. Nagel, E. Fava, Y. Kalaidzidis and M. Zerial (2010). "Systems survey of endocytosis by multi-parametric image analysis." Nature **464**: 243.
- Cooper, M. D. (2015). "The early history of B cells." Nat Rev Immunol **15**(3): 191-197.
- Cromwell, E., O. Hoxha, M. Hammer and O. Sirenko (2018). "Multi-parametric Human Cell-Based Inflammation Assay for Cytokines and Cell Surface Antigens." The Journal of Immunology **200**(1 Supplement): 42.15-42.15.
- Cummings, J., G. Lee, T. Mortsdorf, A. Ritter and K. Zhong (2017). "Alzheimer's disease drug development pipeline: 2017." Alzheimers Dement (N Y) **3**(3): 367-384.
- De Jonghe, C., P. Cras, H. Vanderstichele, M. Cruts, I. Vanderhoeven, I. Smouts, E. Vanmechelen, J. J. Martin, L. Hendriks and C. Van Broeckhoven (1999). "Evidence that A β 42 plasma levels in presenilin-1 mutation carriers do not allow for prediction of their clinical phenotype." Neurobiology of Disease **6**(4): 280-287.
- de Oliveira, A. A., D. Davis and K. P. Nunes (2019). "Pattern recognition receptors as potential therapeutic targets in metabolic syndrome: From bench to bedside." Diabetes and Metabolic Syndrome: Clinical Research and Reviews **13**(2): 1117-1122.
- Degorce, F., A. Card, S. Soh, E. Trinquet, G. P. Knapik and B. Xie (2009). "HTRF: A Technology Tailored for Drug Discovery –A Review of Theoretical Aspects and Recent Applications." Current Chemical Genomics **3**: 22-32.
- EMA. (2009). "GUIDELINES FOR THE VALIDATION OF ANALYTICAL METHODS USED IN RESIDUE DEPLETION STUDIES", from https://www.ema.europa.eu/en/documents/scientific-guideline/vich-topic-gl49-step-4-guidelines-validation-analytical-methods-used-residue-depletion-studies_en.pdf.
- Fabian Pedregosa, Gaël Varoquaux, Alexandre Gramfort, Vincent Michel, Bertrand Thirion, Olivier Grisel, Mathieu Blondel, Peter Prettenhofer, Ron Weiss, Vincent Dubourg,

- Jake Vanderplas, Alexandre Passos, David Cournapeau, Matthieu Brucher, Matthieu Perrot and É. Duchesnay. (2011). "Scikit-learn: Machine Learning in Python ", from <http://jmlr.csail.mit.edu/papers/v12/pedregosa11a.html>.
- Faghihi, M. A., F. Modarresi, A. M. Khalil, D. E. Wood, B. G. Sahagan, T. E. Morgan, C. E. Finch, G. St Laurent, 3rd, P. J. Kenny and C. Wahlestedt (2008). "Expression of a noncoding RNA is elevated in Alzheimer's disease and drives rapid feed-forward regulation of beta-secretase." *Nat Med* **14**(7): 723-730.
- FDA. (2014). "Guidance for Industry and FDA Staff Qualification Process for Drug Development Tools ", from <https://www.fda.gov/downloads/Drugs/GuidanceComplianceRegulatoryInformation/Guidances/UCM230597.pdf>.
- FDA. (2018). "Bioanalytical Method Validation Guidance for Industry ", from <https://www.fda.gov/regulatory-information/search-fda-guidance-documents/bioanalytical-method-validation-guidance-industry>.
- Fellgiebel, A., P. Wille, M. J. Muller, G. Winterer, A. Scheurich, G. Vucurevic, L. G. Schmidt and P. Stoeter (2004). "Ultrastructural hippocampal and white matter alterations in mild cognitive impairment: a diffusion tensor imaging study." *Dement Geriatr Cogn Disord* **18**(1): 101-108.
- Ferretti, M. T., M. Merlini, C. Spani, C. Gericke, N. Schweizer, G. Enzmann, B. Engelhardt, L. Kulic, T. Suter and R. M. Nitsch (2016). "T-cell brain infiltration and immature antigen-presenting cells in transgenic models of Alzheimer's disease-like cerebral amyloidosis." *Brain Behav Immun* **54**: 211-225.
- Foss-Freitas, M. C., N. T. Foss, D. M. Rassi, E. A. Donadi and M. C. Foss (2008). "Evaluation of cytokine production from peripheral blood mononuclear cells of type 1 diabetic patients." *Ann N Y Acad Sci* **1150**: 290-296.
- Fraietta, I. and F. Gasparri (2016). "The development of high-content screening (HCS) technology and its importance to drug discovery." *Expert Opin Drug Discov* **11**(5): 501-514.
- Franchi, L., N. Warner, K. Viani and G. Nuñez (2009). "Function of Nod-like receptors in microbial recognition and host defense." *Immunological reviews* **227**(1): 106-128.
- Gavan, S. P., A. J. Thompson and K. Payne (2018). "The economic case for precision medicine." *Expert Rev Precis Med Drug Dev* **3**(1): 1-9.
- German Federal Ministry of Education and Research. (2013). "Personalised Medicine – Action Plan." from https://www.gesundheitsforschung-bmbf.de/files/Action_Plan_IndiMed_englisch.pdf.
- Géron, A. (2018). *Neural networks and deep learning* Neural networks and deep learning, O'Reilly Media, Inc.
- Ghezzi, L., E. Scarpini and D. Galimberti (2013). "Disease-modifying drugs in Alzheimer's disease." *Drug Des Devel Ther* **7**: 1471-1478.
- Ghoneim, S. (2019). "Accuracy, Recall, Precision, F-Score & Specificity, which to optimize on?", from <https://towardsdatascience.com/accuracy-recall-precision-f-score-specificity-which-to-optimize-on-867d3f11124?gi=b8ef2dd7247d>.
- Goldstein, P. (2018). "Computer Vision: How Feds Can Use AI to Advance Beyond Image Processing ", from <https://fedtechmagazine.com/article/2018/08/computer-vision-how-feds-can-use-ai-advance-beyond-image-processing-perfcon>.

- Gordon, R., E. A. Albornoz, D. C. Christie, M. R. Langley, V. Kumar, S. Mantovani, A. A. B. Robertson, M. S. Butler, D. B. Rowe, L. A. O'Neill, A. G. Kanthasamy, K. Schroder, M. A. Cooper and T. M. Woodruff (2018). "Inflammasome inhibition prevents alpha-synuclein pathology and dopaminergic neurodegeneration in mice." *Sci Transl Med* **10**(465).
- Guo, C., L. Sun, X. Chen and D. Zhang (2013). "Oxidative stress, mitochondrial damage and neurodegenerative diseases." *Neural Regen Res* **8**(21): 2003-2014.
- Habeck, C. and Y. Stern (2010). "Multivariate data analysis for neuroimaging data: overview and application to Alzheimer's disease." *Cell Biochem Biophys* **58**(2): 53-67.
- Hair, J., R. Anderson, R. Tatham and W. Black (1998). *Multivariate Data Analysis*. USA, Upper Saddle River.
- Halle, A., V. Hornung, G. C. Petzold, C. R. Stewart, B. G. Monks, T. Reinheckel, K. A. Fitzgerald, E. Latz, K. J. Moore and D. T. Golenbock (2008). "The NALP3 inflammasome is involved in the innate immune response to amyloid- β ." *Nature Immunology* **9**(8): 857-865.
- Hampel, H., R. Frank, K. Broich, S. J. Teipel, R. G. Katz, J. Hardy, K. Herholz, A. L. Bokde, F. Jessen, Y. C. Hoessler, W. R. Sanhai, H. Zetterberg, J. Woodcock and K. Blennow (2010). "Biomarkers for Alzheimer's disease: academic, industry and regulatory perspectives." *Nat Rev Drug Discov* **9**(7): 560-574.
- Hampel, H., S. E. O'Bryant, S. Durrleman, E. Younesi, K. Rojkova, V. Escott-Price, J. C. Corvol, K. Broich, B. Dubois and S. Lista (2017). "A Precision Medicine Initiative for Alzheimer's disease: the road ahead to biomarker-guided integrative disease modeling." *Climacteric* **20**(2): 107-118.
- Hampel, H., S. E. O'Bryant, J. L. Molinuevo, H. Zetterberg, C. L. Masters, S. Lista, S. J. Kiddle, R. Batrla and K. Blennow (2018). "Blood-based biomarkers for Alzheimer disease: mapping the road to the clinic." *Nat Rev Neurol* **14**(11): 639-652.
- Hampel, H., N. Toschi, C. Babiloni, F. Baldacci, K. L. Black, A. L. W. Bokde, R. S. Bun, F. Cacciola, E. Cavedo, P. A. Chiesa, O. Colliot, C. M. Coman, B. Dubois, A. Duggento, S. Durrleman, M. T. Ferretti, N. George, R. Genthon, M. O. Habert, K. Herholz, Y. Koronyo, M. Koronyo-Hamaoui, F. Lamari, T. Langevin, S. Lehericy, J. Lorenceau, C. Neri, R. Nistico, F. Nyasse-Messene, C. Ritchie, S. Rossi, E. Santarnecchi, O. Sporns, S. R. Verdooner, A. Vergallo, N. Villain, E. Younesi, F. Garaci and S. Lista (2018). "Revolution of Alzheimer Precision Neurology. Passageway of Systems Biology and Neurophysiology." *J Alzheimers Dis* **64**(s1): S47-s105.
- Hampel, H., A. Vergallo, G. Perry and S. Lista (2019). "The Alzheimer Precision Medicine Initiative." *J Alzheimers Dis* **68**(1): 1-24.
- Harden, L. M., S. Kent, Q. J. Pittman and J. Roth (2015). "Fever and sickness behavior: Friend or foe?" *Brain Behav Immun* **50**: 322-333.
- He, Y., H. Hara and G. Nunez (2016). "Mechanism and Regulation of NLRP3 Inflammasome Activation." *Trends Biochem Sci* **41**(12): 1012-1021.
- Heneka, M. T. (2017). "Inflammasome activation and innate immunity in Alzheimer's disease." *Brain Pathol* **27**(2): 220-222.
- Heneka, M. T., M. P. Kummer, A. Stutz, A. Delekate, S. Schwartz, A. Vieira-Saecker, A. Griep, D. Axt, A. Remus, T. C. Tzeng, E. Gelpi, A. Halle, M. Korte, E. Latz and D. T. Golenbock (2013). "NLRP3 is activated in Alzheimer's disease and contributes to pathology in APP/PS1 mice." *Nature* **493**(7434): 674-678.
- Henriksbo, B. D., T. C. Lau, J. F. Cavallari, E. Denou, W. Chi, J. S. Lally, J. D. Crane, B. M. Duggan, K. P. Foley, M. D. Fullerton, M. A. Tarnopolsky, G. R. Steinberg and J. D. Schertzer

- (2014). "Fluvastatin causes NLRP3 inflammasome-mediated adipose insulin resistance." *Diabetes* **63**(11): 3742-3747.
- Heppner, F. L., R. M. Ransohoff and B. Becher (2015). "Immune attack: the role of inflammation in Alzheimer disease." *Nat Rev Neurosci* **16**(6): 358-372.
- Hiller, R. (2015). "Precision Medicine in South Africa – A cost-benefit analysis framework." from <https://www.cpgr.org.za/precision-medicine-in-south-africa-a-cost-benefit-analysis-framework/>.
- Hoeijmakers, W. A. M., R. Bártfai and H. G. Stunnenberg (2013). Transcriptome Analysis Using RNA-Seq. *Malaria: Methods and Protocols*. R. Ménard. Totowa, NJ, Humana Press: 221-239.
- Holleran, G., L. Lopetuso, V. Petito, C. Graziani, G. Ianiro, D. McNamara, A. Gasbarrini and F. Scaldaferri (2017). "The innate and adaptive immune system as targets for biologic therapies in inflammatory bowel disease." *International Journal of Molecular Sciences* **18**(10).
- Honer, M., L. Gobbi, H. Knust, H. Kuwabara, D. Muri, M. Koerner, H. Valentine, R. F. Dannals, D. F. Wong and E. Borroni (2018). "Preclinical evaluation of 18F-RO6958948, 11C-RO6931643, and 11C-RO6924963 as novel PET radiotracers for imaging tau aggregates in Alzheimer disease." *Journal of Nuclear Medicine* **59**(4): 675-681.
- Hoozemans, J. J. M., R. Veerhuis, J. M. Rozemuller and P. Eikelenboom (2011). "Soothing the inflamed brain: Effect of non-steroidal anti-inflammatory drugs on Alzheimer's disease pathology." *CNS and Neurological Disorders - Drug Targets* **10**(1): 57-67.
- Hopkins, J. (2019). "Positron Emission Tomography (PET Scan)." from <https://www.hopkinsmedicine.org/about/index.html>.
- House, U. W. (2015). "The Precision Medicine Initiative ", from <https://obamawhitehouse.archives.gov/precision-medicine>.
- Huang, Y., W. Dai and Y. Li (2018). "Potential associations of testosterone/estradiol ratio, leukocyte hTERT expression and PBMC telomerase activity with aging and the presence of coronary artery disease in men." *Exp Gerontol*.
- Hudd, F., A. Shiel, M. Harris, P. Bowdler, B. McCann, D. Tsivos, A. Wearn, M. Knight, R. Kauppinen, E. Coulthard, P. White and M. E. Conway (2019). "Novel Blood Biomarkers that Correlate with Cognitive Performance and Hippocampal Volumetry: Potential for Early Diagnosis of Alzheimer's Disease." *Alzheimers Dis* **67**(3): 931-947.
- Hugon, J., F. Mouton-Liger, E. Cognat, J. Dumurgier and C. Paquet (2018). "Blood-Based Kinase Assessments in Alzheimer's Disease." *Front Aging Neurosci* **10**: 338.
- Humboldt, S. u. (2015). "Supervised Classification." from http://gsp.humboldt.edu/olm_2015/Courses/GSP_216_Online/lesson6-1/supervised.html.
- Humphries, C. and M. A. Kohli (2014). "Rare Variants and Transcriptomics in Alzheimer disease." *Curr Genet Med Rep* **2**(2): 75-84.
- Hwang, B., J. H. Lee and D. Bang (2018). "Single-cell RNA sequencing technologies and bioinformatics pipelines." *Experimental & Molecular Medicine* **50**(8): 96.
- Ibold, Y., S. Frauenschuh, C. Kaps, M. Sittinger, J. Ringe and P. M. Goetz (2007). "Development of a High-Throughput Screening Assay Based on the 3-Dimensional Pannus Model for Rheumatoid Arthritis." *Journal of Biomolecular Screening* **12**(7): 956-965.
- Jack, C. R., Jr., D. S. Knopman, W. J. Jagust, R. C. Petersen, M. W. Weiner, P. S. Aisen, L. M. Shaw, P. Vemuri, H. J. Wiste, S. D. Weigand, T. G. Lesnick, V. S. Pankratz, M. C. Donohue and

- J. Q. Trojanowski (2013). "Tracking pathophysiological processes in Alzheimer's disease: an updated hypothetical model of dynamic biomarkers." Lancet Neurol **12**(2): 207-216.
- Jones, E., S. Michael and G. S. Sittampalam (2004). Basics of Assay Equipment and Instrumentation for High Throughput Screening. Assay Guidance Manual. G. S. Sittampalam, N. P. Coussens, K. Brimacombe et al. Bethesda (MD).
- Kaczorowski, K. J., K. Shekhar, D. Nkulikiyimfura, C. L. Dekker, H. Maecker, M. M. Davis, A. K. Chakraborty and P. Brodin (2017). "Continuous immunotypes describe human immune variation and predict diverse responses." Proc Natl Acad Sci U S A **114**(30): E6097-e6106.
- Kadhim, M. A. and M. H. Abed (2020). Convolutional neural network for satellite image classification. Studies in Computational Intelligence. **830**: 165-178.
- Kan, A. (2017). "Machine learning applications in cell image analysis." Immunol Cell Biol **95**(6): 525-530.
- Kaufmann, F. N., A. P. Costa, G. Ghisleni, A. P. Diaz, A. L. S. Rodrigues, H. Peluffo and M. P. Kaster (2017). "NLRP3 inflammasome-driven pathways in depression: Clinical and preclinical findings." Brain Behav Immun **64**: 367-383.
- Kehoe, E. G., J. P. McNulty, P. G. Mullins and A. L. W. Bokde (2014). "Advances in MRI biomarkers for the diagnosis of Alzheimer's disease." Biomarkers in Medicine **8**(9): 1151-1169.
- Kenny, A., E. M. Jimenez-Mateos, M. Calero, M. Medina and T. Engel (2018). "Detecting Circulating MicroRNAs as Biomarkers in Alzheimer's Disease." Methods Mol Biol **1779**: 471-484.
- Kensert, A., P. J. Harrison and O. Spjuth (2019). "Transfer Learning with Deep Convolutional Neural Networks for Classifying Cellular Morphological Changes." SLAS Discovery **24**(4): 466-475.
- Kesavardhana, S. and T. D. Kanneganti (2017). "Mechanisms governing inflammasome activation, assembly and pyroptosis induction." Int Immunol **29**(5): 201-210.
- Kleberger, C. A., R. H. Lyles, J. B. Margolick, C. R. Rinaldo, J. P. Phair and J. V. Giorgi (1999). "Viability and recovery of peripheral blood mononuclear cells cryopreserved for up to 12 years in a multicenter study." Clin Diagn Lab Immunol **6**(1): 14-19.
- Kleiveland, C. R. (2015). Peripheral Blood Mononuclear Cells. The Impact of Food Bioactives on Health: in vitro and ex vivo models. K. Verhoeckx, P. Cotter, I. Lopez-Exposito et al. Cham (CH): 161-167.
- Koh, H. X., H. M. Aye, K. S. W. Tan and C. Y. He (2015). "The lysosomotropic drug LeuLeu-OMe induces lysosome disruption and autophagy-independent cell death in *Trypanosoma brucei*." Microbial Cell **2**(8): 288-298.
- Kolařík, M., R. Burget, V. Uher, K. Říha and M. K. Dutta (2019). "Optimized high resolution 3D dense-U-Net network for brain and spine segmentation." Applied Sciences (Switzerland) **9**(3).
- Kovacs, G. G. (2012). "Clinical stratification of subtypes of Alzheimer's disease." Lancet Neurol **11**(10): 839-841.
- Krstic, D., A. Madhusudan, J. Doehner, P. Vogel, T. Notter, C. Imhof, A. Manalastas, M. Hilfiker, S. Pfister, C. Schwerdel, C. Riether, U. Meyer and I. Knuesel (2012). "Systemic immune challenges trigger and drive Alzheimer-like neuropathology in mice." J Neuroinflammation **9**: 151.
- Kutscher, S., C. J. Dembek, S. Deckert, C. Russo, N. Korber, J. R. Bogner, F. Geisler, A. Umgelter, M. Neuenhahn, J. Albrecht, A. Cosma, U. Protzer and T. Bauer (2013). "Overnight

- resting of PBMC changes functional signatures of antigen specific T- cell responses: impact for immune monitoring within clinical trials." *PLoS One* **8**(10): e76215.
- Labzin, L. I., M. T. Heneka and E. Latz (2018). "Innate Immunity and Neurodegeneration." *Annu Rev Med* **69**: 437-449.
- Landmann, R., H. P. Knopf, S. Link, S. Sansano, R. Schumann and W. Zimmerli (1996). "Human monocyte CD14 is upregulated by lipopolysaccharide." *Infect Immun* **64**(5): 1762-1769.
- Larry Jameson, J. and D. L. Longo (2015). "Precision Medicine—Personalized, Problematic, and Promising." *Obstetrical & Gynecological Survey* **70**(10): 612-614.
- Latz, E. and P. Duewell (2018). "NLRP3 inflammasome activation in inflammaging." *Semin Immunol*.
- Lee, D. Y., J. Moon, S. T. Lee, K. H. Jung, D. K. Park, J. S. Yoo, J. S. Sunwoo, J. I. Byun, J. W. Shin, D. Jeon, K. Y. Jung, M. Kim, S. K. Lee and K. Chu (2015). "Distinct Expression of Long Non-Coding RNAs in an Alzheimer's Disease Model." *J Alzheimers Dis* **45**(3): 837-849.
- Lehmann, S., C. Delaby, G. Boursier, C. Catteau, N. Ginestet, L. Tiers, A. Maceski, S. Navucet, C. Paquet, J. Dumurgier, E. Vanmechelen, H. Vanderstichele and A. Gabelle (2018). "Relevance of Abeta42/40 Ratio for Detection of Alzheimer Disease Pathology in Clinical Routine: The PLMR Scale." *Front Aging Neurosci* **10**: 138.
- Li, J. M., L. L. Liu, W. J. Su, B. Wang, T. Zhang, Y. Zhang and C. L. Jiang (2019). "Ketamine may exert antidepressant effects via suppressing NLRP3 inflammasome to upregulate AMPA receptors." *Neuropharmacology* **146**: 149-153.
- Lilly, E. (2004). *Assay Guidance Manual*.
- Lin, C. N., C. C. Huang, K. L. Huang, K. J. Lin, T. C. Yen and H. C. Kuo (2019). "A metabolomic approach to identifying biomarkers in blood of Alzheimer's disease." *Ann Clin Transl Neurol* **6**(3): 537-545.
- Lista, S., S. E. O'Bryant, K. Blennow, B. Dubois, J. Hugon, H. Zetterberg and H. Hampel (2015). "Biomarkers in Sporadic and Familial Alzheimer's Disease." *J Alzheimers Dis* **47**(2): 291-317.
- Llano, D. A., S. Bundela, R. A. Mudar, V. Devanarayan and I. Alzheimer's Disease Neuroimaging (2017). "A multivariate predictive modeling approach reveals a novel CSF peptide signature for both Alzheimer's Disease state classification and for predicting future disease progression." *PLoS One* **12**(8): e0182098.
- Locovei, S., E. Scemes, F. Qiu, D. C. Spray and G. Dahl (2007). "Pannexin1 is part of the pore forming unit of the P2X(7) receptor death complex." *FEBS Lett* **581**(3): 483-488.
- Ma, Y., L. Zhang, T. Jiang, Z. Q. Liu and Q. S. Li (2015). "[The Study of Altered Immune Status of UCMSC upon the Activation of TLR1/2 Pathway]." *Sichuan Da Xue Xue Bao Yi Xue Ban* **46**(5): 679-683, 701.
- Maes, E., B. Landuyt, I. Mertens and L. Schoofs (2013). "Interindividual variation in the proteome of human peripheral blood mononuclear cells." *PLoS One* **8**(4): e61933.
- Magistri, M., D. Velmeshev, M. Makhmutova and M. A. Faghihi (2015). "Transcriptomics Profiling of Alzheimer's Disease Reveal Neurovascular Defects, Altered Amyloid-beta Homeostasis, and Deregulated Expression of Long Noncoding RNAs." *J Alzheimers Dis* **48**(3): 647-665.
- Man, S. M. and T.-D. Kanneganti (2015). "Regulation of inflammasome activation." *Immunological reviews* **265**(1): 6-21.

- Mapstone, M., A. K. Cheema, M. S. Fiandaca, X. Zhong, T. R. Mhyre, L. H. MacArthur, W. J. Hall, S. G. Fisher, D. R. Peterson, J. M. Haley, M. D. Nazar, S. A. Rich, D. J. Berlau, C. B. Peltz, M. T. Tan, C. H. Kawas and H. J. Federoff (2014). "Plasma phospholipids identify antecedent memory impairment in older adults." *Nat Med* **20**(4): 415-418.
- Marcus, C., E. Mena and R. M. Subramaniam (2014). "Brain PET in the diagnosis of Alzheimer's disease." *Clin Nucl Med* **39**(10): e413-422; quiz e423-416.
- Martorana, A., M. Bulati, S. Buffa, M. Pellicanò, C. Caruso, G. Candore and G. Colonna-Romano (2012). "Immunosenescence, inflammation and Alzheimer's disease." *Longevity & healthspan* **1**: 8-8.
- McQuin, C., A. Goodman, V. Chernyshev, L. Kametsky, B. A. Cimini, K. W. Karhohs, M. Doan, L. Ding, S. M. Rafelski, D. Thirstrup, W. Wiegand, S. Singh, T. Becker, J. C. Caicedo and A. E. Carpenter (2018). "CellProfiler 3.0: Next-generation image processing for biology." *PLoS Biology* **16**(7): e2005970.
- Miao, E. A., J. V. Rajan and A. Aderem (2011). "Caspase-1-induced pyroptotic cell death." *Immunological reviews* **243**(1): 206-214.
- Mielke, M. M., C. E. Hagen, J. Xu, X. Chai, P. Vemuri, V. J. Lowe, D. C. Airey, D. S. Knopman, R. O. Roberts, M. M. Machulda, C. R. Jack, Jr., R. C. Petersen and J. L. Dage (2018). "Plasma phospho-tau181 increases with Alzheimer's disease clinical severity and is associated with tau- and amyloid-positron emission tomography." *Alzheimers Dement*.
- Mizote, Y., K. Wakamatsu, S. Ito, A. Uenaka, Y. Ohue, K. Kurose, M. Isobe, A. Ito, Y. Tamura, H. Honda, T. Yamashita, S. Nohara, M. Oka, K. Jimbow and E. Nakayama (2014). "TLR4 and NLRP3 inflammasome activation in monocytes by N-propionyl cysteaminyphenol-maleimide-dextran (NPCMD)." *J Dermatol Sci* **73**(3): 209-215.
- Moghbel, M. C., A. Alavi and D. A. Torigian (2016). PET/MRI: Concepts and clinical applications. *Imaging of the Pelvis, Musculoskeletal System, and Special Applications to CAD*: 497-506.
- Molinuevo, J. L., S. Ayton, R. Batrla, M. M. Bednar, T. Bittner, J. Cummings, A. M. Fagan, H. Hampel, M. M. Mielke, A. Mikulskis, S. O'Bryant, P. Scheltens, J. Sevigny, L. M. Shaw, H. D. Soares, G. Tong, J. Q. Trojanowski, H. Zetterberg and K. Blennow (2018). "Current state of Alzheimer's fluid biomarkers." *Acta neuropathologica* **136**(6): 821-853.
- Molnar, C., I. H. Jermyn, Z. Kato, V. Rahkama, P. Östling, P. Mikkonen, V. Pietiäinen and P. Horvath (2016). "Accurate Morphology Preserving Segmentation of Overlapping Cells based on Active Contours." *Scientific Reports* **6**: 32412.
- Monaco, G., B. Lee, W. Xu, S. Mustafah, Y. Y. Hwang, C. Carré, N. Burdin, L. Visan, M. Ceccarelli, M. Poidinger, A. Zippelius, J. Pedro de Magalhães and A. Larbi (2019). "RNA-Seq Signatures Normalized by mRNA Abundance Allow Absolute Deconvolution of Human Immune Cell Types." *Cell Reports* **26**(6): 1627-1640.e1627.
- Morra, J. H., Z. Tu, L. G. Apostolova, A. E. Green, C. Avedissian, S. K. Madsen, N. Parikshak, X. Hua, A. W. Toga, C. R. Jack, Jr., N. Schuff, M. W. Weiner, P. M. Thompson and I. Alzheimer's Disease Neuroimaging (2009). "Automated 3D mapping of hippocampal atrophy and its clinical correlates in 400 subjects with Alzheimer's disease, mild cognitive impairment, and elderly controls." *Hum Brain Mapp* **30**(9): 2766-2788.
- Mosconi, L., V. Berti, L. Glodzik, A. Pupi, S. De Santi and M. J. de Leon (2010). "Pre-clinical detection of Alzheimer's disease using FDG-PET, with or without amyloid imaging." *J Alzheimers Dis* **20**(3): 843-854.

- Motter, R., C. Vigo-Pelfrey, D. Kholodenko, R. Barbour, K. Johnson-Wood, D. Galasko, L. Chang, B. Miller, C. Clark, R. Green and et al. (1995). "Reduction of beta-amyloid peptide42 in the cerebrospinal fluid of patients with Alzheimer's disease." *Ann Neurol* **38**(4): 643-648.
- Mutz, K. O., A. Heilkenbrinker, M. Lönne, J. G. Walter and F. Stahl (2013). "Transcriptome analysis using next-generation sequencing." *Current Opinion in Biotechnology* **24**(1): 22-30.
- Nagel, A., C. Mobs, H. Raifer, H. Wiendl, M. Hertl and R. Eming (2014). "CD3-positive B cells: a storage-dependent phenomenon." *PLoS One* **9**(10): e110138.
- Nagele, E. P., M. Han, N. K. Acharya, C. DeMarshall, M. C. Kosciuk and R. G. Nagele (2013). "Natural IgG autoantibodies are abundant and ubiquitous in human sera, and their number is influenced by age, gender, and disease." *PLoS One* **8**(4): e60726.
- Nakamura, A., N. Kaneko, V. L. Villemagne, T. Kato, J. Doecke, V. Dore, C. Fowler, Q. X. Li, R. Martins, C. Rowe, T. Tomita, K. Matsuzaki, K. Ishii, K. Ishii, Y. Arahata, S. Iwamoto, K. Ito, K. Tanaka, C. L. Masters and K. Yanagisawa (2018). "High performance plasma amyloid-beta biomarkers for Alzheimer's disease." *Nature* **554**(7691): 249-254.
- Nebel, C., A. Aslanidis, K. Rashid and T. Langmann (2017). "Activated microglia trigger inflammasome activation and lysosomal destabilization in human RPE cells." *Biochem Biophys Res Commun* **484**(3): 681-686.
- Netea, M. G., C. A. Nold-Petry, M. F. Nold, L. A. Joosten, B. Opitz, J. H. van der Meer, F. L. van de Veerdonk, G. Ferwerda, B. Heinhuis, I. Devesa, C. J. Funk, R. J. Mason, B. J. Kullberg, A. Rubartelli, J. W. van der Meer and C. A. Dinarello (2009). "Differential requirement for the activation of the inflammasome for processing and release of IL-1beta in monocytes and macrophages." *Blood* **113**(10): 2324-2335.
- Noble, J. M. and N. Scarmeas (2009). "Application of pet imaging to diagnosis of Alzheimer's disease and mild cognitive impairment." *Int Rev Neurobiol* **84**: 133-149.
- O'Bryant, S. E., M. Edwards, L. Johnson, J. Hall, A. E. Villarreal, G. B. Britton, M. Quiceno, C. M. Cullum and N. R. Graff-Radford (2016). "A blood screening test for Alzheimer's disease." *Alzheimers Dement (Amst)* **3**: 83-90.
- O'Bryant, S. E., M. M. Mielke, R. A. Rissman, S. Lista, H. Vanderstichele, H. Zetterberg, P. Lewczuk, H. Posner, J. Hall, L. Johnson, Y. L. Fong, J. Luthman, A. Jeromin, R. Batrla-Utermann, A. Villarreal, G. Britton, P. J. Snyder, K. Henriksen, P. Grammas, V. Gupta, R. Martins, H. Hampel and A. Biofluid Based Biomarker Professional Interest (2017). "Blood-based biomarkers in Alzheimer disease: Current state of the science and a novel collaborative paradigm for advancing from discovery to clinic." *Alzheimers Dement* **13**(1): 45-58.
- Olaf Ronneberger, P. F., and Thomas Brox (2015). "U-Net: Convolutional Networks for Biomedical Image Segmentation." *arxiv*.
- Patel, S. (2017). "Chapter 2 : SVM (Support Vector Machine)—Theory." from <https://medium.com/machine-learning-101/chapter-2-svm-support-vector-machine-theory-f0812effc72>.
- Payne, K. K., C. K. Zoon, W. Wan, K. Marlar, R. C. Keim, M. N. Kenari, A. L. Kazim, H. D. Bear and M. H. Manjili (2013). "Peripheral blood mononuclear cells of patients with breast cancer can be reprogrammed to enhance anti-HER-2/neu reactivity and overcome myeloid-derived suppressor cells." *Breast Cancer Res Treat* **142**(1): 45-57.

- Pellegrini, M., M. Zoghi and S. Jaberzadeh (2018). "Cluster analysis and subgrouping to investigate inter-individual variability to non-invasive brain stimulation: a systematic review." Rev Neurosci **29**(6): 675-697.
- Pellicano, M., M. Bulati, S. Buffa, M. Barbagallo, A. Di Prima, G. Misiano, P. Picone, M. Di Carlo, D. Nuzzo, G. Candore, S. Vasto, D. Lio, C. Caruso and G. Colonna-Romano (2010). "Systemic immune responses in Alzheimer's disease: in vitro mononuclear cell activation and cytokine production." J Alzheimers Dis **21**(1): 181-192.
- Perry, V. H. (2010). "Contribution of systemic inflammation to chronic neurodegeneration." Acta Neuropathol **120**(3): 277-286.
- Picelli, S., O. R. Faridani, A. K. Bjorklund, G. Winberg, S. Sagasser and R. Sandberg (2014). "Full-length RNA-seq from single cells using Smart-seq2." Nat Protoc **9**(1): 171-181.
- Pirttila, T., P. D. Mehta, H. Frey and H. M. Wisniewski (1994). "Alpha 1-antichymotrypsin and IL-1 beta are not increased in CSF or serum in Alzheimer's disease." Neurobiol Aging **15**(3): 313-317.
- Pluta, R., M. Ulamek-Kozioł, S. Januszewski and S. J. Czuczwar (2018). "Platelets, lymphocytes and erythrocytes from Alzheimer's disease patients: the quest for blood cell-based biomarkers." Folia Neuropathol **56**(1): 14-20.
- Pourahmad, J. and A. Salimi (2015). "Isolated Human Peripheral Blood Mononuclear Cell (PBMC), a Cost Effective Tool for Predicting Immunosuppressive Effects of Drugs and Xenobiotics." Iranian journal of pharmaceutical research : IJPR **14**(4): 979-979.
- Preethi, B. and P. Vinyaga Moorthi (2017). "A review on alzheimer's disease: Pathology, molecular conditions, management, and causes." Asian Journal of Pharmaceutical and Clinical Research **10**(5): 27-30.
- Preische, O., S. A. Schultz, A. Apel, J. Kuhle, S. A. Kaeser, C. Barro, S. Graber, E. Kuder-Buletta, C. LaFougere, C. Laske, J. Voglein, J. Levin, C. L. Masters, R. Martins, P. R. Schofield, M. N. Rossor, N. R. Graff-Radford, S. Salloway, B. Ghetti, J. M. Ringman, J. M. Noble, J. Chhatwal, A. M. Goate, T. L. S. Benzinger, J. C. Morris, R. J. Bateman, G. Wang, A. M. Fagan, E. M. McDade, B. A. Gordon, M. Jucker and N. Dominantly Inherited Alzheimer (2019). "Serum neurofilament dynamics predicts neurodegeneration and clinical progression in presymptomatic Alzheimer's disease." Nat Med.
- Qi, Y., I. Klyubin, A. C. Cuellar and M. J. Rowan (2018). "NLRP3-dependent synaptic plasticity deficit in an Alzheimer's disease amyloidosis model in vivo." Neurobiol Dis **114**: 24-30.
- Qiu, T., Q. Liu, Y. X. Chen, Y. F. Zhao and Y. M. Li (2015). "Aβ42 and Aβ40: similarities and differences." J Pept Sci **21**(7): 522-529.
- Ray, S. (2017). "Understanding Support Vector Machine algorithm from examples." from <https://www.analyticsvidhya.com/blog/2017/09/understaing-support-vector-machine-example-code/>.
- Reitz, C. (2016). "Toward precision medicine in Alzheimer's disease." Ann Transl Med **4**(6): 107.
- Ronneberger, O., P. Fischer and T. Brox (2015). U-net: Convolutional networks for biomedical image segmentation. Lecture Notes in Computer Science (including subseries Lecture Notes in Artificial Intelligence and Lecture Notes in Bioinformatics). **9351**: 234-241.
- Rottger, R. (2016). "Clustering of Biological Datasets in the Era of Big Data." J Integr Bioinform **13**(1): 300.

- Saccenti, E., H. C. J. Hoefsloot, A. K. Smilde, J. A. Westerhuis and M. M. W. B. Hendriks (2014). "Reflections on univariate and multivariate analysis of metabolomics data." *Metabolomics* **10**(3): 361-374.
- Sagar, R. (2018). "What Is The Difference Between Computer Vision And Image Processing?", from <https://www.analyticsindiamag.com/what-is-the-difference-between-computer-vision-and-image-processing/>.
- Sahu, R., R. Bethunaickan, S. Singh and A. Davidson (2014). "Structure and function of renal macrophages and dendritic cells from lupus-prone mice." *Arthritis & rheumatology (Hoboken, N.J.)* **66**(6): 1596-1607.
- Salminen, A., J. Ojala, T. Suuronen, K. Kaarniranta and A. Kauppinen (2008). "Amyloid-beta oligomers set fire to inflammasomes and induce Alzheimer's pathology." *J Cell Mol Med* **12**(6a): 2255-2262.
- Salmon, D. P., S. H. Ferris, R. G. Thomas, M. Sano, J. L. Cummings, R. A. Sperling, R. C. Petersen and P. S. Aisen (2013). "Age and apolipoprotein E genotype influence rate of cognitive decline in nondemented elderly." *Neuropsychology* **27**(4): 391-401.
- Saresella, M., F. La Rosa, F. Piancone, M. Zoppis, I. Marventano, E. Calabrese, V. Rainone, R. Nemni, R. Mancuso and M. Clerici (2016). "The NLRP3 and NLRP1 inflammasomes are activated in Alzheimer's disease." *Mol Neurodegener* **11**: 23.
- Scheiblich, H., A. Schlutter, D. T. Golenbock, E. Latz, P. Martinez-Martinez and M. T. Heneka (2017). "Activation of the NLRP3 inflammasome in microglia: the role of ceramide." *J Neurochem* **143**(5): 534-550.
- Schelker, M., S. Feau, J. Du, N. Ranu, E. Klipp, G. MacBeath, B. Schoeberl and A. Raue (2017). "Estimation of immune cell content in tumour tissue using single-cell RNA-seq data." *Nat Commun* **8**(1): 2032.
- Schenk, D., R. Barbour, W. Dunn, G. Gordon, H. Grajeda, T. Guido, K. Hu, J. Huang, K. Johnson-Wood, K. Khan, D. Kholodenko, M. Lee, Z. Liao, I. Lieberburg, R. Motter, L. Mutter, F. Soriano, G. Shopp, N. Vasquez, C. Vandeventer, S. Walker, M. Wogulis, T. Yednock, D. Games and P. Seubert (1999). "Immunization with amyloid-beta attenuates Alzheimer-disease-like pathology in the PDAPP mouse." *Nature* **400**(6740): 173-177.
- Schroder, K. and J. Tschopp (2010). "The Inflammasomes." *Cell* **140**(6): 821-832.
- Schultze, J. L. and A. C. Aschenbrenner (2019). "Systems immunology allows a new view on human dendritic cells." *Semin Cell Dev Biol* **86**: 15-23.
- Schultze, J. L., E. Mass and A. Schlitzer (2019). "Emerging Principles in Myelopoiesis at Homeostasis and during Infection and Inflammation." *Immunity* **50**(2): 288-301.
- scikit-learn. (2018). "Support Vector Machines." 2018, from <https://scikit-learn.org/stable/modules/svm.html>.
- Sekar, S., J. McDonald, L. Cuyugan, J. Aldrich, A. Kurdoglu, J. Adkins, G. Serrano, T. G. Beach, D. W. Craig, J. Valla, E. M. Reiman and W. S. Liang (2015). "Alzheimer's disease is associated with altered expression of genes involved in immune response and mitochondrial processes in astrocytes." *Neurobiology of Aging* **36**(2): 583-591.
- Sen, P., E. Kempainen and M. Oresic (2017). "Perspectives on Systems Modeling of Human Peripheral Blood Mononuclear Cells." *Front Mol Biosci* **4**: 96.
- Šerý, O., J. Povová, I. Mišek, L. Pešák and V. Janout (2013). "Review paper
Molecular mechanisms of neuropathological changes in Alzheimer's disease: a review." *Folia Neuropathologica* **51**(1): 1-9.

- Shahpasand-Kroner, H., H. W. Klafki, C. Bauer, J. Schuchhardt, M. Hüttenrauch, M. Stazi, C. Bouter, O. Wirths, J. Vogelgsang and J. Wiltfang (2018). "A two-step immunoassay for the simultaneous assessment of A β 38, A β 40 and A β 42 in human blood plasma supports the A β 42/A β 40 ratio as a promising biomarker candidate of Alzheimer's disease." Alzheimer's Research and Therapy **10**(1).
- Shao, B. Z., Q. Cao and C. Liu (2018). "Targeting NLRP3 Inflammasome in the Treatment of CNS Diseases." Front Mol Neurosci **11**: 320.
- Sharman, M. J., E. Gyengesi, H. Liang, P. Chatterjee, T. Karl, Q. X. Li, M. R. Wenk, B. Halliwell, R. N. Martins and G. Münch (2019). "Assessment of diets containing curcumin, epigallocatechin-3-gallate, docosahexaenoic acid and α -lipoic acid on amyloid load and inflammation in a male transgenic mouse model of Alzheimer's disease: Are combinations more effective?" Neurobiology of Disease **124**: 505-519.
- Shattuck, E. C. and M. P. Muehlenbein (2015). "Human sickness behavior: Ultimate and proximate explanations." American Journal of Physical Anthropology **157**(1): 1-18.
- Shi, J. Q., C. C. Zhang, X. L. Sun, X. X. Cheng, J. B. Wang, Y. D. Zhang, J. Xu and H. Q. Zou (2013). "Antimalarial drug artemisinin extenuates amyloidogenesis and neuroinflammation in APP^{swe}/PS1^{dE9} transgenic mice via inhibition of nuclear factor-kappaB and NLRP3 inflammasome activation." CNS Neurosci Ther **19**(4): 262-268.
- Shin, M. S., Y. Kang, N. Lee, S. H. Kim, K. S. Kang, R. Lazova and I. Kang (2012). "U1-small nuclear ribonucleoprotein activates the NLRP3 inflammasome in human monocytes." J Immunol **188**(10): 4769-4775.
- Sirishinha, S. (2014). "Evolutionary insights into the origin of innate and adaptive immune systems: Different shades of grey." Asian Pacific Journal of Allergy and Immunology **32**(1): 3-15.
- Smith, K., F. Piccinini, T. Balassa, K. Koos, T. Danka, H. Azizpour and P. Horvath (2018). "Phenotypic Image Analysis Software Tools for Exploring and Understanding Big Image Data from Cell-Based Assays." Cell Syst **6**(6): 636-653.
- Snyder, H. M., M. C. Carrillo, F. Grodstein, K. Henriksen, A. Jeromin, S. Lovestone, M. M. Mielke, S. O'Bryant, M. Sarasa, M. Sjogren, H. Soares, J. Teeling, E. Trushina, M. Ward, T. West, L. J. Bain, D. W. Shineman, M. Weiner and H. M. Fillit (2014). "Developing novel blood-based biomarkers for Alzheimer's disease." Alzheimers Dement **10**(1): 109-114.
- Sommer, C., C. Straehle, U. Köthe and F. A. Hamprecht (2011). Ilastik: Interactive learning and segmentation toolkit. 2011 IEEE International Symposium on Biomedical Imaging: From Nano to Macro.
- Strimbu, K. and J. A. Tavel (2010). "What are biomarkers?" Current opinion in HIV and AIDS **5**(6): 463-466.
- Strimbu, K. and J. A. Tavel (2010). "What are biomarkers?" Curr Opin HIV AIDS **5**(6): 463-466.
- Sudhagar, A., G. Kumar and M. El-Matbouli (2018). "Transcriptome Analysis Based on RNA-Seq in Understanding Pathogenic Mechanisms of Diseases and the Immune System of Fish: A Comprehensive Review." Int J Mol Sci **19**(1).
- Sugio, T., K. Miyawaki, K. Kato, K. Sasaki, K. Yamada, J. Iqbal, T. Miyamoto, K. Ohshima, T. Maeda, H. Miyoshi and K. Akashi (2018). "Microenvironmental immune cell signatures dictate clinical outcomes for PTCL-NOS." Blood Adv **2**(17): 2242-2252.

- Tamaoka, A., T. Fukushima, N. Sawamura, K. Ishikawa, E. Oguni, Y. Komatsuzaki and S. Shoji (1996). "Amyloid β protein in plasma from patients with sporadic Alzheimer's disease." Journal of the Neurological Sciences **141**(1-2): 65-68.
- Tan, C. and I. Gery (2012). "The unique features of Th9 cells and their products." Crit Rev Immunol **32**(1): 1-10.
- Tan, M. S., J. T. Yu, T. Jiang, X. C. Zhu and L. Tan (2013). "The NLRP3 inflammasome in Alzheimer's disease." Molecular Neurobiology **48**(3): 875-882.
- Tanamati, F., N. B. Stafuzza, D. F. J. Gimenez, A. A. S. Stella, D. J. A. Santos, M. I. T. Ferro, L. G. Albuquerque, E. Gasparino and H. Tonhati (2019). "Differential expression of immune response genes associated with subclinical mastitis in dairy buffaloes." Animal: 1-7.
- Tatebe, H., T. Kasai, T. Ohmichi, Y. Kishi, T. Takeya, M. Waragai, M. Kondo, D. Allsop and T. Tokuda (2017). "Quantification of plasma phosphorylated tau to use as a biomarker for brain Alzheimer pathology: pilot case-control studies including patients with Alzheimer's disease and down syndrome." Mol Neurodegener **12**(1): 63.
- Thomas, N. (2010). "High-content screening: a decade of evolution." Journal of Biomolecular Screening **15**(1): 1-9.
- Togo, T., H. Akiyama, E. Iseki, H. Kondo, K. Ikeda, M. Kato, T. Oda, K. Tsuchiya and K. Kosaka (2002). "Occurrence of T cells in the brain of Alzheimer's disease and other neurological diseases." J Neuroimmunol **124**(1-2): 83-92.
- van der Bruggen, T., S. Nijenhuis, E. van Raaij, J. Verhoef and B. Sweder van Asbeck (1999). "Lipopolysaccharide-Induced Tumor Necrosis Factor Alpha Production by Human Monocytes Involves the Raf-1/MEK1-MEK2/ERK1-ERK2 Pathway." Infection and Immunity **67**(8): 3824-3829.
- Varghese, J. F., R. Patel and U. C. S. Yadav (2019). "Sterol regulatory element binding protein (SREBP) -1 mediates oxidized low-density lipoprotein (oxLDL) induced macrophage foam cell formation through NLRP3 inflammasome activation." Cellular Signalling **53**: 316-326.
- Vérité, J., G. Page, M. Paccalin, A. Julian and T. Janet (2018). "Differential chemokine expression under the control of peripheral blood mononuclear cells issued from Alzheimer's patients in a human blood brain barrier model." PLoS ONE **13**(8).
- Villegas-Llerena, C., A. Phillips, P. G. Reitboeck, J. Hardy and J. M. Pocock (2016). "Microglial genes regulating neuroinflammation in the progression of Alzheimer's disease." Current Opinion in Neurobiology **36**: 74-81.
- Vogel, J. W., N. Mattsson, Y. Iturria-Medina, O. T. Strandberg, M. Schöll, C. Dansereau, S. Villeneuve, W. M. van der Flier, P. Scheltens, P. Bellec, A. C. Evans, O. Hansson, R. Ossenkoppele, I. The Alzheimer's Disease Neuroimaging and F. S. The Swedish Bio (2019). "Data-driven approaches for tau-PET imaging biomarkers in Alzheimer's disease." Human Brain Mapping **40**(2): 638-651.
- Walker, K. A., R. C. Hoogeveen, A. R. Folsom, C. M. Ballantyne, D. S. Knopman, B. G. Windham, C. R. Jack, Jr. and R. F. Gottesman (2017). "Midlife systemic inflammatory markers are associated with late-life brain volume: The ARIC study." Neurology **89**(22): 2262-2270.
- Wang, J., R. Dong and S. Zheng (2019). "Roles of the inflammasome in the gut-liver axis (Review)." Molecular medicine reports **19**(1): 3-14.

- Weinstein, G., A. S. Beiser, S. R. Preis, P. Courchesne, V. Chouraki, D. Levy and S. Seshadri (2016). "Plasma clusterin levels and risk of dementia, Alzheimer's disease, and stroke." Alzheimers Dement (Amst) **3**: 103-109.
- Wojsiat, J., K. Laskowska-Kaszub, A. Mietelska-Porowska and U. Wojda (2017). "Search for Alzheimer's disease biomarkers in blood cells: hypotheses-driven approach." Biomark Med **11**(10): 917-931.
- Wojsiat, J., C. Prandelli, K. Laskowska-Kaszub, A. Martin-Requero and U. Wojda (2015). "Oxidative Stress and Aberrant Cell Cycle in Alzheimer's Disease Lymphocytes: Diagnostic Prospects." J Alzheimers Dis **46**(2): 329-350.
- Wyss-Coray, T. (2006). "Inflammation in Alzheimer disease: Driving force, bystander or beneficial response?" Nature Medicine **12**(9): 1005-1015.
- Xu, R. and D. C. Wunsch, 2nd (2010). "Clustering algorithms in biomedical research: a review." IEEE Rev Biomed Eng **3**: 120-154.
- Yates, L. R., J. Seoane, C. Le Tourneau, L. L. Siu, R. Marais, S. Michiels, J. C. Soria, P. Campbell, N. Normanno, A. Scarpa, J. S. Reis-Filho, J. Rodon, C. Swanton and F. Andre (2018). "The European Society for Medical Oncology (ESMO) Precision Medicine Glossary." Ann Oncol **29**(1): 30-35.
- Yokogawa (2015). User manual: CellVoyager CV7000 Analysis Software.
- Zanella, F., J. B. Lorens and W. Link (2010). "High content screening: Seeing is believing." Trends in Biotechnology **28**(5): 237-245.
- Zilka, N., Z. Kazmerova, S. Jadhav, P. Neradil, A. Madari, D. Obetkova, O. Bugos and M. Novak (2012). "Who fans the flames of Alzheimer's disease brains? Misfolded tau on the crossroad of neurodegenerative and inflammatory pathways." J Neuroinflammation **9**: 47.
- Zimmermann, K. A. (2018). "Immune System: Diseases, Disorders & Function." from <https://www.livescience.com/26579-immune-system.html>.

7. Appendix

Index I: Full table of clinical information of the Disease Donor (DD) samples

ID	Sex	Diagnosis	Age	MMSE	CSF t-tau	CSF p-tau	CSF Ab42	Ab42/40 ratio	AD CSF Biomarkers	Comorbidity	MRI	Drugs
DD01	Female	Depression	55	24	133	30	995	1.1		Recurrent depressive episodes, currently not depressed, hyperhomocysteinemia, folic acid deficit, hyperthyreosis, discus prolaps	-	sertralain 200mg, amitriptylin 75mg
DD02	Female	AD	73	23	175	36	333	0.32		Hypercholesterinemia, prior subtotal thyroidectomy, suspected hereditary narcolepsia	-	sertralain 200mg, melperon 50mg, donepezil 5mg, simvastatin 20mg, thyranojod 100ug
DD03	Male	Other	76	21	140	34	1169	1.2	Negative	Hypertension, 1955 traumatic brain injury, lumbago, ileus 1997, gonarthrosis, hypothyreosis, adipositas, smoking	-	rivastigin 9.6mg pflaster, lthyroxin 50ug, ASS10 mg
DD04	Male	Other	82	25	335	65	911	1.3		Prostate hyperplasia, tbc (lung, 60 years before)	-	citalopram 10 mg, spasmolyt 15 mg, galantamin 24 mg, mirtazapin 30mg
DD05	Male	Other	76	-	-	-	-	-		Coronary heart disease, previous myocardial infarction, diabetes type2, nephrosclerosis, renal insuff. Stage 3, sleen annee, hvnertension	-	amlodipin 5mg, ass 100 mg, bisoprolol 10mg l-thyroxin 125 ug, 1.alpha.0.5ug, xinamid 10mg
DD06	Male	Other	83	25	-	-	-	-		Hypakusis, hypertension, benign prostate hyperplasia	-	exelon 9.5mg, others unknown
DD07	Female	Other	78	26	263	51	1302	0.74	Negative	Hypothyreosis, osteoporosis, iron deficit	Unspecific white matter lesions	aricept 10mg, pantozol, jodid 50 ug, calcium, ferrum, lactulose, moringa, aledronsäure
DD08	Male	AD	64	30	362	68	501	0.46		Polyneuropathy, diabetes type2, hypertension, hyperlipidemia, anaukusis left since childhdhod	-	diovan 60mg, bisoprolol 5mg, siofor 1000 mg, xelevia 100mg, inegy 10/20, omacor
DD09	Male	AD	54	21	500	84	441	0.46	Positive	Hyperhomocysteinemia, sensorymotoric polyneuropathy, fracture left hand 2000	Minor white matter lesions	ASS100
DD10	Male	Other	73	29	-	-	-	-		Myocardial ichemia 2011, reanimation, sinus bradycardia, pAVK, hyperhomocysteinemia, parotitis during childhood	Bitemporal atrophy	ASS100, iscover 75mg, torem cor 5mg, concor cor, ramipril 10mg, amlodipin 5mg, omeop 40mg, simva donepezil 10 mg, escitalopram 15 mg, pantoprazol 40 mg, simvastatin 20 mg, laxoberal 10
DD11	Female	Other	76	24	238	35	1041	1.2	Negative	Lumbago, hypercholesterinemia, anemia, blindness right eye	-	donepezil 10mg, enalapril 5mg, toraseid 10 mg, citalopram 40 mg, pantoprazol 20mg, marcumar duloxetin 120mg, agomelatin 50mg, pregabalin 3x75 mg, amiodaron 200mg, pantoprazol 40mg, atorvastatin, leflunomid 20mg, ramipril 5mg, hct 25mg, lthyroxin 100ug, allopurinol 100mg, carmen
DD12	Female	AD	77	18	683	125	843	0.49	Positive	Hypertension, atrial fibrillation permanent, pacemaker, hypercholesterinemia, hyperhomocysteinemia, aortic and mitral valve	-	donepezil 10mg, bisoprolol 5mg, iron 100mg, furosemid 40mg, pantoprazol 40mg
DD13	Male	Depression	58	-	189	36	936	0.96		Leukocytoclastic vasculitis, renal insufficiency, pancreatitis, cardiomyopathy, sarcoidosis, hyperlipidemia, hyperthyreosis, Atrial fibrillation, coronary heart disease, myocardial infarction with reanimation 2007, diabetes type 2, polyneuropathy,	-	donepezil 10mg, bicalutamid 50mg, sertralain 50mg, jodid 200mg, spasmolyt 30mg, piracetam mirtazapin 45mg, ass 100mg, pantoprazol 20mg, medy 1, venlafaxin 300mg
DD14	Female	Depression	81	-	-	-	-	-	Negative		-	donepezil 10mg, bisoprolol 5mg, iron 100mg, furosemid 40mg, pantoprazol 40mg
DD15	Female	AD	82	20	282	56	641	0.39	Positive	Hypertension, coronary heart disease	-	donepezil 10mg, bicalutamid 50mg, sertralain 50mg, jodid 200mg, spasmolyt 30mg, piracetam mirtazapin 45mg, ass 100mg, pantoprazol 20mg, medy 1, venlafaxin 300mg
DD16	Male	AD	77	26	360	83	596	0.45	Positive	Recurrent depressive episodes, currently non-depressed, sleep apnoe, prostate cancer 2002, hypakusis	Normal	donepezil 10mg, bicalutamid 50mg, sertralain 50mg, jodid 200mg, spasmolyt 30mg, piracetam mirtazapin 45mg, ass 100mg, pantoprazol 20mg, medy 1, venlafaxin 300mg
DD17	Male	Depression	68	-	-	-	-	-		Lumbago, media ischemia right 2009, nicotin addiction, 40 pack years	-	donepezil 10mg, bisoprolol 5mg, iron 100mg, furosemid 40mg, pantoprazol 40mg
DD18	Male	Other	71	25	485	105	792	0.55	Positive	Prostate hyperplasia, urge incontinence, hypertension, traumatic brain injury 42 years before	-	enalapril 10,g, hct 1.5mg, lercanidipin 01mg, trospium 30mg
DD19	Female	Depression	53	-	-	-	-	-		Adipositas, struma nodosa	-	quetiapin 400mg, sertralain 150mg, ramipril 10, metoprolol 2x95mg, lthyroxin 75ug
DD20	Female	Other	77	25	162	46	813	2.3		Hyperhomocysteinemia, hyperuricemia, hypertension, incontinence (urine)	-	allopurinol 300mg, donepezil 10mg, pantoprazol 40mg, mirtazapin 15mg

Index II: All features that were collected from the multi-parametric analysis

Donor ID	Disease	Sex	MMSE	CSF_t_tau	CSF_p_tau	CSF_Ab42	Ab42_40_Ratio	Mean_Cell_Per_Well_Untreated_NigericinPlate	Mean_Normalized_Activation_Rate_Untreated_NigericinPlate	Mean_Normalized_Intracellular_TNF_a_Cells_Percentage_Untreated_NigericinPlate	Mean_Monocyte_Percentage_Untreated_NigericinPlate	Mean_T_Cell_Percentage_Untreated_NigericinPlate	Mean_B_Cell_Percentage_Untreated_NigericinPlate	Mean_Marker_Negative_Percentage_Untreated_NigericinPlate
DD01	Depression	2	2	133	30	995	1.1	2100.75	7.2947804	15.77384257	1.03485572	55.365107	4.57447978	18.38837883
DD02	AD	2	2	175	360	333	0.32	1089.375	3.325861439	8.924013347	10.3853724	36.878177	10.0259855	33.13699442
DD03	Other	1	2	140	34	1169	1.2	3204.5	1.727293033	2.55615738	11.1289867	37.099284	3.62686732	34.90564507
DD04	Other	1	1	335	65	911	1.3	2316.375	0.623916975	3.864001624	15.9191493	36.877006	5.36594427	30.58445849
DD05	Other	1	NA	NA	NA	NA	NA	2156.25	0.394585986	2.054514013	16.7808049	40.255596	2.8136308	30.81926288
DD06	Other	1	1	NA	NA	NA	NA	3231	4.143776966	4.406803581	3.51124602	43.936718	3.39907735	26.28786409
DD07	Other	2	1	263	51	1302	0.74	3685.5	6.992763558	28.33291322	1.18651188	41.65428	8.99850176	32.40627174
DD08	AD	1	1	362	68	501	0.46	3097.125	0.761235964	6.949310196	15.5027889	21.983022	16.2131039	36.48497538
DD09	AD	1	2	500	84	441	0.46	2807	0.219859572	5.197332633	19.4665192	27.315084	8.51166524	28.89398786
DD10	Other	1	1	NA	NA	NA	NA	3345.75	0.285115246	1.927939655	22.652344	25.762646	16.722008	21.47150491
DD11	Other	2	2	238	35	1041	1.2	2868.75	25.0256291	29.46516697	1.38164827	44.755376	6.85942804	33.02870535
DD12	AD	2	3	683	125	843	0.49	3513.75	0.304261036	3.87011268	11.119898	38.792713	4.64521076	29.15953386
DD13	Depression	1	NA	189	36	936	0.96	3281.125	0.543660039	3.109144743	24.1669281	17.558983	2.56888781	38.74969442
DD14	Depression	2	NA	NA	NA	NA	NA	3437.375	1.216316013	10.73216651	13.1260722	39.265024	7.50031097	27.17088859
DD15	AD	2	3	282	56	641	0.39	2332.375	0.793187973	4.585121594	14.2108265	41.705822	3.45686878	30.87145512
DD16	AD	1	1	360	83	596	0.45	1949	0.703700192	6.870602364	9.05331311	38.31216	10.4037089	31.72855002
DD17	Depression	1	NA	NA	NA	NA	NA	2952.75	0.202830432	2.901488187	31.2201831	26.591196	10.8700734	24.03039952
DD18	Other	1	1	485	105	792	0.55	2049	0.737315295	9.031304443	13.5788893	39.745891	3.29859088	29.29306185
DD19	Depression	2	NA	NA	NA	NA	NA	3038.75	0.254346137	7.322767368	17.0529239	49.996449	4.65262884	20.57490559
DD20	Other	2	1	162	46	813	2.3	1769.25	0.281058771	3.823034823	20.3557887	38.008852	5.56047668	30.08741654
HD04.1	Healthy donor	NA	NA	NA	NA	NA	NA	3539.625	0.685667458	4.018433482	35.1296985	21.531331	11.1504696	19.01282661
HD04.2	Healthy donor	NA	NA	NA	NA	NA	NA	3040.5	0.83633605	3.08932593	35.4869735	13.560662	11.8134902	27.42877623
HD04.3	Healthy donor	NA	NA	NA	NA	NA	NA	3093.625	1.072180383	4.059087089	26.7178019	20.735926	9.34643396	32.89789565
HD04.4	Healthy donor	NA	NA	NA	NA	NA	NA	3641	0.676466792	3.732703212	30.8002459	18.373476	9.69485831	30.06172448
HD05.1	Healthy donor	NA	NA	NA	NA	NA	NA	3633.375	1.533039056	3.032145465	16.8389526	56.486385	6.46624025	9.180847696
HD05.2	Healthy donor	NA	NA	NA	NA	NA	NA	3506.875	1.358977224	4.075597831	18.8065441	41.291515	8.90235704	19.3263703
HD05.3	Healthy donor	NA	NA	NA	NA	NA	NA	3392.625	1.65828351	5.219984043	14.8993021	56.115205	5.92307423	14.96470767
HD05.4	Healthy donor	NA	NA	NA	NA	NA	NA	3241.25	1.383387628	4.562670756	13.1765735	53.787109	6.89202732	16.4409244
HD06.1	Healthy donor	NA	NA	NA	NA	NA	NA	2581.375	5.075451842	4.892786039	20.9725609	30.968158	11.7108823	17.1182493
HD06.2	Healthy donor	NA	NA	NA	NA	NA	NA	3036.125	5.514057867	8.249763863	15.9557683	27.028078	10.6638012	28.37349952
HD06.3	Healthy donor	NA	NA	NA	NA	NA	NA	2849.25	6.37373688	9.904835264	17.0674269	31.468553	10.4951881	26.74258318
HD06.4	Healthy donor	NA	NA	NA	NA	NA	NA	2974.75	3.819271496	11.85345239	18.8579977	28.345637	11.7427543	29.40229616

Donor ID	Mean_Normalized_TNFa_Release_Untreated_LeuLeuOMePlate	Mean_CelI_Per_WeII, LPS_NigericinPlate	Mean_Normalized_Activation_Rate, LPS_NigericinPlate	Mean_Normalized_Intracellular_TNFa_Cells_Percentage_LPS_NigericinPlate	Mean_Monocyte_Percentage_LPS_NigericinPlate	Mean_T_Cell_Percentage_LPS_NigericinPlate	Mean_B_Cell_Percentage_LPS_NigericinPlate	Mean_Marker_Negative_Percentage_LPS_NigericinPlate	Mean_Cellular_Debris_Percentage_LPS_NigericinPlate	Mean_Unclassified_Cell_Percentage_LPS_NigericinPlate	Mean_Normalized_IL-1b_Release_LPS_NigericinPlate	Mean_Normalized_TNFa_Release_LPS_NigericinPlate	Mean_CelI_Per_WeII, LPS_LeuLeuOMePlate	Mean_Normalized_Activation_Rate_LPS_LeuLeuOMePlate
DD01	0.2918151	1957.5	8.845999	25.36906279	1.0662027	51.3413086	4.4059663	17.43649	15.1219	10.62818079	0	0	2060	5.21161686
DD02	0	1173.625	21.03511	89.21194596	11.465807	34.86421277	8.41657609	29.308235	7.59065	8.354523696	0.438565778	2.6221416	1380.125	28.7572026
DD03	0	3183.625	3.432633	29.90754514	7.9143542	34.09495457	3.82038326	35.806302	11.1442	7.219778565	0	0.6798894	3239	3.11900567
DD04	0	2571.25	7.980482	50.93794656	9.9630733	37.60430783	4.719829	33.742949	9.46974	4.500104775	0.441559635	1.2433278	2474.375	10.4972201
DD05	0	2194.375	1.725483	33.70860244	15.40781	37.8350021	2.59427452	32.931694	7.56265	3.668573862	0	0.7638742	2870.125	2.70359406
DD06	0	2548.375	3.469469	5.612673004	2.9232058	34.59199604	2.90203709	23.841557	18.3739	17.3673311	0.021404102	0.0667818	2099.875	8.22892174
DD07	0.0307237	3490.75	6.482887	55.01132399	0.9575961	34.23466197	8.64416044	30.044185	10.8044	15.3149599	0	0.3470479	2790.875	1.63854659
DD08	0.0217373	2944.375	6.223232	62.87779198	9.7705585	16.59142127	12.4743205	40.290114	7.87895	12.99463423	0.208647138	1.0900035	2415.25	6.38677842
DD09	0.0020411	2540.875	5.523608	43.48690274	13.067125	21.76241792	7.6232663	27.466022	12.3494	17.73175192	0.253609961	1.5159307	2235.875	4.95201113
DD10	0.0241781	2932.375	4.534121	45.96025346	16.228993	21.46704518	13.8936077	25.225648	8.78732	14.397383	0.189270074	0.9522196	3230.25	5.57605331
DD11	0.3904835	3117.875	18.50264	32.78930722	0.8434979	39.33987336	5.63593732	31.225211	8.86786	14.08762203	0.19017876	1.109383	2861.833	59.906736
DD12	0.1381855	3609.75	6.654323	60.74427748	8.4130434	33.79087082	3.75147614	28.093148	10.8092	15.14225083	0.386366156	1.3536245	3592.75	6.0158776
DD13	0.0362313	3194.5	9.696446	58.30019208	16.193395	14.53388093	2.38197345	38.970746	14.4224	13.49759701	0.494455172	1.5306227	3474	9.10288372
DD14	0.1228823	3213.75	4.882555	43.00160003	9.619484	35.16548174	7.49250518	26.236996	8.03121	13.45432694	0.432370227	0.4612688	3359.25	4.40894299
DD15	0.1007398	2491	15.08231	81.93395375	11.49222	35.66108397	3.86108211	28.934804	8.05733	11.99348036	0.880048626	1.9907849	2841	11.3842693
DD16	0.0753938	2108.375	7.44694	46.04194293	6.8506121	35.27053044	8.46864456	31.581405	6.63968	11.18912479	0.334470069	0.8206321	1805.5	8.33274884
DD17	0.0458962	3349.25	1.466368	38.7050154	25.212923	22.33329943	8.61460769	26.28277	6.25476	11.30163445	0.077958001	0.7353981	3052.625	1.51949537
DD18	0.1132914	2615	5.908775	71.69955839	12.781271	33.06466666	3.26462744	27.831199	10.0596	12.99868419	0.346592678	1.6719981	1487	3.67219549
DD19	0.1052977	3337.75	3.303832	69.41921689	15.21493	47.11556927	4.03012409	17.110393	5.0592	11.46978577	0.22353049	1.3320914	2451.25	2.63540515
DD20	0.0596406	1797.75	8.716357	79.69333548	16.021974	36.17600324	4.53478451	28.019552	5.53889	9.708795844	0.437796054	1.5174434	1747.5	9.42169807
HD04.1	0	3050.375	8.155016	59.56081343	29.328051	17.50233365	10.3014379	20.663891	15.4323	6.771974362	0.299933358	1.5118426	3287.25	6.67687931
HD04.2	0.0476294	3163.125	7.855479	50.1382107	26.419628	11.24280724	9.93927069	28.097206	11.0648	13.23631381	0.267763611	1.2626895	3322.25	7.46483546
HD04.3	0.0524624	3108.125	7.949067	63.29581163	25.026837	16.8992733	8.49033874	29.602213	8.73979	11.24154927	0.32752587	1.3759951	3442.125	6.67393392
HD04.4	0.0532093	3680.375	6.341115	80.32188386	29.871639	15.58514496	8.64348723	27.527612	9.01063	9.361491599	0.238590062	1.1235263	3167.75	5.64159462
HD05.1	0	3068.5	7.693257	79.69655208	16.332632	48.23669399	5.9310735	9.2394278	13.2216	7.038612819	0.173017214	2.1993424	3517.25	5.73466104
HD05.2	0.0421487	3532.625	7.734862	63.7591012	15.90542	34.73357389	6.25834602	17.777006	12.4959	12.82975189	0.311266111	1.9676727	3250.375	9.43264185
HD05.3	0.0284219	3638	6.502343	75.85749806	12.535951	51.0396506	5.60158992	12.534948	4.77147	13.51638715	0.26355485	1.9037393	3841.375	5.65415445
HD05.4	0.0555784	3650.625	7.424198	104.2164601	12.036171	53.26248628	5.12386508	14.922754	4.22971	10.42501244	0.261929855	1.5544294	3299.25	5.2769715
HD06.1	0	2634.375	12.71665	82.97149544	21.043665	27.45047677	10.425229	18.842178	17.3037	4.934745826	0.364302916	2.040128	2851.5	11.640498
HD06.2	0.0534887	2850.25	17.17173	86.03773287	17.433764	16.36185398	9.31345358	27.434974	15.3555	14.10041672	0.598519703	2.3289526	2581.625	18.3673571
HD06.3	0.0387929	3082.75	12.11001	78.04840111	16.6756	25.46765263	9.23040453	25.907463	10.4496	12.26929831	0.266438307	1.1769587	3060.375	12.2051719
HD06.4	0.0604892	2944.5	10.80459	98.38533957	21.816633	27.02559642	10.5194594	25.605494	6.8501	8.182712576	0.347429189	1.6040993	2308.625	8.26342619

Donor ID	Mean_Norm alized_Intracel lular_TNFa_Ce lLS_Percentag e_LPS_LeuLe uOMePlate	Mean_M onocyte_ Percenta ge_LPS_L euLeuOM ePlate	Mean_T_C ell_Percent age_LPS_L euLeuOMe Plate	Mean_B_ Cell_Perc entage_L PS_LeuLe uOMe plate	Mean_Mark er_Negative _Percentage _LPS_LeuLe uOMePlate	Mean_Cellua lr_Debris_Pe rcentage_LP S_LeuLeuOM ePlate	Mean_Unc lassified_C ell_Percen tage_LPS_ LeuLeuOM ePlate	Mean_Nor malized_IL- 1b_Releas e_LPS_Leu LeuOMePla te	Mean_No rmalized_ TNFa_R elease_L PS_LeuLe uOMePla te	Mean_Ce ll_Per_W ell_LPS + Nigericin	Mean_No rmalized _Activati on_Rate_ LPS + Nigericin	Mean_Norm alized_Intra cellular_TNF a_Cells_Perc entage_LPS + Nigericin	Mean_N ormalize d_IL- 1b_Relea se_LPS + Nigericin	Mean_No rmalized_ TNFa_Rel ease_LPS + Nigericin
DD01	15.13394298	1.827784	57.179238	4.629557	17.3540451	15.358797	3.650579	0	0	2013.75	67.62552	22.6433376	0	0
DD02	65.90606077	11.89381	38.684651	8.407297	30.5614131	8.08403864	2.368794	0.0799525	1.194026	1257.917	145.6051	71.3440105	4.08988	1.990952
DD03	23.3926954	11.66811	34.513028	4.829064	32.787961	11.4413488	4.760492	0.0370933	0.478686	2934.333	53.55203	34.9302567	1.47007	0.643667
DD04	52.09913161	11.31293	34.230675	5.08002	33.610731	11.9331815	3.832463	1.6685975	0.704176	2336.5	62.85357	46.7509908	1.88623	1.168632
DD05	29.99873006	15.67632	35.838627	2.091592	31.5947238	9.03405019	5.764683	0.897736	0.305913	1762.167	73.17221	37.6552079	1.58095	0.856169
DD06	7.93575574	2.162898	38.475274	2.578364	24.7133953	14.4579974	17.61207	0	0	2626.417	15.45694	3.50065686	0	0.101851
DD07	11.86844939	0.596279	35.000385	6.194174	31.3026759	8.10702282	18.79946	0	0.054093	3619.333	49.24174	27.4162389	0	0.274013
DD08	40.55309645	9.225805	17.003947	10.42602	43.6815208	7.08564216	12.57707	0.7151146	1.90058	2775.083	69.12815	35.784102	2.96548	1.694782
DD09	41.72599033	12.48322	33.266817	6.506056	28.9960411	10.390024	8.357837	0.2523528	1.708531	2478.333	58.1724	44.3101035	3.70218	1.023484
DD10	55.24574626	16.4788	21.977768	9.090779	33.4458614	8.2994102	10.70738	0.4040384	2.153629	3067.833	56.60121	35.4801642	2.6877	0.702411
DD11	50.51029541	1.008489	38.705067	4.629269	32.1976799	9.54054575	13.91895	0.3398377	0.283333	3245.917	68.64985	17.8335059	1.84024	1.231757
DD12	64.86679949	9.845999	33.626454	3.275789	30.5788504	9.70505784	12.96785	0.4483245	1.550479	3376.583	71.89397	54.2385237	4.78055	1.097426
DD13	61.2546618	18.8578	13.773863	2.04309	41.2965809	13.5103828	10.51828	0.4622477	1.628135	3064.833	70.99442	61.8867953	4.3769	1.139891
DD14	36.24485219	10.37167	36.080879	6.973511	27.0008585	7.1650573	12.40803	0.5593434	0.65572	3169.5	59.80905	25.417036	3.73336	0.38203
DD15	73.44411831	9.948217	36.86156	3.467837	27.8864523	8.04386509	13.79207	0.813063	2.179164	2599.667	67.22657	56.9567619	3.7891	1.246229
DD16	53.30814088	7.074161	31.183518	5.382994	35.9592526	7.17701688	13.22306	0.2742749	1.780567	2047.583	53.95014	35.9162573	1.77075	0.47223
DD17	35.50027908	21.12728	22.421378	6.361813	30.8408302	5.70760424	13.54109	0.0670959	1.083179	3283.667	65.60379	42.2932657	2.65349	0.429158
DD18	66.519437	13.92224	31.657362	2.478371	30.0547516	8.47580726	13.41147	0.5179918	2.825886	2597	66.69418	62.7143689	3.49727	1.117843
DD19	55.57589006	16.24388	43.384924	3.725775	19.3222207	4.35002786	12.97317	0.294498	2.19818	3551.417	66.44944	56.828868	4.10496	0.668699
DD20	68.28816144	15.75334	35.143708	4.327096	26.2114888	5.76576693	12.7986	0.5598759	2.113565	1896.167	62.92078	56.6040261	2.79866	0.69039
HD04.1	40.28326113	30.94178	18.415824	11.31545	19.664177	16.5555296	3.107238	0.1898414	0.780997	2775.833	83.19278	75.5501736	1.96641	1.517907
HD04.2	50.63288123	30.72028	9.8935815	8.174485	28.6933249	12.832955	9.68537	0.3589833	1.8614	2400.083	83.41952	75.6581635	4.09386	1.207594
HD04.3	61.80970001	26.32336	16.686061	9.397251	30.2686732	7.6253272	9.699325	0.395168	1.740056	3043.167	76.97188	73.4687055	4.26208	1.07197
HD04.4	74.93001016	30.5031	16.310306	8.427739	26.269446	8.65704703	9.83236	0.408999	1.865795	3085.5	77.2716	77.4416228	3.22135	0.605703
HD05.1	57.16166765	17.98447	49.631145	7.095436	8.55715375	13.8990801	2.832715	0.1116664	1.256214	2263.75	107.3498	96.9031855	4.33923	2.755881
HD05.2	81.81179061	17.53319	33.81163	5.29958	19.9220686	11.9207611	11.51277	0.5830575	3.260862	2673.333	83.9358	73.427246	5.43557	1.436746
HD05.3	74.19422864	13.91423	47.484162	4.856413	13.8784061	6.4773495	13.38944	0.3580344	2.324521	3643.667	64.22906	68.865948	4.97479	1.285434
HD05.4	82.03772258	12.64513	50.490264	5.349062	15.5083581	6.06633266	9.940853	0.3342559	2.280632	3550.417	76.02599	74.6626023	3.91414	0.763438
HD06.1	56.5687234	25.70501	25.125026	12.43741	16.0356281	17.3384651	3.358459	0.1457397	0.970585	1943.75	123.6257	101.653579	5.25458	2.266105
HD06.2	89.84148976	18.01845	19.480554	9.410317	30.5602694	13.2791352	9.251278	0.815272	3.507623	1764.417	149.286	129.845879	9.75142	2.585736
HD06.3	80.37808759	18.54043	25.223574	8.141056	27.241196	10.760681	10.09306	0.4008186	1.815916	2618.833	88.71154	85.1602329	5.81181	1.236084
HD06.4	96.3810278	22.75837	23.837311	9.948874	25.3093552	7.31292208	10.83316	0.4373096	2.21489	2402.667	103.2694	107.178865	4.60777	0.916758

Donor ID	Mean_Cell_Per_Well_Nigericin	Mean_Normalized_Activation_Rate_Nigericin	Mean_Normalized_Intracellular_TNFa_Cells_Percentage_Nigericin	Mean_Normalized_IL-1b_Release_Nigericin	Mean_Normalized_TNFa_Release_Nigericin	Mean_Cell_Per_Well_LeuLeuOMe	Mean_Normalized_Activation_Rate_LPS + LeuLeuOMe	Mean_Normalized_Intracellular_TNFa_Cells_Percentage_LPS + LeuLeuOMe	Mean_Normalized_IL-1b_Release_LPS + LeuLeuOMe	Mean_Normalized_TNFa_Release_LPS + LeuLeuOMe	Mean_Cell_Per_Well_LeuLeuOMe	Mean_Normalized_Activation_Rate_LPS + LeuLeuOMe	Mean_Normalized_Intracellular_TNFa_Cells_Percentage_LPS + LeuLeuOMe	Mean_Normalized_IL-1b_Release_LPS + LeuLeuOMe	Mean_Normalized_TNFa_Release_LPS + LeuLeuOMe
DD01	2285.41667	21.2813894	10.79236165	2.54232365	0	2312.91667	21.093424	9.867478524	0	0	2269.917	9.85790778	6.326325274	0.39448899	0
DD02	1491.41667	76.5649817	4.213890985	0	0.287318914	1348.75	88.4032351	57.61626764	2.29629398	0.25172162	1523.167	26.6542744	3.064976136	0	0
DD03	3576.5	21.1611658	3.512352392	0	0.351967322	2974.58333	18.6136967	27.54616098	1.29024497	0.08115377	3292.333	2.35885126	1.929177922	0.21340231	0
DD04	2637	25.8323838	4.383652196	0	1.16274297	2326.41667	27.9075514	56.19523891	2.09546895	0.24402832	2455.583	3.40685832	3.108675044	0.65007211	0
DD05	1924.5	15.8224625	3.136246187	0	0.943244613	1877.25	20.2940538	42.40910122	2.24222021	0.18882989	2072.75	3.71721397	1.451387348	0	0
DD06	2883.91667	13.4584828	3.39768949	1.713443319	0.043011617	2408.41667	9.27646854	6.440487138	0	0.04959992	2233.667	5.23863719	4.61268867	0.0239497	0.268151
DD07	3872.91667	29.7086377	9.724963414	1.831241194	0.193440399	3056.41667	6.64616421	7.338765595	0	0.05344827	3197.583	2.79548712	4.240578275	0	0.043851
DD08	3189.58333	38.1288037	1.346333552	1.75892351	0.068835088	2145.16667	35.6200989	25.27360313	7.22196509	2.77847441	2438.583	11.4047993	1.898697348	0.06096645	0.259741
DD09	2734.58333	30.6139912	2.533197263	0.222308829	0.042443571	2043.91667	37.4808866	29.75340805	4.44998979	1.87127063	2287.667	6.15207507	1.140534133	0	0.035094
DD10	3623.66667	28.717912	2.250088198	0.140045068	0.004020592	2974.75	47.1612232	36.28330701	5.48118112	1.8239524	3159.083	9.52977495	1.550580299	0.01267093	0.026525
DD11	3242.41667	36.1782647	8.99079712	0.128884898	1.277442419	2974.33333	16.7406909	36.66604337	0.12407717	1.0719687	2978.25	9.11937846	14.0939409	0.2061884	0.417733
DD12	3990.16667	15.8392238	3.367207951	0.030686304	0.059856885	3655.25	9.35145373	67.59851269	0.85555568	1.50711292	3856	0.33192132	2.357566171	0.03310384	0.051675
DD13	3171.83333	26.3319757	4.520512263	0.078288802	0.036317669	3480.33333	12.2224751	58.87069085	0.73053453	1.4985711	3430.25	0.68910644	1.93302246	0.00724076	0.029035
DD14	3487.16667	22.0099627	1.079168298	0.462855744	0.150805723	3369.83333	7.07787973	32.42932181	0.87836024	0.84202761	3663.083	0.62724536	0.888105763	0.11904388	0.063326
DD15	2891.5	40.3778239	4.644660176	0.16117199	0.075465549	2979	18.5420507	62.2719022	1.53632259	2.00668415	3199.833	0.55171762	2.795196261	0.03696448	0.132206
DD16	1925.25	15.8839112	2.490304774	0.222609341	0.050982679	1561.75	31.4523014	31.03052376	3.33851717	1.6749742	1908.75	5.9729845	3.170948072	0.05969692	0.067502
DD17	3544.83333	19.4793872	4.360657914	0.03374812	0.010845351	2421.75	26.1428088	44.0656911	3.21074722	1.32566408	2650.833	6.75349532	1.190284896	0.0161169	0.02841
DD18	2551.16667	46.3811462	10.65520572	0.205279216	0.066286572	1879	29.9835044	35.29523828	4.51618513	2.15903243	1625.417	12.9643282	2.398579239	0.17265441	0.16621
DD19	3908.41667	22.167104	3.846596341	0.2204274	0.045743897	3283.5	26.0027595	30.54870895	3.81436914	1.8758477	2563.333	4.17622117	1.694026481	0.34911206	0.191746
DD20	2293.41667	12.3289299	4.900609847	0.069242574	0.015975277	1575.41667	36.2794741	51.13506888	4.69558286	2.43190723	1946.583	4.56519955	2.808988538	0.00629794	0.119691
HD04.1	2895.33333	36.2455809	4.119859825	0	0	3139.66667	23.6795284	53.36382944	2.05414392	0.38378118	3333.833	3.68308296	3.183811198	0.06583756	0
HD04.2	2669.75	40.2156352	3.250289324	0.350878197	0.029007089	2746.66667	52.3984686	46.0124256	6.02984278	2.13939798	2836.083	15.8068886	3.793927889	0.11429838	0.050406
HD04.3	3094.5	39.7084834	4.499010877	0.122279842	0.05924703	3589.83333	9.66753435	64.21677661	0.6150644	1.51891412	3411.167	1.10659806	3.402011428	0.00820669	0.066794
HD04.4	3562	26.142482	4.043037523	0.081543316	0.016497409	3044.5	24.0702343	70.22977856	2.4727045	1.88829375	3106.917	4.10550177	3.311403212	0.0126862	0.065179
HD05.1	2935.83333	36.743465	2.093623121	0	0	3115.91667	32.9013245	73.85637637	3.10882018	0.53682524	3339.5	4.59525591	2.310127734	0.35236613	0
HD05.2	2986.83333	43.9921522	2.031617585	0.534144719	0.034231147	2593.91667	71.0707245	69.26102633	9.08977227	3.43786159	2476.167	18.7880877	2.830490027	0.02603147	0.073692
HD05.3	3412.66667	34.8115332	3.353717151	0.119489566	0.061748115	4123	11.3242018	71.59120686	1.01897698	2.11460334	3600.333	2.05106037	2.053494323	0.01944473	0.061133
HD05.4	3600.16667	24.8165575	2.730164137	0.071027375	0.044776892	3774.75	29.569101	70.65634992	2.96663313	1.99436957	3196.917	5.783522	1.918902599	0.02798681	0.135568
HD06.1	2553.41667	44.7786695	4.53313204	0	0	2630.75	40.3468678	66.31930591	3.06609069	0.47139345	2601.333	8.00974352	4.318440914	0.30095188	0
HD06.2	1875	79.8872205	6.066755141	0.409277988	0.049916484	1823.58333	83.999466	72.0198388	15.7761768	4.60012198	1662.333	34.9621955	6.730571341	0.43346899	0.038329
HD06.3	2420.58333	44.9526258	5.913240772	0.06613653	0.122371196	3051	18.4713611	76.85417004	1.38398996	1.88625699	2966.333	4.65548919	6.206884827	0.01865047	0.114213
HD06.4	2738.66667	31.0435527	6.711076447	0.060317598	0.066456793	2587.66667	29.838334	78.89529097	3.57505314	2.13656066	2537.75	8.74593224	4.591881254	0.01984485	0.101346

8. List Of abbreviations

A1ACT	α 1-antichymotrypsin
AD	Alzheimer disease
ADDF	Alzheimer's Drug Discovery Foundation
AI	Artificial intelligence
ALRs	Absent in melanoma 2 like receptors
ANOVA	Analysis of variance
APCs	Antigen presenting cells
APMI	Alzheimer precision medicine initiative
ApoE	Apolipoprotein E
APP	Amyloid Precursor Protein
Aβ	Amyloid beta
B cell	B lymphocyte
BBB	Blood-brain barrier
BMBF	German Federal Ministry of Education and Research
BSA	Bovine serum albumin
CASP or caspase	cysteine-aspartic acid protease
CNN	Convolved neuronal network
CNS	Central nervous system
CP	Choroid plexus
CRF	Core Research Facility
CSF	Cerebrospinal fluid
CV	Coefficient of Variation
CV microscope	CellVoyager microscope
CV6000	CellVoyager 6000
DAMPs	danger-associated molecular patterns
DKR	German Red Cross
DMSO	Dimethyl sulfoxide Cell culture grade
ELISA	Enzyme-linked immunosorbent assays

fAD	Familial Alzheimer's disease
GUI	Graphic user interface
HCS	High-content screening
HD	Healthy sample
HTRF	Homogeneous Time Resolved Fluorescence
IDAF	Data Analysis Facility
IDAF	Image and Data Analysis Facility
IFNγ	Interferon type 2
IL-1β	Interleukin 1 beta
IL-6	Interleukin-6
ilastik	Interactive Learning and Segmentation Toolkit
LAT	Laboratory Automation Technologies
LeuLeuOMe	L- Leucyl- L- leucine methyl ester
LN2	Liquid nitrogen tank
LPS	Lipopolysaccharide
MCI	Mild cognitive impairment
ML	Machine learning
MMSE	Mini-Mental State Exam
MRI	Magnetic resonance imaging
NF-kB	Nuclear factor kB
NfL	Neurofilament light chain
NK	Natural killer
NLR	NOD-like receptor
NLRP	NOD-, LRR- and pyrin domain- containing
NLRP1	NLR- pyrin domain (PYD)-containing 1
NOD	Nucleotide oligomerization domain
NPV	Negative predictive value
p-tau	Phosphorylated tau
PAMPs	Pathogen-associated molecular patterns
PBMC	Peripheral blood mononuclear cell
PBMCs	Human peripheral blood mononuclear cell

PBS	Dulbecco's phosphate-buffered saline
PCA	Principal components analysis
PDGM	Pancoll Density Gradient Medium
PDGM	Density Gradient Medium
PET	Positron-emission tomography
PDFG-PET	2-[P18PF]fluoro-2-Deoxy-D-glucose
PM	Precision medicine
PMI	Precision Medicine Initiative
PPR	Pattern recognition receptor
PPV	Positive predictive value
PRRs	Pattern recognition receptors
PSEN1	Presenilin1
PSEN2	Presenilin2
PTCL	Peripheral T-cell lymphoma
PYCARD	Apoptosis-associated speck-like protein containing a CARD
RA	Rheumatoid arthritis
RAGE	Receptor for advanced glycation endproducts
RBC	Red Blood Cell
RBCs	Red Blood Cells
RGEPs	Cell type-specific reference gene expression profiles
RT	Room temperature
sAD	Sporadic" Alzheimer's disease
SVM	Support vector machine
T cell	T lymphocyte
t-tau	Total tau
T1DM	Type 1 diabetic mellitus
Tau	Microtubule-associated protein
TLR	Toll-like receptor
TNFα	Tumour necrosis factor alpha
Treg	Regulatory T cell

UKB University clinic of Bonn
UKB University clinic of Bonn

9. List of figures

Figure 1: The formation of senile plaques.	2
Figure 2: Precision medicine aims to stratify patients, according to the genetic, biomarker, phenotypic, and psychosocial characteristics of the individual. From (Antman and Loscalzo 2016)	11
Figure 3: Understanding the immune variation within a population of patients or even healthy population could help a lot to predict the outcome of the healthcare procedures. Such individual stratification based upon immunotyping is a growing strategy in the context of precision medicine. Image from (Brodin and Davis 2017).	12
Figure 4: Variation in immune cells of healthy adults. Principal immune cell populations like monocytes, T and B cells are showing different cellular composition percentage from one healthy adult to another. Thus, inter-individual variation should be considered during the analysis of the immune status for both healthy and patient populations. Adjusted from (Brodin and Davis 2017).	16
Figure 5: Inflammasome activation. A. Inflammasome composes of NLRP sensor molecule, the adaptor protein ASC [apoptosis-associated speck-like protein containing a caspase activation and recruitment domain (CARD)] and caspase 1 (CASP1). Adapted from (Broz and Dixit 2016). B. Inflammasome activation needs two signal processes; priming of TLR4 and activation signals via inflammasome activators like Nigericin and LeuLeuOMe. Modified from (Choi and Ryter 2014).	18
Figure 6: Example of automated image acquisition of stimulated PBMCs using the confocal microscope CellVoyager 6000 (CV6000).	24
Figure 7: A simple example of image analysis workflow to detect nuclei of PBMCs using CellVoyager CV7000 Analysis Software. (A) Input image. (B) Nuclei segmentation. Nuclei were segmented using the signal from the Hoechst33342 staining. (C) Cell area defining. The cellular area was defined by extending nuclear area into an estimated distance.	26
Figure 8: Principle concept of convoluted neural network.	29
Figure 9: U-net network design of the lowest resolution (32x32 pixels) example.	29
Figure 10: PBMC isolation from buffy coat.	38
Figure 11: Liquid pipetting accuracy of the 96-head Biomek NX ^P .	39
Figure 12: Assay plate design	41
Figure 13: ilastik software to label PBMCs.	44
Figure 14: Assay plate design for the patient PBMC screening assay.	46
Figure 15: A. General overview of the PBMC project workflow.	51
Figure 16: Potential phenotypes that can be obtained from the cell-based assay.	53
Figure 17: Schematic of PBMC multi-parametric assay workflow	54
Figure 18: PBMC multi-parametric assay workflow	55
Figure 19: Intracellular TNF α production.	57
Figure 20: Inflammasome PYCARD speck formation assay.	58
Figure 21: The image analysis workflow.	60
Figure 22: Comparison of the two image analysis workflows (Yokogawa versus CellProfiler)	61
Figure 23: Priming status and inflammasome activation upon Nigericin activation	62
Figure 24: Priming status and inflammasome activation upon LeuLeuOMe treatment.	63
Figure 25: HTRF [®] cytokine assay using Nigericin as an inflammasome activator	65
Figure 26: HTRF [®] cytokine assay using LeuLeuOMe as inflammasome activator	65
Figure 27: Comparison of the HTRF [®] and AYOXXA LUNARIS [™] assays for the quantification of IL-1 β release.	66
Figure 28: Manual versus automated PBMC seeding, priming, and activation.	68
Figure 29: Inter-well variation of the automated cell seeding.	70
Figure 30: Assay stability experiment	71
Figure 31: Cell titration experiment	73
Figure 32: Nigericin titration experiment.	74
Figure 33: LeuLeuOMe titration experiment.	75
Figure 34: LPS titration experiment.	76
Figure 35: Performance of three healthy donors (using Nigericin as inflammasome activator).	78
Figure 36: Immune response of three healthy donors using LeuLeuOMe as inflammasome activator.	79
Figure 37: Percentage of viable cells recovered from thawing PBMC vial per day (Recovery rate)	80

Figure 38: The inflammasome activation rate and the percentage of viable cells	81
Figure 39: Cell surface marker staining.	82
Figure 40: Time-lapse of stimulated PBMCs.	84
Figure 41: YAPiC learning phase.	86
Figure 42: The accuracy of YAPiC prediction output.	87
Figure 43: YAPiC prediction consistency was evaluated using untreated PBMCs	88
Figure 44: YAPiC prediction consistency was evaluated using LPS-treated PBMCs	89
Figure 45: Normalization of inflammasome activation rate to the monocyte number	91
Figure 46: Percentage of viable cells recovered from cryopreserved PBMCs of the patient and the healthy volunteer samples	94
Figure 47: Cellular composition of the untreated PBMC samples of the patient and healthy donors	95
Figure 48: Assessment of intracellular TNF α production for each donor in the plates of Nigericin as an inflammasome activator	96
Figure 49: Assessment of intracellular TNF α production for all samples in the plates of LeuLeuOMe as an inflammasome activator	97
Figure 50: Assessment of TNF α release in response to Nigericin-mediated inflammasome activation normalized to the percentage of monocytes.	98
Figure 51: Assessment of TNF α release in response to LeuLeuOMe-mediated inflammasome activation normalized to the percentage of monocytes.	99
Figure 52: Assessment of the inflammasome activation rate in response to Nigericin-mediated inflammasome activation normalized to the percentage of monocytes	100
Figure 53: Assessment of the inflammasome activation rate for each donor in response to LeuLeuOMe activation.	101
Figure 54: Assessment of IL-1 β release into the cell culture supernatant for each donor upon Nigericin activation	102
Figure 55: Assessment of IL-1 β release into the supernatant for each donor upon LeuLeuOMe activation	102
Figure 56: Data aggregation according to disease status (Nigericin plates)	104
Figure 57: Data aggregation according to disease status (LeuLeuOMe plates)	105
Figure 58: The status of gene expression in samples healthy versus diseased donors	107
Figure 59: Immune linked up- and down-regulated pathways in the patient samples.	107
Figure 60: Sample prediction accuracy: Confusion matrix analysis	110
Figure 61: Heatmap of the most representative features for disease prediction	111

10. List of tables

Table 1. Reagents and compounds	35
Table 2. Antibodies	36
Table 3. Kits	36
Table 4. Software	49
Table 5: Clinical information of the Disease Donor (DD) samples.	92